Nonlinear Optical Probes and Processes in Polymers and Liquid Crystals

by

Oksana G. Ostroverkhova

Submitted in partial fulfillment of the requirements
For the degree of Doctor of Philosophy

Thesis Advisor: Prof. Kenneth D. Singer

Department of Physics

CASE WESTERN RESERVE UNIVERSITY

August 2001

To my parents

Table of Contents

List of Tables

List of Figures

Acknowledgments

The nearly five years which I spent working towards my PhD degree were not only a great professional experience, but also a great cultural experience. I am happy that I have met so many wonderful people who made my stay here full of meaning and fun.

First of all, I would like to thank my advisor, Prof. Ken Singer, for his high standards for work, attention, optimism and overall support. In graduate work, the role of advisor is extremely important, and I was very lucky to have Prof. Singer as an advisor.

For me, graduate study here was not only classes and experiments, but also an immersion in a diversity of cultures and customs. I am grateful to Profs. S. Machlup and B. Segall for our musical discussions and concert tickets, to Profs. R. Petschek, R. Brown and C. Taylor for nice conversations in the corridor, to Angie Amato, Lori Rotar, Lucy Rosenberg and Juanita for their support and participation in my life.

I would like to acknowledge all the former and current members of our NLO group as well as collaborators, especially Dr. Jingwen Zhang, Prof. Yu.Reznikov and Dr. Toemsak Srikhirin. Thanks to Andy Stickrath who did his senior project in our lab - our work was a very rewarding teaching experience for me. Special thanks to Prof. J. Andrews who patiently read my papers and provided me with many useful comments. Also, it was an immense pleasure to work with Dr. Irina Shiyanovskaya, who became my close friend.

I am proud to have such a good friend as Dr. Tim Doerr who was always ready to help with anything - from correcting my grammar at any time to discussing physics and life problems.

I was very happy to meet here Zlatko Dimcovic whose kind heart, loyal friendship and overall support have been the source of joy and optimism during all these years.

Most of all, I would like to thank my husband Victor, whose understanding, commitment and devotion have helped tremendously in my work and life here.

Nonlinear Optical Probes and Processes
in Polymers and Liquid Crystals

Abstract

by

Oksana G. Ostroverkhova

Nonlinear optical (NLO) techniques are important for materials research due to their high sensitivity to the molecular properties of the system. In this thesis, I consider both theoretical and experimental background for three NLO effects - the photorefractive (PR) effect, second harmonic generation (SHG) and electric field induced second harmonic generation (EFISHG) in polymers and liquid crystals. I introduce the theoretical molecular model that describes the PR effect in polymers. The dynamics of both photoconductivity and photorefractive grating development is numerically simulated and analyzed. Factors limiting the PR speed in polymers are discussed. A procedure to determine various photoconductivity rates from experiments and, from them, to predict the PR speed is detailed. A complete study of the photoconductive and PR properties of various PVK-based composites is presented. An optimal polymer composite for the PR dynamical

performance is suggested.

Dynamical EFISHG studies of chromophore orientation in PVK-based PR polymer composites are performed. The relationship between the speed of chromophore orientation as observed in EFISHG and in four-wave mixing (FWM) holographic experiments is established.

Surface SHG studies of polymeric Langmuir-Blodgett (LB) films and adsorbed liquid crystal (LC) monolayers are described. The molecular distribution in the monolayers is calculated using the polarization and angle dependence of SHG. The temperature stability of the LB films is studied by measuring the SHG temperature dependence.

The azimuthal angle and polarization dependence of the SHG signal for various point symmetry groups are numerically simulated. Then, using the azimuthal angle dependence of the SHG signal in various polarizations of the fundamental and second harmonic light, the in-plane anisotropy of the UV-illuminated adsorbed LC monolayer is explored.

Chapter 1

Introduction

From ancient times people were interested in light and the interaction of light with matter. With the development of technology, not only has the scientific interest grown immensely, but it has also become possible to use light more extensively for many kinds of applications, from acquiring scientific knowledge about the depths of matter to real life needs such as optical communications, medical surgery and diagnostics using optical tools and techniques, as well as many others. Lasers penetrate our lives so extensively that we may not be aware of the scale. If forty years ago a laser was a luxury and mostly for scientific use, now lasers can be found in places quite remote from science. The invention of lasers also led to a materials science revolution since many potentially useful material properties became accessible for studies and research. The whole field of nonlinear optics emerged forty years ago and developed tremendously in parallel with laser development. Nonlinear optical techniques have proven to be sensitive and reliable for characterization of optical materials. The

work I am presenting here describes several nonlinear optical techniques and their applications for the study of physics of organic optical materials such as polymer composites and liquid crystals.

In nonlinear optics, the nonlinear optical response is described by expressing the dipole moment per unit volume, or polarization density $P(t)$ of a material, as a power series in the electric field $E(t)$ as [1]

$$P(t) = P_0 + \chi^{(1)}E(t) + \chi^{(2)}E^2(t) + \chi^{(3)}E^3(t) + ..., \tag{1.1}$$

where P_0 is the intrinsic polarization, $\chi^{(1)}$ is the linear susceptibility, $\chi^{(2)}$ and $\chi^{(3)}$ are the second- and third-order nonlinear optical susceptibilities. Generally, the nth order optical susceptibility $\chi^{(n)}$ is a tensor of rank $n+1$.

The polarization density is important for the description of nonlinear optical phenomena since a time-varying polarization acts as a source of new components of the electromagnetic field. This is described by the wave equation in nonlinear optical form as

$$\nabla^2 E - \frac{n^2}{c^2}\frac{\partial^2 E}{\partial t^2} = \frac{4\pi}{c^2}\frac{\partial^2 P}{\partial t^2} \tag{1.2}$$

where n is the refractive index and c is the speed of light in vacuum.

For nonlinear optical studies, it appears convenient to work in the frequency domain rather than in the time domain. In this case, if the optical electric field of a laser beam is represented as $E(t) = E\exp(-i\omega t) + c.c.$, then the ω Fourier component

of the polarization density is [2]

$$\begin{aligned} P_i^{\omega} &= P_0 + \chi_{ij}^{(1)}(-\omega;\omega)E_j^{\omega} \\ &+\chi_{ijk}^{(2)}(-\omega;\omega_1,\omega_2)E_j^{\omega_1}E_k^{\omega_2} + \chi_{ijkl}^{(3)}(-\omega;\omega_1,\omega_2,\omega_3)E_j^{\omega_1}E_k^{\omega_2}E_l^{\omega_3} + ... \end{aligned} \tag{1.3}$$

where the summation over repeated indices is assumed. The notation for a frequency domain susceptibility $\chi(-\omega;\omega_1,\omega_2,...)$ is widely used in nonlinear optics [1] and implies that the outcoming wave with frequency ω (the first term in brackets) is generated as a result of interaction between incoming waves with frequencies $\omega_1,\omega_2,....$

When microscopic (individual molecules) rather than macroscopic (molecules packed in the bulk) effects are studied, the microscopic version of Eq. 1.3 is used:

$$\begin{aligned} p_i^{\omega} &= \mu_i + \alpha_{ij}(-\omega;\omega)f_j^{\omega} \\ &+\beta_{ijk}(-\omega;\omega_1,\omega_2)f_j^{\omega_1}f_k^{\omega_2} + \gamma_{ijkl}(-\omega;\omega_1,\omega_2,\omega_3)f_j^{\omega_1}f_k^{\omega_2}f_l^{\omega_3} + ... \end{aligned} \tag{1.4}$$

where $\mathbf{p}$ is the total dipole moment of the molecule, μ is the molecular permanent dipole moment, α_{ij} is the linear polarizability, β_{ijk} is the molecular second order susceptibility (hyperpolarizability), γ_{ijkl} is the molecular third order susceptibility, and $\mathbf{f}$ is a local electric field.

The linear susceptibility $\chi_{ij}^{(1)}(-\omega;\omega)$ is responsible for phenomena such as refraction and absorption. There are many effects due to second order nonlinear susceptibility $\chi^{(2)}$, out of which in this work I will concentrate on second harmonic generation (SHG) described by nonlinear polarization $P_i^{2\omega} = \chi_{ijk}^{(2)}(-2\omega;\omega,\omega)E_j^{\omega}E_k^{\omega}$ and the lin-

ear electro-optic effect $P_i^{\omega} = \chi_{ijk}^{(2)}(-\omega;\omega,0)E_j^{\omega}E_k^0$. For the nonlinear susceptibility $\chi^{(n)}$ with even n (which for most practical purposes is limited to $n = 2$) to have a nonzero value, and thus for the second order effects such as SHG and linear electro-optic effect to exist, a noncentrosymmetric medium is required. The reason is that in a centrosymmetric medium, if we change the sign of the electric field E, then the sign of the induced polarization density P must also change due to inversion symmetry. In second order processes this leads to the relation for the nonlinear polarization density $P = -P$ which suggests that $\chi^{(2)} = 0$. So, second order nonlinear optical effects can be observed only in noncentrosymmetric media which includes crystals of certain symmetry groups that do not possess inversion symmetry, nonlinear optical polymers in which the symmetry is broken by an applied electric field or some other way, media with interfaces and other systems.

These requirements for media do not exist for the effects due to $\chi^{(n)}$ with odd n. The studied odd n nonlinear effects are mostly limited to $n = 3$, although recently a phase-conjugation experiment by nondegenerate six-wave mixing that involves $\chi^{(5)}$ was performed [2]. Examples of the third order optical susceptibility $\chi_{ijkl}^{(3)}(-\omega;\omega_1,\omega_2,\omega_3)$ include third harmonic generation

$$P_i^{3\omega} = \chi_{ijkl}^{(3)}(-3\omega;\omega,\omega,\omega)E_j^{\omega}E_k^{\omega}E_l^{\omega},$$

electric field induced second harmonic generation (EFISHG)

$$P_i^{2\omega} = \chi_{ijkl}^{(3)}(-2\omega;\omega,\omega,0)E_j^{\omega}E_k^{\omega}E_l^0,$$

degenerate four-wave mixing and the optical Kerr effect (intensity dependent refractive index)

$$P_i^{\omega} = \chi_{ijkl}^{(3)}(-\omega;\omega,\omega,-\omega)E_j^{\omega}E_k^{\omega}E_l^{-\omega}$$

and others. Third order effects dealt with in this work include degenerate four-wave mixing, the optical Kerr effect, EFISHG.

Although most of the nonlinear optical effects can be described by the nonlinear polarization density defined in 1.1 through the nonlinear susceptibility $\chi^{(n)}$, there are exceptions. One of these exceptions is the photorefractive (PR) effect which involves a change in refractive index of an optical material that results from the optically induced redistribution of charge [1]. Although it may sound similar to the Kerr effect, in the PR effect, the steady state refractive index change is independent of the intensity of the light that induces the change which is in contrast to the Kerr effect where the refractive index change is directly proportional to the light intensity. The PR effect cannot be described by a nonlinear susceptibility $\chi^{(n)}$ for any value of n and is elaborated by special methods which will be a main part of this work.

This thesis is organized in the following way.

Chapter 2 is devoted to the theoretical aspects of the photorefractive (PR) effect.

The definition, the main processes involved and conventional experimental geometries used for studies and applications of the PR effect are considered in Section 2.1.2.

The photorefractive effect in polymeric materials is governed by photoconductivity

and orientation of nonlinear chromophores under an electric field. Both photoconductivity and chromophore orientation in polymers are complex processes that require separate theoretical treatments.

The processes that contribute to photoconductivity include photogeneration of free charge, charge transport, trapping and recombination. Commonly used theoretical models will be described for each of these processes in Section 2.2. Then, the microscopic model of the PR effect that combines all of the photoconductivity processes will be presented, and the theory of the PR effect will be elaborated. In particular, I will consider the contribution of photogeneration, transport, trapping and recombination in the dynamics of the PR grating formation. Both a semi-empirical approach and numerical simulations that model both photoconductivity and photorefractive dynamical performance in PR polymers will be presented in Section 2.3.

The orientational part of the PR effect involves the ability of the chromophores (dipoles) to orient in both external and internal electric fields. The theory describing these properties in polymer composites will be summarized in Section 2.4. Later, in Chapter 4, the experimental study of chromophore orientations will be presented.

Chapter 3 is the experimental counterpart of Chapter 2. In this chapter, I will describe several photorefractive polymer composites and analyze their photoconductive and photorefractive performance. The main experimental techniques used for studies of photogeneration, charge transport and other photoconductivity processes

(Section 3.3) as well as photorefraction (Section 3.4) will be considered. I will describe some general trends such as temperature, electric field and light intensity dependencies, for each of the processes studied.

As a connection between theoretical Chapter 2 and experimental Chapter 3, the complete theoretical and experimental study of several PR polymer composites is presented in Section 3.5. Using the theoretical procedure developed in Chapter 2 (Section 2.3) and our measurements of various photoconductivity parameters, we predict the photorefractive dynamics. Then, we perform photorefractive measurements and compare experimental results with theoretical predictions [3, 4].

Chapter 4 describes electric field induced second harmonic generation studies of photorefractive polymeric composites. Although EFISHG is not straightforwardly related to photorefraction, this technique can be efficiently used for studies of the chromophore orientation under electric field which, as it was mentioned above, is a part of the photorefractive effect. We performed a set of EFISHG experiments with various photorefractive materials to explore how the orientational speed depends on the electric field, glass transition temperature of the composite, etc. This study became a basis for Andy Stickrath's senior project and Chapter 4 of my thesis.

Chapter 5 is not directly connected to Chapters 2 through 4. It is related to my earlier study of second harmonic generation in polymers and liquid crystals. A study of polarization, angle and temperature dependence of SHG in nonlinear optical

polymeric Langmuir-Blodgett films was a part of collaboration with Dr. Toemsak Srikhirin and Prof.J.Lando from the Dept. of Macromolecular Science at CWRU [5]. Surface SHG of liquid crystal monolayers that reveals the alignment of liquid crystal molecules on fused quartz substrate was a part of the project with Prof.Yu.Reznikov from the Institute of Physics of Ukrainian Academy of Sciences [6].

Finally, Chapter 6 summarizes all the described work.

References

[1] R. Boyd. *Nonlinear optics*. Academic press, San Diego, 1992.

[2] M. G. Kuzyk and C. W. Dirk, editors. *Characterization Techniques and Tabulations for Organic Nonlinear Optical Materials*, volume 60 of *Optical Engineering*. Marcel Dekker, New York, 1998.

[3] O. Ostroverkhova and K. D. Singer. Space-charge dynamics in photorefractive polymers II: Material considerations. *submitted to J. Appl. Phys.*, 2001.

[4] O. Ostroverkhova and K. D. Singer. Space-charge dynamics in photorefractive polymers I: Theoretical considerations. *Submitted to J. Appl. Phys.*, 2001.

[5] J. Lando, T. Srikhirin, D. Schuele, O. Ostroverkhova, K. Singer, P. Taylor, and J. A. Mann. Electronic and optical properties of polysiloxanes with polar sidechains. *Bull. Am. Phys. Soc.*, 44:1737, 1999.

[6] Y. Reznikov, O. Ostroverkhova, K.D. Singer, J.-H. Kim, S. Kumar, O. Lavrentovich, B. Wang, and J.L. West. Photoalignment of liquid crystals by liquid crystals. *Phys. Rev. Lett.*, 84:1930, 2000.

Chapter 2

Photorefractive effect: Phenomenological considerations

2.1 Introduction to the photorefractive effect

The photorefractive (PR) effect is the spatial modulation of the refractive index generated by a specific mechanism: light-induced charge redistribution in a material in which the index of refraction depends upon electric field [1]. The effect arises when the charge carriers photogenerated by spatially modulated light intensity separate by diffusion and drift and become trapped to create a nonuniform space charge distribution. The resulting internal space charge field then modulates the refractive index to produce a phase grating (hologram) that can diffract a light beam.

2.1.1 History of the photorefractive effect

The PR effect was first observed thirty-five years ago in inorganic crystals $LiNbO_3$ and $LiTaO_3$ by Ashkin *et al.* [2] and was considered to be "highly detrimental to

the optics of nonlinear devices based on these crystals", "although interesting in its own right". The effect was called "optical damage" since for the purpose of frequency doubling which was the first priority for studies performed on these crystals, it was harmful. A new material, KTN (potassium tantalate niobate) with similar behavior was reported by F. S. Chen (1967) [3] soon afterwards. The main difference was that the "optical damage" occurred only in the presence of an applied electric field. A little later F. S. Chen *et al.* [4] realized that the "damage" reproduces the original intensity variation in the form of varying dielectric constant, hence it is suitable for holographic recording. Since then, many potentially important applications have been proposed and demonstrated for PR inorganic crystals, including high density optical data storage, image processing (correlation, pattern recognition), phase conjugation, optical limiting, simulations of neural networks and associative memories, and programmable optical interconnection [5]. A number of PR inorganic crystals such as $LiNbO_3$, $KNbO_3$, $BaTiO_3$, $Bi_{12}SiO_{20}$(BSO), $Sr_xBa_{1-x}NbO_3$, InP:Fe, GaAs were characterized for these applications and extensively studied. However, the difficult crystal growth and sample preparation required for PR inorganic crystals has limited the widespread use of these applications.

There are many effects such as photochromism, thermochromism, thermorefraction, $\chi^{(3)}$ Kerr effect and others that can be mistaken for the PR effect. Similarly to the PR effect, all of these effects can be attributed to the mechanisms that can

modify the refractive index of a material in response to an optical beam. However, these mechanisms are local and lack the nonlocal property of the PR effect arising from the physical motion of charges in the material. This charge transport leads to a spatial phase shift between the incident light intensity interference pattern and refractive index modulation. In local mechanisms, the spatial phase shift is equal to zero. A consequence of the nonzero phase shift in PR materials is energy transfer, so called asymmetric two-beam coupling (2BC), between two light beams interfering in a PR medium. If the coupling is sufficiently strong, so that the 2BC gain exceeds the absorption and reflection losses, then optical amplification occurs. This cannot happen in local materials, and thus the presence of energy transfer is a distinct feature of the PR effect in a material. So, when a new material is tested for photorefractive properties, 2BC is the first experiment to perform to ensure the presence of energy transfer due to the PR effect. Also, based on 2BC gain, many applications have been proposed such as coherent image amplification, novelty filtering, self-pumped phase conjugation, beam fanning optical limiters and others [5].

Given such a variety of proposed applications for PR materials, questions of optimization, low cost and easy fabrication have arisen. This is how organic PR materials and in particular polymeric PR materials have entered the scene. One motivation for pursuing the development of organic PR materials is the possibility of achieving a high figure-of-merit that compares the refractive index change possible in different

materials. The figure-of-merit may be defined as [1] $Q = n^3 r_e/\varepsilon$, where n is the optical refractive index, r_e is the effective electro-optic coefficient, and ε is the DC dielectric constant. The figure-of-merit Q approximately measures the ratio of the optical nonlinearity to the screening of the internal space-charge distribution by the polarization. For inorganic materials, Q does not vary much for different materials, which is a result of the fact that the optical nonlinearity in this materials is due to large ionic polarizability [1] and thus an increase in electro-optic coefficient r_e is accompanied by an increase in dielectric constant ε which is not helpful for improving the figure-of-merit Q. For organic materials, however, the nonlinearity is a molecular property which is due to asymmetry of the electronic charge distributions in the ground and excited states [6]. For this reason, large electro-optic coefficients in organic materials are not associated with large DC dielectric constants, and thus a potential improvement in PR performance is possible with organic PR materials.

The first observation of the PR effect in an organic material was reported in nonlinear organic crystal 2-cyclooctylamino-5-nitropyridine (COANP) doped with 7,7,8,8-tetracyanoquinodimethane (TCNQ) [7] in 1990. However, the growth of high-quality doped organic crystals is difficult since most dopants are expelled during the crystal preparation. This problem is easily avoided in polymer composites. Polymers can be easily doped with various molecules and can be cast into a variety of configurations as required by the application. Also, in polymer composites containing nonlinear optical

chromophores, the second order nonlinearity (electro-optic effect) can be produced by electric field poling which breaks the symmetry and therefore allows for the second order effects to occur. This is in contrast to crystals where, as it was mentioned in Chapter 1, there is a limited number of symmetry groups that do not possess inversion symmetry, and so only these noncentrosymmetric crystals are considered as candidates for PR materials.

The first polymer composite that exhibited PR effect was made in 1990 and consisted of an optically nonlinear epoxy polymer bisphenol-A-diglycidylether-4-nitro-1,2-phenylenediamine (bisA-NDPA) doped with hole transport agent diethylamino-benzaldehyde-diphenylhydrazone (DEH) [8]. Since then, the photorefraction in polymers has developed into an active field. Numerous PR polymer composites with improved performance were subsequently studied . However, there are still many unrevealed mysteries in the PR performance of materials and polymers in particular. These are related to the complexity of both the PR effect itself, and to polymers as a disordered medium. All of the work I am presenting here in Chapters 2 and 3 was directed towards obtaining some understanding of these processes in PR polymer composites.

2.1.2 Origin of photorefractivity in polymer composites

The basic phenomena contributing to the PR effect are photoconductivity and the electro-optic effect. The specific processes required for the PR effect include: photo-

generation of charge carriers, transport of mobile carriers, trapping of these carriers in regions of destructive interference and a change of the refractive index in response to the space charge field. In terms of material design, these properties that are necessary to create a PR grating, are generally provided by a photoinduced charge generator, transport medium and nonlinear optical (NLO) chromophores introduced in the composite. In polymer composites, traps are plentiful due to the structure of polymers themselves and also, some NLO chromophores can serve as traps as it will be shown in Section 3.5. Thus, no special agents for creating traps in such a material are needed. However, the simple presence of all of the "necessary" elements in the composite does not guarantee the presence of the PR effect in this composite. Even if a diffraction grating is produced, the two-beam coupling experiment should be performed to prove that the grating is photorefractive.

In the basic experimental configuration, two coherent beams of wavelength λ are incident on the PR slab symmetrically at angles $\pm\theta$ as shown schematically in Figure 2.1. The electric fields of the beams 1 and 2 can be represented as two plane waves

$$\mathcal{E}_1 = \tilde{\mathcal{E}}_{10} e^{i\varphi_1} e^{-i\mathbf{k_1}\cdot\mathbf{r}}, \quad \mathcal{E}_2 = \tilde{\mathcal{E}}_{20} e^{i\varphi_2} e^{-i\mathbf{k_2}\cdot\mathbf{r}} \tag{2.1}$$

where $\tilde{\mathcal{E}}_{10}$ and $\tilde{\mathcal{E}}_{20}$ are the amplitudes of the electric fields of beams 1 and 2, φ_1 and φ_2 are the respective phases, $\mathbf{r}$ is a radius vector and $\mathbf{k_1}$ and $\mathbf{k_2}$ are the wave vectors defining the propagation directions of beams 1 and 2. The physical quantity that

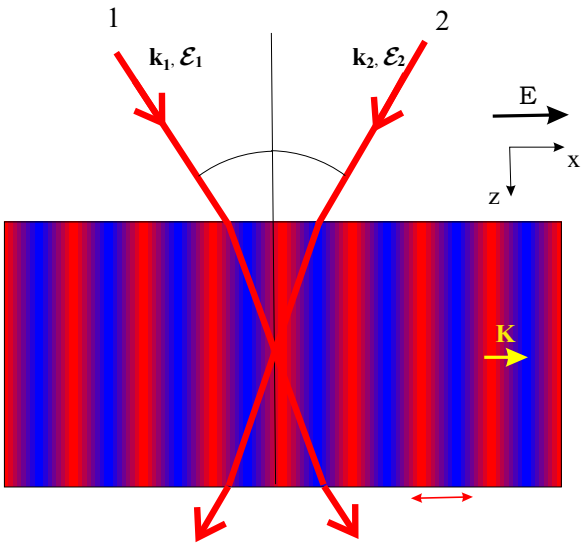

Figure 2.1: Schematic experimental arrangement for two-wave mixing in PR materials.

drives the whole PR process is the interference pattern created by beams 1 and 2. The spatial variation of intensity across the slab can be described by the modulus square of the total electric field created by beams 1 and 2 (Eqs. 2.1)

$$I = |\mathcal{E}_1 + \mathcal{E}_2|^2 = \tilde{\mathcal{E}}_{10}^2 + \tilde{\mathcal{E}}_{20}^2 + 2\tilde{\mathcal{E}}_{10}\tilde{\mathcal{E}}_{20}\cos(\mathbf{K}\cdot\mathbf{r} + \varphi_1 - \varphi_2) \tag{2.2}$$

where $\mathbf{K} = \mathbf{k_1} - \mathbf{k_2}$ is the grating vector. This relationship between the beam wave vectors and the grating vector assumes that the Bragg condition is satisfied. The interference pattern described by Eq. 2.2 has a spatial wavelength (periodicity) given by

$$\Lambda = \frac{\lambda}{2n\sin\tilde{\theta}} \tag{2.3}$$

where n is the refractive index of the material and $\tilde{\theta}$ is the internal angle of incidence for each beam with the respect to surface normal. The physical processes that occur

after the interference pattern is created in a PR material are illustrated in Figure 2.2. Here the x-axis is denoted as the grating vector **K** direction. Since all of these processes are strongly electric field dependent in organic materials, we also consider that the external electric field is applied to the PR slab as shown in Figure 2.1, and is directed along x-axis. Let us consider the process of photorefractive grating formation (Figure 2.2) step by step.

Step 1(Figure 2.2a). Charge photogeneration. Since the PR material is photoconductive (this is one of the major requirements for a PR material), its response to the absorbed optical radiation is the generation of mobile charge. In polymer composites, photoinduced charge generation is provided by a sensitizer molecule that absorbs light and then becomes reduced, injecting a hole into the material. At this step, there is an equal number of mobile holes and immobile ionized acceptors (sensitizers) created in phase with the interference pattern. In polymers, the charge photogeneration process is strongly electric field dependent as will be discussed in detail in Section 2.2.1.

Step 2(Figure 2.2b). Charge transport. At this step, the immobile ions (ionized acceptors) stay in places where they were created, while the mobile generated charge (in organic materials, it is mostly holes - see Section 3.2 for a brief discussion) is transported by either diffusion due to charge density gradients or drift in an externally applied electric field. Both diffusion and drift proceed by hopping of the charge from transport site to transport site (refer to Section 2.2.2 for details). In polymers, charge

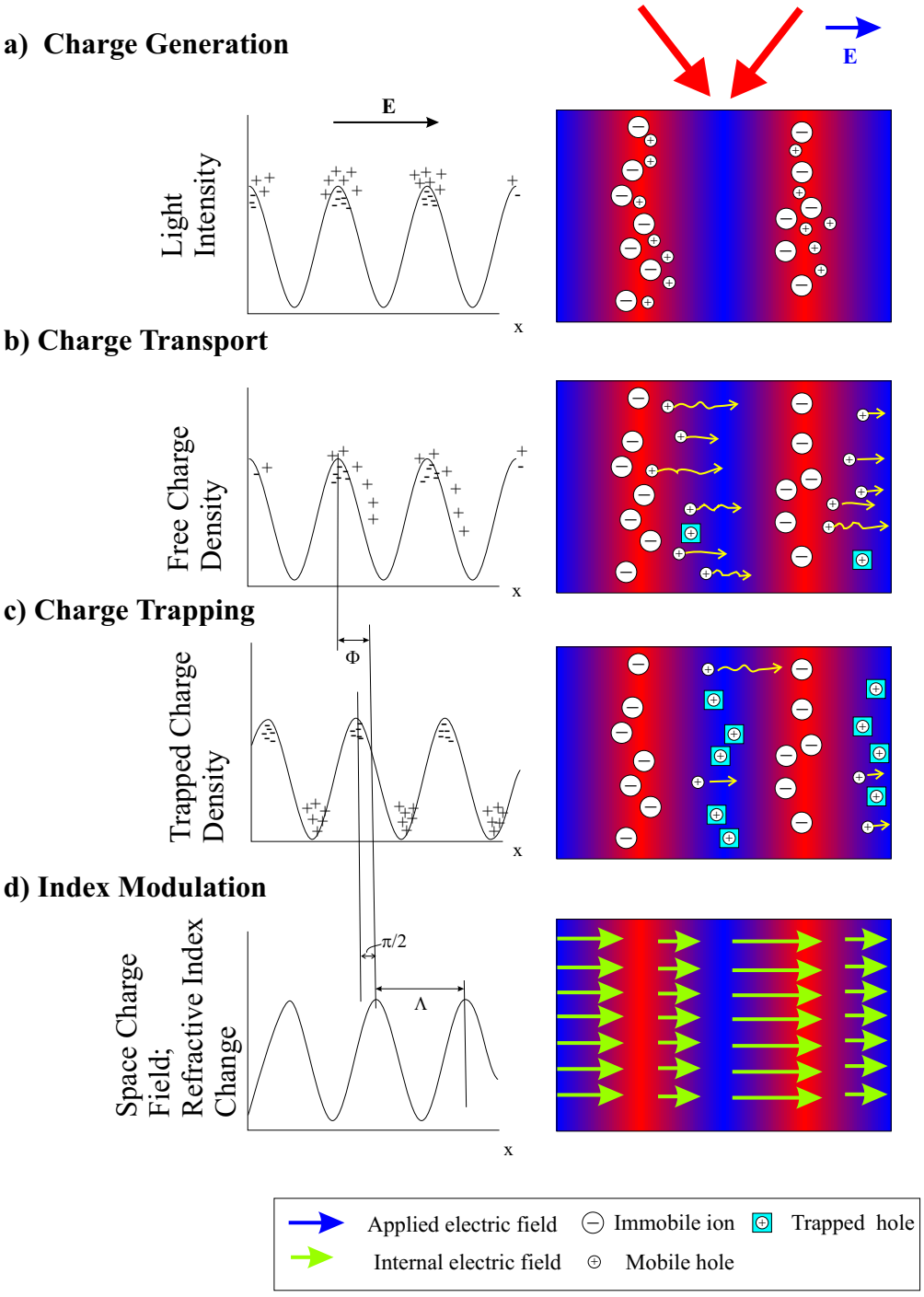

Figure 2.2: Photorefractive grating formation: a) charge photogeneration; b) charge transport; c) charge trapping; d) space charge field formation and refractive index change.

transport is mostly due to drift rather than diffusion, so that the diffusion in most cases can be neglected. Due to Step 2, the created diffraction grating which is the result of the PR effect is phase shifted (Φ in Figure 2.2c) with respect to the light intensity ($\varphi_1 - \varphi_2$, where $\varphi_{1,2}$ are defined in Eqs. 2.1). As already mentioned, $\Phi \neq 0$ is a distinct feature of the PR effect.

Step 3 (Figure 2.2c). Charge trapping. Although it is possible to observe a PR grating created with free charges [5], the presence of trapping sites that would hold the mobile charge is necessary for longer grating lifetimes. On the other hand, for applications that require repeated grating formation and erasing, very deep traps with infinitely large release (detrapping) times are undesirable and not considered here. Thus, we will view a trapping site as a local region of the material where the mobile charge is prevented from participating in transport for some finite period of time. Types, characteristics and nature of traps will be discussed in Section 2.2.3. The resulting space charge density ρ_{total} which occurs after separation of charge carriers (Figure 2.2c) produces a sinusoidal space charge field E_{sc} shifted in space by $\pi/2$ relative to trapped charge (Figure 2.2d) by means of Poisson's electrostatic equation $\nabla E_{sc} = (e/\varepsilon_0 \varepsilon)\rho_{total}$.

Step 4 (Figure 2.2d). Refractive index change in response to the local electric field. Due to the sinusoidal space charge electric field, a spatial modulation of the refractive index occurs. If the material exhibits a linear electro-optic effect, the change in the

refractive index $\triangle n$ is related to space charge field E_{sc} by equation

$$\triangle n = -\frac{n^3 r_e}{2} E_{sc} \tag{2.4}$$

where r_e is the effective electro-optic coefficient. Another effect which leads to the refractive index field dependence in polymer composites is Kerr orientational effect ($\chi^{(3)}$). This orientational effect called "orientational enhancement" is present in PR polymer composites in contrast to both inorganic and organic crystals. The physical mechanism responsible for orientational enhancement is the orientation of NLO chromophores which are the necessary constituents of a PR polymer composite by the local spatially varying space charge field E_{sc}. This effect will be considered in more detail later in Section 2.4.

At this point, the spatially modulated index of refraction and thus, the diffraction grating, is created.

Now, as the PR effect has been introduced, it is time to consider experimental geometries under which it is observed.

2.1.3 Experimental methods for photorefractive studies

The two main experimental techniques used for study of the photorefractive performance of a material are two-beam coupling (2BC) and four-wave mixing (FWM). In this section, we consider the physical grounds for both 2BC and FWM geometries to be employed as PR effect probes.

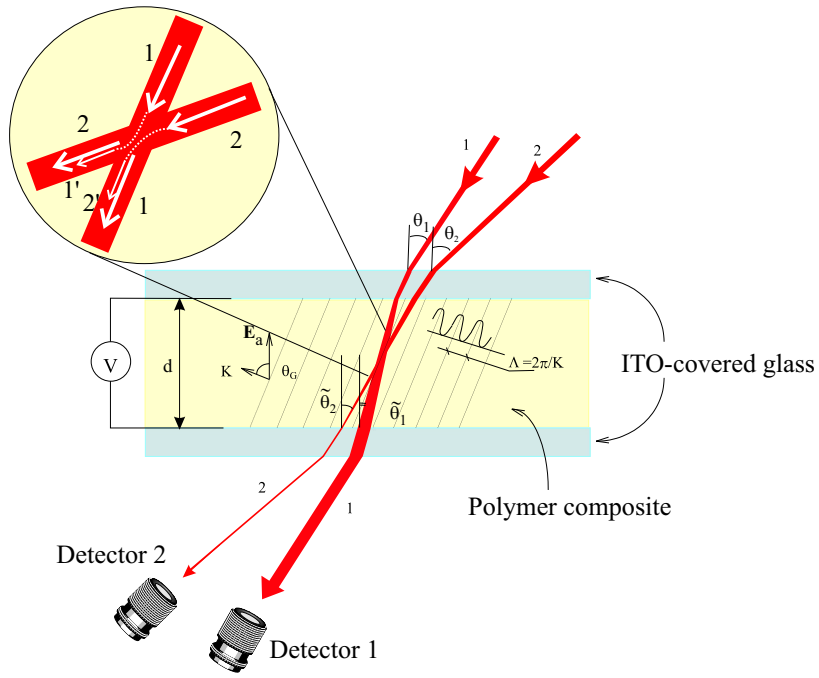

Figure 2.3: Experimental geometry for the two-beam coupling experiment.

Two-beam coupling

As already mentioned before, the two-beam coupling experiment is the first experiment to perform when a new material is tested for PR performance. The geometry of a typical experiment is shown in Figure 2.3. A typical PR polymer sample consists of two ITO-covered glass slides with a PR polymer film of $30-100\,\mu m$ thickness in between. To the best of my knowledge, no PR effect can be observed in polymer composites without an external electric field (typically $\sim 1-150\,V/\mu m$) applied. Optical beams 1 and 2 are incident at angles θ_1 and θ_2 respectively, and interfere in the PR material, creating a nonlocal ($\Phi \neq 0$) diffraction grating. Then the same beams 1 and 2 partially diffract from the grating they have just created (beams 1' and 2' in

Figure 2.3). Due to nonlocality of the grating, one diffracted beam (for example, 1') interferes destructively with its companion beam 2, and the other diffracted beam 2' interferes constructively with beam 1. As a result, the beam 1 is amplified (energy gain) while the beam 2 experiences energy loss. The direction of energy transfer depends on the sign of the electro-optic coefficient and the sign of the charge carrier. The experiment involves measurement of the transmitted beam intensities. In the case of a purely local grating, there is no energy transfer and thus, the intensities of the transmitted beams will be the same as those of the incident beams (if we neglect absorption and reflection losses).

As one notices in Figure 2.3, the beams 1 and 2 are incident at some angles (θ_1 and θ_2) with respect to a sample surface normal. This choice of experimental geometry is governed by several factors. First, all the processes in polymers that are responsible for space charge field build-up are strongly electric field dependent. Therefore, to assist in charge transport along the grating vector $\mathbf{K}$, a large component of external electric field $\mathbf{E_a}$ in the direction of the vector $\mathbf{K}$ is needed. Second, since the NLO chromophores that are part of the PR polymer composite are aligned in the direction of applied field, it is necessary to provide a nonzero component of electro-optic response along the grating vector $\mathbf{K}$.

Ideally, the beams 1 and 2 would be incident symmetrically from opposite sides of the sample, so that the directions of applied electric field $\mathbf{E_a}$ and grating vector $\mathbf{K}$

coincide. However, due to refraction at the air-glass interface, the smallest internal angle of incidence for each beam $\tilde{\theta}$ is equal to 54°, and then for a material with the refractive index $n = 1.6$ which is typical for polymer composites, the largest grating spacing Λ calculated using Eq. 2.3 for the light beam of wavelength $\lambda = 633\, nm$ is approximately equal to 0.25 μm. This is far below the preferable range of grating spacings of $1-5\, \mu m$, since it was shown [9] that the PR gain as measured by 2BC experiment, is a function of grating spacing which peaks at around 1 μm, rapidly decreasing for $\Lambda < 1\, \mu m$ and slowly decreasing for $\Lambda > 1\, \mu m$. For this reason, the oblique geometry such as shown in Figure 2.3, with external angles $\theta_1 = 30° - 45°$ and $\theta_2 = 60° - 75°$, is the usual choice for PR experiments. Also, for such a geometry, Eq. 2.3 which defines the grating period is transformed into

$$\Lambda = \frac{\lambda}{2n \sin[(\tilde{\theta}_2 - \tilde{\theta}_1)/2]} \tag{2.5}$$

After considering all the experimental details relevant to PR polymer samples and experimental geometries, the question that may arise is how to describe the energy transfer in terms of material constants. To answer this question, we consider Maxwell's equations for a PR medium with a spatially modulated refractive index and thus, optical dielectric constant. The optical dielectric constant is related to the refractive index by the simple relation $\varepsilon = n^2$. If the refractive index is spatially modulated through the space charge field E_{sc} and electro-optic effect (Eq. 2.4), then

the dielectric constant is also spatially modulated with the spatially modulated part

$$\Delta\varepsilon = -\varepsilon^2 r_e E_{sc} \tag{2.6}$$

Now we investigate how this change in dielectric constant affects the incident beams. For simplicity, we go back to the geometry shown in Figure 2.1. The analysis for oblique incidence is essentially the same, but the results are more cumbersome which could obscure the main purpose of this discussion. So, the beams 1 and 2 described by fields $\mathcal{E}_1$ and $\mathcal{E}_2$ are incident upon the PR material symmetrically at angles $\pm\theta$. In principle, one should consider internal angles of incidence, but for now we will omit this part as well and operate in terms of θ. It is convenient to present the optical fields of the beams in the following form [5]:

$$\mathcal{E}_1 = \frac{1}{2}[\mathcal{E}_{10}e^{-i\mathbf{k_1 r}} + c.c.], \qquad \mathcal{E}_2 = \frac{1}{2}[\mathcal{E}_{20}e^{-i\mathbf{k_2 r}} + c.c.] \tag{2.7}$$

Similarly, we present the space charge field in the form

$$E_{sc} = \frac{1}{2}[E_{sc,max}e^{-i\mathbf{Kr}} + c.c.] \tag{2.8}$$

where $\mathbf{K} = \mathbf{k_1} - \mathbf{k_2}$ as before. Then, substituting Eq. 2.8 into Eq. 2.6, we obtain the spatially varying part of the dielectric constant

$$\Delta\varepsilon = Fe^{-i\mathbf{Kr}} + c.c. \tag{2.9}$$

where

$$F = -\frac{\varepsilon^2 r_e E_{sc,max}}{2} \tag{2.10}$$

The equation to be solved is the wave equation

$$\nabla^2\mathcal{E} - \mu_0\varepsilon_0\varepsilon\frac{\partial^2\mathcal{E}}{\partial t^2} = 0 \tag{2.11}$$

where $\mathcal{E}$ is the total optical electric field, and dielectric constant consists of non-perturbed part ε^0 and spatially varying part $\Delta\varepsilon$: $\varepsilon = \varepsilon^0 + \Delta\varepsilon$.

The total optical electric field $\mathcal{E}$ in Eq. 2.11 is a vectorial quantity, and in principle must be solved for each component of $\mathcal{E}$. This is where the polarizations of incident beams come into play and as a consequence, influence the coupling constant describing the energy transfer. We will not go into the details and assume the simplest case of optical field directed along y-axis (s-polarized wave). Then, taking into account Eqs. 2.7, the total field $\mathcal{E}$ is given by

$$\mathcal{E} = \frac{1}{2}[\mathcal{E}_{10}(z)e^{-i\mathbf{k_1 r}} + \mathcal{E}_{20}(z)e^{-i\mathbf{k_2 r}} + c.c.] \tag{2.12}$$

where we assumed that the amplitudes of both beams change with z as the beams propagate through the PR slab (Figure 2.1). Substituting Eq. 2.12 and Eq. 2.9 in the Eq. 2.11, we obtain

$$\begin{aligned} &e^{-i\mathbf{k_1 r}}(\nabla^2\mathcal{E}_{10} - 2i\mathbf{k_1}\nabla\mathcal{E}_{10} + k_0^2F\mathcal{E}_{20}) \\ &+e^{-i\mathbf{k_2 r}}(\nabla^2\mathcal{E}_{20} - 2i\mathbf{k_2}\nabla\mathcal{E}_{20} + k_0^2F^*\mathcal{E}_{10}) + c.c. = 0 \end{aligned} \tag{2.13}$$

where $k_0 = 2\pi/\lambda$. Eq. 2.13 can be satisfied if the coefficients in front of exponents vanish separately. Hence, we obtain the coupled equations

$$-2i\mathbf{k_1}\nabla\mathcal{E}_{10} + k_0^2F\mathcal{E}_{20} = 0 \tag{2.14}$$

$$-2i\mathbf{k_2}\nabla\mathcal{E}_{20} + k_0^2 F^*\mathcal{E}_{10} = 0$$

Expressing the wave vectors $\mathbf{k_1}$ and $\mathbf{k_2}$ in coordinates as $\mathbf{k_1} = k(\hat{\mathbf{z}}\cos\theta + \hat{\mathbf{x}}\sin\theta)$, $\mathbf{k_2} = k(\hat{\mathbf{z}}\cos\theta - \hat{\mathbf{x}}\sin\theta)$ where $k = k_0\sqrt{\varepsilon^0}$ $(= 2\pi\sqrt{\varepsilon^0}/\lambda)$, we rewrite the Eqs. 2.14 in the form

$$\begin{aligned}\frac{\partial\mathcal{E}_{10}}{\partial z} + i\frac{Fk_0}{2\sqrt{\varepsilon^0}\cos\theta}\mathcal{E}_{20} = 0 \\ \frac{\partial\mathcal{E}_{20}}{\partial z} + i\frac{F^*k_0}{2\sqrt{\varepsilon^0}\cos\theta}\mathcal{E}_{10} = 0\end{aligned} \tag{2.15}$$

Here we recall that $F \sim E_{sc,max}$. The amplitude of space charge field $E_{sc,max}$ depends on the depth of the intensity modulation

$$m = \frac{2\mathcal{E}_{10}\mathcal{E}_{20}^*}{|\mathcal{E}_{10}|^2 + |\mathcal{E}_{20}|^2} \tag{2.16}$$

as [5]

$$E_{sc,max} = mE_w \tag{2.17}$$

where E_w is the part of the space charge field that does not depend on the intensity of the incident beams. Substitution of Eqs. 2.16, 2.17 and Eq. 2.10 into Eqs. 2.15 yields

$$\begin{aligned}\frac{\partial\mathcal{E}_{10}}{\partial z} - i\frac{n^3 r_e E_w k_0}{2\cos\theta}\frac{|\mathcal{E}_{20}|^2\mathcal{E}_{10}}{|\mathcal{E}_{10}|^2 + |\mathcal{E}_{20}|^2} = 0 \\ \frac{\partial\mathcal{E}_{20}}{\partial z} - i\frac{n^3 r_e E_w k_0}{2\cos\theta}\frac{|\mathcal{E}_{10}|^2\mathcal{E}_{20}}{|\mathcal{E}_{10}|^2 + |\mathcal{E}_{20}|^2} = 0\end{aligned} \tag{2.18}$$

It is obvious that the differential Eqs. 2.18 are not only coupled but also nonlinear which means that there is no guarantee that they can be solved analytically. However, it turns out that they can be integrated. At this point, it is convenient to transform Eqs. 2.18 for optical electric fields into the system of equations operating with beam intensities, so that their connection to the 2BC experiment becomes transparent. For this, we explicitly introduce the phase shift Φ (Figure 2.2c) into the expression for the space charge field

$$E_w = |E_w| e^{i\Phi} \tag{2.19}$$

We also change the variables from fields $\mathcal{E}_{10}$, $\mathcal{E}_{20}$ to intensities

$$I_1 = |\mathcal{E}_{10}|^2, I_2 = |\mathcal{E}_{20}|^2 \tag{2.20}$$

and introduce a coupling constant

$$\Gamma = \frac{k_0 n^3 r_e |E_w|}{\cos\theta} \tag{2.21}$$

Then, after the substitution of Eqs. 2.19, 2.20 and 2.21 into Eqs. 2.18, we obtain the system of differential equations for incident beam intensities:

$$\begin{aligned} \frac{dI_1}{dz} + \Gamma \frac{I_1 I_2}{I_1 + I_2} \sin\Phi = 0 \\ \\ \frac{dI_2}{dz} - \Gamma \frac{I_1 I_2}{I_1 + I_2} \sin\Phi = 0 \end{aligned} \tag{2.22}$$

which are integrated to yield

$$I_1 = I_{10}\frac{1+\beta}{\beta+\exp\left(\tilde{\Gamma}z\right)} = \frac{\beta I_0}{\beta+\exp\left(\tilde{\Gamma}z\right)}$$
$$I_2 = I_{20}\frac{1+\beta}{1+\beta\exp\left(-\tilde{\Gamma}z\right)} = \frac{I_0}{1+\beta\exp\left(-\tilde{\Gamma}z\right)} \tag{2.23}$$

where $I_{10,20}$ are input intensities, $\beta = \frac{I_{10}}{I_{20}}$ is the input beam ratio, $I_0 = I_1 + I_2$ is the total intensity (as it is obvious from Eqs. 2.22, the total intensity does not change with the spatial variable z which reflects the energy conservation law) and $\tilde{\Gamma} = \Gamma \sin\Phi$ is the coupling constant.

It is now easy to analyze Eqs. 2.23. Obviously, when there is no phase shift ($\Phi = 0 \;\Rightarrow\; \tilde{\Gamma} = 0$), then the output intensities are the same as the input intensities ($I_{1,2} = I_{10,20}$). When the input beam ratio is high ($\beta \gg 1$), the weaker beam intensity grows exponentially (assuming that $\tilde{\Gamma} > 0$) while the stronger beam intensity remains almost constant for low values of $\tilde{\Gamma}z$. If the input beam ratio $\beta = 1$, then beam 1 experiences energy loss while beam 2 gains energy. Also, now it is obvious why the electro-optic coefficient and the sign of the carriers determine the direction of energy transfer as stated above: the sign of carriers is responsible for the sign of $\sin\Phi$ while the electro-optic coefficient is responsible for the sign of Γ which are combined in the coupling constant $\tilde{\Gamma}$. As seen from the Eqs. 2.23, the coupling constant $\tilde{\Gamma}$ contains information about energy transfer direction. In inorganic PR crystals, the direction of energy transfer is fixed since the electro-optic tensor is fixed and is determined by

the symmetry group of the crystal and the direction of the c-axis [1]. In PR polymers, the materials are poled *in situ* during the experiment, and the sign of the electro-optic response is determined by the direction of the applied electric field. Thus, the energy transfer direction can be reversed by changing the polarity of the electric field.

In summary of the 2BC technique section, the parameters of interest extracted from the 2BC experiment are the coupling coefficient Γ and phase shift Φ from which other quantities such as the space charge field amplitude can be calculated using Eq. 2.21. Commonly, the 2BC experiment is performed as a function of applied electric field E_a and incident beam polarization. The experimental traits of these dependencies will be considered in Chapter 3. As a final comment to the description of 2BC technique as the PR effect probe, it is important that the energy transfer persists in steady state since there are techniques (moving gratings, frequency detuning etc. [5]) that exhibit transient asymmetric energy exchange in materials with local (non-photorefractive) response.

Four-wave mixing

The experimental geometry for the four-wave mixing experiment is shown in Figure 2.4. It is quite similar to the 2BC experimental geometry - two writing beams are obliquely incident on the PR sample. The difference is that in the FWM experiment, there is also a probe beam (beam 3 in Figure 2.4) in addition to the writing beams 1 and 2. The probe (reading) beam 3 is partially diffracted from the grating created

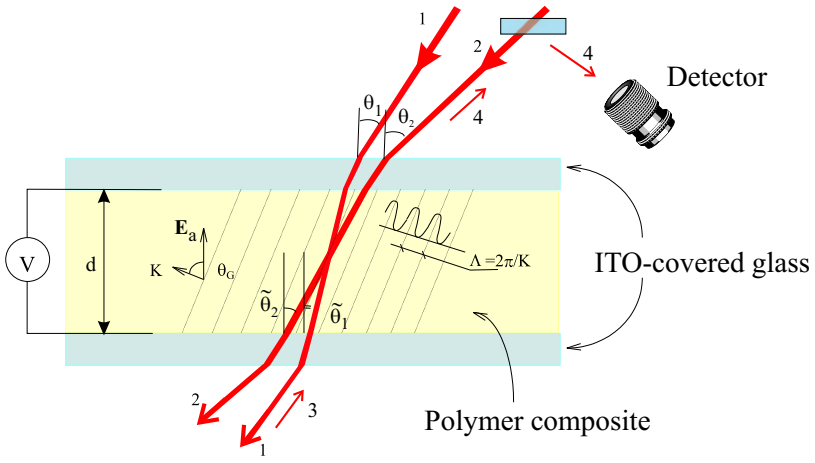

Figure 2.4: Four-wave mixing experimental geometry.

by beams 1 and 2. The intensity of the diffracted part (e.g. of beam 4) is the quantity measured in the FWM experiment. The parameter of interest obtained from the FWM experiment is the diffraction efficiency, defined as the ratio of the diffracted and incident (reading) beam intensities: $\eta = I_4/I_3$. Depending on the application, either the steady-state diffraction efficiency or its dynamics (PR speed) are of primary interest. In this thesis, I was mostly concerned with the PR rise time, or how fast the diffraction grating formed in the PR material. A large part of this manuscript will be devoted to the PR speed and factors that determine the PR dynamical performance.

The geometry shown in Figure 2.4, with the probe beam counter-propagating to one of the writing beams is most often used, since it allows for background-free detection of weak diffracted signals.

Another important feature of the experiment is that the probe beam should be

much weaker than the writing beams and of different polarization, so that it does not affect the grating. Usually, the writing beams are s-polarized, and the probe is p-polarized. The reason for that is that 1) *s*-polarized writing beams experience a weaker energy transfer and 2) the *p*-polarized probe beam experiences a larger diffraction efficiency. This is due to the polarization dependence of the electro-optic response of the material. In general, the electro-optic coefficient is a tensor, and so different polarizations of the optical field couple to different components of the electro-optic tensor which leads to the differences in the diffraction efficiency.

It should be mentioned that in the geometry where the probe beam is counter-propagating to one of the writing beams, special attention has to be paid to the alignment. Essentially, this is a question of how precise the counter-propagation is. If the wavelength of the probe beam is the same as that of the writing beams, then the allowance for the angle of deviation of the probe beam from exact counter-propagation to the writing beam is on the order of $\Delta\theta \sim \Lambda/2d$ where d is the thickness of the sample. $\Delta\theta$ is the width of half maximum in the simplest geometry of symmetric rather than oblique incidence (Figure 2.1)[10]. At the usual grating spacing of $\Lambda = 2\,\mu m$ and sample thickness of $d = 50\,\mu m$, $\Delta\theta \sim 1^\circ$ which shows that the alignment has to be rather accurate.

All the FWM measurements I present here in Chapter 3 are done in the degenerate FWM geometry which means that the wavelength of the reading beam is the same as

that of writing beams. If these wavelengths are different, the experimental geometry should be modified since the reading beam angle of incidence θ' has to be calculated from the Bragg condition $\sin\theta' = \lambda'/(2n\Lambda)$ for a new wavelength λ'.

The coupled wave theory for thick holograms was worked out in detail by Kogelnik [10]. Similar to the approach we used in the previous section to derive the coupled equations for the optical fields of the incident beams (Eqs. 2.18), the wave equation (Eq. 2.11) was solved in the presence of dielectric (refractive) grating described by Eq. 2.9 and absorption grating described by an equation analogous to Eq. 2.9 for conductivity. Since for all the PR composites we used for the PR measurements, the only relevant gratings are dielectric ones, we will consider here only dielectric gratings. Then, the diffraction efficiency observed in the transmission geometry shown in Figure 2.4 with an *s*-polarized reading beam is given by [10]

$$\eta = e^{-\alpha d(1/c_R + 1/c_S)} \frac{\sin^2\sqrt{\upsilon^2 - \varsigma^2}}{\sqrt{\upsilon^2 - \varsigma^2}} \tag{2.24}$$

where c_R and c_S are geometrical factors in terms of the appropriate angles in the notations of Figure 2.4 as

$$c_R = \cos\tilde{\theta}_1 \ , \quad c_S = \cos\tilde{\theta}_2 \tag{2.25}$$

α is the absorption coefficient,

$$\upsilon = \frac{\pi \Delta n d}{\lambda\sqrt{c_R c_S}} \ , \quad \varsigma = \frac{\alpha d}{2}\left(\frac{1}{c_R} - \frac{1}{c_S}\right) \tag{2.26}$$

where d is the thickness of the sample and Δn is given by Eq. 2.4 when orientational enhancement is negligible. If orientational enhancement is important, the relation for Δn is more complicated than Eq. 2.4 [9] and will be considered further, in Section 2.4.

For materials with low absorption such as the PR polymer composites described in this thesis, Eq. 2.24 is simplified to the form

$$\eta = e^{-\alpha d(1/c_R + 1/c_S)} \sin^2\left(\frac{\pi \Delta n d}{\lambda\sqrt{c_R c_S}}\right) \tag{2.27}$$

which is easily extendable to the analogous expression for a p-polarized reading beam [1]

$$\eta = e^{-\alpha d(1/c_R + 1/c_S)} \sin^2\left(\frac{\pi \Delta n d \cos(\tilde{\theta}_2 - \tilde{\theta}_1)}{\lambda\sqrt{c_R c_S}}\right) \tag{2.28}$$

There are a number of limitations to the theory we just applied [10], for which we will list the most important ones.

First, Eqs. 2.27 and 2.28 are derived for thick gratings which implies that diffraction orders higher than the first order are neglected. As a measure of grating thickness, the parameter $\tilde{Q} = 2\pi\lambda d/n\Lambda^2$ was introduced [10]. The grating is regarded as thick when the condition $\tilde{Q} \gg 1$ holds [10]. In commonly used geometries ($\Lambda \sim 2\,\mu m$), a PR polymer ($n = 1.6$) sample of thickness $d = 50\,\mu m$ yields $\tilde{Q} \sim 30$ for a wavelength of $\lambda = 633\,nm$. This is a reasonable approximation of a thick grating.

Second, the derivation assumes a sinusoidal grating described by Eq. 2.9. In PR polymers, at sufficiently high external electric fields ($E_a > 50\,V/\mu m$), terms with spatial dependence $\sim \exp(-2i\mathbf{Kr})$ and higher can appear in Eq. 2.9. This

leads to non-sinusoidal gratings (grating bending) [11]. In this thesis, most of the photorefractive measurements have been done at electric fields lower than $50\,V/\mu m$ and thus, in all calculations we assume a sinusoidal grating.

In contrast to the 2BC experiment, the presence of a diffraction efficiency $\eta \neq 0$ as observed in the FWM experiment is not a proof of the PR effect. Since the phase shift Φ between the interference pattern and diffraction grating does not enter in the expressions for diffraction efficiency (Eqs. 2.27, 2.28), one cannot tell whether the grating is local or non-local. Also, in case of degenerate FWM (with the reading beam wavelength being the same as that of writing beams), the presence of beam 4 (Figure 2.4) due to $\chi^{(3)}(-\omega;\omega,\omega,-\omega)$ Kerr effect can be mistaken for the diffracted from the PR grating beam. Therefore, the FWM experiment should be performed on materials that are already proven to be photorefractive.

The FWM experiment is a good choice for temporal behavior (writing and erasing) studies since it allows one to probe the grating properties non-destructively. Both theoretical and experimental studies of the grating dynamics as observed in the FWM experiment will be presented further in Sections 2.3.2 and 3.5, respectively.

In summary of this section, we considered the definition of the photorefractive effect, requirements for PR materials, and experimental techniques used for PR studies. The main features of PR polymer composites are their photoconductivity (photoinduced charge generation and transport), and the linear electro-optic response and the

ability to reorient in the space charge field (orientational enhancement).

In Section 2.2, we will consider the molecular theory of the photoconductive part (Step 1 through Step 3) of the PR effect. We will determine semi-empirically and by numerical simulations how various photoconductivity parameters influence the PR performance of a polymer composite. Section 2.4 will briefly summarize the theory of orientational enhancement, which is the basis for the orientational part of the PR performance (Step 4). Later, in Chapter 3, we will perform both photoconductive and photorefractive experiments and compare the results to the theoretical predictions made in Chapter 2.

2.2 Molecular theory of the photorefractive effect

In this section, we will introduce the molecular model for the PR effect in polymers. First, we describe the relevant effects and parameters that characterize these processes. Then, we consider existent theoretical models for photogeneration, transport, trapping and recombination and relate the microscopic properties of the polymers on which these models are based to relevant for the PR effect parameters.

The first theoretical description of PR in polymers was adapted from Kukhtarev's [12] theory of inorganic crystals by Schildkraut and Buettner [13]. They included the rate equation for traps in the system of PR dynamical equations and took into account the field dependence of both photogeneration of mobile carriers and mobility. The

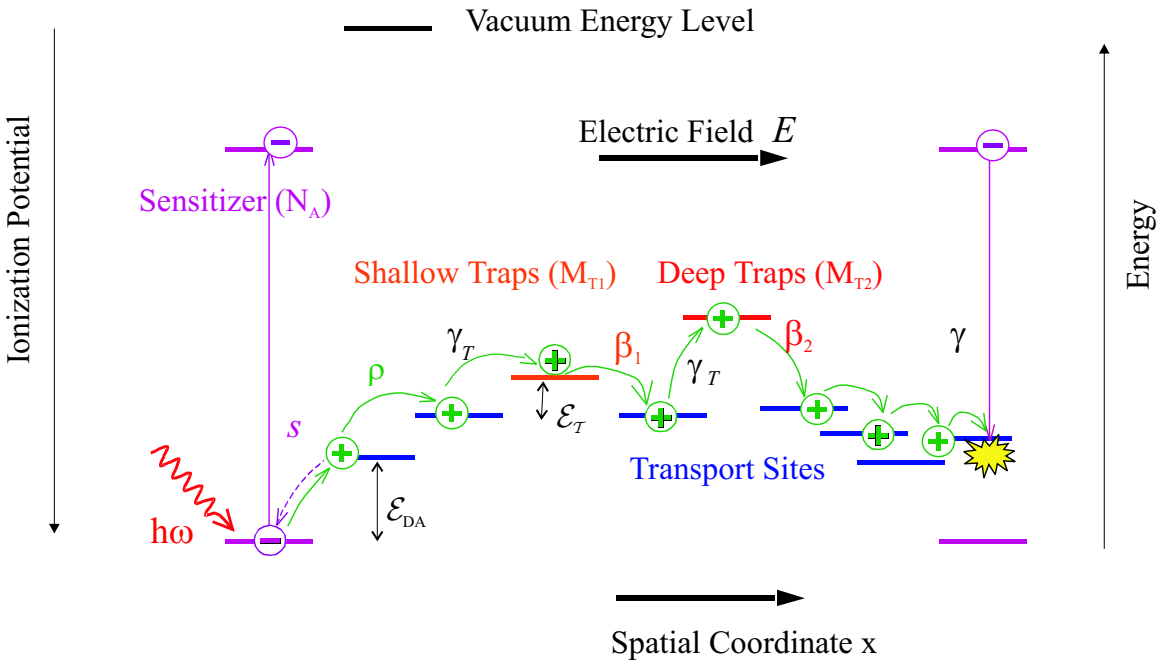

Figure 2.5: Schematic representation of the modified model for photorefractive polymers. Symbols are described in the text.

modified model presented here differs from Schildkraut and Buettner's by introducing two kinds of traps - shallow and deep. Here, by the term "deep," we mean that the rate of thermal detrapping for these traps is at least an order of magnitude lower than that of shallow traps, but still has a nonzero probability for detrapping. The processes taken into account in here are depicted in Figure 2.5. A sensitizer (acceptor) with density N_A is excited and subsequently ionized by light of frequency ω with cross-section s. A free hole is injected into the transport manifold and hops between transport sites until it either becomes trapped or recombines with ionized acceptors with rate γ. Although, generally, the energy spectrum of trapping sites has a continuous distribution [14], we consider only two kinds of traps with well-defined

energy levels (ionization potential) – shallow traps of number density M_{T1} and deep traps of number density M_{T2}. We assume that trapping is not an activated process [15, 16], so that the trapping rate does not depend on the trap depth. Thus, shallow and deep traps are filled with the same trapping rate γ_T. The trapped hole can become free again with a thermal excitation rate β_1 for shallow traps or β_2 for deep traps. Optical detrapping is not considered because the depth of both shallow and deep traps ($< 0.5\,eV$) is much smaller than the photon energy $\hbar\omega$ ($\sim 1.96\,eV$ for HeNe $633\,nm$ light), and so the trapped hole cannot be optically detrapped back to the transport manifold. To verify the absence of optical detrapping, we simulated the time evolution of the DC photocurrent as we describe in Section 2.3.1 with and without optical detrapping. The best agreement between simulated and experimental data occurred in the absence of optical detrapping. Then, the modified system of nonlinear equations describing the PR dynamics are given by:

$$\begin{aligned}
\frac{\partial \rho}{\partial t} &= \frac{\partial N_A^i}{\partial t} - \frac{\partial M_1}{\partial t} - \frac{\partial M_2}{\partial t} - \frac{1}{e}\frac{\partial J}{\partial x} \\
\frac{\partial M_1}{\partial t} &= \gamma_T (M_{T1} - M_1)\rho - \beta_1 M_1 \\
\frac{\partial M_2}{\partial t} &= \gamma_T (M_{T2} - M_2)\rho - \beta_2 M_2 \\
\frac{\partial N_A^i}{\partial t} &= sI(N_A - N_A^i) - \gamma N_A^i \rho \\
\frac{\partial E}{\partial x} &= \frac{e}{\varepsilon_0 \varepsilon}\left(\rho + M_1 + M_2 - N_A^i\right) \\
J &= e\mu\rho E - e\mu\xi\frac{\partial \rho}{\partial x}
\end{aligned} \tag{2.29}$$

Here ρ is the free charge (hole) density, N_A the total density of acceptors, N_A^i the density of ionized acceptors, M_1, M_2, M_{T1}, M_{T2} the densities of filled shallow traps, filled deep traps, and total shallow and deep trapping sites, respectively, E the electric field, and I the incident light intensity. J is the current density, μ the charge carrier drift mobility, ξ is the diffusion coefficient given by $\xi = k_B T/e$. The quantity s is the cross-section of photogeneration, $\gamma_T, \beta_1, \beta_2$ the trapping rate and detrapping rates for shallow and deep traps, respectively, γ the recombination rate, and ε the dielectric constant.

Since the creation of a photorefractive hologram assumes a non-uniform light intensity pattern created by the interfering beams, the incident light intensity can be expressed as a periodic function of x :

$$I = I_0 + I_1 \cos Kx \tag{2.30}$$

where K is the grating vector chosen to be parallel to x -direction.

We consider the parameters s, μ, γ_T and γ to be electric field dependent assuming the following dependencies [17]:

$$s = s(E_{ref})(E/E_{ref})^p, \quad \mu = \mu(E_{ref})e^{\beta_\mu(E^{1/2} - E_{ref}^{1/2})} \tag{2.31}$$

$$\gamma = \gamma(E_{ref})e^{\beta_\mu(E^{1/2} - E_{ref}^{1/2})}, \quad \gamma_T = \gamma_T(E_{ref})e^{\beta_\gamma(E^{1/2} - E_{ref}^{1/2})}$$

Here E_{ref} is the relevant reference electric field for each of the parameters. During photorefractive grating formation, the reference electric field for photogeneration ef-

ficiency is the external applied field, while for mobility, trapping and recombination rates the reference electric field is the projection of the applied field on the grating vector. Electric field dependencies given by Eqs. 2.31 are derived from the photogeneration and charge transport theories for polymers [18]. The most commonly used theories leading to Eqs. 2.31 will be summarized later in this section.

The molecular theory of the PR effect presented by Eqs. 2.29, 2.31 takes into account only the photoconductivity part of the PR performance (Step 1 through Step 3 as introduced in Section 2.1.2). As it can be seen from Figure 2.5 and Eqs. 2.29, the photoconductivity part of the PR effect involves a number of parameters. One of the goals of my work with PR materials was to investigate what parameters are the most crucial for the PR performance, in particular PR speed. Further, we wanted to study whether it is possible to predict the PR speed of a PR polymer composite based on its photoconductive properties. Then, the next step would be to study the photoconductive and PR properties of different materials, observe how good the theoretical prediction was and design an "ideal" PR polymer composite. This is what we actually did and what I am going to describe in the next sections. We start from the brief theoretical description of the relevant PR processes that are characterized by the parameters shown in Figure 2.5.

2.2.1 Photogeneration

The first process we consider is photogeneration, which is represented by cross-section s in Eqs. 2.29 (Figure 2.5). The photogeneration of carriers through the absorption of a photon $\hbar\omega$ in the presence of electric field can be schematically represented as

$$N_A + \hbar\omega \xrightarrow{s} N_A^i + hole \tag{2.32}$$

where similar to Eqs. 2.29 notation is used for the corresponding densities - the acceptor (sensitizer) N_A and the ionized acceptor (acceptor anion) N_A^i.

There are several theoretical models that attempt to describe the photogeneration process [18]. The most frequently used models of photogeneration in organic materials and semiconductors are based on geminate recombination. Geminate recombination is the recombination of an electron with its parent cation. Geminate recombination models assume that the formation of a free electron-hole pair involves the dissociation of an intermediate charge-transfer state. Out of the geminate recombination models, the Onsager formalism [19] has received the most attention in the past decade.

In the Onsager formalism, free carriers are assumed to be created by a multi-step process. The first step is photon absorption and creation of a hot localized electron-hole pair. Then, the hot electron loses its kinetic energy by scattering and becomes thermalized at a mean distance r_0 from its parent cation. This process is described by a primary quantum yield ϕ_0. The final step is either dissociation of the charge-transfer state into a free electron and free hole, or recombination. The

photogeneration efficiency ϕ then is the product of the primary quantum yield and the pair dissociation probability. In the Mozumder approximation [20] of the Onsager formalism, the photogeneration efficiency is given by

$$\phi(r_0, E) = \phi_0 \left(1 - \frac{kT}{eEr_0} \sum_{j=0}^{\infty} A_j \left(\frac{eEr_0}{kT} \right) A_j \left(\frac{e^2}{\varepsilon r_0 kT} \right) \right) \tag{2.33}$$

where

$$A_j(x) = A_{j-1}(x) - \frac{e^{-x}x^j}{j!},\ A_0 = 1 - e^{-x}$$

E is electric field, k is the Boltzmann constant, T is the absolute temperature, r_0 is the initial separation between the electron and its parent cation, ε is the dielectric constant. The Onsager formalism leads to strongly electric field-dependent photogeneration efficiencies that saturate at high fields. At low fields, the efficiencies approach nonzero values as the field goes to zero. The temperature dependencies decrease with increasing field and increasing thermalization distance. The limitation of the Onsager formalism is that it does not describe the process of thermalization which is important in this formalism. As a consequence, the typical thermalization distances obtained for polymers are $\sim 20 - 30\,\text{Å}$ which is much larger than intermolecular distances ($\sim 5\,\text{Å}$) and inconsistent with spectroscopic evidences for mainly nearest-neighbor electron-transfer interactions [18].

Recently, in the PR polymers-related literature, the Marcus treatment [21] developed for charge transfer in chemical reactions started to appear as a description for the process of photogeneration. Similar to Onsager formalism, in Marcus the-

ory photogeneration efficiency depends on the donor-acceptor charge transfer and electron-hole dissociation rates [22]. The charge transfer rate k_{CT} depends on the energy difference $\Delta\mathcal{E}_{DA}$ between highest occupied molecular orbital (HOMO) levels of donor and acceptor [21, 22] (Figure 2.5)

$$k_{CT} = k_0 \exp(-b\Delta R) \exp[-(\Delta\mathcal{E}_{DA} - \lambda_0)^2/(4\lambda_0 k_B T)] \tag{2.34}$$

where k_0 and b are prefactors, ΔR is the distance between reaction centers, and λ_0 is the reorganization energy. The other factor is the electron-hole dissociation [22]. The dissociation probability is directly proportional to the sum of electron and hole mobilities μ [23] and inversely proportional to the thermalization radius r_0. The electric field dependencies obtained from Marcus formalism are very similar to those of Onsager formalism. However, the calculated thermalization distances are considerably lower than those calculated from Onsager theory and therefore, much closer to experimental values.

The final remark in this section is how the parameters introduced in the photogeneration theories correspond to the photogeneration cross-section s that appears in Eqs. 2.29 and is of interest for the PR effect. It is quite easy to relate s to the photogeneration efficiency ϕ which in the Onsager formalism is given by Eq. 2.33. In terms of ϕ, the photogeneration cross-section s is

$$s = \alpha\phi/(\hbar\omega N_A) \tag{2.35}$$

where α is the absorption coefficient, N_A is the acceptor (sensitizer) number density and ω is the light frequency. The quantum (photogeneration) efficiency ϕ can be calculated from the experimentally measured quantities and thus, it is a convenient link to experiments. The xerographic discharge technique which is used for ϕ-measurements will be discussed in more detail in Section 3.3.1.

As promised above, when listing the electric field dependencies of the PR-relevant rates (Eqs. 2.31), I comment on the field dependence of photogeneration cross-section $s \sim E^p$. As seen from Eq. 2.35, the field dependence of s is determined by the field dependence of the quantum efficiency ϕ which according to Eq. 2.33 has a very complicated electric field dependence. Fortunately, it turns out that the field dependence given by Eq. 2.33 in the usual external electric field range ($E = 10 - 100\, V/\mu m$) for polymers can be approximated by a simple form $\phi \sim E^p$, with typical values for the parameter $p \sim 2-3$. At fields lower than $10\, V/\mu m$ and higher than $100\, V/\mu m$, the field dependence is weaker and so these regions must be considered separately.

It is not straightforward to relate the photogeneration cross-section s to the charge-transfer rates defined in Marcus theory, so the quantitative connection to any experimentally accessible value is not clear. However, this formalism is useful for relative measurements. We will use it when discussing the reasons for the differences in s for various PR polymer composites.

2.2.2 Charge transport

In recent years, most studies of charge transport in organic materials have been described by the disorder formalism [24], polaron arguments [25], or Scher-Montroll formalism [26]. The parameter that characterizes charge transport is the free carrier mobility, μ. Transport in PR polymers is usually unipolar (see Section 3.2 for details), with hole mobilities exceeding electron mobilities by a factor of $\sim 10^3$. The typical range for the hole mobility μ in polymers is 10^{-8}–$10^{-5}\, cm^2/(Vs)$. Mobilities are both electric field and temperature dependent. Also, the content of the polymer composite and purity of constituents play crucial role in charge transport. On the molecular level, mobility depends on various characteristics of the system which differ from model to model. We consider the disorder formalism in more detail here, mention the Scher-Montroll model when discussing experimental techniques in Section 3.3.2, and for other models refer to the extensive literature [27, 28, 29, 30].

In the disorder model, it is assumed that the elementary transport step in polymers is the charge transfer between adjacent molecules or sites [18]. Because of the absence of long-range order, hopping sites in polymers are located in statistically different environments, thus both the hopping site energies and intersite distances are subject to a distribution. The distributions arise from fluctuations of dipole-dipole and ion-dipole intermolecular potentials [24]. Electronic states of polymers are considered to be completely localized (Figure 2.6), and the density-of-states (DOS)

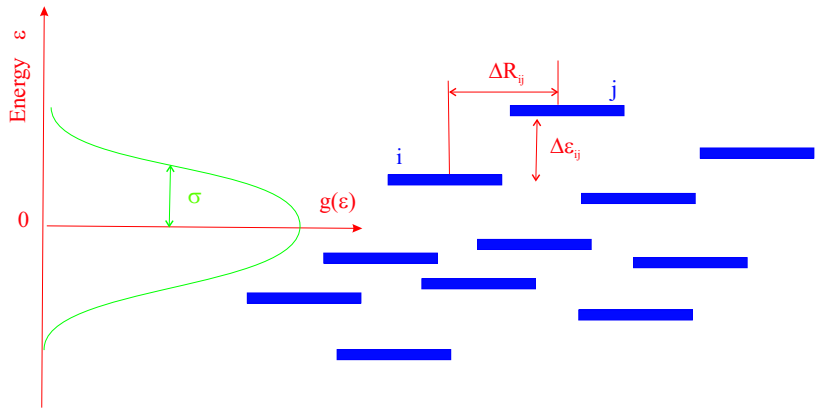

Figure 2.6: Schematic representation of the charge transport manifold in polymers.

distribution is assumed to be of Gaussian shape because it depends on a large number of configurational coordinates, each varying randomly by a small amount. Also, the site energies are uncorrelated. Since the site energies would appear on the diagonal of an energy matrix, this aspect of disorder is described as diagonal disorder, while off-diagonal, or positional, disorder describes fluctuations of intersite distances ΔR_{ij} [31]. The site energy distribution is given by

$$g(\varepsilon) = \frac{1}{\sqrt{2\pi}\sigma} \exp(-\varepsilon^2/2\sigma^2) \tag{2.36}$$

where ε is the site energy relative to the center of DOS and σ its Gaussian width (Figure 2.6). The principal assumptions of the disorder formalism are: 1) the distributions of site energies and distances are Gaussian (Eq. 2.36);

2) the hopping rates can be described by Miller-Abrahams expression [32]. This is a key assumption which will be considered below;

3) electron-phonon coupling is sufficiently weak that polaronic effects can be ne-

glected, yet strong enough to guarantee coupling to a heat bath;

4) the process is incoherent, characterized by the loss of phase memory after each jump.

The Miller-Abrahams expressions for the hopping rates between sites i and j are determined by the product of a prefactor, an electronic wavefunction overlap factor, and a Boltzmann factor for jumps upward in energy. Then, the hopping rates are given by

$$\upsilon_{ij} = \upsilon_0 \exp(-2\delta\Delta R_{ij}) \exp[-(\varepsilon_j - \varepsilon_i)/kT],\ \varepsilon_j > \varepsilon_i \tag{2.37}$$

$$\upsilon_{ij} = \upsilon_0 \exp(-2\delta\Delta R_{ij}),\ \varepsilon_j < \varepsilon_i \tag{2.38}$$

where υ_0 is a frequency prefactor and δ an inverse wavefunction decay constant. As is obvious from Eqs. 2.37, 2.38, the downward energy jumps are non-activated since the probability of such a jump does not depend on the energy difference between sites. The upward jumps are thermally activated which is introduced by the Boltzmann factor in Eq. 2.37. Here "downward" and "upward" energy jumps refer to the electrons. For the holes, the terminology is reversed: "downward" jumps are activated, and "upward" jumps are non-activated. The physical explanation for the asymmetry in hopping rates is that phonons can always be emitted so that energy may be conserved in hops to a lower site, but the probability to absorb a phonon and hop to a higher state is scaled by the probability that such a phonon is available [18]. The electric field dependence of the hopping rates which leads to the electric field dependence of

charge carrier mobility arises from the fact that the electric field changes the effective energy barrier for upward hops. In the presence of an electric field E, the total energy of a carrier is $\tilde{\varepsilon}_i = \varepsilon_i + eE\Delta R_{ij}$ and therefore, the height of the barrier $\Delta\tilde{\varepsilon}_{ij} = \varepsilon_j - \tilde{\varepsilon}_i$ is reduced in comparison to the zero-field value of $\Delta\varepsilon_{ij} = \varepsilon_j - \varepsilon_i$.

As mentioned before, the intersite distance ΔR_{ij} is also subject to local variation and more importantly, coupling between the transport molecules depends on their mutual orientation [33] and, therefore, also contributes to disorder. This means that the overlap parameter $\Upsilon = 2\delta\Delta R_{ij}$ (see Eqs. 2.37, 2.38) possesses a distribution. A characteristic quantity of this kind of disorder (off-diagonal disorder) is $\Sigma = \sqrt{2\Delta\Upsilon}$ where $\Delta\Upsilon$ is the variance of Υ.

Altogether, in the disorder formalism, the characteristic quantities describing the transport properties of the material, are the DOS width σ describing diagonal, or energetic disorder, and the parameter Σ describing off-diagonal, or positional, disorder. In terms of these quantities, the electric field and temperature dependence of mobility μ are given by

$$\mu(\sigma, \Sigma) = \mu_0 \exp[-(2\sigma/3kT)^2] \exp\{C[(\sigma/kT)^2 - \tilde{\Sigma}^2]E^{1/2}\} \tag{2.39}$$

where $\tilde{\Sigma} = \Sigma,\ \Sigma \geq 1.5$ and $\tilde{\Sigma} = 2.25,\ \Sigma \geq 1.5$. In Eq. 2.39, μ_0 is a prefactor, and C is an empirical constant of $2.9 \times 10^{-4}\,(cm/V)^{1/2}$, assuming an intersite distance of 6 Å.

Eq. 2.39 explains the form of the electric field dependence of the mobility we chose

in Eqs. 2.31 ($\mu \sim \exp[\beta_\mu E^{1/2}]$). Eq. 2.39 implies that if the energetic disorder associated with σ prevails, the mobility is an increasing function of electric field. Under conditions with positional disorder dominating, the mobility decreases as the electric field increases [34]. In most polymer composites, at electric fields $E > 20\,V/\mu m$ the energetic disorder prevails and mobility increases as a function of electric field. Some polymers exhibit the dominance of positional disorder at low fields ($E < 10\,V/\mu m$), with decreasing mobility at increasing field [35], but such behavior is rather rare. As for the temperature dependence, for most polymer materials studied, the mobility increases as a function of temperature.

Experimentally, the most frequently used technique for measuring the mobility μ is so-called time-of-flight (TOF) method. We will describe this method in detail in Section 3.3.2. Usually, the TOF measurement in polymers is performed as a function of electric field and temperature which allows one to determine σ and Σ using Eq. 2.39.

Eq. 2.39 is valid for temperatures lower than the glass transition temperature ($T < T_g$). At temperatures above T_g, the nature of disorder in the polymer changes. The potential at a given transport site acquires a significant fluctuating component (dynamic disorder) [36] due to the onset of large-scale motions. Fluctuating local potentials can act to partially cancel the static disorder potential which leads to weaker temperature dependence of mobility than described by Eq. 2.39.

2.2.3 Charge trapping and detrapping

As already mentioned, charge trapping is important for PR grating formation. This process can be schematically represented as

$$Tr_0 + hole \xrightarrow{\gamma_T} Tr^+ \tag{2.40}$$

where Tr_0 denotes an unoccupied trap and Tr^+ represents an occupied (filled) trap. Corresponding to Tr_0 and Tr^+ densities used in the equations that describe the PR effect (Eqs. 2.29) are the difference between total and filled trap densities $M_{T1,2} - M_{1,2}$ and filled trap density $M_{1,2}$.

The rates in the PR model described in Section 2.2 related to traps are the trapping rate γ_T (Eqs. 2.29, 2.40) and detrapping rates $\beta_{1,2}$ for shallow and deep traps, respectively.

There are several considerations related to the process of trapping. One is to treat trapping similarly to hopping in the disorder formalism described in Section 2.2.2. Then, the trapping process is a non-activated downward electron jump (or upward for holes), and the detrapping is an activated electron upward jump (downward for holes), with probability of these processes given by the Miller-Abrahams expressions (Eqs. 2.37, 2.38). In the simplified representation, a trapping site can be imagined as one of the higher energy sites shown in Figure 2.6. If the Miller-Abrahams mechanism is assumed, the trapping rate γ_T does not depend on the trap depth $\mathcal{E}_T$ (Figure 2.5). It rather depends on mobility and trapping cross-section (essentially the probability

of the process itself as given by Eq. 2.38). Assuming that the trapping cross-section does not depend on the electric field, we approximate the form of the trapping rate field dependence with that of the mobility ($\gamma_T \sim \exp[\beta_\gamma E^{1/2}]$).

The detrapping process can be viewed as an inverse to trapping:

$$Tr^+ \overset{\beta_{1,2}}{\rightarrow} hole + Tr_0 \tag{2.41}$$

The detrapping rates $\beta_{1,2}$ are essentially determined by the trap depth $\mathcal{E}_T$ and overlap integral, so that a form similar to Eq. 2.37 (with $\mathcal{E}_T$ instead of $\varepsilon_j - \varepsilon_i$) could be assumed. When we considered charge transport in the presence of an electric field (Section 2.2.2), we said that the electric field reduces the energy barrier, so that the upward electron jumps become more probable and thus, the mobility increases. It appears that the same argument can be used for detrapping which implies that the detrapping rate $\beta_{1,2}$ should increase as a function of electric field. However, since the trap depth $\mathcal{E}_T$ is much larger than the energy difference $\varepsilon_j - \varepsilon_i$ between any transport sites i and j, the relative effect of electric field is much smaller for detrapping than for charge transport. Thus, we consider the detrapping rates $\beta_{1,2}$ independent of electric field.

Another treatment of the trapping process is similar to the Marcus charge transfer theory as applied to photogeneration. In this case, the trapping rate γ_T would be dependent on the trap depth $\mathcal{E}_T$. Then, Eqs. 2.29 would contain the shallow trapping rate γ_{T1} and the deep trapping rate γ_{T2} instead of γ_T. This would further complicate

Eqs. 2.29 and so, we will assume below that the Miller-Abrahams rather than Marcus formalism is applicable to trapping process.

Charge trapping mechanisms in PR polymers are still not clearly understood, although several experimental techniques such as two-beam coupling, [9] absorption spectroscopy [37] and comparison of external photocurrent efficiency to the photogeneration efficiency [38] have been employed to study the properties of traps. The problem is that there are no direct methods to probe the rates and densities appropriate for PR. In Section 2.3.1, I will describe the procedure which allows determination of important trap characteristics. Also, the nature of traps and their influence on PR performance of polymer composites will be discussed in detail theoretically in Section 2.3 and experimentally in Section 3.5.

2.2.4 Recombination

The last process contributing in the dynamic PR effect shown in Figure 2.5 is recombination of the free hole ρ with an ionized acceptor N_A^i characterized by rate γ (see Eqs. 2.29 and Figure 2.5). This process can be schematically represented as

$$hole + N_A^i \xrightarrow{\gamma} N_A \tag{2.42}$$

For such a recombination in PR materials, the most commonly used [13] theoretical approach is the Langevin treatment [15]. It describes the carrier recombination as a random process and assumes that the oppositely charged carriers (in our case these

are holes and acceptor anions) are produced statistically independent of each other. The important initial requirement is that the mean free path ℓ of the carriers be less than the coulombic radius of capture of one carrier by the other r_C:

$$\ell < r_C = \frac{e^2}{4\pi\epsilon_0\epsilon kT} \tag{2.43}$$

where ϵ is the dielectric constant and kT is the thermal energy.

Although the condition given by Eq. 2.43 holds for many organic solids, it may not hold for some type of materials such as radical-ion salts and polymer composites [15].

The process of recombination can be viewed similarly to trapping. The recombination rate is expected to depend on mobility and capture cross-section. However, the major difference between trapping and recombination is that trapping involves the interaction between a hole and neutral trap (Tr_0), while recombination occurs between two charged particles - a hole and an acceptor anion (N_A^i). Thus, due to the Coulomb interaction between charged particles, one expects that the capture cross-section relevant for recombination is higher than that for trapping. As we will see in Section 3.5, this is exactly what is observed experimentally.

If the Langevin approach is assumed, the recombination rate γ is expressed in terms of mobility μ in a following simple way:

$$\gamma = \frac{e\mu}{\epsilon_0\epsilon} \tag{2.44}$$

However, Eq. 2.44 was derived under the assumption of electric-field independent mobility which is not true for polymers. In polymers, the recombination rate is a function of electric field, and it generally departs from the simple Eq. 2.44 [15]. In spite of this fact, we chose the electric field dependence for the recombination rate γ to possess the form similar to mobility (Eq. 2.31) $\gamma \sim \exp\left[\beta_\mu E^{1/2}\right]$.

Although there are experimental techniques such as electroluminescence (EL) or fluorescence (FL) [15] that probe recombination rates, it is important to ensure the connection between the rate found in the EL or FL experiment and γ defined in Eqs. 2.29 which is relevant for photorefraction. Thus, there is a need for a method which allows the measurement of the very same recombination rate γ introduced in Eqs. 2.29 in PR materials. Such a method will be described in the next section.

2.3 Semi-empirical and numerical analysis of the photorefractive model

In the previous section, we introduced a model which describes the PR effect in polymers and considered molecular characteristics of the participating processes. In this section, we will explore how these processes influence the PR performance, especially PR dynamics, of a material.

In principle, what we need to do is solve Eqs. 2.29, 2.30, 2.31 and determine the space charge field which is a direct link to the coupling coefficient (Eq. 2.21) or diffraction efficiency (Eqs. 2.27, 2.28) measured experimentally. However, Eqs. 2.29

are nonlinear and cannot be solved analytically. It is possible to determine the exact space charge field and charge density distributions by numerically solving Eqs. 2.29, 2.31, 2.30. However, it would be nice to obtain some analytical insight about the dynamics of the processes in the PR polymer.

The spatial periodicity of intensity given by Eq. 2.30 suggests the use of spatial Fourier analysis for the analysis of Eqs. 2.29. In small modulation approximation expressed by the condition

$$m = I_1/I_0 \ll 1 \tag{2.45}$$

the approach seems quite straightforward since the spatially variant term in Eq. 2.30 can be considered as a perturbation. This implies that the general spatial dependence of Eq. 2.30 will also apply to the response of the polymeric material, so that all the densities (free charge ρ, filled traps $M_{1,2}$, ionized acceptors N_A^i) and electric field E will assume a spatial dependence similar to that of Eq. 2.30. For example, the electric field E would be expressed as

$$E = E_0 + \tilde{E}_1 \cos(Kx + \Phi) \tag{2.46}$$

where E_0 is the external electric field (or, more precisely, the projection of the applied electric field E_a on x-direction), $\tilde{E}_1$ is the space charge field amplitude, and Φ is a phase shift with respect to the intensity pattern.

If the small modulation approximation is not valid, nonlinear Eqs. 2.29 may lead to all kinds of solutions including higher harmonics, subharmonics and even chaos [5].

So, in this case the form of the solution similar to Eq. 2.46 is no longer valid. In the literature describing the PR effect in inorganic crystals (the field of PR inorganic crystals is about 25 years older than that of PR polymers), the assumption of the small modulation is usually used [39]. Also, there is an abundant amount of literature exploring the possible ways of extension the formalism developed for small m. However, in the PR polymer scientific community, this assumption is often neglected: the theory based on the small modulation assumption is compared to the experiments conducted with writing beams of equal intensities which implies that $I_0 = I_1$ and thus, $m = 1$.

In the PR theory for inorganic crystals in the small modulation approximation, the steady-state space charge field $\tilde{E}_1$ is directly proportional to the modulation m (Eq. 2.45) and does not depend on intensities I_0 and I_1 separately. However, the PR speed depends on the uniform part of intensity I_0 and thus, is not affected by m. Experimentally, the same kind of behavior of the steady-state $\tilde{E}_1$ and PR speed in PR inorganic crystals is observed proving the validity of the theory.

To investigate whether the same trends hold in polymers, we performed the PR experiments (to be described in Section 3.4.2) where we studied how the steady-state space charge field $\tilde{E}_1$ and PR speed change with m. Our experiments show that, similar to inorganic crystals, the steady-state space charge field depends only on m, although the direct proportionality is impaired. However, this fact may reflect

the difference in the basic processes leading to the PR effect in inorganic crystals and polymers [11] such as the importance of trap dynamics in polymer composites. Schildkraut and Cui [17] showed that for the steady-state, the numerically calculated results at $m = 1$ for the free charge density and the amplitude and phase of space charge field were in a good agreement with the corresponding values obtained from the Fourier analysis of the equations analogous to our Eqs. 2.29. This suggests that the small modulation approximation is not crucial for PR polymers.

Our experiments showed that, similar to inorganic crystals, the PR speed does not depend on m, but rather on the intensity I_0. Therefore, the violation of small modulation approximation will not drastically affect the PR speed calculated from Eqs. 2.29. Since we are mostly concerned with the PR dynamics rather than steady-state values, we will not specify m to be small and proceed with Fourier analysis of Eqs. 2.29, 2.30 and 2.31 leaving the zeroth and first order terms only. We will use a Fourier decomposition of all the densities, electric field and current and separate the equations on the basis of the spatial dependence of the terms. Then, the solution of the Eqs. 2.29 can be written in the following form:

$$\zeta = \zeta_0(t) + \zeta_1(t)(C_{\zeta 1} \cos Kx + C_{\zeta 2} \sin Kx) \tag{2.47}$$

where $\zeta = \rho, M_1, M_2, N_A^i, J$. Since the mobility and all of the relevant charge generation, trapping and recombination rates are field-dependent, we assume a form similar to Eq. 2.47 for each of these parameters as well as for the electric field E with time-

independent ζ_0 [17]. We substitute Eq. 2.47 in Eqs. 2.29 and separate the spatially independent zeroth order and spatially varying first order systems of equations.

The significance of the zeroth and first spatial order separation of the (Eq. 2.47) is that the PR grating formation which is the first order process is separated from the processes that occur under uniform light illumination (zeroth order). These zeroth order processes are the basis for photoconductivity in the PR polymers. Further, the photoconductivity described in terms of the zeroth order version of Eqs. 2.29 should contain the same parameters of the PR polymer $(s, \mu, \gamma, ...)$ that determine the first order process, i.e. photorefraction. Moreover, the photoconductivity can be measured quite easily. So, if the PR model described by Eqs. 2.29, 2.30, 2.31 and the Fourier decomposition approach (Eq. 2.47) are valid, we should be able to determine all the rates from photoconductivity (zeroth order), and on this basis predict the PR dynamics (first order). As we proceed, we first develop the zeroth order theory for the DC photoconductivity. Then we will use it for the analysis of photoconductivity experimental data to theoretically predict the PR dynamics (first order). Finally, we will compare the predicted PR behavior to real data obtained from the PR experiments.

So, we start from the zeroth order equations that describe photoconductivity in PR polymers under homogeneous illumination of intensity I_0.

2.3.1 Zeroth Order: Photoconductivity in photorefractive polymers

In this section we explore how the information about rates relevant for PR grating formation can be extracted from the dynamics of photocurrent. The zeroth order system of equations derived from Eqs. 2.29 is written as follows:

$$\begin{aligned}
\frac{dM_{10}(t)}{dt} &= \gamma_T(E_0)(M_{T1} - M_{10}(t))\rho_0(t) - \beta_1 M_{10}(t) \\
\frac{dM_{20}(t)}{dt} &= \gamma_T(E_0)(M_{T2} - M_{20}(t))\rho_0(t) - \beta_2 M_{20}(t) \\
\frac{dN^i_{A0}(t)}{dt} &= s(E_0)I_0(N_A - N^i_{A0}(t)) - \gamma(E_0)N^i_{A0}(t)\rho_0(t) \\
\rho_0(t) &+ M_{10}(t) + M_{20}(t) - N^i_{A0}(t) = 0
\end{aligned} \tag{2.48}$$

One more equation that is not included in Eqs. 2.48 but provides a link to DC photoconductivity experiments is the equation for the photocurrent $J_0(t)$ that is given by the expression $J_0(t) = e\mu(E_0)\rho_0(t)E_0$. Eqs. 2.48 describe the dynamics of free charge generation followed by transport, trapping, detrapping and recombination in the photorefractive polymers under external electric field E_0. We consider the electric field E_0 to be constant and given by $E_0 = V/d$, where V is the applied voltage, and d is the thickness of the polymeric film. Then, the time evolution of the photocurrent $J_0(t)$ is the probe for the dynamics of free charge density $\rho_0(t)$ that is connected through the Eqs. 2.48 to the generation, trapping, detrapping and recombination processes in the PR polymers. The rates describing these processes $(s, \gamma_T, \beta_{1,2}, \gamma)$ are the intrinsic characteristics of the polymer composites, and our goal is to determine their influence

on the both photoconductivity and photorefractive speed. It should also be mentioned that since all the rates are electric field dependent, the photoconductivity experiments have to be conducted at the range of external electric field E_0 that covers both applied electric field in PR experiment E_a and its projection on the grating vector $\tilde{E_a}$ in order to proceed with calculating the space charge field dynamics (first order) on the basis of parameters determined from the photoconductivity (zeroth order).

To study the temporal behavior of the free charge ρ, trapped charge M_1, M_2 and ionized acceptor N_A^i densities, it appears to be convenient to transform the Eqs. 2.48 to a dimensionless form. The time scale is normalized by the average drift time of the free carrier before it is trapped by a shallow trap: $\tau = t/\tau_0$, where $\tau_0 = 1/(\gamma_T(E_0)M_{T1})$. The reason for this choice of time scale will be explained later in the Section 2.3.1. We express all the densities in terms of total acceptor density N_A: $\varrho = \rho/N_A$, $m_{T1,2} = M_{T1,2}/N_A$, $m_{1,2} = M_{1,2}/N_A$, $n_A^i = N_A^i/N_A$. We also introduce the relative photogeneration, recombination and detrapping parameters $\tilde{s}I_0 = sI_0\tau_0$, $\tilde{\gamma} = \gamma N_A \tau_0$ and $\tilde{\beta}_{1,2} = \beta_{1,2}\tau_0$ respectively. The dimensionless analog of Eqs. 2.48 is then written as follows:

$$\begin{aligned}
\tfrac{dm_{10}}{d\tau} &= (1 - \tfrac{m_{10}}{m_{T1}})\varrho_0 - \tilde{\beta}_1 m_{10} \\
\tfrac{dm_{20}}{d\tau} &= \tfrac{m_{T2}}{m_{T1}}(1 - \tfrac{m_{20}}{m_{T2}})\varrho_0 - \tilde{\beta}_2 m_{20} \\
\tfrac{dn_{A0}^i}{d\tau} &= \tilde{s}I_0(1 - n_{A0}^i) - \tilde{\gamma} n_{A0}^i \varrho_0 \\
\varrho_0(\tau) + m_{10}(\tau) + m_{20}(\tau) - n_{A0}^i(\tau) &= 0
\end{aligned} \tag{2.49}$$

This is a nonlinear system that cannot be solved analytically. However, we can consider different cases depending on the total trap densities with respect to the acceptor density in the material, leading to simplifications of these equations.

Case 1. Both total shallow and deep trap densities are smaller or on the order of the acceptor density: $m_{T1,2} \lesssim 1$.

Case 2. The total deep (shallow) trap density is smaller or on the order of acceptor density, but the total shallow (deep) trap density is much larger than the acceptor density: $m_{T2} \lesssim 1, \;\; m_{T1} \gg 1$ or vice versa. In this case, the ratio $m_{10}/m_{T1} \ll 1$ (or $m_{20}/m_{T2} \ll 1$) is always valid, and the first (second) equation in the Eqs. 2.49 is simplified.

Case 3. Both deep and shallow total trap densities are much larger than the acceptor density: $m_{T1,2} \gg 1$. In this case both ratios $m_{10}/m_{T1} \ll 1$ and $m_{20}/m_{T2} \ll 1$ are always valid, so that both first and second equations in the Eqs. 2.49 become linear.

Based on the high value of the trapping product $\gamma_T M_{T1}$ exhibited by all PVK-based PR composites which we studied [40](see Section 3.5), we can exclude the *Case 1* from consideration. However, both *Case 2* and *Case 3* can be applicable depending on the chromophore ionization potential and concentration which will be detailed in Section 3.5 [40]. Since *Case 3* is easier to handle, we start our analysis from *Case 3* and then extend it to *Case 2*.

Trap-unlimited regime

In this section we consider the case when the total density of both shallow and deep traps is much higher than the acceptor density $m_{T1,2} \gg 1$ (*Case 3*). Then, the Eqs. 2.49 are simplified to:

$$\begin{aligned} \frac{dm_{10}}{d\tau} &= \varrho_0 - \tilde{\beta}_1 m_{10} \\ \frac{dm_{20}}{d\tau} &= \frac{m_{T2}}{m_{T1}}\varrho_0 - \tilde{\beta}_2 m_{20} \\ \frac{dn^i_{A0}}{d\tau} &= \tilde{s} I_0 (1 - n^i_{A0}) - \tilde{\gamma} n^i_{A0} \varrho_0 \\ \varrho_0(\tau) + m_{10}(\tau) + m_{20}(\tau) - n^i_{A0}(\tau) &= 0 \end{aligned} \tag{2.50}$$

We also assume that the density of total shallow traps is much larger than the density of total deep traps $m_{T1} \gg m_{T2}$ which seems to be relevant for all the composites we studied [40](see Section 3.5). Then, we can separately consider different time scales at which either shallow ("short time scale") or deep ("long time scale") trap dynamics prevails in order to provide insight into the experimentally observed trapping, detrapping and recombination rates as deduced from DC photoconductivity.

Short time scale On the short time scale, the dynamics of the system is entirely determined by shallow traps. To probe the behavior of our system, we first consider the initial rise in photocurrent as the nonlinear term $\tilde{\gamma}\varrho_0 n^i_{A0}$ in the third equation of Eqs. 2.50 is much smaller than the linear term $\tilde{s} I_0 n^i_{A0}$ in that same equation. This transforms the nonlinear system of Eqs. 2.50 into a linear one that can be solved

analytically. Then, we seek a solution of the form $\varsigma = \varsigma_0 e^{-\tilde{\lambda}\tau}$, where $\varsigma = m_{10}, m_{20}, n^i_{A0}$, and then solve for the three characteristic rates $\tilde{\lambda}$ that determine the dynamics of DC photoconductivity:

$$\begin{aligned} \tilde{\lambda}_1 &= 1 + m_{T2}/m_{T1} \approx 1 \\ \tilde{\lambda}_2 &= \tilde{s} I_0 \\ \tilde{\lambda}_3 &\approx \tfrac{\tilde{\beta}_2 + (m_{T2}/m_{T1})\tilde{\beta}_1}{1+(m_{T2}/m_{T1})} \approx \tilde{\beta}_2 + (m_{T2}/m_{T1})\tilde{\beta}_1 \end{aligned} \tag{2.51}$$

In Eqs. 2.51, we assume that the detrapping parameters $\tilde{\beta}_1$ and $\tilde{\beta}_2$ are much smaller than 1 and (m_{T2}/m_{T1}) correspondingly. This assumption holds when the free charge density is much smaller than the density of filled traps as observed in a variety of materials [41, 38]. We have also confirmed this in our photoconductivity experiment for materials described in Section 3.5. For this reason and also in keeping with our experimental observations that the charge generation rate at reasonable experimental intensities $I_0 < 1\, W/cm^2$ is much smaller than the trapping parameter $1/\tau_0$ i.e. $\tilde{s} I_0 \ll 1$, we can assume that $\tilde{\lambda}_2 \ll \tilde{\lambda}_1$ and $\tilde{\lambda}_3 \ll \tilde{\lambda}_1$. Thus, the fastest photoconductivity dynamics is given by unity $\tilde{\lambda}_1 \approx 1$ in the dimensionless form. This fact explains our choice of the time scale being normalized with respect to $\tau_0 = 1/(\gamma_T M_{T1})$.

Thus, in the DC photoconductivity experiments, the fastest photocurrent dynamics ($J_0(t) \sim \rho_0(t)$) is determined by the value for the shallow trapping product $\gamma_T M_{T1}$. This feature is illustrated in Figure 2.7 where the photocurrent dynamics $J_0(t) \sim \rho_0(t)$ is simulated using Eqs. 2.50 with various shallow trapping product values $\gamma_T M_{T1}$. As

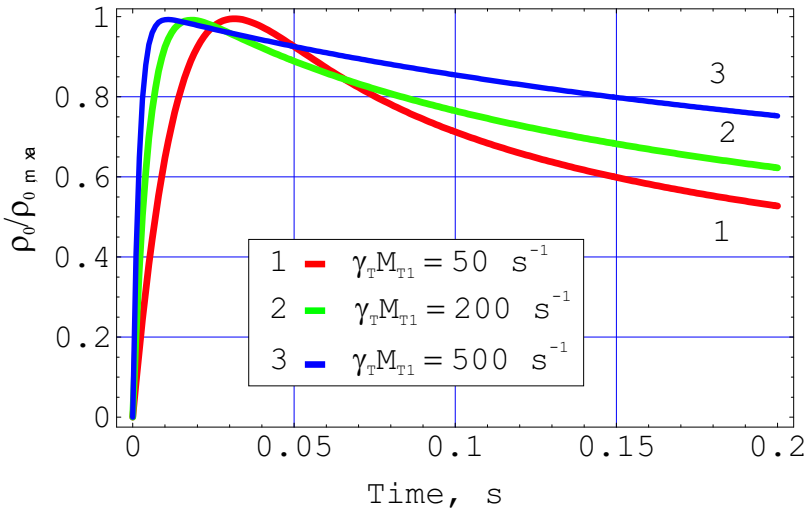

Figure 2.7: Photocurrent dynamics normalized by the maximum photocurrent value for various values of shallow trapping product $\gamma_T M_{T1}$ as simulated using Eqs. 2.50.

it can be seen from Figure 2.7, the larger the trapping product $\gamma_T M_{T1}$, the faster the photocurrent reaches its maximum.

The next longer time regime (though still in the shallow trapping fast limit) we need to consider that the free charge density has reached a maximum and, at sufficiently large recombination rates $\tilde{\gamma}$, starts to decrease. Figure 2.8 shows how the free charge density dynamics ($\varrho_0(\tau)$) reflects differences in the recombination rate $\tilde{\gamma}$. At smaller recombination rates at which the photocurrent does not exhibit decay on the short time scale, the determination of γ from the DC photoconductivity experiment could be difficult. In the polymer composites we studied, the recombination is quite large, so that the photocurrent has a well-defined peak that can be analyzed using the approach which I am about to describe.

We consider the time regime when the free charge density has reached its maximum

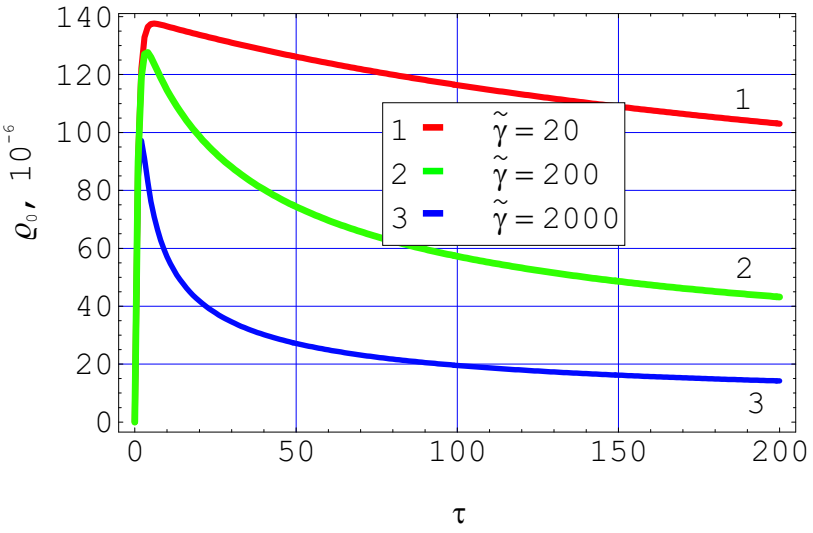

Figure 2.8: Photocurrent dynamics for various recombination rates $\tilde{\gamma}$ simulated using Eqs. 2.50.

and started to decrease. Then, to linearize the third equation in the Eqs. 2.50, we replace the free charge density function $\varrho_0(\tau)$ in the nonlinear term of the third equation in Eqs. 2.50 with a quasi-steady value $\overline{\varrho_0}$. We again obtain three time constants – $\tilde{\lambda}_1$ and $\tilde{\lambda}_3$ the same as in Eq. 2.51, with $\tilde{\lambda}_2$ given by: $\tilde{\lambda}_2 = \tilde{s}I_0 + \tilde{\gamma}\overline{\varrho_0}$. Note, we still have $\tilde{\lambda_2} \ll \tilde{\lambda}_1$ in accordance with our assumption of active traps. In this intermediate time regime, $\tilde{\lambda}_2$ contains information regarding the recombination parameter $\tilde{\gamma}$, while the slowest rate $\tilde{\lambda}_3$ is beyond the time scale here.

Summarizing the dynamics of the photoconductivity on a short time scale (for PVK-based materials we studied (Section 3.2), this corresponds to $\tau \lesssim 50$), we obtain the following expressions for DC photoconductivity rates: $\tilde{\lambda}_1 \approx 1$; $\tilde{\lambda}_2 = \tilde{s}I_0 + \tilde{\gamma}\overline{\varrho_0}$. In keeping with our experiments, in the low intensity regime (below $1W/cm^2$), we can

simplify these to: $\tilde{\lambda}_1 \approx 1;\ \tilde{\lambda}_2 \approx \tilde{\gamma}\overline{\varrho_0}$.

Thus, in DC photoconductivity experiments the short time scale dynamics can be fit with a bi-exponential function, where the faster rate λ_1 yields the shallow trapping product $\gamma_T M_{T1}$, and the slower rate λ_2 is directly related to the recombination rate γ. As we already mentioned above, for the PVK-based materials we studied, we considered the range of $\tau \leq 50$ to be the "short time scale". This range corresponded to $t \leq 0.1-1\,s$ depending on the applied electric field for the samples with low chromophore and plasticizer content ("unplasticized") and $t \leq 2$–$20\,s$ for the samples with high chromophore or plasticizer content (see Section 3.5 for details).

To test our approximations, we performed numerical simulations fixing $\tilde{s}I_0 = 10^{-3}\tau_0$, $m_{T2}/m_{T1} = 0.1$, $\tilde{\beta}_1 = 0.1\tau_0$, $\tilde{\beta}_2 = 0.001\tau_0$, and varying the average carrier lifetime τ_0 and the recombination parameter $\tilde{\gamma}$. This choice of parameters used for the simulation was suggested by the corresponding physical values determined experimentally and listed in Section 3.5. First, at $\tilde{\gamma} = 5 \cdot 10^4\tau_0$ we substituted various values of the parameter τ_0 into Eqs. 2.50, and numerically solved this system to find the dependence of $\varrho_0(\tau)$ for $\tau \leq 50$. On this time scale, the free charge density grows as charge is injected into the transport manifold, reaches a maximum $\varrho_{0,\max}$ and then decreases, due to recombination and trapping. We then fit the calculated curve of the free charge density $\varrho_0(\tau)$ with a bi-exponential function

$$\varrho_{fit} = A\left(1 - Be^{-\tilde{\lambda}_{10}\tau} + (B-1)e^{-\tilde{\lambda}_{20}\tau}\right) \tag{2.52}$$

to determine $\tilde{\lambda}_{10}$ (the faster constant) and compare it to $\tilde{\lambda}_1 = 1$. At $B > 1$ Eq. 2.52 describes the photocurrent rise with the rate $\tilde{\lambda}_{10}$ and then the photocurrent decay with the rate $\tilde{\lambda}_{20}$. We found that the faster constant in the bi-exponential fit yields values equal to unity within 10%, as anticipated. To extract the slower rate, we used a fixed $\tau_0 = 5\,ms$ (typical value for an unplasticized sample observed in DC photoconductivity experiment at $E_0 \sim 30\,V/\mu m$ and $I_0 \sim 50\,mW/cm^2$) for different recombination parameters $\tilde{\gamma}$, found $\varrho_0(\tau)$, and fit it to Eq. 2.52 to determine $\tilde{\lambda}_{20}$. We found that $\tilde{\lambda}_{20}$ agrees with $\lambda_2 = \tilde{\gamma}\overline{\varrho_0}$ ($\overline{\varrho_0} = \varrho_{0,\max}$) within a factor of three. As we show later in Section 2.3.2, an error of this magnitude in the recombination rate actually has a negligible effect on the PR speed. This agreement is remarkable since we dealt so crudely with the nonlinear term containing the charge density.

As an example, consider the dynamics of the DC photocurrent simulated using the parameters $\tilde{s}I_0 = 5\cdot 10^{-5}$, $m_{T2}/m_{T1} = 0.1$, $\tilde{\beta}_1 = 5\cdot 10^{-4}$, $\tilde{\beta}_2 = 5\cdot 10^{-6}$, $\tilde{\gamma} = 2.5\cdot 10^2$ (solid line in Figure 2.9). The dashed line in the figure is a bi-exponential fit of the short time behavior using Eq. 2.52. The faster inverse time constant of this fit $\tilde{\lambda}_{10} = 1.1$ reflects the expected unity value within 10%. The slower speed $\tilde{\lambda}_{20} = 1.9\cdot 10^{-2}$ divided by the dimensionless free charge density in its maximum $\varrho_{0,\max} \approx 4.4\cdot 10^{-5}$ yields, according to $\tilde{\lambda}_{20} = \tilde{\gamma}\varrho_{0,\max}$, a recombination parameter $\tilde{\gamma} \approx 4.3\cdot 10^2$, which is within the expected range of values given the input value $\tilde{\gamma} = 2.5\cdot 10^2$. The bi-exponential of Eq. 2.52 fits the $\varrho_0(\tau)$ dependence perfectly at $\tau < 50$ (Inset of Figure 2.9), but as the processes

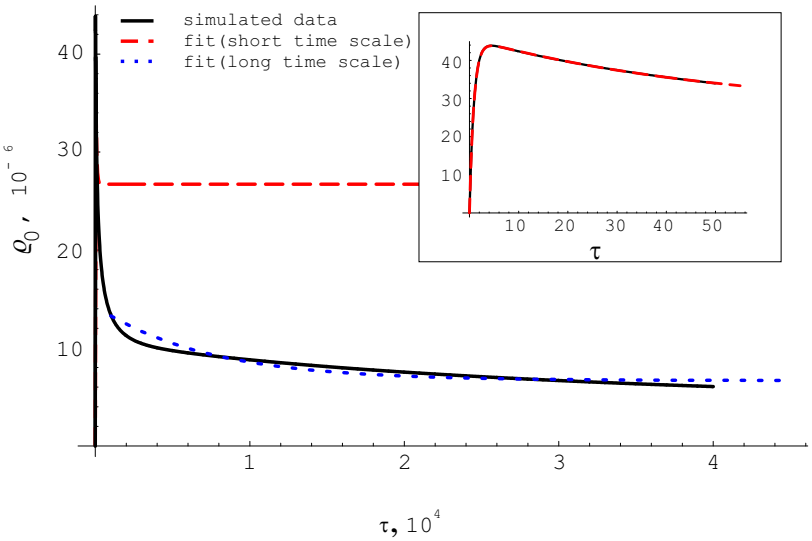

Figure 2.9: Simulated dynamics of DC photocurrent for the case $m_{T1} \gg m_{T2} \gg 1$ (Eqs. 2.50). Inset shows the short time scale part of the photocurrent transient.

which are not taken into account at short time scale take over at $\tau \gg 50$, the short time scale fit does not describe the photocurrent dynamics anymore (dashed line in Figure 2.9), and thus long time scale analysis should be applied.

We now use a procedure to produce a better time evolution for ϱ_0 that will also yield the detrapping parameter for shallow traps. Although it is not obvious how to analytically extract the detrapping parameter for shallow traps $\tilde{\beta}_1$, $\varrho_0(\tau)$ at short time scales is rather sensitive to changes in $\tilde{\beta}_1$. Figure 2.10 shows how the photocurrent transient differs for the materials with various values of $\tilde{\beta}_1$. The order of magnitude of the shallow detrapping rate β_1 can be estimated from the PR decay experiment as we show in Section 3.4.2. This estimated value can be used as an initial approximation which can be further fine-tuned. To fine-tune the detrapping parameter $\tilde{\beta}_1$ and the

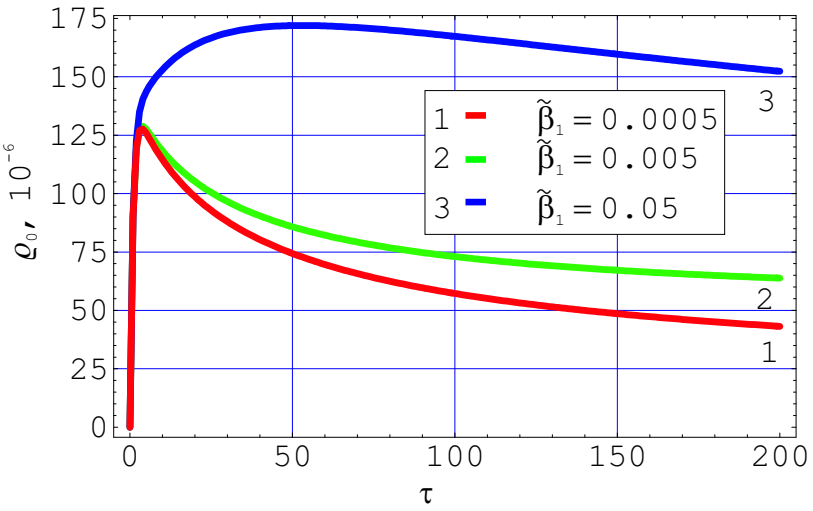

Figure 2.10: Photocurrent dynamics simulation for different shallow detrapping rates $\tilde{\beta}_1$.

recombination parameter $\tilde{\gamma}$, we used the β_1 estimated from the PR decay and $\tilde{\gamma}$ estimated from $\tilde{\lambda}_{20}$ as the initial value in Eqs. 2.50 and varied both $\tilde{\beta}_1$ and $\tilde{\gamma}$. At every step we calculated the dimensionless free charge density $\varrho_0(\tau)$ and fitted it to Eq. 2.52. Then we transformed the dimensionless fit parameter $\tilde{\lambda}_{20}$ to the dimensional form $\lambda_{20} = \tilde{\lambda}_{20}/\tau_0$ and compared them to the analogous parameters of a bi-exponential fit of DC photoconductivity data. The comparison was executed by searching for a minimum of the function

$$f = \left(\frac{\lambda_{20,\mathrm{exp}} - \lambda_{20}}{\lambda_{20,\mathrm{exp}}}\right)^2 + \left(\frac{B_{\mathrm{exp}} - B}{B_{\mathrm{exp}}}\right)^2 \tag{2.53}$$

where $\lambda_{20,\mathrm{exp}}, B_{\mathrm{exp}}$ are the experimental parameters analogous to corresponding parameters λ_{20}, B introduced in Eq. 2.52.

We should note that for the numerical simulations we performed to determine $\tilde{\beta}_1$

and $\tilde{\gamma}$, the correct estimate of initial values is more crucial for $\tilde{\gamma}$ than for $\tilde{\beta_1}$. So, it is not necessary to use the initial $\tilde{\beta_1}$ value from the PR decay experiment. This makes the evaluation of these rates completely determined by the DC photoconductivity experimental data.

Summarizing the short time scale DC photoconductivity dynamics for the case $m_{T1} \gg m_{T2} \gg 1$, we are able to determine the shallow trapping parameter $\gamma_T M_{T1}$, recombination rate γ and shallow detrapping rate β_1.

Long time scale On the long time scale ($\tau \gg 10^3$), shallow traps have reached equilibrium, and deep traps determine the dynamics of the DC photoconductivity. The dimensionless parameters to be determined here are the ratio of total deep traps with respect to shallow traps m_{T2}/m_{T1} and the thermal detrapping parameter of deep traps $\tilde{\beta}_2$. We performed a numerical simulation fixing the parameters $\tilde{s}I_0 = 5 \cdot 10^{-5}$, $\tilde{\beta}_1 = 5 \cdot 10^{-4}$, $\tilde{\gamma} = 2.5 \cdot 10^2$, and varying m_{T2}/m_{T1} and $\tilde{\beta}_2$. Similar to the short time scale approach, we fit the free charge density $\varrho_0(\tau)$ with a bi-exponential similar to Eq. 2.52 (dotted line in Figure 2.9). The faster speed $\tilde{\lambda}_{10}$ was kept fixed equal to unity. Then, our fit yielded two coefficients – the slower speed $\tilde{\lambda}_{20,long}$ and the exponential prefactor B_{long}. Although at this time scale, it is not straightforward to relate the constants of the fit to the parameters of the material directly, our simulations show that the deep to shallow trap density ratio m_{T2}/m_{T1} and deep detrapping parameter $\tilde{\beta}_2$ can be found from the fit constants in a similar to the short time scale analysis

manner. When dealing with the experimental data, we constructed the function

$$f_1 = \left(\frac{\lambda_{20,\exp,long} - \lambda_{20,long}}{\lambda_{20,\exp,long}} \right)^2 + \left(\frac{B_{\exp,long} - B_{long}}{B_{\exp,long}} \right)^2$$

where $\lambda_{20,\exp,long}$ and $B_{\exp,long}$ are the experimental constants analogous to $\lambda_{20,long} = \tilde{\lambda}_{20,long}/\tau_0$ and B_{long}. Similar to a short time scale approach, we sought values for m_{T2}/m_{T1} and $\tilde{\beta}_2$ that would minimize the function f_1.

Summarizing the long time scale DC photoconductivity dynamics for the case $m_{T1} \gg m_{T2} \gg 1$, we are able to determine experimentally the product $\gamma_T M_{T2}$ and the detrapping rate β_2.

Trap-limited regime

In this section, we consider the DC photoconductivity dynamics when the total density of traps is on the order or less than the acceptor density. We will limit our discussion to the case when the regime is "trap-limited" only with respect to deep traps (*Case 2*) that appears to be relevant for the materials we studied [40] (see Section 3.5). So, further in this section, we assume that $m_{T1} \gg 1$ and $m_{T2} \leq 1$. In this case, the condition $m_{T1} \gg m_{T2}$ is satisfied automatically and thus, the time scale division onto "short" and "long" is still appropriate. Also, since for shallow traps the condition $m_{T1} \gg 1$ is the same as in the previous Section 2.3.1, all the short time scale considerations are valid. However, the long time scale behavior is no longer the same as in trap-unlimited regime, mainly because in this case the condition $m_{20}/m_{T2} \ll 1$

is no longer valid, so the following system of equations has to be solved:

$$\begin{aligned} \tfrac{dm_{10}}{d\tau} &= \varrho_0 - \tilde{\beta}_1 m_{10} \\ \tfrac{dm_{20}}{d\tau} &= \tfrac{m_{T2}}{m_{T1}}(1 - \tfrac{m_{20}}{m_{T2}})\varrho_0 - \tilde{\beta}_2 m_{20} \\ \tfrac{dn^i_{A0}}{d\tau} &= \tilde{s} I_0 (1 - n^i_{A0}) - \tilde{\gamma} n^i_{A0} \varrho_0 \\ \varrho_0(\tau) + m_{10}(\tau) + m_{20}(\tau) - n^i_{A0}(\tau) &= 0 \end{aligned} \tag{2.54}$$

The Eqs. 2.54 contain one more parameter than the Eqs. 2.50, so that it is not enough to determine the ratio m_{T2}/m_{T1} because of m_{T2} in the term m_{20}/m_{T2}. Our simulations show that if $m_{T2} \sim 1$ then the use of simplified Eqs. 2.50 instead of Eqs. 2.54 is still possible which allows us to determine the ratio m_{T2}/m_{T1} within 10% error. However, if $m_{T2} < 1$, then the Eqs. 2.54 must be solved since the error becomes $> 100\%$. This complicates the analysis of the long time scale behavior. Also, when the density of total deep traps becomes of the order of 1% or less then the acceptor density ($m_{T2} \leq 0.01$), it appears to be impossible to detect deep traps in the material by using DC photoconductivity. We simulated the long time scale evolution of the dimensionless free charge density $\varrho_0(\tau)$ with the fixed parameters $\tilde{s} I_0 = 5 \cdot 10^{-5}$, $\tilde{\beta}_1 = 5 \cdot 10^{-4}$, $\tilde{\beta}_2 = 5 \cdot 10^{-6}$, $\tilde{\gamma} = 2.5 \cdot 10^2$, $m_{T1} = 10$ and varying m_{T2} from 0.01 to 1. Figure 2.11 shows the deep-trap limited behavior of the photoconductivity for various total deep trap densities. As can be seen from Figure 2.11, when $m_{T2} = 0.01$, the decay of $\varrho_0(\tau)$ is less than 3% over the time scale corresponding to the experimental run of duration $\geq 10^3 s$ for the PVK-based composites we studied [40] (Section 3.5),

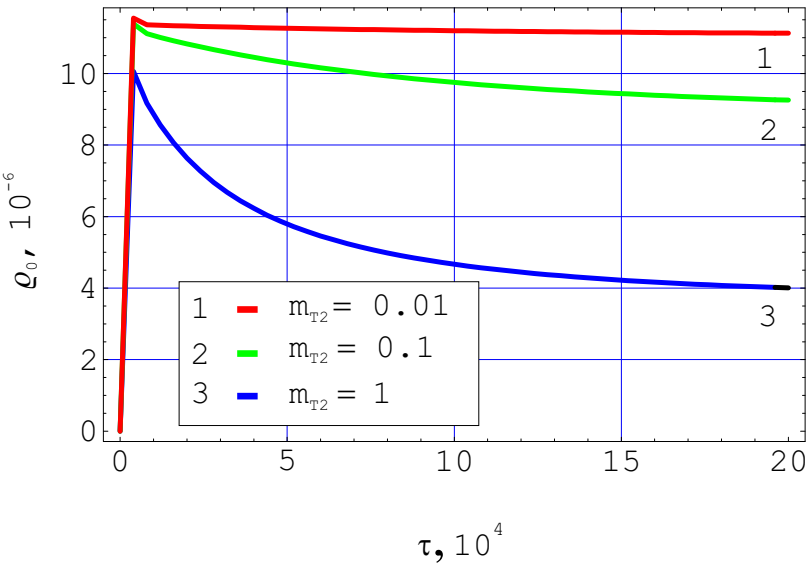

Figure 2.11: Long time scale dynamics of DC photocurrent in the deep trap-limited case as calculated from Eqs. 2.54.

so that it would be hard to obtain a reliable fit to such data and thus trap densities below 0.01 cannot be detected by this method.

Time evolution of ionized acceptor density n^i_{A0}

So far, we have been mostly discussing the DC photocurrent dynamics ($J_0(t) \sim \rho_0(t)$) since this is relatively easy to measure and compare with numerical simulations. However, recently, several groups performed spectroscopic experiments to directly observe the dynamics of ionized acceptor density $N^i_A(t)$ (or corresponding dimensionless parameter $n^i_A(t)$) [37, 42]. In these references, the link between the growth of n^i_A and PR performance in different materials was mentioned and speculated on, but the theoretical basis for such a behavior has not been established. In this section, we simulate the dynamics of ionized acceptors for various materials. Further, in Sec-

tion 2.3.2, we show how the ionized acceptor density temporal behavior influences the PR performance.

According to the last equation in Eqs. 2.48, the free charge and ionized acceptor densities are constrained by the charge neutrality equation. Thus, the photocurrent and the density of ionized acceptors dynamics are directly connected to each other. Figure 2.12a shows the simulated time growth of the ionized acceptor density $n^i_{A0}(\tau)$ using the fixed parameters listed in the previous Section 2.3.1 and varying the total deep trap density m_{T2} from 0.01 (deep trap-limited regime) to 10 (deep trap-unlimited regime). As can be seen in Figure 2.12a, the more deep traps that are available in the material, the more pronounced is the ionized acceptor density growth. Also, the trap depth is the factor that affects the time evolution of n^i_{A0}. Figure 2.12b shows how the depth of the traps (thermal detrapping rate) affects the formation of ionized acceptors. For this simulation we used the same parameters as for the simulation shown in Figure 2.12a, but with fixed $m_{T2} = 1$ and varied $\tilde{\beta}_2$ from $5 \cdot 10^{-7}$ to $5 \cdot 10^{-5}$.

In summary, the density and depth of available traps are directly responsible for the variations in the growth of ionized acceptors n^i_A experimentally observed by several groups [37, 42]. Later, in the Section 2.3.2 when we consider PR dynamics, we will show how this affects the PR performance of the materials.

We have determined many of the parameters of Figure 2.5, and, in the next section, will show how these may be used to predict the PR dynamics. Here we provide a

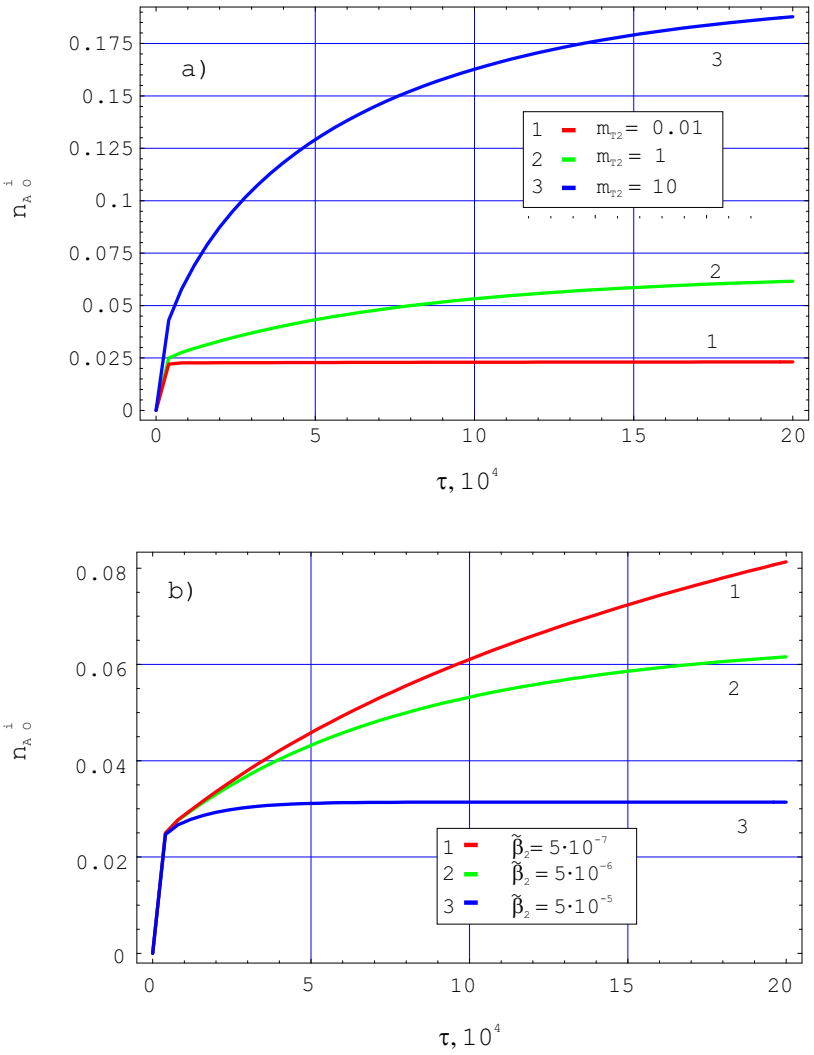

Figure 2.12: Calculated from Eqs. 2.54 a)time evolution of ionized acceptor density for deep trap-unlimited and deep trap-limited regime. b)time evolution of ionized acceptor density for deep traps of different depth (thermal excitation rates).

numerical simulation of the dynamics of the free charge and ionized acceptors for materials with deep traps, and in Section 3.5 we consider experimental data for different PVK-based composites and discuss the nature of traps in these materials.

2.3.2 First Order: Photorefraction

In this section, we consider the formation of the first spatial Fourier component of the free charge, filled traps and ionized acceptors densities as well as space charge field and hence PR dynamics. Here it appears more convenient to use dimensional equations rather than dimensionless for easier comparison of the simulated PR dynamics with the experiment. After substitution of the Eq. 2.47 into the Eqs. 2.29, and separately collecting terms with $\sin Kx$ and $\cos Kx$, we obtain a system of ten equations — eight differential equations (with respect to time) and two equations relating the space charge field to free charge, filled traps and ionized acceptor densities. We consider that the photogeneration cross-section, mobility, recombination and trapping rates are electric field dependent and assume the dependencies given in Eqs. 2.31. As we already mentioned in the Section 2.2, due to these field dependencies all the parameters acquire a spatially varying part upon formation of the space charge field. Using Eqs. 2.31 and the approach suggested by Schildkraut and Cui [17], we can express all the rates in terms of space charge field as follows:

$$s = s(E_a)(1 + p(E_1/E_a))$$

$$\mu = \mu(\tilde{E_a})(1 + (1/2)\beta_\mu \tilde{E_a}^{-1/2} E_1)$$

$$\gamma = \gamma(\tilde{E_a})(1 + (1/2)\beta_\mu \tilde{E_a}^{-1/2} E_1)$$

$$\gamma_T = \gamma_T(\tilde{E_a})(1 + (1/2)\beta_\gamma \tilde{E_a}^{-1/2} E_1)$$

where E_a is the applied electric field, $\tilde{E_a}$ is the projection of the applied field on the grating vector, E_1 is the space charge field given in accordance with Eq. 2.47 by the relation

$$E_1 = E_{11}(t)\cos Kx + E_{12}(t)\sin Kx \tag{2.55}$$

It should be noted that in Section 2.3.1 we assumed the external electric field $E_0 = V/d$ a constant determined by the applied voltage V. This implies that the condition

$$\int_0^d E_1 dx = 0 \tag{2.56}$$

must hold. In the Fourier analysis approach which we chose as a theoretical treatment for Eqs. 2.29, the condition given by Eq. 2.56 is not used explicitly. Thus, when comparing the experimentally determined space charge field with the theory, one should check whether Eq. 2.56 is valid. In practice, you cannot usually ask for a strict zero, and Eq. 2.56 transforms into a milder version given by

$$\int_0^d E_1 dx \ll V \tag{2.57}$$

which in PR polymers is expected to be valid for moderate external electric fields ($E_0 \lesssim 80\, V/\mu m$). It was certainly valid for all the PR measurements we performed which will be described in Sections 3.4 and 3.5.

The first order system of equations describing PR dynamics is:

$$
\begin{aligned}
\frac{dE_{11,12}}{dt} &= -\mu\frac{e}{\varepsilon_0\varepsilon}\left(\left(1+\frac{\beta_\mu\tilde{E_a}^{1/2}}{2}\right)\rho_0(t)E_{11,12}(t) - \tilde{E}_a\rho_{11,12}(t) \mp K\xi\rho_{11,12}(t)\right)\\
\frac{dM_{11,12}}{dt} &= \gamma_T M_{T1}\left(\rho_{11,12}(t) - \frac{\beta_\gamma\tilde{E_a}^{-1/2}}{2}E_{11,12}(t)\rho_0(t)\right) - \beta_1 M_{11,12}(t)\\
\frac{dM_{21,22}}{dt} &= \gamma_T M_{T2}\left(\rho_{11,12}(t) - \frac{\beta_\gamma\tilde{E_a}^{-1/2}}{2}E_{11,12}(t)\rho_0(t)\right) - \beta_2 M_{21,22}(t)\\
\frac{dN^i_{A11}}{dt} &= sN_AI_1 - (sI_0+\gamma\rho_0(t))N^i_{A11}(t) - \gamma N^i_{A0}(t)\rho_{11}(t)\\
&\quad - \left(sN_AI_0\frac{p}{E_a} - \gamma\frac{\beta_\mu\tilde{E_a}^{-1/2}}{2}\rho_0(t)N^i_{A0}(t)\right)E_{11}(t)\\
\frac{dN^i_{A12}}{dt} &= -(sI_0+\gamma\rho_0(t))N^i_{A12}(t) - \gamma N^i_{A0}(t)\rho_{12}(t)\\
&\quad - \left(sN_AI_0\frac{p}{E_a} - \gamma\frac{\beta_\mu\tilde{E_a}^{-1/2}}{2}\rho_0(t)N^i_{A0}(t)\right)E_{12}(t)\\
E_{11}(t) &= \frac{e}{\varepsilon_0\varepsilon k}\left(\rho_{12}(t)+M_{12}(t)+M_{22}(t)-N^i_{A12}(t)\right)\\
E_{12}(t) &= -\frac{e}{\varepsilon_0\varepsilon k}\left(\rho_{11}(t)+M_{11}(t)+M_{21}(t)-N^i_{A11}(t)\right)
\end{aligned}
\tag{2.58}
$$

Here $E_{11}, M_{11}, M_{21}, N^i_{A11}$ are the time-dependent amplitudes of space charge field, filled shallow traps, filled deep traps and ionized acceptors, respectively. These have a spatial dependence $\cos Kx$ (in-phase with the incident light illumination). The quantities $E_{12}, M_{12}, M_{22}, N^i_{A12}$ are the corresponding amplitudes of functions with a spatial dependence $\sin Kx$ (90^0 out-of-phase with the intensity of incident light).

It is conventional [14, 41, 13] to assume that the PR dynamics is much slower than the photoconductive dynamics, which is analogous to setting the zeroth order ($\rho_0(t), N^i_{A0}(t)$) functions to be constant in time in Eqs. 2.58. In this case, Eqs. 2.58 can be solved analytically as linear equations with constant coefficients. This approach can be applied on the short time scale. However, longer times require accounting for

deep traps, which result in slowly changing components of both $\rho_0(t)$ and $N^i_{A0}(t)$, requiring Eqs. 2.58 to be solved numerically. It should be pointed out that when studying PR dynamics, the analytical solution is not useful since the characteristic equation derived from Eqs. 2.58 yields eight complex time constants (out of which four are complex conjugates of four others) for the space charge field formation, while the PR experimental data is usually fitted with a bi-exponential function. Further, usually only one of two exponents is attributed to the photoconductivity and the other one to the reorientation of chromophores due to orientational enhancement [43, 44, 45]. Thus, it is not enough to know the theoretical time constants on their own, but rather to know how they are combined together to yield the observed PR dynamics. In the next section, we will concentrate on obtaining the four-wave mixing (FWM) dynamics from the theory and photoconductivity parameters.

Photorefractive rise

In this section we examine the factors that affect the PR rise time. First of all, it is important to perform a simulation using conditions as close as possible to a real experiment. We chose the FWM experiment for PR dynamics studies, and so we will model the dynamics of diffraction efficiency introduced in Section 2.1.3. As described in Section 2.1.3, the rigorous analysis leads to a diffraction efficiency in the following form (derived from Eqs. 2.27, 2.28)

$$\eta \sim \sin^2(C\Delta n) \sim \sin^2\left(\tilde{C}\sqrt{E_{i1}^2 + E_{i2}^2}\right) \tag{2.59}$$

where $C, \tilde{C}$ are constants determined by the geometry of the experiment, Δn is the change in refractive index as introduced in Section 2.1.2, and E_{11}, E_{12} are the components of the space charge field defined in Eq. 2.55.

For sufficiently small space charge fields, the $\sin(C\Delta n)$ in Eq. 2.59 can be replaced with $C\Delta n$ which simplifies the diffraction efficiency to the following form:

$$\eta \sim (C\Delta n)^2 \sim \tilde{C}^2 \left(E_{11}^2 + E_{12}^2\right) \tag{2.60}$$

In our PR experiments (refer to Section 3.4 for details), the simplified form given by Eq. 2.60 was appropriate, and thus, we proceed with numerical simulations assuming that form for the diffraction efficiency η.

So, a real experiment (FWM) (details are described in Section 3.4) is performed as follows: we turn on the electric field with one writing beam on, then in 10 s we turn on another writing beam and monitor the space charge field formation. In the Eqs. 2.58 that describe the PR dynamics, we need to define the behavior of zeroth order functions $\rho_0(t)$ and $N_{A0}^i(t)$, so first we simulate the time evolution of these functions under the appropriate experimental conditions. Figure 2.13 shows how the free charge density ρ_0 and ionized acceptor density N_A^i evolve as one beam is turned on, and then in $10s$ another beam of the same intensity $I_0/2$ is turned on.

The dependence of these zeroth order functions on the experimental conditions is responsible for the history dependence of the PR performance, as we will explore theoretically later in this section and experimentally in Section 3.5. So, as we de-

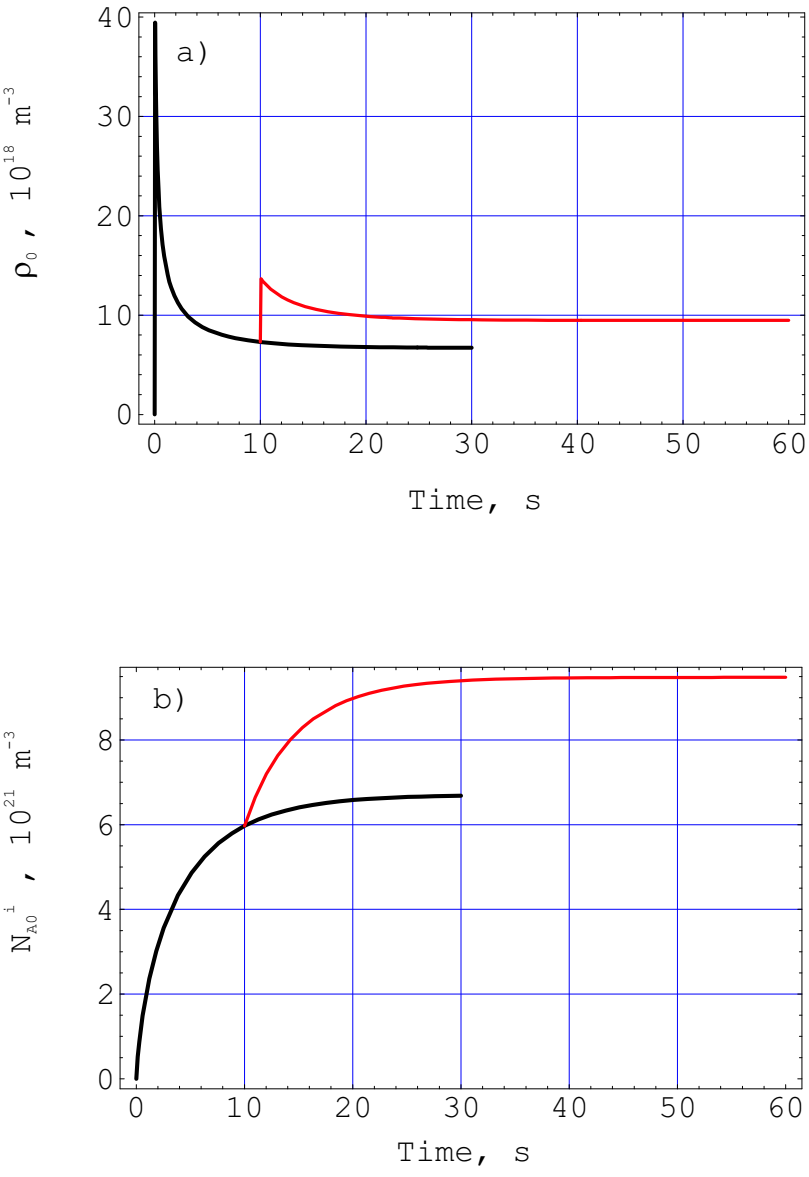

Figure 2.13: Time evolution of: a) free hole density ρ_0 and b) ionized acceptor density N_A^i. At time $t=0$, the beam with intensity $I_0/2$ is turned on with external electric field applied. At time $t=10\,s$, the second beam of the same intensity is turned on.

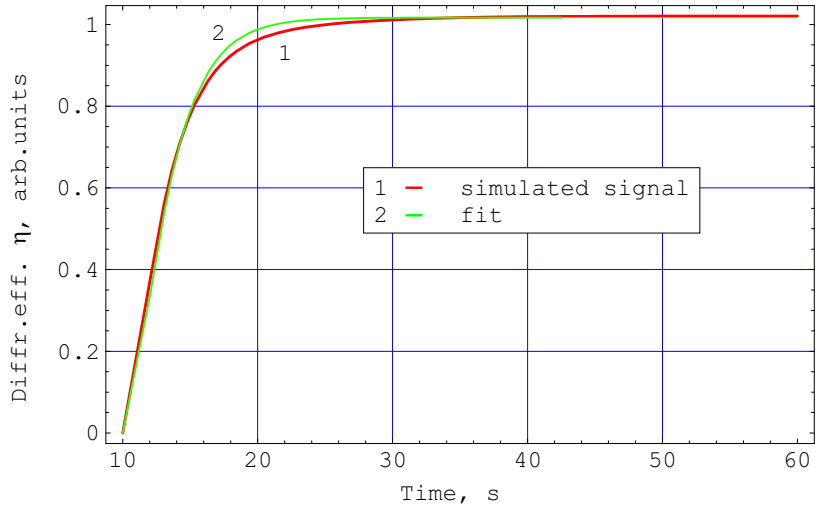

Figure 2.14: Diffraction efficiency simulated using Eqs. 2.58, 2.61 and fitted to Eq. 2.62.

termined $\rho_0(t)$ and $N^i_{A0}(t)$ for the time span of our PR experiment, we use them in Eqs. 2.58 to simulate the evolution of the space charge field. We then calculate the diffraction efficiency using the simplified form (Eq. 2.60):

$$\eta(t) \sim E^2_{11}(t) + E^2_{12}(t) \tag{2.61}$$

and fit it to a single exponential,

$$\eta = \eta_0 \left(1 - e^{-\nu t}\right)^2 \tag{2.62}$$

where the parameter ν is the PR speed.

Figure 2.14 shows the simulated PR grating formation using Eqs. 2.58 and 2.61 and the fit to the single exponential function of Eq. 2.62. This approach works when deep traps do not contribute on the experimental time scale. The experimental data is fitted with a bi-exponential function where the faster constant is attributed to

photoconductivity, and the slower one to chromophore reorientation which will be considered in Section 3.5 [43]. When the PR experiment is conducted on a longer time-scale or the depth of the deep traps is such that both the faster and slower experimental time constants are due to photoconductivity, the simulated data should also be fitted with a bi-exponential function [40], as we will discuss it in Section 3.5. Here, for simplicity, we only deal with time scales that are determined by fast shallow trap dynamics, and thus we use single exponential fits (Eq. 2.62) to describe the initial rise.

To explore the factors that affect the speed of space charge field formation, we modelled the PR experiment by varying the photogeneration rate s, thermal detrapping rate β_1, recombination rate γ, total density of shallow trapping sites M_{T1} and mobility μ. For each set of parameters we calculated PR speed ν from Eqs. 2.58, 2.61 and 2.62. Although some of these parameters depend on each other and, strictly speaking, cannot be varied independently, this simulation still can provide some insight into factors determining the PR speed.

Our simulation shows that the PR speed is nearly insensitive to the shallow trap release rate: the change in parameter β_1 over four orders of magnitude barely changed the PR speed by a factor of two (Figure 2.15a).

Larger effects were observed when changing other parameters: a decrease in the total density of shallow trapping sites of a factor of 500 led to a six-fold increase in PR

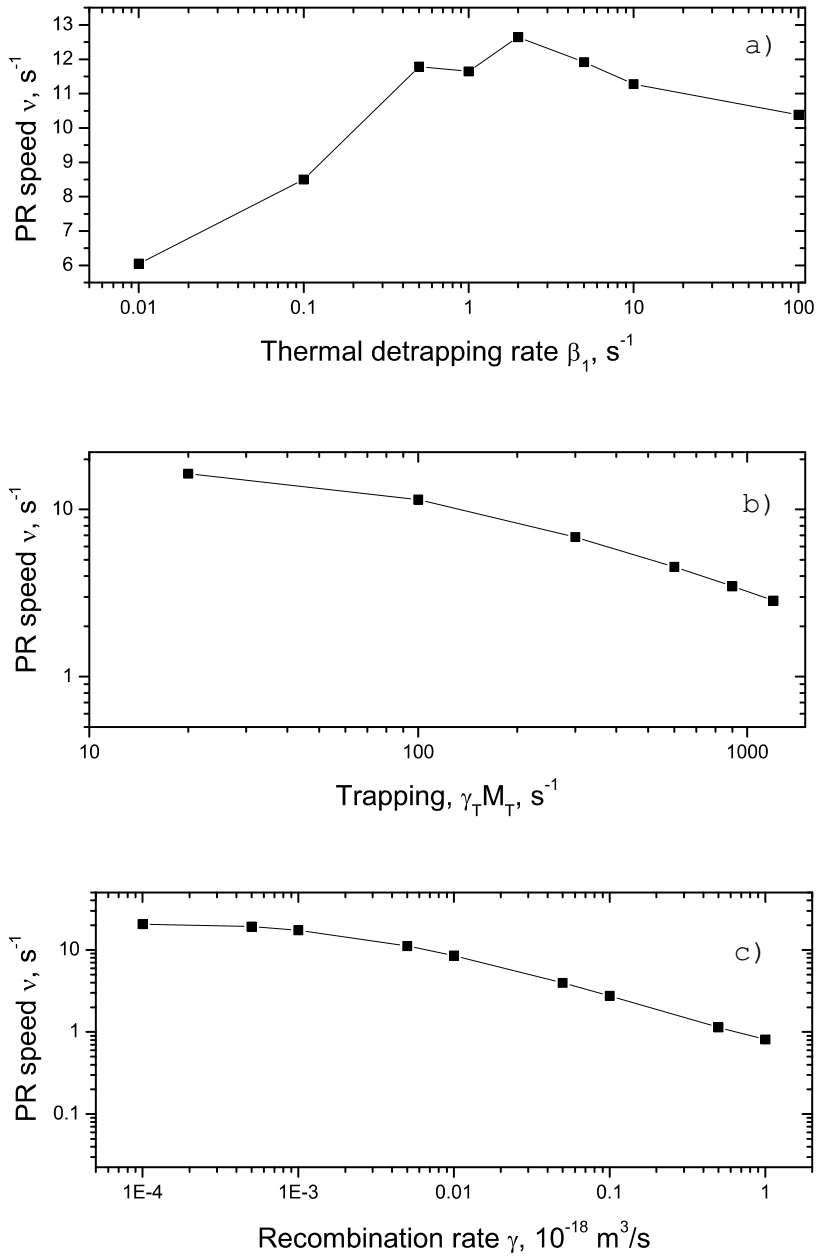

Figure 2.15: PR speed ν calculated from Eqs. 2.58, 2.61 and 2.62 as a function of: a) shallow detrapping rate β_1; b) shallow trapping product $\gamma_T M_{T1}$; c) recombination rate γ.

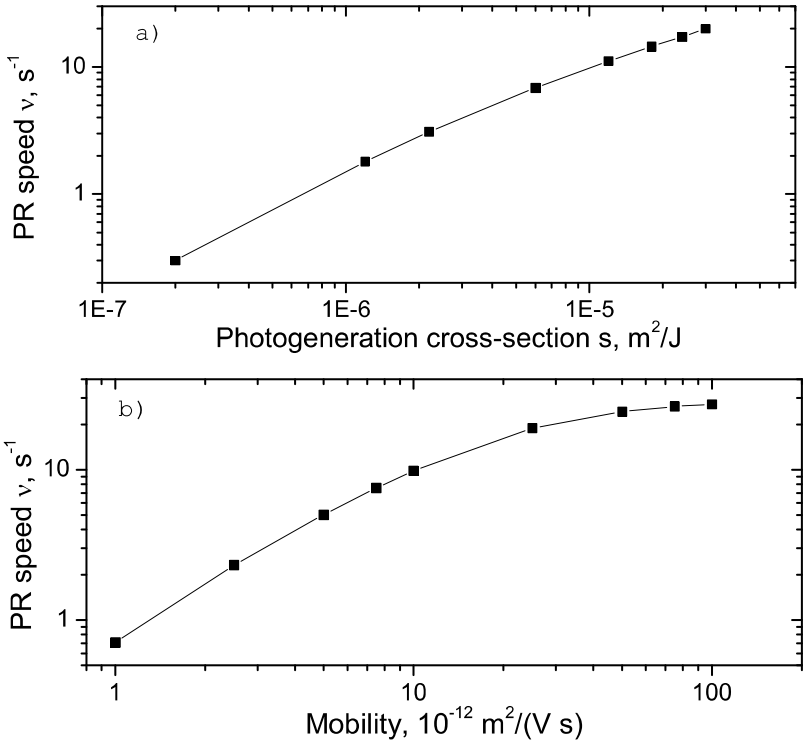

Figure 2.16: Dependence of photorefractive speed on: a) photogeneration cross-section; b) charge carrier mobility as calculated from Eqs. 2.58, 2.61 and 2.62.

speed (Figure 2.15b), and a four order of magnitude decrease in the recombination rate yielded a thirty-fold increase in PR speed (Figure 2.15c). It should be noted that a decrease in total trap density may decrease the diffraction efficiency. Thus, in this case there is a trade off between PR speed and steady-state diffraction efficiency.

As shown in Figure 2.16, the changes in mobility and photogeneration cross-section had the largest impact on a PR speed. However, it should be mentioned that an independent variation of the photogeneration cross-section is more justified than an independent variation of mobility, because the recombination rate is mobility-dependent and affects the PR speed the opposite way to the mobility itself. Thus, in

a real system the effect from a change in mobility will be smaller than that shown in Figure 2.16.

We now explore the illumination history dependence of the PR speed. As an example, we consider a composite with deep traps that led to decay of the DC photoconductivity and the slow growth of the ionized acceptor density. We used the density of acceptors $N_A = 3.8 \cdot 10^{24}\, m^{-3}$, shallow trapping parameter $\gamma_T M_{T1} = 480\, s^{-1}$ and deep trapping product $\gamma_T M_{T2} = 5\, s^{-1}$, detrapping rate for shallow traps $\beta_1 = 0.9\, s^{-1}$, detrapping rate for deep traps $\beta_2 = 0.001\, s^{-1}$, recombination rate $\gamma = 10^{-20}\, m^3/s$, photogeneration cross-section $s = 2.9 \cdot 10^{-5}\, m^2/J$, mobility $\mu = 3 \cdot 10^{-11}\, m^2/(V \cdot s)$, grating constant $\Lambda = 1.8\, \mu m$, dielectric constant $\varepsilon = 7.9$, mobility field-dependence parameter $\beta_\mu = 5.76 \cdot 10^{-4}\ (m/V)^{1/2}$, trapping rate field-dependence parameter $\beta_\gamma = 3.26 \cdot 10^{-4}\, (m/V)^{1/2}$, photogeneration efficiency field-dependence parameter $p = 2.04$, external field $E_a = 40\, V/\mu m$ and intensity of light $I_0 = 500\, mW/cm^2$ each beam. We simulated a FWM experiment using a fresh sample and both beams being turned on simultaneously, then the same experiment after illuminating the sample with one beam for 10 s and then turning on another one and so on up to homogeneous illumination with one beam for 5000 s prior to the PR experiment. The results of the simulation are presented in Figure 2.17. As it can be deducted from Figure 2.17, there is a substantial history dependence of the PR speed, in particular the response time degradation in materials with deep traps, as reported in previous measurements [46, 44].

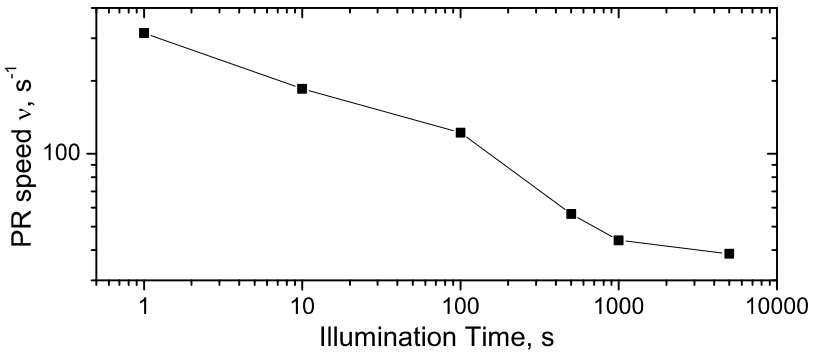

Figure 2.17: Dependence of the photorefractive speed on the time of the homogeneous illumination prior to photorefractive experiment as calculated from Eqs. 2.58, 2.61 and 2.62.

Photorefractive decay

The theoretical approach we used in previous sections to study the PR rise, also can be applied to the PR decay. We will not explore the PR decay in detail, but rather will show how the detrapping rate for shallow traps can be estimated from the PR decay with no erasing beam ($I_0 \approx 0$). To study the PR decay, we simulate the whole experiment: we turn on the external electric field and both optical beams, so that space charge field forms and reaches its quasi-steady state. At this point we determine all the steady-state parameters ($\rho_{11,12}$, $M_{11,12,21,22}, \ldots$) that will serve as initial conditions when we turn off both beams and simulate a "dark" decay of the PR grating. The space charge field decay in the absence of the erasing beam in materials with low dark current is determined by the thermal detrapping rate for shallow traps β_1. As a matter of fact, two out of eight complex conjugated time constants that are determined analytically from Eqs. 2.58 at quasi-steady values of free charge density

$\rho_0(t) \approx \tilde{\rho}_0$ and ionized acceptor density $N_{A0}^i(t) \approx \tilde{N}_{A0}^i$ have real parts equal to the thermal detrapping rate β_1. However, as we have already mentioned in Section 2.3.2, it is important how all these eight time constants are combined together to yield one or two constants that are extracted from the experimental data. Therefore, here we speculate only about estimating β_1 rather than determining it from the experiment. So, at time $t = t_0$ we turn off both beams and similarly to the PR rise described in the previous section, first simulate the decay of the zeroth order free charge $\rho_0(t)$ and ionized acceptor density $N_A^i(t)$. Then, we substitute these functions into Eqs. 2.58 and numerically solve this system with no interference ($I_1 = 0$) and no homogeneous illumination other than the probe beam ($I_0 = I_{probe}$) which is assumed to be too weak to disturb the grating. Similar to the PR rise, we calculate the diffraction efficiency from Eq. 2.61 and fit it with a single exponential decay function

$$\eta = \eta_0 e^{-2\nu_{decay}(t-t_0)} \tag{2.63}$$

as well as bi-exponential function

$$\eta = \eta_0 \left(a e^{-\nu_{decay}^{fast}} + (1-a) e^{-\nu_{decay}^{slow}} \right)^2 \tag{2.64}$$

Figure 2.18 shows an example of simulated PR decay with no erasing beam ($I_0 = I_{probe} \approx 0$) with fits to Eqs. 2.63 and 2.64.

We repeated the same procedure for different detrapping rates β_1 to find out how the fit parameters ν_{decay}, ν_{decay}^{fast} and ν_{decay}^{fast} reflect the change in β_1. It turns out that

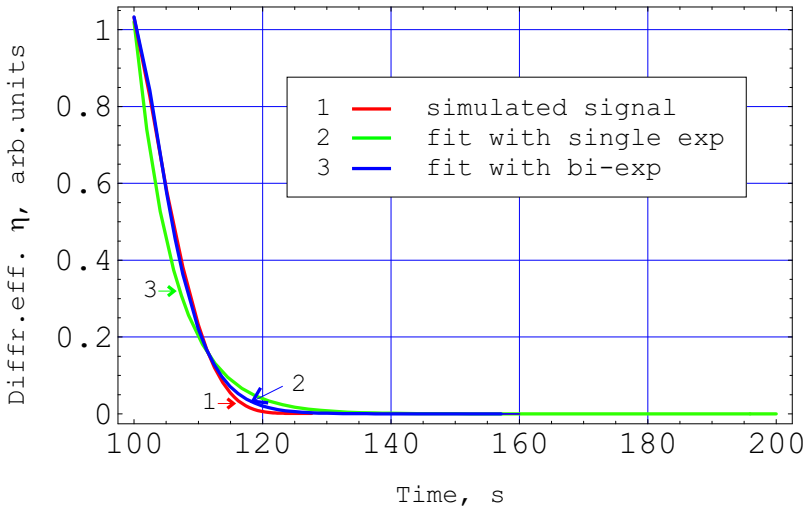

Figure 2.18: PR decay simulated using Eqs. 2.58, 2.61 and fit to Eqs. 2.63 and 2.64.

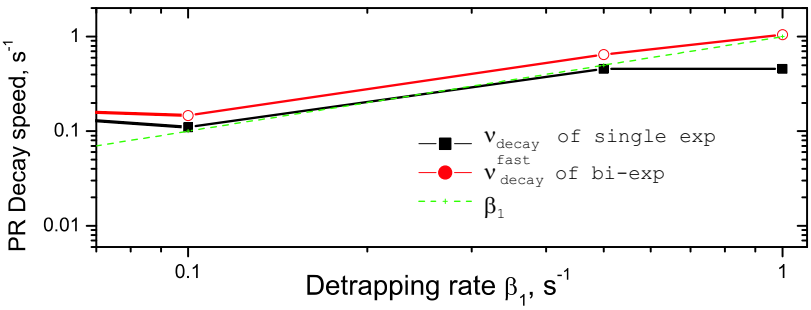

Figure 2.19: Speed of the PR decay as a function of the shallow detrapping rate β_1.

both the decay speed ν_{decay} of Eq. 2.63 and the faster decay speed ν_{decay}^{fast} defined in Eq. 2.64 provide a reasonable estimate of the detrapping rate β_1 in the range of interest for PVK-based composites (Figure 2.19).

This estimate can be used as an initial value in the procedure that allows to determine and fine-tune the detrapping rate β_1 and recombination rate γ developed earlier in Section 2.3.1.

In summary of Section 2.3, we studied theoretically the photoconductivity part of

the PR performance, in particular dynamics, of the polymer PR materials.

We developed a procedure that allows to determine the shallow trapping parameter $\gamma_T M_{T1}$, the recombination rate γ and the shallow detrapping rate β_1 from the short time scale DC photoconductivity experiment. Also, we demonstrated how the deep trap parameter $\gamma_T M_{T2}$ and deep detrapping rate β_2 can be determined from the long scale DC photoconductivity experiment. The contribution of various photoconductivity parameters to the PR grating dynamics was studied by numerical simulations.

In the next section, we briefly consider the theory of the orientational part of the PR polymer performance [43].

2.4 Theory of orientational enhancement effect

The theory of the orientational enhancement effect was worked out by Moerner *et al.*[43], so I will briefly present the effect, consider how it affects the PR performance of the polymer composites and discuss in which measurements it shows up and how to deal with this.

As already discussed in Section 2.1.2, the main mechanisms that lead to the PR effect in polymers are photoconductivity and NLO chromophore orientation. The role of photoconductivity was discussed in detail in Sections 2.2 and 2.3. In this section, we will discuss the role of orientational effects in the PR effect in polymer composites.

In Section 2.1.2, the four main steps leading to the PR in polymers were stated. So far we described the first three steps which are related to photoconductive properties of the material. The last, fourth, step is concerned with the refractive index change in response to the space charge field produced during steps 1 through 3 (Eq. 2.4). Historically, this step was attributed to the linear electro-optic effect which is the only mechanism for the step 4 in inorganic crystals and so, it was automatically considered as the primary mechanism for the PR polymers as well. However, it turned out that the experimentally observed two-beam coupling gain and diffraction efficiencies in polymers were much higher than expected due to the linear electro-optic effect which, by analogy to Moerner *et al.* [43], we will call the "simple electro-optic effect". Therefore, another mechanism which, in addition to the simple electro-optic effect, leads to the PR grating formation was introduced. The essence of this mechanism called "orientational enhancement" is that the NLO chromophores which are necessary constituents of a PR polymer composite can be aligned not only by the externally applied electric field E_a but also *in situ* by the sinusoidally varying space charge field E_{sc} itself during grating formation. Additional components of the refractive index change are then due to the optical anisotropy of the chromophore.

We start from the description of the expected diffraction efficiency due to the simple electro-optic effect and then expand the analysis to take into account the orientation enhancement mechanism.

2.4.1 "Simple" electro-optic effect

We assume that the space charge field is already produced and is given by $\mathbf{E_{sc}} = \hat{\mathbf{K}} E_{sc}^0 \exp[-i\mathbf{Kr}]$ where $\hat{\mathbf{K}}$ is the unit vector along the grating wave vector direction (see Figure 2.4). The sinusoidal space charge field leads to a change in the dielectric constant (Eq. 2.6) which can be transformed through the relation $\Delta\varepsilon = \Delta\chi$ (in mks units) into the change in susceptibility $\Delta\chi$. Also, now it is important to rewrite Eq. 2.6 in the tensorial form

$$(\Delta\chi)_{ij} \sim \varepsilon_{il}(r_e^{lmn} E_{sc}^0 K_n)\varepsilon_{mj} \tag{2.65}$$

where ε_{ij} is the dielectric tensor and r_e^{ijk} is the third-rank electro-optic tensor. The electro-optic tensor r_e^{ijk} depends on the symmetry of the material. In our case of PR polymer films, with the NLO chromophores aligned in the external electric field, it is the $C_{\infty v}$ symmetry of the poled polymer [47]. For this symmetry, the electro-optic tensor in the contracted notations [48] is reduced to

$$r_e = \begin{bmatrix} 0 & 0 & r_{13} \\ 0 & 0 & r_{13} \\ 0 & 0 & r_{33} \\ 0 & r_{13} & 0 \\ r_{13} & 0 & 0 \\ 0 & 0 & 0 \end{bmatrix} \tag{2.66}$$

Then, using the simplified dependence of the diffraction efficiency (for small diffraction efficiencies) on the change in refractive index $\eta \sim (\Delta n)^2$ (Eq. 2.60) and Eqs. 2.65, 2.66, we obtain [43]

$$\eta \sim (\Delta\chi)^2 \tag{2.67}$$

which depending on the polarization of the probe beam 3 (see Figure 2.4) is given by

$$\eta_{s,simpleEO} = (Bn^4 r_{13} \cos\theta_G E_{sc}^0)^2 \tag{2.68}$$

for the s-polarized probe beam and

$$\eta_{p,simpleEO} = (Bn^4 \cos(\tilde{\theta}_2 - \tilde{\theta}_1) E_{sc}^0 [r_{13} \cos\tilde{\theta}_1 \cos\tilde{\theta}_2 \cos\theta_G \tag{2.69}$$

$$+ r_{13} \sin(\tilde{\theta}_1 + \tilde{\theta}_2) \sin\theta_G + r_{33} \sin\tilde{\theta}_1 \sin\tilde{\theta}_2 \cos\theta_G])^2$$

for a p-polarized beam. The angles used in Eqs. 2.68, 2.69 are the same as we introduced in Section 2.1.2 and showed in Figure 2.4. The factor B is given by [43]

$$B = \frac{\pi d}{2n\lambda\sqrt{\cos\tilde{\theta}_1 \cos\tilde{\theta}_2}} \tag{2.70}$$

The form of Eqs. 2.68 and 2.69 suggests that it is convenient to introduce the polarization anisotropy factor η_p/η_s which is independent of E_{sc}^0 [43]:

$$\left(\frac{\eta_p}{\eta_s}\right)_{\text{simple EO}} = \cos^2(\tilde{\theta}_1 - \tilde{\theta}_2) \left[\cos\tilde{\theta}_1 \cos\tilde{\theta}_2 + \sin(\tilde{\theta}_1 + \tilde{\theta}_2) \tan\theta_G + \left(\frac{r_{33}}{r_{13}}\right) \sin\tilde{\theta}_1 \sin\tilde{\theta}_2\right]^2 \tag{2.71}$$

The polarization anisotropy factor defined in Eq. 2.71 is determined by the geometry of the experiment (angles) and the ratio of the electro-optic tensor components r_{33}/r_{13}. For poled isotropic polymers, this ratio can be well approximated by [47] $r_{33}/r_{13} \approx 3$. This means that knowing the experimental angles of beam incidence (θ_1, θ_2) and the refractive index n, the polarization anisotropy factor can be easily calculated from

Eq. 2.71 and compared to the measured ratio of the diffraction efficiencies at *s*- and *p*-polarized reading beams. Therefore, the polarization anisotropy factor can serve as a test for the simple electro-optic model, and we will use this test when discussing our experimental data for diffraction efficiencies in Sections 3.4 and 3.5.

In most low T_g polymer composites, this test fails. In this case, "fails" means that the measured ratio η_p/η_s is much higher than predicted for a given geometry value given by Eq. 2.71. This is where the name "orientational enhancement" originates, and now we will discuss its basics.

2.4.2 Orientational enhancement

We start by stating some facts from the theoretical background for both the first order and second order response in poled polymers [47, 49]. In Chapter 4, where we will consider molecular orientation in the external electric field, this theory will be discussed in more detail. Here we just mention the facts that are necessary for the description of the orientational enhancement effect. For orientational purposes, the PR polymer composite is approximated by a polymer matrix that contains NLO chromophores possessing a dipole moment that can be oriented by a poling electric field E_{pole}. Also, an azimuthally symmetric distribution of the dipoles (NLO molecules) is assumed.

First order response

One of the mechanisms that contributes to the first-order response is the electronic response that arises from a collection of the molecules with fixed positions and orientations [49]. The bulk response of such a system will be given by

$$\chi_{ij}^{(1)} = N\langle\alpha\rangle_{ij} \tag{2.72}$$

where α is the dressed polarizability, N is the dipole concentration and the brackets denote an orientational average. The orientational average can be expressed explicitly through the rotation matrix $R(\Omega)$ and the orientational distribution function $G(\Omega)$ as follows (see Chapter 4 for details):

$$\chi_{ij}^{(1)} = \frac{N}{4\pi^2}\int d\mathbf{\Omega}\alpha_{i'j'}R_{i'i}(\Omega)R_{j'j}(\Omega)G(\Omega) \tag{2.73}$$

where $\mathbf{\Omega}$ represents the three Euler angles (see Chapter 4). Assuming azimuthal symmetry about the laboratory z-axis (direction of the external electric field in Figure 2.4), the orientational distribution function can be expanded in a series of orthogonal Legendre polynomials, $P_l(\cos\theta)$ [49]:

$$G(\cos\theta) = \sum_{l=0}^{\infty}\frac{2l+1}{2}\langle P_l\rangle P_l(\cos\theta) \tag{2.74}$$

where the coefficients $\langle P_l\rangle$ are the order parameters defined as

$$\langle P_l\rangle = \int_{-1}^{+1} d(\cos\theta)G(\cos\theta)P_l(\cos\theta) \tag{2.75}$$

For one-dimensional molecules whose long axis we denote as the 3-axis, the dressed polarizability α has one non-vanishing component α_{33}. Then, the evaluation of the integral 2.73 yields [49]

$$\chi_{zz}^{(1)} = \frac{N}{3}(1 + 2\langle P_2 \rangle)\alpha_{33} \tag{2.76}$$
$$\chi_{xx}^{(1)} = \chi_{yy}^{(1)} = \frac{N}{3}(1 - \langle P_2 \rangle)\alpha_{33}$$

In the limit of perfect alignment ($\langle P_2 \rangle = 1$), the bulk response is one-dimensional. For an isotropic material ($\langle P_2 \rangle = 0$), the susceptibility is isotropic. For a polymer poled in an electric field E_{pole} and containing NLO chromophores having a dressed dipole moment m^*, the order parameter $\langle P_2 \rangle$ is given by

$$\langle P_2 \rangle = \int_{-1}^{+1} d(\cos\theta) \times \left[\frac{\exp\left(\frac{m^* E_{pole}}{kT}\cos\theta\right)}{\int_{-1}^{+1} d(\cos\theta) \exp\left(\frac{m^* E_{pole}}{kT}\cos\theta\right)} \right] \left(\frac{3}{2}\cos^2\theta - \frac{1}{2}\right) \tag{2.77}$$

which after integration becomes:

$$\langle P_2 \rangle = 1 + \frac{3}{(m^* E/kT)^2} - \frac{3}{(m^* E/kT)} \coth\left(\frac{m^* E}{kT}\right) \tag{2.78}$$

At the infinite poling field limit ($E_{pole} \to \infty$)), the order parameter $\langle P_2 \rangle \to 1$ as expected for a perfectly ordered material. At low poling fields, the $\coth(m^* E/kT)$ can be expanded in a series ($\coth\xi = 1/\xi + \xi/3 - \xi^3/45 + ...$). Then, including the first three terms, the order parameter is

$$\langle P_2 \rangle \approx \frac{1}{15}\left(\frac{m^* E}{kT}\right)^2 \tag{2.79}$$

If we define a change in the susceptibility due to the poling electric field $\Delta\chi$, then taking into account Eq. 2.79, we can rewrite the Eqs. 2.76 as follows:

$$\Delta\chi^{(1)}_{zz} = \frac{2N\alpha_{33}}{45}\left(\frac{m^*E}{kT}\right)^2 \tag{2.80}$$
$$\Delta\chi^{(1)}_{xx} = \Delta\chi^{(1)}_{yy} = -\frac{N\alpha_{33}}{45}\left(\frac{m^*E}{kT}\right)^2$$

Moerner *et al.* [43] in their derivation of the orientational enhancement mechanism used a form similar to Eqs. 2.80. The only difference was that instead of a one-dimensional molecule that possesses just one polarizability component α_{33}, a molecule with two components - $\parallel$ (corresponding to 33) and $\perp$ (corresponding to $11 = 22$) was considered. The replacement α_{33} with the difference $\alpha_\parallel - \alpha_\perp$ takes care of this case. Introducing the notation

$$C_{BR} = \frac{2N(\alpha_\parallel - \alpha_\perp)}{45}\left(\frac{m^*}{kT}\right)^2 \tag{2.81}$$

and recalling the relationship between a change in susceptibility $\Delta\chi^{(1)}$ and a change in the refractive index Δn ($\Delta n = (1/2n)\Delta\chi^{(1)}$), we write the change in the refractive index as follows:

$$\Delta n_{zz,BR} = (1/2n)C_{BR}E^2_{pole} \tag{2.82}$$
$$\Delta n_{xx,BR} = -(1/4n)C_{BR}E^2_{pole}$$

The role of orientational enhancement effect in the first order (birefringence) response given by Eqs. 2.82 is that the poling field E_{pole} is determined not only by the

applied electric field E_a, but also the space charge field E_{sc}:

$$\mathbf{E}_{pole} = \mathbf{E}_T \tag{2.83}$$

where the total electric field E_T is given by

$$\mathbf{E}_T(\mathbf{r}) = [E_{sc}(\mathbf{r}) \sin\theta_G]\hat{\mathbf{x}} + [E_a + E_{sc}(\mathbf{r}) \cos\theta_G]\hat{\mathbf{z}} \tag{2.84}$$

Eqs. 2.82, 2.83 and 2.84 summarize the birefringence (first-order susceptibility) part of the orientational enhancement effect.

Second order response

An additional quadratic in electric field effect produces a susceptibility change due to the second order susceptibility $\chi^{(2)}$ (see Chapter 1 for definition), or on the molecular level, due to the hyperpolarizability β.

The treatment for determining the susceptibility change $\Delta\chi^{(2)}$ is similar to that of $\Delta\chi^{(1)}$ discussed in the previous section. We can write the second-order analog of the Eq. 2.73 as follows

$$\chi^{(2)}_{ijk} = \frac{N}{8\pi^2} \int d\mathbf{\Omega} \beta_{i'j'k'} R_{i'i}(\Omega) R_{j'j}(\Omega) R_{k'k}(\Omega) G(\Omega) \tag{2.85}$$

Assuming the one-dimensional molecule whose the only non-vanishing component of the hyperpolarizability tensor is β_{333}, the integration of the expression 2.85 yields two components that are independent of the second order bulk response:

$$\chi^{(2)}_{zzz} = N\beta_{333}\frac{m^* E_{pole}}{5kT} \tag{2.86}$$
$$\chi^{(2)}_{xxz} = N\beta_{333}\frac{m^* E_{pole}}{15kT}$$

As a side note, in Section 2.4.1, we said that the ratio of the electro-optic tensor components $r_{33}/r_{13} \approx 3$. Eqs. 2.86 reflect exactly this fact since $r_{33}/r_{13} = \chi^{(2)}_{zzz}(-\omega;\omega,0)/\chi^{(2)}_{xxz}(-\omega;\omega,0)$ [47] where the zzz and xxz components of the $\chi^{(2)}$-tensor are given by Eqs. 2.86.

The refractive index change due to the change in susceptibility given by Eqs. 2.86 taking into account Eq. 2.83 is

$$\Delta n_{zz,EO} = (1/2n)\Delta\chi^{(2)}_{zzz}E_T = (1/2n)C_{EO}E_T^2 \tag{2.87}$$

$$\Delta n_{xx,EO} = (1/2n)\Delta\chi^{(2)}_{xxz}E_T = (1/6n)C_{EO}E_T^2$$

where we introduced the coefficient C_{EO} as

$$C_{EO} = N\beta_{333}\frac{m^*}{5kT} \tag{2.88}$$

Eqs. 2.86 and 2.88 represent the electro-optic contribution (second-order response) to the orientational enhancement mechanism.

Orientation enhancement observation

After some theoretical considerations, we describe how orientational enhancement is observed in the PR experiments.

If we combine Eqs. 2.81, 2.88 and introduce the notation

$$C = C_{BR} + C_{EO} \tag{2.89}$$

$$A = \frac{C_{EO}}{3} - \frac{C_{BR}}{2}$$

or, in terms of microscopic quantities

$$C = \frac{N}{45(kT)^2}[9kTm^*\beta_{333} + 2m^{*2}(\alpha_\parallel - \alpha_\perp)] \tag{2.90}$$
$$A = \frac{N}{45(kT)^2}[3kTm^*\beta_{333} - m^{*2}(\alpha_\parallel - \alpha_\perp)]$$

then the diffraction efficiencies for s- and p-polarized probe beams can be expressed as follows [43]

$$\begin{aligned} \eta_s &= (BE_aE^0_{sc}(2A\cos\theta_G))^2 \qquad (2.91)\\ \eta_p &= (BE_a\cos(\tilde{\theta}_2 - \tilde{\theta}_1)E^0_{sc}[2A\cos\tilde{\theta}_1\cos\tilde{\theta}_2\cos\theta_G \\ &\quad +(C-A)\sin(\tilde{\theta}_1+\tilde{\theta}_2)\sin\theta_G + 2C\sin\tilde{\theta}_1\sin\tilde{\theta}_2\cos\theta_G])^2 \end{aligned}$$

where the coefficient B is defined by Eq. 2.70. The polarization anisotropy ratio η_p/η_s introduced in Section 2.4.1, with the diffraction efficiencies of Eqs. 2.91, is given by

$$\begin{aligned} \left(\frac{\eta_p}{\eta_s}\right) &= \cos^2(\tilde{\theta}_1 - \tilde{\theta}_2)\left[\cos\tilde{\theta}_1\cos\tilde{\theta}_2 + \frac{1}{2}\left(\frac{C}{A} - 1\right)\sin(\tilde{\theta}_1+\tilde{\theta}_2)\tan\theta_G \right.\\ &\quad \left. + \left(\frac{C}{A}\right)\sin\tilde{\theta}_1\sin\tilde{\theta}_2\right]^2 \qquad (2.92) \end{aligned}$$

The polarization anisotropy ratio in the presence of orientational enhancement effect given by Eq. 2.92 can be compared to that of Eq. 2.71 which is due to simple electro-optic effect.

In the limit in which the birefringence modulation is ignored so that $C/A = 3$ (see Eqs. 2.90), the polarization anisotropy ratio becomes the same as for the simple electro-optic effect. However, if one compares the definitions for the diffraction

efficiencies themselves (Eqs. 2.27, 2.28 and 2.91), one notices that both η_p and η_s are enhanced in case of orientational enhancement.

In the two beam coupling experiment discussed in Section 2.1.3 where the measurable quantity is the coupling constant Γ, or gain (see, for example Eqs. 2.23), the orientational enhancement effect shows as follows. The ratio of the gain for p- and s-polarized beams is expressed by [9]

$$\frac{\Gamma_p}{\Gamma_s} = \frac{1}{2}\cos(\tilde{\theta}_2 - \tilde{\theta}_1)\left[\frac{C}{A} - 1 + \left(\frac{C}{A} + 1\right)\cos(\tilde{\theta}_2 - \tilde{\theta}_1)\right] \tag{2.93}$$

For small angles between the incident beams $\cos(\tilde{\theta}_2 - \tilde{\theta}_1) \approx 1$, Eq. 2.93 transforms into the simple ratio

$$\frac{\Gamma_p}{\Gamma_s} = \frac{C}{A} \tag{2.94}$$

So, from the two beam coupling experiment, one can extract the ratio C/A. We will use this fact in the Section 3.4.1 where the two beam coupling measurements will be discussed.

2.5 Summary of Chapter 2

This section summarizes the main points introduced in Chapter 2.

First, we defined the photorefractive (PR) effect as the refractive index spatial modulation under spatially variant intensity pattern created by interfering optical beams. The main mechanisms that participate in the PR effect in polymer composites are photoconductivity and chromophore orientation in the electric field.

The photoconductivity part of the PR effect consists of several processes such charge photogeneration, transport and trapping. For each of these processes we considered theoretical models from literature. The microscopic theoretical model for the PR effect was analyzed and developed to study the influence of each process on the PR performance, in particular, the dynamics of the PR material. We also developed the procedure for predicting the PR speed on the basis of photoconductive properties of the material.

The orientational part of the PR effect is based on the ability of NLO chromophores that are the necessary constituents of the PR polymer composite, to orient in the electric field. We considered how the orientation of the chromophores in the total electric field given by a sum of applied external field and internal space charge field affects the PR properties.

We also discussed the main experimental techniques for probing the PR performance of a material: two beam coupling (2BC) and four wave mixing (FWM).

In the next Chapter, we will consider in detail the experimental methods for measuring both photoconductive and photorefractive figures-of-merit. Both strong and weak points and the applicability of each method will be discussed.

References

[1] W. E. Moerner, A. Grunnet-Jepsen, and C. Thompson. Photorefractive polymers. *Annu. Rev. Mater. Sci.*, 27:585–623, 1997.

[2] A. Ashkin, G. M. Boyd, J. M. Dziedzic, R. G. Smith, A. A. Ballman, J. J. Levinstein, and K. Nassau. Optically-induced refractive index change inhomogeneities in $LiNbO_3$ and $LiTaO_3$. *Appl. Phys. Lett.*, 9(1):72–74, 1966.

[3] F. S. Chen. A laser-induced inhomogeneity of refractive indices in KTN. *J. Appl. Phys.*, 38(8):3418–3420, 1967.

[4] F. S. Chen, J. T. LaMacchia, and D. B. Fraser. Holographic storage in lithium niobate. *Appl. Phys. Lett.*, 13(7):223–225, 1968.

[5] L. Solymar, D. J. Webb, and A. Grunnet-Jepsen. *The physics and applications of photorefractive materials*, volume 11 of *Oxford series in optical and imaging sciences*. Clarendon press, Oxford, 1996.

[6] D. S. Chemla and J. Zyss, editors. *Nonlinear optical properties of organic molecules and crystals*, volume 1,2. Academic, Orlando, 1987.

[7] K. Sutter and P. Gunter. Photorefractive gratings in the organic-crystal 2-cyclooctylamino-5-nitropyridine doped with 7,7,8,8-tetracyanoquinodimethane. *J. Opt. Soc. Am. B*, 7:2274–2278, 1990.

[8] S. Ducharme, J. C. Scott, R. J. Twieg, and W. E. Moerner. Observation of the photorefractive effect in a polymer. *Phys. Rev. Lett.*, 66(14):1846–1849, 1991.

[9] A. Grunnet-Jepsen, C. L. Thompson, and W. E. Moerner. Systematics of two-wave mixing in a photorefractive polymer. *J. Opt. Soc. Am. B*, 15(2):905–913, February 1998.

[10] H. Kogelnik. Coupled wave theory for thick hologram gratings. *The Bell system technical journal*, 48(9):2909–2947, 1969.

[11] K. Meerholz, E. Mecher, R. Bittner, and Y. Nardin. Competing photorefractive gratings in organic thin-film devices. *J. Opt. Soc. Am. B*, 15:2114, 1998.

[12] N. V. Kukhtarev, V. B. Markov, M. Soskin, and V. L. Vinetskii. Holographic storage in electro-optic crystals. *Ferroelectrics*, 22:961, 1979.

[13] J. S. Schildkraut and A. V. Buettner. Theory and simulation of the formation and erasure of space-charge field gratings in photoconductive polymers. *J. Appl. Phys.*, 72(5):1888–1893, 1992.

[14] Y. Cui, B. Swedek, N. Cheng, J. Zieba, and P. N. Prasad. Dynamics of photorefractive grating erasure in polymeric composites. *J. Appl. Phys.*, 85:38–43, January 1999.

[15] M. Pope and C. Swenberg. *Electronic Processes in Organic Crystals and Polymers*. Oxford University Press, 1999.

[16] B. Movaghar. Transport in polymers. *Phil. Mag. B*, 65(4):811–816, 1992.

[17] J. Schildkraut and Y. Cui. Zero order and first order theory of the formation of space-charge gratings in photoconductive polymers. *J. Appl. Phys.*, 72(11):5055–5061, December 1992.

[18] P. M. Borsenberger and D. S. Weiss. *Organic photoreceptors for xerography*, volume 59 of *Optical engineering*. Marcell Dekker, Inc., New York, 1998.

[19] L. Onsager. Initial recombination of ions. *Phys. Rev.*, 54:554–557, 1938.

[20] A. Mozumder. Effects of an external electric field on the yield of free ions. II The initial distribution of ion pairs in liquid hydrocarbons. *J. Chem. Phys.*, 60(11):4305–4310, 1974.

[21] P. Marcus and P. Siders. Theory of highly exothermic electron transfer reactions. *J. Phys. Chem.*, 86:622, 1982.

[22] E. Hendrickx, B. Kippelen, S. Thayumanavan, S. Marder, A. Persoons, and N. Peyghambarian. High photogeneration efficiency of charge-transfer complexes formed between low ionization potential arylamine and C_60. *J. Chem. Phys.*, 112(21):9557–9561, 2000.

[23] C. L. Braun. Electric-field assisted dissociation of charge-transfer states as a mechanism of photocarrier production. *J. Chem. Phys.*, 80(9):4157–4161, 1984.

[24] H. Bassler. Charge transport in disordered organic photoconductors - a monte-carlo simulation study. *Phys. Status Solidi (b)*, 175(1):15–56, January 1993.

[25] L. Schein. Comparison of charge transport models in molecularly doped polymers. *Phil. Mag. B*, 65(4):795–810, 1992.

[26] H. Scher and E. W. Montroll. Anomalous transit-time dispersion in amorphous solids. *Phys. Rev. B*, 12:2455–2477, 1975.

[27] S. V. Novikov and A. V. Vannikov. Field-dependence of charge mobility in polymer matrices. *Chem. Phys. Lett.*, 182(6):598–602, August 1991.

[28] N. F. Mott and E. A. Davis. *Electronic processes in non-crystalline materials.* Clarendon press, Oxford, 1971.

[29] M. Silver, K. Risko, and H. Bassler. A percolation approach to exciton diffusion and carrier drift in disordered media. *Philos. Mag. B*, 40(3):247–252, 1979.

[30] A. I. Rudenko. *Non-Cryst. Solids*, 22:215, 1976.

[31] R. Eiermann, G. M. Parkinson, H. Bassler, and J. M. Thomas. Structural investigations of amorphous tetracene and pentacene by low-temperature electron-diffraction. *J. Phys. Chem.*, 87(4):544–551, 1983.

[32] A. Miller and E. Abrahams. Impurity conditions at low concentrations. *Phys. Rev.*, 120(1):745–755, 1960.

[33] J. Slowik and I. Chen. Effect of molecular rotation upon charge transport between disordered carbazole units. *J. Appl. Phys.*, 54(8):4467–4473, 1983.

[34] P. Borsenberger and D. Weiss. *Organic Photoreceptors for Imaging systems.* Marcel Dekker, Inc., 1993.

[35] A. Goonesekera, S. Ducharme, J. M. Takacs, and L. Zhang. Low-field hole mobility in a photorefractive polymer. *J. Chem. Phys.*, 107(20):8709–8712, November 1997.

[36] M. Abkowitz, M. Stolka, and M. Morgan. Behavior of the drift mobility in the glass transition region of some hole-transporting amorphous organic films. *J. Appl. Phys.*, 52(5):3453–3457, 1981.

[37] A. Grunnet-Jepsen, D. Wright, B. Smith, M. S. Bratcher, M. S. DeClue, J. S. Siegel, and W. E. Moerner. Spectroscopic determination of trap density in -sensitized photorefractive polymers. *Chem. Phys. Lett.*, 291(5-6):553–561, July 1998.

[38] T. K. Daubler, R. Bittner, K. Meerholz, V. Cimrova, and D. Neher. Charge carrier photogeneration, trapping and space-charge field formation in pvk-based photorefractive materials. *Phys. Rev. B*, 61(20):13515–13527, 2000.

[39] P. Yeh. *Introduction to photorefractive nonlinear optics.* Wiley series in pure and applied optics. Wiley, New York, 1993.

[40] O. Ostroverkhova and K. D. Singer. Space-charge dynamics in photorefractive polymers II: Material considerations. *submitted to J. Appl. Phys.*, 2001.

[41] P. Gunter and J.-P. Huignard, editors. *Photorefractive Materials and Their Applications I.* Springer-Verlag, Berlin, 1988.

[42] J. A. Herlocker, C. Fuentes-Hernandez, K. B. Ferrio, E. Hendrickx, P.-A. Blanche, N. Peyghambarian, and B. Kippelen. Stabilization of the response time in photorefractive polymers. *Appl. Phys. Lett.*, 77(15):2292–2294, October 2000.

[43] W. E. Moerner, S. M. Silence, F. Hache, and G. C. Bjorklund. Orientationally enhanced photorefractive effect in polymers. *J. Opt. Soc. Am. B*, 11(2):320–330, February 1994.

[44] J. A. Herlocker, K. B. Ferrio, E. Hendrickx, B. D. Guenther, S. Mery, B. Kippelen, and N. Peyghambarian. Direct observation of orientation limit in a fast photorefractive polymer composite. *Appl. Phys. Lett.*, 74(16):2253–2255, April 1999.

[45] K. S. West, D. P. West, M. D. Rahn, J. D. Shakos, F. A. Wade, K. Khand, and T. A. King. Photorefractive polymer composite trapping properties and link with a chromophore structure. *J. Appl. Phys.*, 84(11):5893–5899, 1998.

[46] S. M. Silence, G. C. Bjorklund, and W. E. Moerner. Optical trap activation in a photorefractive polymer. *Opt. Lett.*, 19(22):1822–1824, November 1994.

[47] K. D. Singer, M. G. Kuzyk, and J. E. Sohn. 2nd-order nonlinear-optical processes in orientationally ordered materials - relationship between molecular and macroscopic properties. *J. Opt. Soc. Am. B*, 4:968–976, 1987.

[48] R. Boyd. *Nonlinear optics.* Academic press, San Diego, 1992.

[49] M. G. Kuzyk and C. W. Dirk, editors. *Characterization Techniques and Tabulations for Organic Nonlinear Optical Materials*, volume 60 of *Optical Engineering.* Marcel Dekker, New York, 1998.

Chapter 3

Photorefractive effect: Material considerations

3.1 Introduction

Chapter 3 is fully devoted to the experimental techniques for photoconductivity and photorefraction studies in polymers.

In Section 3.2, the materials used in my study of both photoconductivity and photorefraction will be described.

Then, in Section 3.3.3, we will consider the experimental techniques for photoconductivity measurements. These include the xerographic discharge measurements for photogeneration efficiency studies, the time-of-flight (TOF) method for measuring the free charge carrier mobility and DC photoconductivity for trapping, detrapping and recombination studies. For each of these measurements, we will present characteristic trends and dependencies that are used for polymer and polymer composite characterization.

Next, in Section 3.4, we will discuss the details of the PR measurements.

Finally, the connection of the PR experimental results to the theory elaborated in Chapter 2 and the photoconductivity experiments described in Section 3.3 will be presented in Section 3.5.

We start by introducing the materials used in my studies and the sample preparation.

3.2 Materials

The choice of materials for the studies I am presenting in Chapter 3 was induced by the primary goal of this research which is PR polymer composite performance and the requirements for a polymer composite to be suitable for the PR effect. These requirements originate from the mechanisms leading to the PR effect in polymers (see Section 2.1.2). There are different approaches to creating a PR polymeric material. The choices for the PR polymer or polymer composite design include the following [1]: 1) the NLO property is incorporated into the polymer, while the functional groups responsible for charge generation and transport are incorporated as guest molecules in the polymer matrix; 2) the polymer provides charge transport, while the charge generator and NLO chromophores are added as guest molecules; 3) all the functional groups are attached to the polymer backbone.

The PR polymer composites we have used belong to the class 2), so when de-

scribing some general features of the PR polymers, we will mean a composite based on a photoconductive polymer with added charge generator (sensitizer) and NLO chromophore.

3.2.1 Composition of photorefractive polymer materials

The first requirement for the PR polymer composite is that the material should be sensitive to the optical beams at their wavelength which means that it has to absorb at this wavelength. To optimize the PR performance, the absorption properties of various components of the polymer composite should be carefully chosen. Most host polymers have their absorption band in the UV region, while most NLO chromophores are strongly absorbing in the blue and green portion of the visible [1]. The optimal situation for the PR effect is when the light is absorbed by only one component - the charge generator - that leads to the "useful" outcome of photogeneration of mobile charge. Absorption by any of the other components will increase the background absorption and will not contribute to the PR effect. Thus, the charge generator, or sensitizer, is chosen to possess the longest wavelength absorption. Most PR studies in polymers are done using the red spectral part (for example, $632.8\,nm$ of HeNe laser [2, 3, 4] or $676\,nm$ of Kr^+ laser [5]), so the sensitizer has to provide absorption at these wavelengths. At these wavelengths, the most widely used sensitizers are fullerene C_{60} and 2,4,7-trinitro-9-fluorenone (TNF) [6]. In our studies, the C_{60} was used. (Figure 3.1).

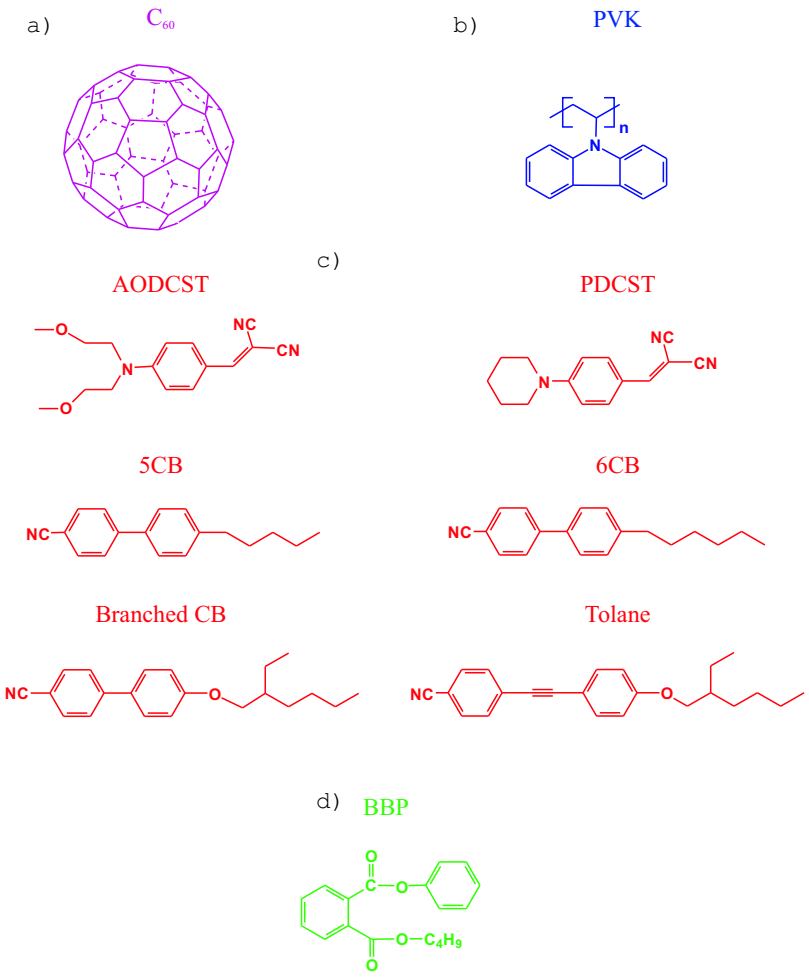

Figure 3.1: Materials used in this study: a) charge generator; b) photoconductor; c) NLO chromophores; d) plasticizer.

The second requirement is that the material should be photoconductive. In addition, for electron-transfer photosensitization to occur, the photoconductor has to have an ionization potential smaller than that of the charge generator [7] (see Figure 2.5). In our case, the role of the transport agent is assigned to the photoconductive polymer poly(N-vinylcarbazole) (PVK) (Figure 3.1) which forms a charge-transfer complex with the sensitizer C_{60}.

PVK exhibits unipolar charge transport, with holes being the mobile carrier. This transport property is determined by the chemical nature of the transport group (in case of PVK, the carbazole group) which is donor-like in its neutral state [8]. If as a result of the photogeneration process some carbazole moieties are positively charged, then under the influence of the applied electric field, neutral molecules (carbazole groups) will repetitively transfer electrons to their neighboring cations. The net result of this process is the motion of a positive charge (hole) across the bulk of the sample film. This is strictly electronic and not an ionic transport process since no mass displacement is involved. In PVK, the pendant carbazole groups are on every other carbon atom on the chain. Since the backbone is saturated, any orientation around the $C-C$ bonds is permitted, so the carbazole groups are arranged at all angles around the polymer backbone [9]. Each chain consists of a high concentration of carbazole molecules, and the chains are twisted and coiled. The ability of PVK to conduct depends upon how close to each other the active groups are, since charge

transport is only conducted through the π-molecular orbitals of the carbazole groups while the vinyl backbone of PVK merely provides the mechanical stability of the film and is irrelevant for transport purposes [10, 11].

The third requirement is that the material possesses NLO properties, so that the linear electro-optic effect is possible. In our case, this is achieved by adding NLO chromophores (Figure 3.1) into the polymer composite.

In order to lower the glass transition temperature T_g of the composite, another constituent, a plasticizer (Figure 3.1), is often added to the system. For example, the T_g of PVK is $\sim 200^0\,C$, so the room temperature at which most of the measurements are conducted is much lower than that. The main reason for lowering T_g of the composite down to the room temperature is to enhance the orientational effects. In other words, at $T_g \approx T_{room}$, the NLO molecules (dipoles) can more easily orient in the electric field. The photoconductive properties of the polymer composite also change as the temperature at which the experiments are conducted approaches the glass transition temperature, but this effect is minor in comparison to the orientational effects. This topic will be discussed in more detail in Section 3.5.

Typical concentrations of the PR polymer composite constituents used in these studies include: $\sim 0.1-1\,\%$ of C_{60}, $\sim 0-40\,\%$ of the plasticizer BBP (see Figure 3.1), $\sim 1-40\,\%$ of NLO chromophore, and finally $\sim 50-100\,\%$ of PVK.

3.2.2 Sample preparation

The polymer composites based on the materials described in the previous section were prepared as follows.

The photoconductive polymer PVK (commercially available as a powder) was dissolved in the 4:1 mixture of toluene and cyclohexanone at wt. concentration $\sim 10-12\,\%$ depending on the desired polymer film thickness. Usually, PVK is easily soluble at room temperature. Ideally, the solution is transparent and clear (without any coloration). The purity of both PVK powder and the solvents can be a concern, since the solution changes its color with time - from clear to dark yellow. Since this changes the property of the polymer (for example, the free carrier mobility decreases), both PVK and solvents should be pure, and the solution used for making the samples should be fresh.

The next component is the sensitizer C_{60}. This powder is dissolved in toluene and added to the PVK solution. C_{60} is not dissolved easily, thus it is not desirable to add it to the PVK solution without dissolving it first. Even if one attempts to dissolve $1\,wt.\,\%$ of C_{60} in toluene, there will be undissolved C_{60} molecules. So, the procedure includes making the $C_{60}(\sim 1\,wt\,\%)$/toluene solution, then its filtration and weighting the precipitate to determine the true concentration of C_{60} molecules in solution (usually not more that $0.1\,wt\,\%$ out of $1\,wt.\,\%$ prepared initially). If all the weighing and filtering is done carefully, it is possible to calculate the number density

N_A of the C_{60} molecules (see Figure 2.5 and Eqs. 2.29). As we will see further, this quantity is useful for the anticipated PR speed calculation.

When PVK solution is mixed with the C_{60} solution, the chromophore and the plasticizer (if needed) are added. It is not a problem to dissolve any of the chromophores depicted in Figure 3.1 in the PVK solution. However, large concentrations of the chromophores are not desirable because of phase separation that takes place in such composites as observed with naked eye or with a microscope. For example, in PVK/5CB composite (no plasticizer), the maximal wt. concentration at which the phase separation does not happen yet, is $\sim 50\,\%$ of 5CB. For other chromophores, it is often lower than that: $\sim 40\,\%$ for AODCST, $\sim 30\,\%$ for PDCST etc.

For the measurements to be described later in this chapter (Sections 3.3 and 3.4), two kinds of samples - with Al electrodes and ITO electrodes - were made.

One type (with Al electrodes) was prepared as follows. The film made of the polymer composite was spin-coated on the glass substrate coated with Al. Then, the film dried in the oven at $\sim 90^\circ C$ overnight to evaporate the solvent. The thickness of such spin-coated films, as determined using a Dektac profilometer, varied from $5-15\,\mu m$ depending on the concentration of PVK in the solution. The second Al electrode was deposited directly on top of the films using a Denton vacuum apparatus for electron beam deposition. The thickness of the deposited Al layer was $\sim 200\,$Å which was sufficiently conductive and, on the other hand, semitransparent. The Al samples were

used for photoconductivity experiments - xerographic discharge (Section 3.3.1), TOF (Section 3.3.2) and DC photoconductivity (Section 3.3.3). For some composites, usually with high content of the plasticizer or a chromophore like 5CB or similar, the Al deposition on top of the film failed. For such samples, all the studies were conducted using a different, sandwich kind of the samples.

The sandwich kind of samples was prepared as follows. First, two semi-transparent ITO-covered glass slides were cleaned with acetone and methanol. Then, the films were cast from solution and dried in the oven at $\sim 90^\circ C$ overnight to evaporate the solvent. Next, the two slides with films on them were pressed together and placed in vacuum oven where the sandwich was baked for $\sim 1\,h$ at the temperature much higher than the glass transition temperature of the composite (usually $T \sim 120^\circ - 180^\circ C$ depending on T_g). Such samples were used for the PR studies (Section 3.4) and for photoconductivity experiments for some of the composites. The thickness of the sandwich samples was usually measured with a microscope or calculated from the capacitance measurements and the known dielectric constant.

In both types of samples, when the sample itself is ready, the contacts are made with a silver conductive epoxy, so that an electric field can be applied to the sample.

We now consider different techniques targeting various photoconductive properties of the polymeric materials.

3.3 Photoconductivity experiments

In this section, we review the experimental techniques used for photoconductive studies of polymers. We will consider the applicability of the techniques, necessary equipment, details of the experimental set-up and data analysis. Also, typical data will be presented, and the characteristic behavior will be discussed.

3.3.1 Xerographic discharge technique

The photoinduced (xerographic) discharge technique is one of the most widely used techniques for measurement of photogeneration efficiencies in polymers [12, 2, 3]. Other techniques allowing such a measurement include transient photocurrent measurements (essentially TOF experiment which will be described in Section 3.3.2), photoacoustical measurements, fluorescence quenching etc. [13]. For my purposes, the xerographic discharge technique appeared the most suitable, and so we will consider it in detail.

The idea of the experiment is that the sample is charged by a corona or contact method, then the rate of discharge is measured when the sample is exposed to radiation of an appropriate wavelength [14]. There are advantages and disadvantages for both the corona and the contact poling method. In corona poling, the sample surface is charged by a needle which is kept under high voltage. This method is non-contact, and therefore it allows one to conduct measurements at higher electric field than the

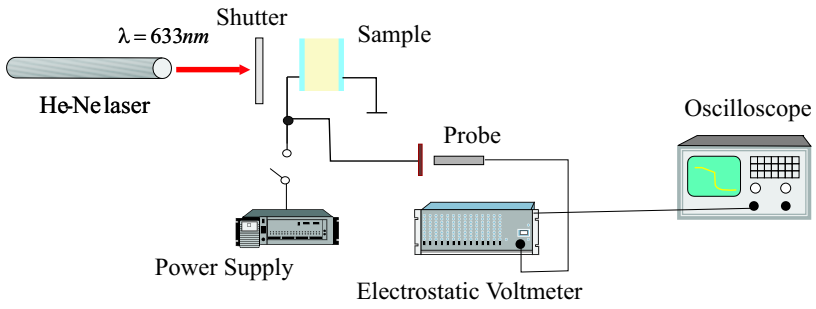

Figure 3.2: Experimental set-up for xerographic discharge technique

contact method without dielectric breakdown. However, the electric field produced in the film is inhomogeneous. Also, the chromophores can diffuse from the surface to the bulk or evaporate [15] which can obstruct the concentration dependent measurements. We also used contact poling, so that one of the sample electrodes was charged to a potential V_0 and then disconnected from the power supply (Figure 3.2). The decrease in the surface potential $V(t)$ was monitored using a Monroe static voltmeter. First, the decay of the potential $V(t)$ due to dark current ("dark" discharge) was observed, and then the light was turned on, and the decay of the potential $V(t)$ under illumination ("light" discharge) was recorded with a digital oscilloscope.

For photogeneration measurements, the discharge is usually measured with low-intensity monochromatic exposures. For my studies, the target was the PR polymer composites sensitized with C_{60} (see Section 3.2), and so the wavelength of interest for photogeneration efficiency measurements was $\lambda = 632.8\,nm$ of a HeNe laser.

For xerographic discharge measurements of the photogeneration efficiency, the conditions of emission-limited discharge should be met. This means that the charge

photogenerated in the bulk during a transit time t_T is small compared to the surface charge Q_s. The transit time can be defined as

$$t_T = \frac{d^2}{\mu V} \tag{3.1}$$

where d is the thickness of the sample, μ is the mobility, and V is applied voltage. The surface charge Q_s is given by

$$Q_s = \frac{\varepsilon_0 \varepsilon V}{de} \tag{3.2}$$

The number of carriers emitted into the bulk during a transit time is

$$N_h = \frac{I_0 \alpha d}{\hbar\omega} \phi t_T \tag{3.3}$$

where I_0 is the incident light intensity, ω is the light frequency, α the absorption of the material at light frequency ω, and ϕ is the photogeneration (quantum) efficiency. Eq. 3.3 also assumes low absorption, so that the absorbed intensity is given by

$$I_0[1 - \exp(-\alpha d)] \approx I_0 \alpha d \tag{3.4}$$

Taking into account Eqs. 3.2, 3.3 and 3.1, we rewrite the condition of emission-limited discharge $N_h \ll Q_s$ as a condition for incident light intensity:

$$I_0 \ll \frac{\varepsilon_0 \varepsilon \hbar\omega}{e\alpha d^4} \frac{\mu}{\phi} V^2 \tag{3.5}$$

This is where the requirement of "low intensity" comes from. However, in practice, it is hard to estimate the limit of "low intensity" from Eq. 3.5, since the quantum

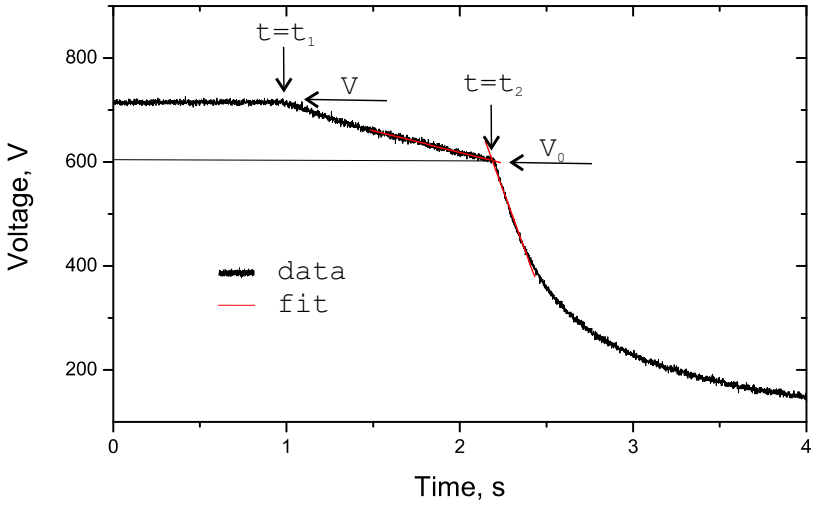

Figure 3.3: Typical experimental data from the xerographic discharge measurement.

efficiency ϕ is an unknown quantity which is supposed to be determined in this experiment. So, the safest way is to count the quantum efficiency $\phi \approx 1$ when calculating the intensity limit using Eq. 3.5.

Typical data from the xerographic discharge experiment is shown in Figure 3.3 for our composite PVK(59 %)/C_{60}(1 %)/6CB(40 %). The voltage V was applied to the sample and then at $t = t_1$ the power supply was disconnected, and dark decay was observed until $t = t_2$ when the light beam was opened with a shutter. The quantities we extract from Figure 3.3 are the dark and total (dark + light) discharge rates $(dV/dt)_{dark}$ and $(dV/dt)_{total}$ respectively. These are given by the slopes of the corresponding parts of the function $V(t)$ near the cusp (see Figure 3.3) which are obtained with a linear fit. Also, for materials with non-negligible dark discharge, the voltage at which the photogeneration is actually measured is not the initially applied

voltage V, but the voltage V_0 at which the light is turned on (see Figure 3.3). Then, the quantum efficiency ϕ is calculated as [13]

$$\phi = -\frac{\varepsilon_0 \varepsilon \hbar \omega}{e \alpha d^2 I_0} \left[\left(\frac{dV}{dt} \right)_{total} - \left(\frac{dV}{dt} \right)_{dark} \right] \tag{3.6}$$

The quantum efficiency ϕ is measured as a function of electric field $E_0 = V_0/d$ and calculated from Eq. 3.6, and is described by the Onsager theory discussed in Section 2.2.1. The experimentally determined dependence $\phi(E_0)$ on E_0 is fit by the Onsager function (Eq. 2.33) to determine the primary quantum yield ϕ_0 and thermalization radius r_0 (see Section 2.2.1).

Some useful checks that the quantum efficiency ϕ was measured correctly include ensuring the absence of both incident intensity I_0 and sample thickness d dependencies of ϕ. In other words, the discharge rate $(dV/dt)_{light} = (dV/dt)_{total} - (dV/dt)_{dark}$ should scale with intensity and thickness. If ϕ shows intensity or thickness dependence at constant applied electric field, the measurement has been done incorrectly. there are several possibilities. The simplest one is that the condition given by Eq. 3.5 has not been met. The more complicated ones are that the material has too strong trapping and recombination, and in this case, Eq. 3.6 is not applicable [13]. For all the composites we studied, this problem did not occur, and so we applied Eq. 3.6 for all of the calculations of ϕ. However, there was another problem with calculating ϕ using Eq. 3.6 related to difficulties in measuring the absorption coefficient α (see Eq. 3.6). In the composites we studied, the absorption at $\lambda = 632.8\,nm$ is only due

to the sensitizer C_{60} whose content in the polymer composite is on the order of 1 % or less and thus, it is too low to be measured accurately. With $\alpha \sim 10\, cm^{-1}$ for such composites, the thickness at which the absorption could be easily measured is difficult to obtain, and so special attention should be paid to obtaining low-background absorption measurements.

In addition to the quantum efficiency ϕ, the photogeneration cross-section s introduced in Eqs. 2.29 is of interest since we want to use the measured value of s together with other photoconductivity parameters to predict the PR speed using Eqs. 2.58 and procedure developed in Section 2.3.

As mentioned in Section 2.2.1, the photogeneration cross-section s is connected to the quantum efficiency ϕ by the relation

$$s = \alpha\phi/(\hbar\omega N_A) \tag{3.7}$$

where N_A is the acceptor (sensitizer, or in our case C_{60}) density. Then, using Eqs. 3.7 and 3.6, we can calculate the cross-section of photogeneration s from the slope of the intensity dependence of the rate of discharge due to illumination:

$$\left|\frac{dV}{dt}\right|_{light} = \frac{sd^2eN_A}{\varepsilon_0\varepsilon} I_0 \tag{3.8}$$

Performing the xerographic discharge experiment at various applied electric fields allows one to determine the dependence $s(E_0)$. In Section 2.2.1, where we considered the theoretical background of photogeneration, we introduced the simplified electric

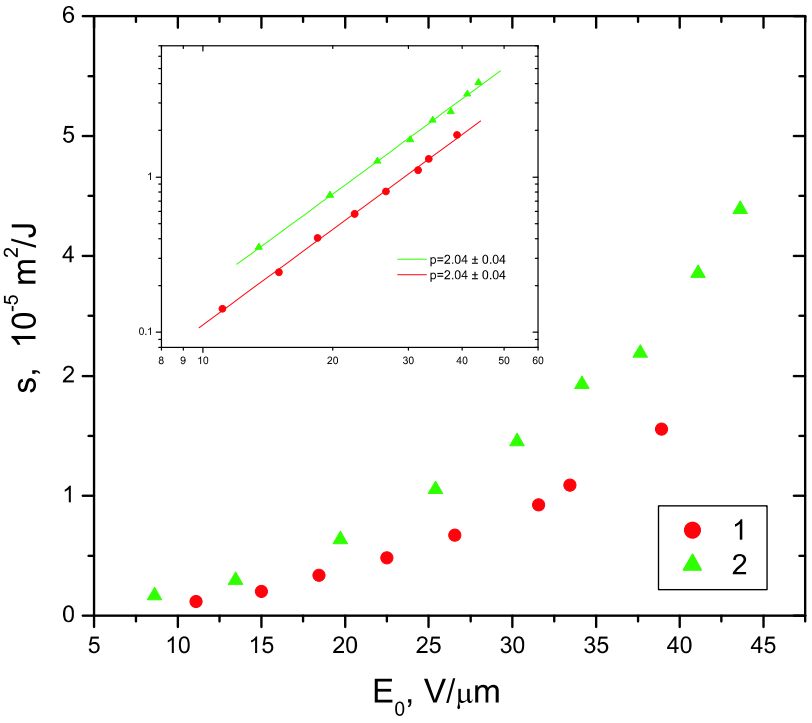

Figure 3.4: Electric field dependence of the photogeneration cross-section for: 1) PVK(89 %)/C_{60}(1 %)/PDCST(10 %); 2) PVK(89 %)/C_{60}(1 %)/AODCST(10 %). Inset shows the same dependencies plotted on a log-log scale, with linear fits whose slopes yield the parameter p.

field dependence $s \sim E_0^p$ (see Section 2.2.1) and indicated that the parameter p is determined experimentally. Figure 3.4 shows the electric field dependence of the photogeneration cross-section for several composites. Parameter p is extracted from a linear fit to a log-log plot of $s(E_0)$, as shown in the inset of Figure 3.4.

The limitation of the xerographic discharge technique can be noted when observing Figure 3.3. If the material possesses high dark current, then the dark discharge is large, and for low quantum efficiencies, the discharge that is due to the light only, will be obscured. We observed this feature in composites with a high plasticizer or NLO

chromophore content (PVK(49 %)/C_{60}(1 %)/NLO(x %)/BBP(50-x %) where x varied from $0-40$ %). These composites exhibit high ionic current, so at low electric fields where the quantum efficiency is low, the xerographic discharge measurement cannot be used for obtaining the photogeneration (quantum) efficiency. In such cases, other methods are used, e.g. onset of DC photoconductivity measurements which we will consider in Section 3.3.3.

3.3.2 Time-of-flight technique

A number of experimental techniques are available for the study of electrical conduction processes, and the choice of a particular method depends on sample shape, bulk conductivity, carrier lifetimes, and mobility [16]. When the quantity of interest is the carrier drift mobility μ in PR polymers and composites, the choice usually narrows to the time-of-flight (TOF) technique [16], the holographic time-of-flight (HTOF) technique [17] or DC photoconductivity [18]. In this section, we will consider in detail the TOF method.

The TOF experiment is performed by injecting a thin carrier sheet from the surface of the sample film and measuring the time t_T (transit time defined in Eq. 3.1) it takes the sheet to drift across the sample under the influence of an applied electric field. In photoconductive materials, the sheet of charge is produced by a flash of light which is absorbed within a small fraction of the sample thickness d. The experimental set-up that we used for the TOF experiment is shown in Figure 3.5. The source of the light

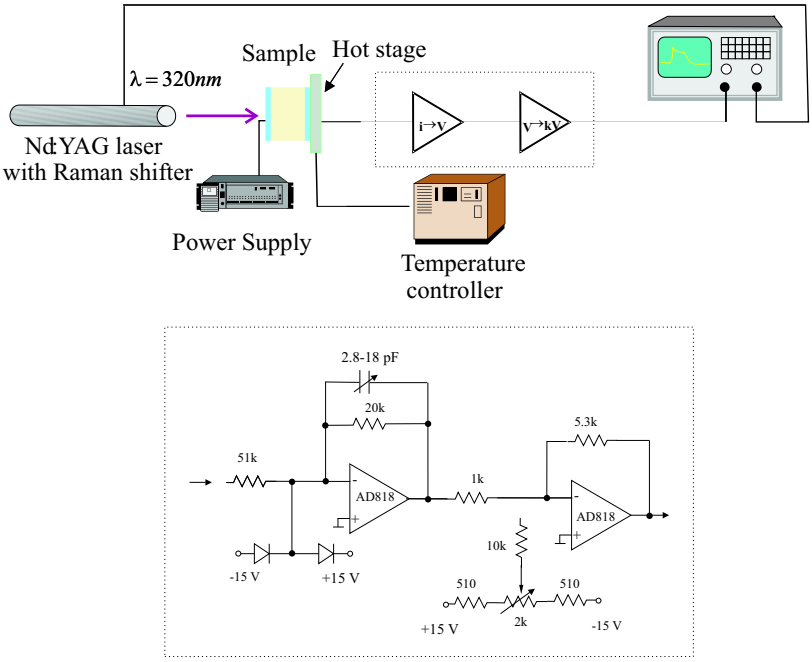

Figure 3.5: Experimental set-up for the time-of-flight (TOF) technique. The home-made circuit includes a current to voltage converter conjugated with a preamplifier.

.

flash was the third anti-stokes of H_2 - stimulated Raman-shifted $532\,nm$ of Nd:YAG laser (with a wavelength of $320\,nm$) with a $3.5\,ns$ pulse of $\sim 5\,\mu J/pulse$. The current through the sample was transformed to a voltage, amplified and monitored with an oscilloscope. The requirement for the external circuit is that its response time has to be much faster than the transit time t_T. In our case, the response time of the circuit is $\sim 1\,\mu s$ which is well below the typical transit times of $\gtrsim 0.5\,ms$ observed in PVK-based materials at the usual operating electric fields of $\lesssim 80V/\mu m$.

The choice of the operating wavelength of $320\,nm$ is suggested by the absorption spectrum of PVK, with a UV cut-off at about $350\,nm$, to ensure strong absorption. Since for PVK-based materials, only hole transport takes place, the illuminated electrode has to be charged positively, so that holes the generated by the flash would move towards the opposite electrode.

Another requirement for the TOF experiment is that the charge due to injected carriers is much smaller than the charge stored on the electrodes of the sample (CV). In this case, the electric field in the sample $E_0 = V/d$ can be considered constant throughout the experiment. This condition is similar to that of the xerographic discharge low intensity limit requirement considered in the previous section.

Ideally, when the sheet of carriers starts to travel across the sample, a constant current $i = qE_0\mu/d$ is flowing in the external circuit until the sheet reaches the opposite electrode at the time $t_T = d/(\mu E_0)$, which causes an abrupt drop of the current to

zero. In these equations, q is the total charge injected into the sample by the incident light flash.

In disordered solids such as polymers, deviations from the ideal rectangular current pulse are observed. These arise from statistical fluctuations of the microscopic processes a carrier experiences as it drifts across the solid. Namely, diagonal and off-diagonal disorder (see Section 2.2.2) cause the carriers propagating through the solid to experience a distribution of hopping times. Consequently, the carrier packet that was injected as a thin sheet at the surface of the sample broadens as it penetrates the bulk. Such behavior was predicted on the basis of Gaussian statistics [8], which describes the carrier packet of Gaussian shape moving across the bulk, so that the mean position of the packet $\langle l \rangle$ increases in time as $\langle l \rangle \sim t$, and the Gaussian spread σ increases as $\sigma \sim \sqrt{t}$. However, for many disordered solids, including the PVK-based polymer composites we studied, this behavior is not observed. Instead, the current pulses with a typical shape similar to those shown in Figure 3.6a exhibits so called "dispersive transport", is common for polymers. This current transient shape (Figure 3.6a) as well as the dependence of the transit time t_T for holes on sample geometry and applied electric field cannot be described in terms of conventional theories based on Gaussian statistics.

Scher and Montroll proposed the continuous-time random walk (CTRW) treatment of hopping of a carrier among a random set of localized sites [19] as a model for

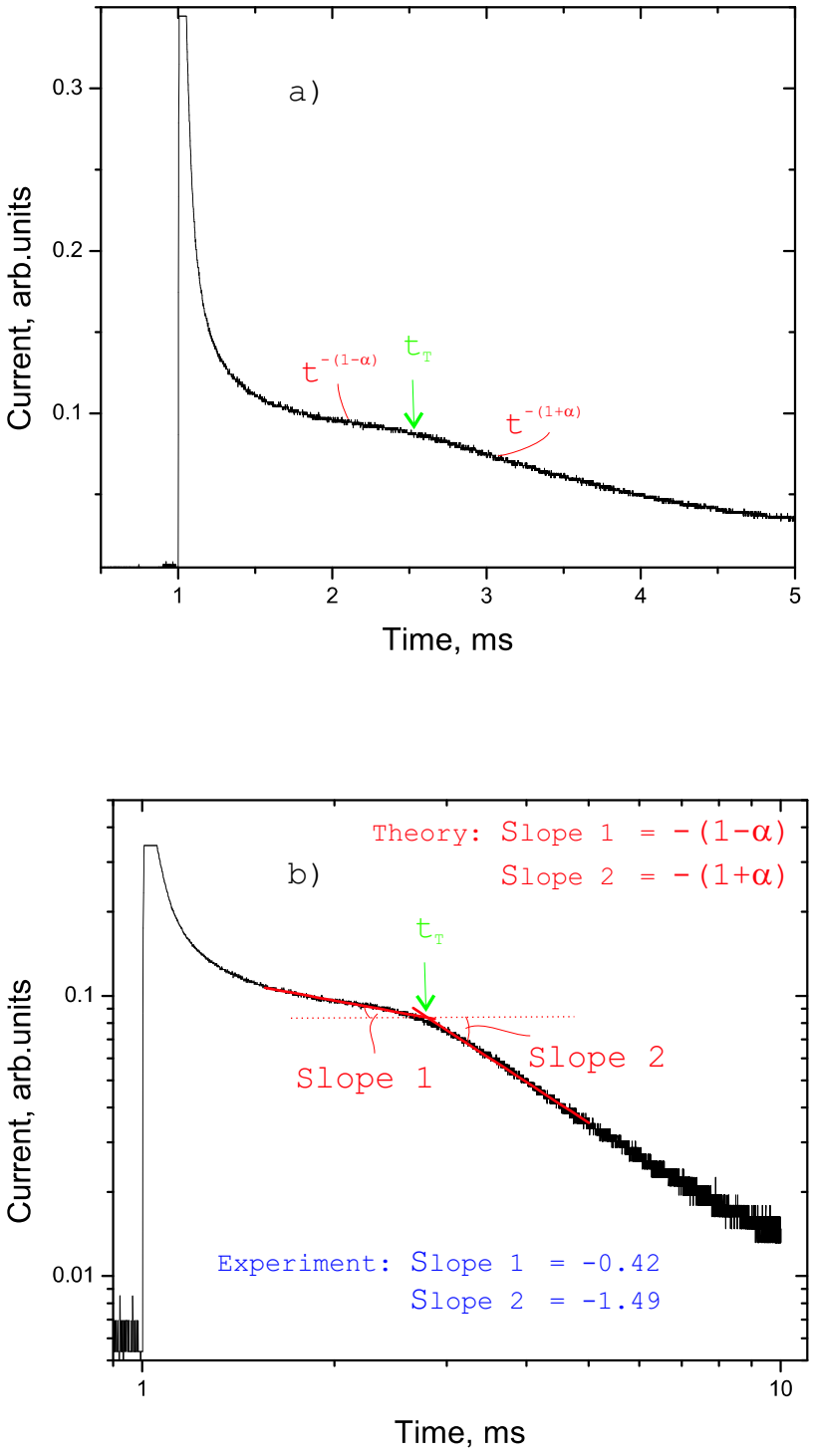

Figure 3.6: Example of a current pulse as observed in PVK with the TOF technique indicating dispersive transport: a)linear scale plot; b) log-log plot.

non-Gaussian charge transport. In the CTRW model, the assumption is made that the transition times between nearest-neighbor sites occur at random time intervals determined by a probability distribution function $\psi(t)$, where $\psi(t)dt$ is the probability that a carrier will arrive at a given site during the time interval between t and $t+dt$ if the time of arrival at a neighboring site is taken as $t=0$. The form of $\psi(t)$ used by Scher and Montroll was

$$\psi(t) \sim t^{-(1+\alpha)} \tag{3.9}$$

where $0 < \alpha < 1$, instead of $\psi(t) \sim \exp(-\xi t)$ used in Gaussian statistics. If the distribution function of Eq. 3.9 is assumed, the transient current shows the following time dependence, as illustrated in Figure 3.6:

$$i \sim t^{-(1-\alpha)}, t < t_T \tag{3.10}$$

$$i \sim t^{-(1+\alpha)}, t > t_T$$

According to Eqs. 3.10, the sum of slopes on the $\log i$ versus $\log t$ curves for $t<t_T$ and $t>t_T$ is equal to -2, independent of α. In reality, this does not always hold, which means that some of the approximations used in the Scher-Montroll formalism may not apply. Even for neat PVK, the sum of the slopes departs from -2 as it can be seen from Figure 3.6b. For the PVK-based composites the deviation from the theory is larger than that for neat PVK.

Among other results of the CTRW model, is the thickness dependence of the transit time $t_T \sim d^{(1/\alpha)}$ which leads to the thickness dependence of the mobility μ

given by

$$\mu = \frac{d}{Et_T} \tag{3.11}$$

This fact implies that the concept of carrier mobility as it was initially introduced is not necessarily meaningful.

In practice, the extraction of the transit time t_T from log-log plots similar to that shown in Figure 3.6 is widely used. Then, the mobility μ of Eq. 3.11 is calculated from the transit time t_T and applied electric field $E_0 = V/d$. If one needs to compare the carrier mobilities in two different materials, one makes the samples of approximately equal thickness, so that the effect of thickness dependence of the mobility does not affect the results.

Regarding the general trends for electric field and temperature dependence of the mobility, the Scher-Montroll theory agrees with the disorder formalism described in Section 2.2.2. As the electric field or temperature increases (for $T < T_g$), the current transients become less dispersive. For example, the transient evolution observed in PVK at increasing temperature is illustrated Figure 3.7. As the temperature or electric field increases, the energy barrier between hopping sites reduces (see Section 2.2.2), i.e. the disorder in the system decreases, and thus the current shapes display the transition from dispersive to non-dispersive regime. Mathematically, this transition can be expressed through the quantity W called "tail-broadening parame-

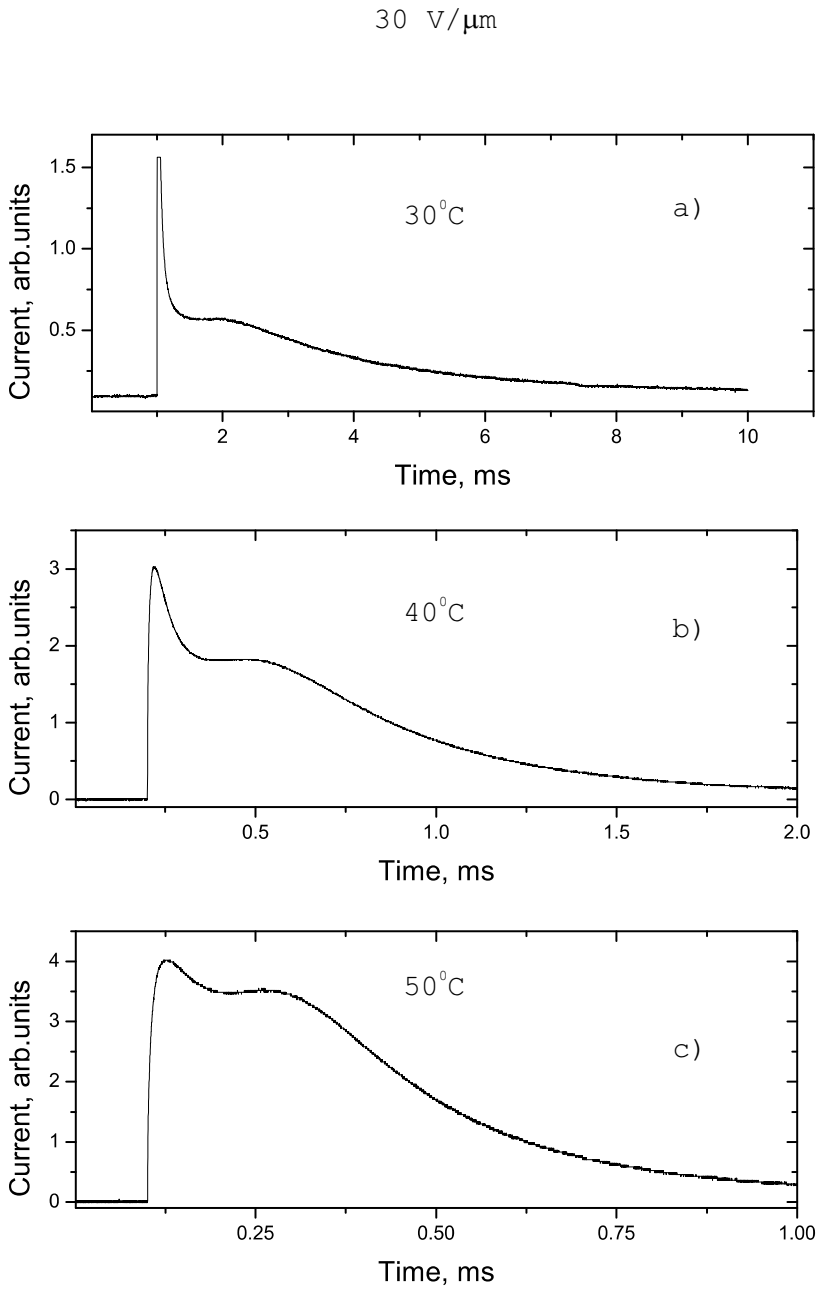

Figure 3.7: Current transients as observed in PVK using TOF technique at various temperatures at the electric field $30\,V/\mu m$.

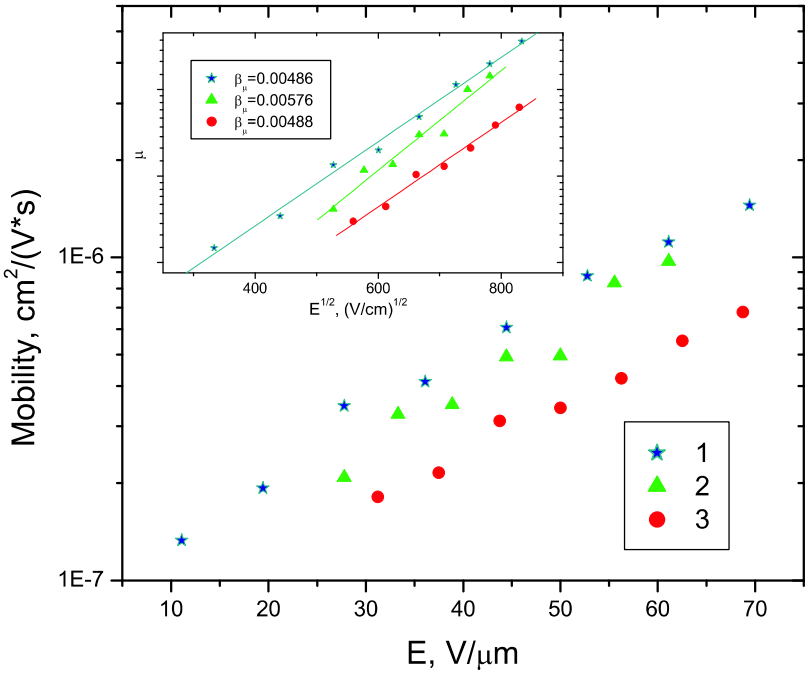

Figure 3.8: Dependence of the mobility on the electric field for composites: 1 - PVK(99 %)/C_{60}(1 %) ; 2 - PVK(89 %)/C_{60}(1 %)/AODCST(10 %); 3 - PVK(89 %)-/C_{60}(1 %)/PDCST(10 %). Inset shows a linear fit of the mobility versus the square root of the electric field. The slope of the linear fit is the mobility electric field parameter β_μ. The parameters β_μ are given in units of $(cm/V)^{1/2}$.

ter". W is defined as [20]

$$W = \frac{t_{1/2} - t_T}{t_{1/2}} \tag{3.12}$$

and introduced to describe the dispersion of the photocurrent transients. In Eq. 3.12, $t_{1/2}$ is the time required for the current to decrease to one-half of its value at t_T.

Due to the decrease of disorder with electric field and temperature, the mobility increases as a function of both electric field and temperature (Figures 3.8, 3.9). Using Eq. 2.39 and the measured field and temperature dependencies of the carrier mobility, one can extract parameters of the system such as the DOS width σ and off-diagonal

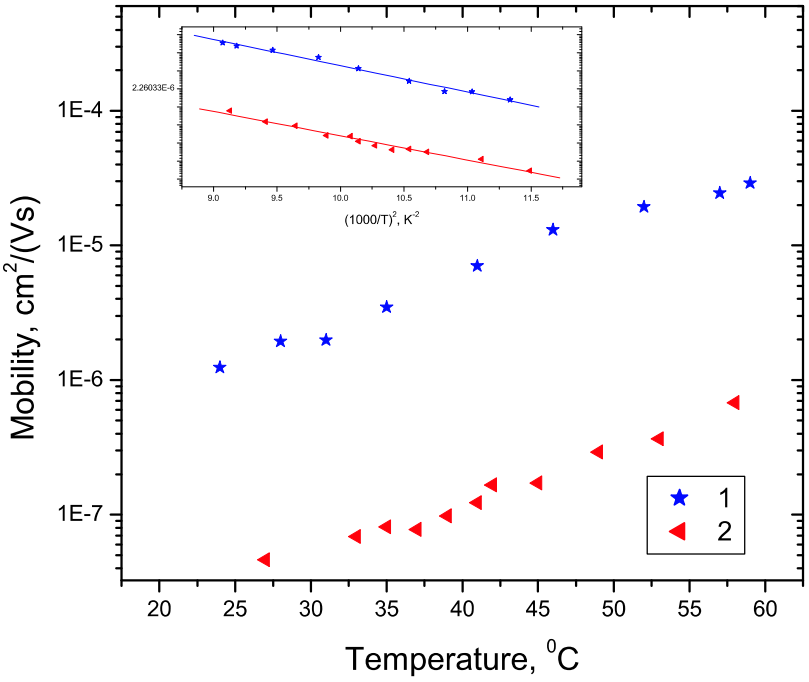

Figure 3.9: Dependence of the mobility on temperature for composites: 1 - PVK(99 %)/C_{60}(1 %) ; 2 - PVK(59 %)/C_{60}(1 %)/CBB(30 %)/Tolane(10 %). Inset show the linear fit of the mobility to the inverse quadratic function of the absolute temperature. From the slope of this fit, the energetic disorder parameter σ can be calculated.

disorder parameter Σ which were introduced in Section 2.2.2. We will not go into the details of this analysis. Instead, we mention how to experimentally determine the mobility field dependence parameter β_μ defined in Eqs. 2.31 ($\mu \sim \exp[\beta_\mu E_0^{1/2}]$). For that, we plot the mobility using a ln scale versus $E_0^{1/2}$ (inset of Figure 3.8), and determine the parameter β_μ from a linear fit.

We will need this parameter in Section 3.5 where we predict the PR speed on the basis of photoconductivity properties.

As in every technique, there are some limitations for using the TOF method for determining the carrier mobility. For example, at high concentrations of some NLO chromophores or plasticizer, the current transients can become too dispersive due to high degree of the disorder which is brought into the system by the chromophore or plasticizer, so that the transient time t_T is not possible to obtain even using a log-log plot. If the disorder is high enough, an increase in temperature or electric field which in principle should decrease the disorder does not influence the transients noticeably. This behavior is illustrated in Figure 3.10a where the highly dispersive transients are shown as a function of temperature together with much less dispersive transients (Figure 3.10b). For composites such as PVK(49 %)/C_{60}(1 %)/PDCST(35 %)/BBP(15 %) which exhibit highly dispersive transients (Figure 3.10a), another method for measuring the carrier mobility should be employed. One will be discussed in the next section.

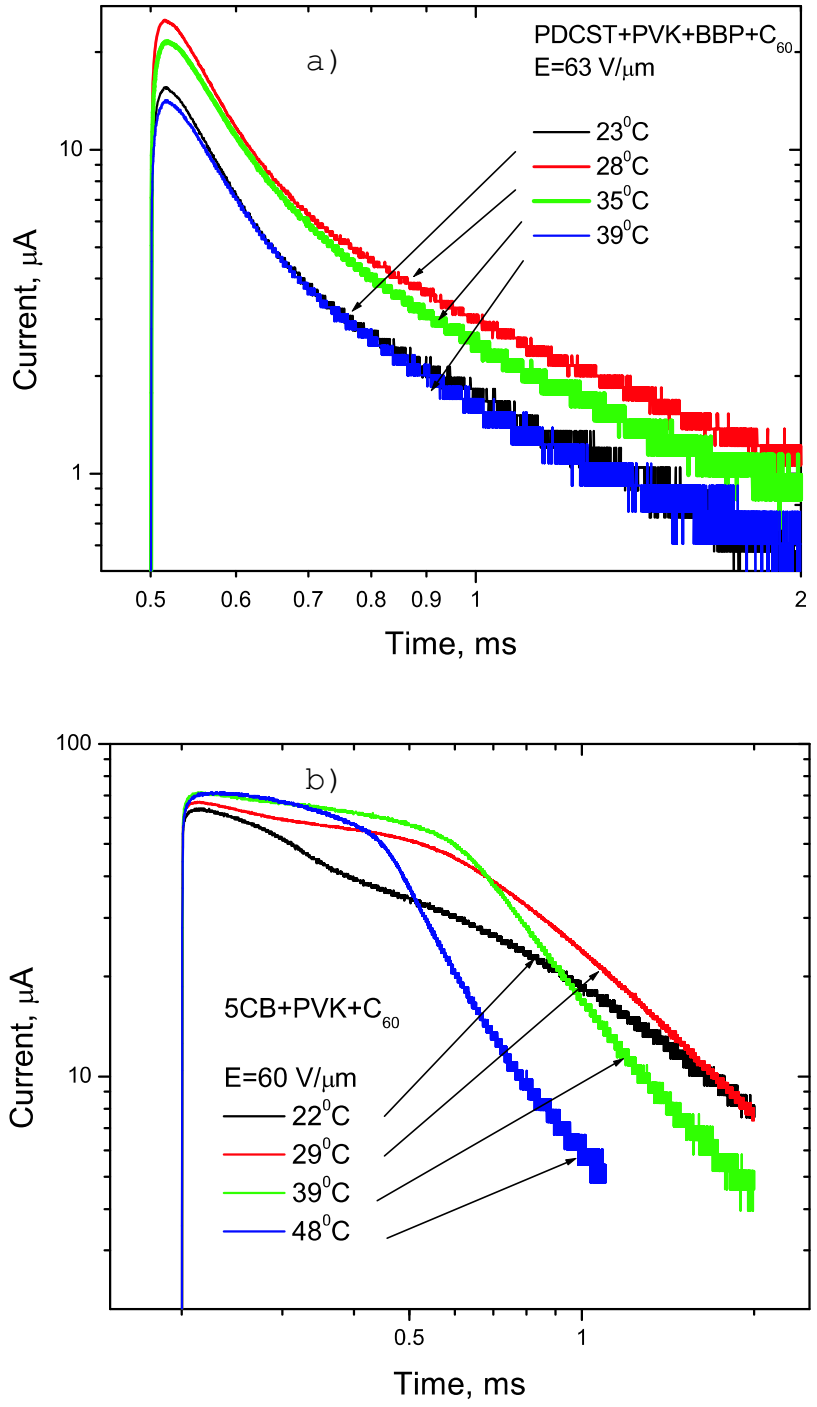

Figure 3.10: Current transients at various temperatures: a) highly dispersive, for composite PVK(49 %)/C_{60}(1 %)/PDCST(35 %)/BBP(15 %); b) much less dispersive, for composite PVK(59 %)/C_{60}(1 %)/5CB(40 %).

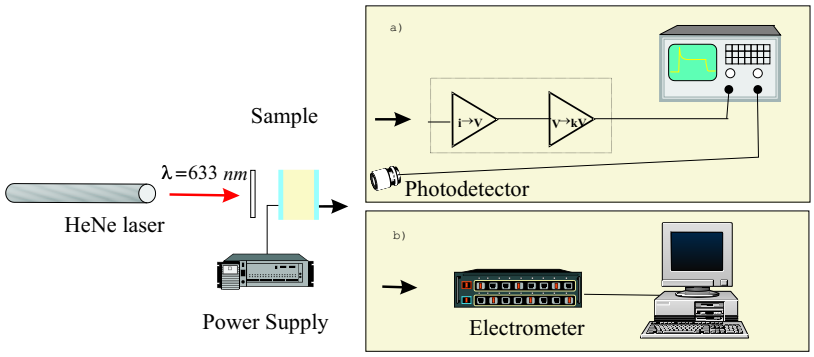

Figure 3.11: Experimental set-up for DC photoconductivity measurements: a) short time scale; b) long time scale.

3.3.3 DC photoconductivity

The DC photoconductivity experiment involves the measurement of the photocurrent induced in the photoconductive material by continuous light illumination. In our case, as we were interested in the photoconductivity of the PR polymer composites sensitized with C_{60}, we measured the photoconductivity at the wavelength $\lambda = 632.8\,nm$ of a HeNe laser.

For the short time scale measurements (see Section 2.3.1 for the definition of the time scales), the experimental set-up is very similar to that of TOF and is shown in Figure 3.11a. In this measurement, we applied an electric field to the sample and waited until all the transient processes disappeared, then opened a shutter (switching time below $40\,\mu s$) and recorded the sample current under 632.8 nm illumination with an oscilloscope. For the long time scale measurement, the sample current was monitored using a Keithley 6517 electrometer (Figure 3.11b).

Conventionally, in the DC photoconductivity experiment, the steady-state value of the photocurrent i_0 is of interest and is used for the calculation of the steady-state photoconductivity $\sigma_0 = i_0/(E_0 S)$ where E_0 is the applied electric field, and S is the electroded area of the sample. However, as we showed in Section 2.3.1, the temporal behavior of the DC photocurrent in PR materials can be useful for determining such crucial for PR parameters as trapping, detrapping and recombination rates which are hard to assess with other experimental techniques.

Here are some precautions concerning studies of the photocurrent dynamics. Eqs. 2.29 introduced in Section 2.2 and therefore, the procedure of photocurrent dynamics analysis developed in Section 2.3.1, are valid for the bulk material of infinite extent. In real experiments, the external circuit and electrodes may influence the observed behavior [21, 8, 22]. Ideally, for DC photoconductivity studies, the contacts should be ohmic. Because of the high degree of disorder, specifics of sample preparation and field dependence of all of the photoelectric parameters in polymers, it is hard to estimate what kind of contact was made and how much the observed signals are affected by the electrodes since the simple current-voltage characteristics that serve the purpose in inorganic crystals, do not apply here. Therefore, a systematic analysis of current-voltage characteristics for different electrodes and their combinations is necessary to fully elucidate the electrical characteristics [23, 24, 25, 26].

Schildkraut and Cui [27] found good agreement between the steady state values

for the free carrier density, amplitude and phase of the space charge field calculated from the bulk dynamic equations (e.g. Eqs. 2.29) for no boundary conditions (infinite bulk), ohmic boundary conditions ("infinite" supply of charge from the electrodes) and blocking boundary conditions (Schottky barrier). However, this does not mean that the same good agreement will be observed in the dynamical performance. We performed the DC photoconductivity experiments with two types of electrodes - Al and ITO, and for our experimental conditions (range of electric fields and intensities) did not find differences between the parameters calculated from the photocurrent transients. Thus, we assume Eqs. 2.29 well approximate our samples and the contacts do not noticeably affect the results.

Another effect that is undesirable for our purposes and which may affect the DC photocurrent dynamics, especially at the long time scale, is the "parasitic" space charge field build-up. Here the term "parasitic" is used to distinguish between the "useful" space charge field which forms in the process of PR grating formation and the "parasitic" space charge field which forms inside the sample due to the filling of uncompensated traps with injected charge and the accumulation of non-neutralized ions at the electrodes [28]. This "parasitic" space charge field ruins the uniformity of the electric field in the sample, so that the relation $E_0 = V/d$ is no longer valid. We would not expect this effect to influence the performance of the composites with low NLO chromophore or plasticizer content, although the highly plasticized compos-

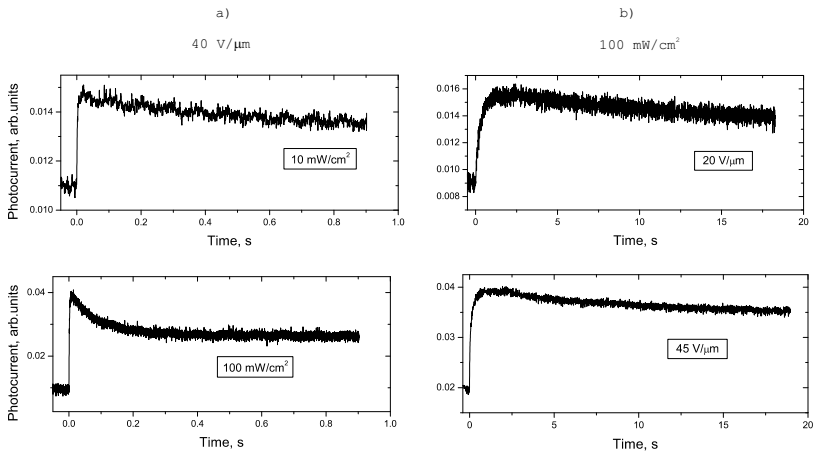

Figure 3.12: Typical photocurrent transients observed on the short time scale DC photoconductivity experiment: a) at different light intensities for PVK/C_{60}; b) at different electric fields for PVK(49 %)/C_{60}(1 %)/AODCST(30 %)/BBP(20 %).

ites that are characterized by high ionic conductivity can be affected unless special measures are undertaken, as we will discuss in Section 3.5.

Now, as we are done with precautions, let us consider the main points of the data analysis.

Short time scale

Typical transients as observed in the short time scale experiment at various electric fields and incident intensities are shown in Figure 3.12. The trends observed in light intensity and electric field dependence of the photocurrent transients are similar for all the composites we studied. As the illumination intensity increases, not only does the photocurrent magnitude increases, but also the peak becomes sharper due to enhanced recombination (Figure 3.12a). As the electric field increases, the magnitude of the photocurrent increases, and the peak becomes sharper for the same reason as all the

processes are electric field dependent. Also, one may notice in Figure 3.12b that at higher field the photocurrent reaches its maximum faster. This due to the electric field dependence of the trapping rate γ_T, which determines the speed of photocurrent rise as we discussed in Section 2.3.1.

In the PVK-based composites with low chromophore or plasticizer content ("unplasticized" composites), the short time scale corresponds to times $t \lesssim 4\,s$ depending on the electric field and light intensity. Figure 3.12a illustrates the behavior of such composites.

For highly plasticized (either by high concentration of the chromophore or plasticizer) composites which we consider in detail in Section 3.5, all the photoconductivity-related dynamics is slower, the short time scale is extended to times $t \lesssim 40\,s$. This case is represented by the composite PVK(49 %)/C_{60}(1 %)/AODCST(30 %)/BBP(20 %) whose transient is shown in Figure 3.12b.

The photocurrent transients can be fit to a bi-exponential function [29] (see Section 2.3.1)

$$\rho_{fit} = A\left(1 - Be^{-\lambda_{10}t} + (B-1)e^{-\lambda_{20}t}\right) \tag{3.13}$$

and the product of trapping rate and density of available shallow traps $\gamma_T M_{T1}$, the recombination rate γ and the shallow trap detrapping rate β_1 are determined as functions of intensity and electric field in accordance with the procedure described in Section 2.3.1 [29].

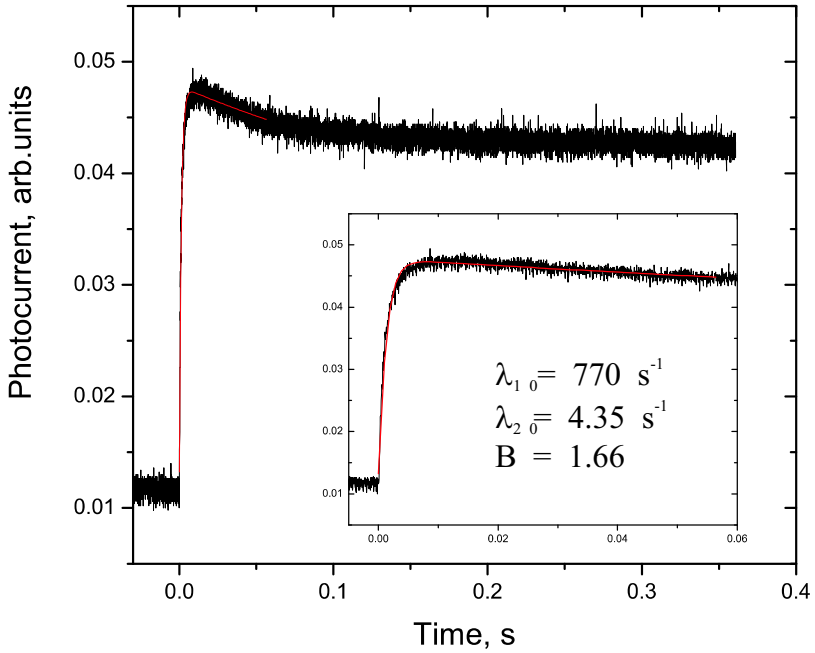

Figure 3.13: Example of the photocurrent transient analysis. Smooth line represents the bi-exponential fit of Eq. 3.13.

As an example, consider the photocurrent transient obtained in PVK(89%)/ C_{60}(1%)/PDCST(10%) at $E_0 = 40\, V/\mu m$ and incident light intensity $I_0 = 100\, mW/cm^2$ (Figure 3.13). The main part of the Figure 3.13 shows the whole transient as measured. Only small part of this transient is fitted with Eq. 3.13 since for our procedure of data analysis, we need the time regime at which the current just started to decay (refer to Section 2.3.1). The fitted part is shown separately in the inset.

The bi-exponential fit of Eq. 3.13 yields $\lambda_{10} = 770\, s^{-1}$, $\lambda_{20} = 4.35\, s^{-1}$, and $B = 1.66$. As shown in Section 2.3.1, the fit constant λ_{10} represents the shallow trapping parameter $\gamma_T M_{T1} = \lambda_{10} = 770\, s^{-1}$ to a good approximation. With the other parameters, the analysis is not as straightforward, and so the full procedure described in Section 2.3.1

has to be performed to extract the recombination rate γ and shallow detrapping rate β_1 which for that particular transient shown in Figure 3.13 are determined to be $8 \cdot 10^{-21}\, m^3/s$ and $0.3\, s^{-1}$ respectively (see Table 3.1 in Section 3.5). If one repeats the measurement and data analysis for a set of electric fields, the field dependence parameters, for example, β_γ defined in Eq. 2.31, can be obtained.

Experimentally, all the rates γ_T, γ and β_1 are electric field dependent. While the electric field dependence is taken into account in the case of γ_T and γ (Eqs. 2.31), the detrapping rate β_1 was approximated as field-independent (Section 2.2.3) which apparently does not hold in practice.

Another trend which cannot be explained by the PR model introduced in Chapter 2, is the intensity dependence of the shallow trapping parameter $\gamma_T M_{T1}$ (Figure 3.14) which is not accounted for in Eqs. 2.29 representing the current microscopic model of the PR effect. The intensity dependence of this parameter could mean that some bi-molecular processes are not properly taken into account in Eqs. 2.29. So, in Section 3.5, where we are going to predict the intensity dependence of the PR speed on the basis of photoconduction parameters, we will use empirical polynomial fits of the experimentally measured functions $\gamma_T M_{T1}(I_0)$ since at this moment, there is no physical model for this behavior.

The short time scale DC photoconductivity experiment can also be used for estimates of the photogeneration cross-section s and carrier mobility μ. It is especially

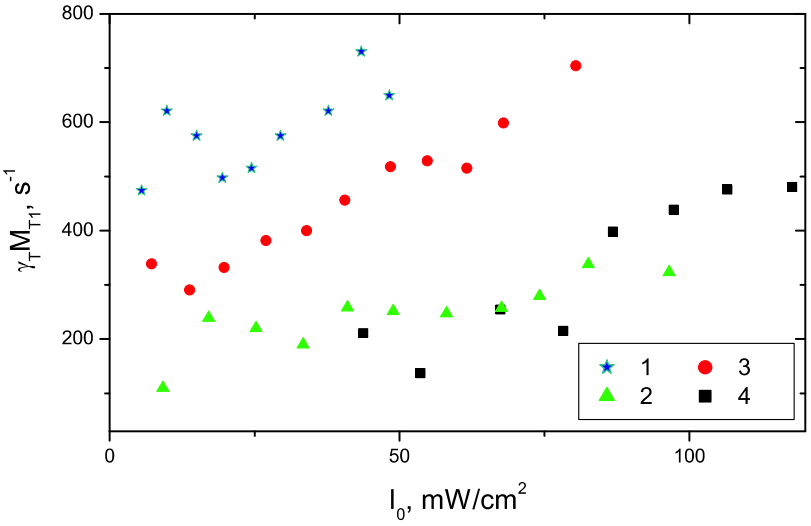

Figure 3.14: Trapping parameter $\gamma_T M_{T1}$ as a function of illumination intensity I_0 for composites: 1 - PVK/C_{60}; 2 - PVK(89 %)/C_{60}(1 %)/AODCST(10 %); 3 - PVK(89 %)-/C_{60}(1 %)/PDCST(10 %); 4 - PVK(89 %)/C_{60}(1 %)/5CB(10 %).

useful when it is impossible to use other experimental techniques as in case of highly plasticized composites at low electric fields (see Sections 3.3.1, 3.3.2).

The photogeneration cross-section can be estimated from the DC photoconductivity as described in Ref. [18] using the formula $s = (\overline{\rho_0}\gamma_T M_{T1})/(I_0 N_A)$ where $\overline{\rho_0}$ is the free charge density at its maximum [29] (Figure 2.9). We ensured consistency of this calculation by comparing the photogeneration cross-sections determined from DC photoconductivity and xerographic discharge for the samples with low chromophore and plasticizer content where the xerographic discharge technique described in Section 3.3.1 provided reliable data.

The mobility can be estimated from the DC photoconductivity measurements using the formula [18] $\mu = d^2(\gamma_T M_{T1})/(2V)$. Such an estimate showed reasonable

agreement with the TOF results for low chromophore and plasticizer content samples, thus we used it to calculate the low electric field ($E_0 \lesssim 20\,V/\mu m$) mobility for highly plasticized samples which could not be accurately measured by TOF technique.

Long time scale

In the long time scale DC photoconductivity experiment, the photocurrent was monitored over an extended period of time (at least 20 min). A typical experimental run included the following: the electric field was turned on, and the dark current (j_{dark}) was recorded for $\sim$ 20 min. Then, the electric field was turned off and then in 2 min turned on again, and dark current was monitored again for $\sim$ 20 min. If the first two dark current runs reproduced, then the light was turned on, and the current under illumination (j_{light}) was monitored for another $\sim$ 20 min. Then, the photocurrent j_{photo} was calculated using $j_{photo} = j_{light} - j_{dark}$. If the first two dark current runs did not reproduce, a third dark current run was executed, and for all the samples under study the third run reproduced the second. Careful monitoring of the dark current in these measurements is not important for the composites with low chromophore and plasticizer content since the dark current for these materials is only due to injection from the electrodes and is at least an order of magnitude smaller than the photocurrent at the incident intensity $100\,mW/cm^2$ at an applied field of $E_0 \sim 40\,V/\mu m$ (Figure 3.15a). In highly plasticized samples the dark current is due to both injection from the electrodes and to impurity ions moving towards opposite

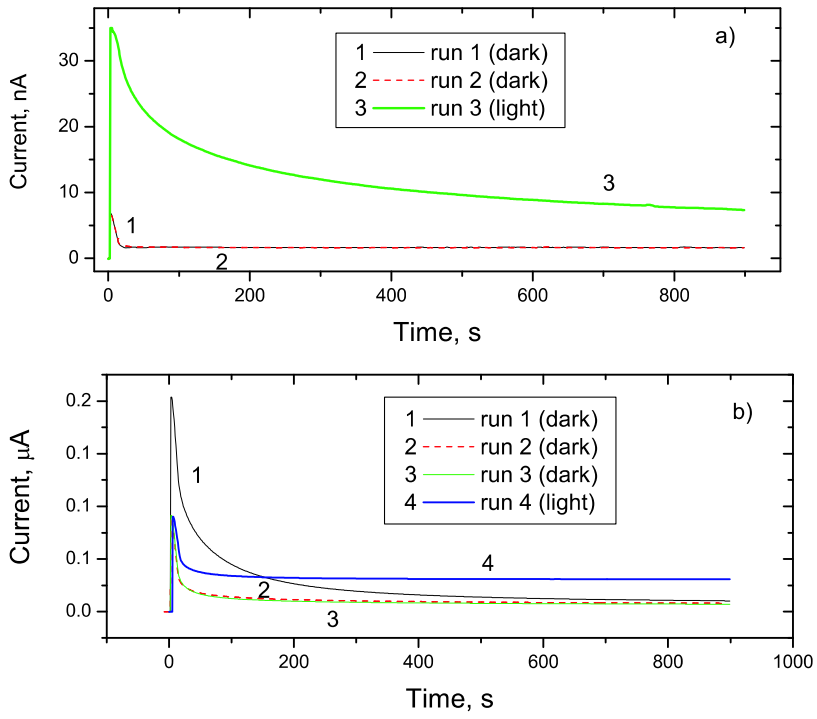

Figure 3.15: Long time scale photocurrent dynamics for: a) unplasticized composite PVK(89 %)/C_{60}(1 %)/PDCST(10 %), at the electric field $E_0 = 40\, V/\mu m$ and incident intensity $I_0 = 100\, mW/cm^2$; b) highly plasticized composite PVK(49 %)/C_{60}(1 %)-/BBP(50 %) at the electric field $E_0 = 10\, V/\mu m$ and incident intensity $I_0 = 40\, mW/cm^2$

electrodes. At low electric fields ($E_0 \sim 10\, V/\mu m$) the dark current in these samples is $\sim 30\,\%$ of the photocurrent at the incident intensity $I_0 \sim 40\, mW/cm^2$ (Figure 3.15b), so it is important to take careful measurements of dark current to reliably determine the photocurrent. This issue will be addressed later, in Section 3.5, where we will discuss the photoconductivity characteristics of highly plasticized samples.

The photocurrent transients we obtained are fit to a bi-exponential function of Eq. 3.14 similar to that of Eq. 3.13 to determine the fit parameters $\lambda_{20,long}$ and B_{long}:

$$\rho_{fit,long} = A\left(1 - B_{long}e^{-\lambda_{10}t} + (B_{long} - 1)e^{-\lambda_{20,long}t}\right) \tag{3.14}$$

As an example, we consider the long time scale photocurrent transient obtained for the composite PVK(89 %)/C_{60}(1 %)/PDCST(10 %) at electric field $E_0 = 40\, V/\mu m$ and the incident intensity $I_0 = 100\, mW/cm^2$ (Figure 3.16). Before we analyze the long time scale transient shown in Figure 3.16, we have to estimate at what time after the beginning of light exposure, the long time scale approach is actually applicable for this composite. In Section 2.3.1 we estimated that the long time scale corresponds to times $t \gg 10^3\tau_0$, where $\tau_0 = 1/(\gamma_T M_{T1})$. Since this is the same composite as we used for the illustration of the short time scale analysis (Figure 3.13), we know the shallow trapping parameter $\gamma_T M_{T1} = 770\, s^{-1}$ and thus, the lower limit of the "long time scale" which is $\sim 10^4\tau_0 \sim 20\, s$. Thus, the part of the curve in Figure 3.16 to be fitted starts at $20\, s$ after the light is on. Another good reason to first perform the short time scale experiment is that if the faster constant λ_{10} which describes

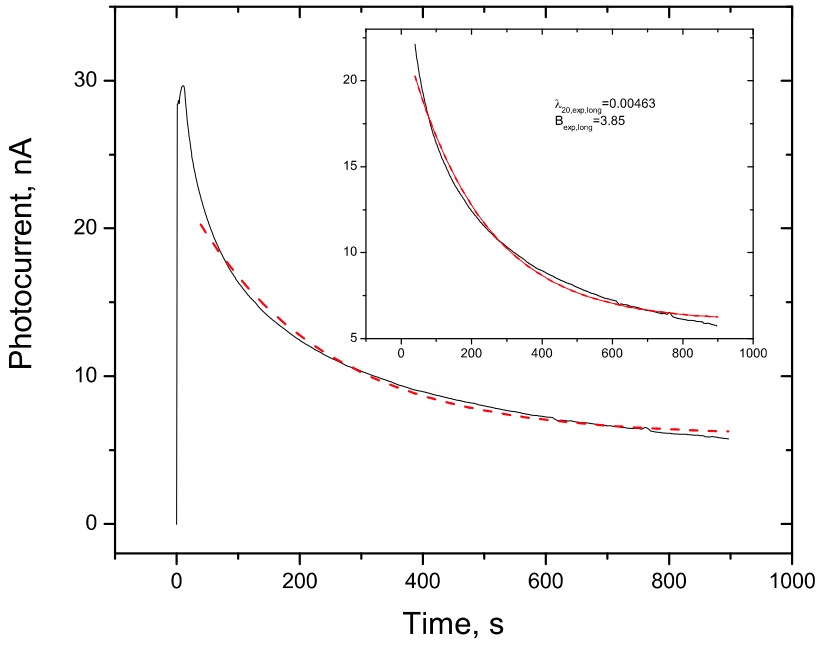

Figure 3.16: Example of the photocurrent dynamics analysis at long time scales. Inset shows the part of the transient fitted with a bi-exponential of Eq. 3.14.

the onset of the photocurrent, is already known and can be fixed when the long time scale fit of Eq. 3.14 is performed. So, we fix $\lambda_{10} = 770\,s^{-1}$ and fit the part $t \gtrsim 20\,s$ of the photocurrent transient with Eq. 3.14. The fit yields $\lambda_{20,exp,long} = 0.00463\,s^{-1}$ and $B_{exp,long} = 1.66$. Unfortunately, it is not straightforward to extract the parameters that characterize deep traps (at least I am not aware of a simple recipe), from the fit parameters $\lambda_{20,exp,long}$ and $B_{exp,long}$. So, the tedious procedure described in Section 2.3.1 should be performed. The outcome of this procedure is the product of trapping rate and total density of deep traps $\gamma_T M_{T2}$ and the detrapping rate β_2 for deep traps which for the transient shown in Figure 3.16 turned out to be $23\,s^{-1}$ and $1.5 \cdot 10^{-4}\,s^{-1}$ respectively.

In summary of the section describing various photoconductivity techniques, we considered the main techniques for the measurement of the photogeneration efficiency (xerographic discharge method), drift mobility (time-of-flight) and other parameters (DC photoconductivity).

Next section will be devoted to the photorefractive experimental techniques - two-beam coupling (2BC) and four-wave mixing (FWM).

3.4 Photorefractive experiments

As we already discussed in Section 2.1.3, the most widely used experimental techniques for photorefractive studies are two-beam coupling (2BC) and four-wave mixing (FWM). In this section we will consider the actual experimental set-ups used for these measurements, typical data, and data analysis. Also, we will explore the general trends of the PR quantities such as gain Γ and diffraction efficiency η introduced in Section 2.1.3.

3.4.1 Two-beam coupling

In two-beam coupling (2BC) experiments, the measurable quantities are the gain coefficient (coupling constant $\tilde{\Gamma}$ introduced in Section 2.1.3) and phase shift Φ between the interference pattern and created diffraction grating (Section 2.1.2). I will skip the discussion about the phase shift measurements. We found the techniques used in the literature [30, 31] for this purpose inefficient. However, the phase shift can be

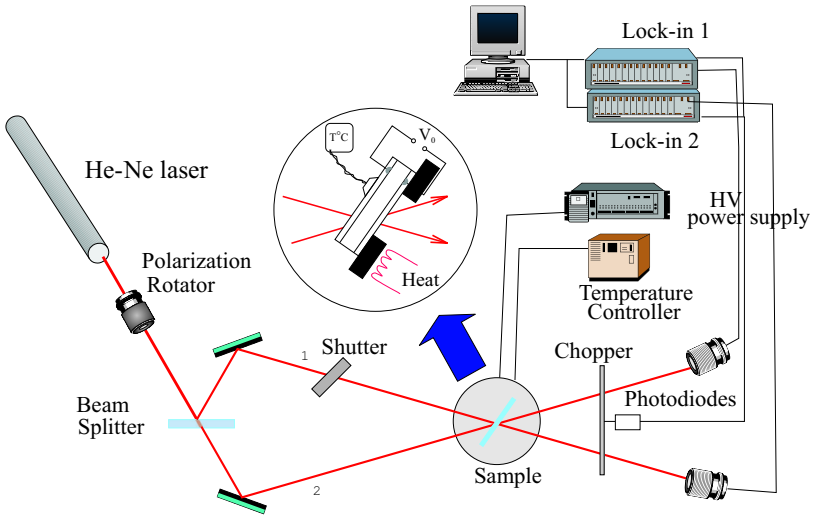

Figure 3.17: Experimental set-up for the two-beam coupling experiment.

extracted from the simultaneous fit of the electric field dependencies of the gain at p- and s-polarized beams. We will not go into the details about this procedure. Instead, in this section we will concentrate on the photorefractive gain measurements.

The experimental set-up for the 2BC experiment is shown in Figure 3.17. A typical experimental run included the following steps. First, the electric field was applied to the sample, with the pump beam (beam 1) on. Then, the signal beam (beam 2) was turned on, and the temporal development of the power of both beams was recorded. Typical data observed, for example, in PVK(59.8 %)/C_{60}(0.2 %)/5CB(40 %) at $E_a = 30\,V/\mu m$, is shown in Figure 3.18. Asymmetric energy transfer is clearly visible, as beam 2 is amplified while beam 1 is weakened by an equivalent amount. For this experiment, the input beam ratio $\beta = I_{10}/I_{20} = 1$ was used. Here it is important that this ratio is equal to 1 with internal incident intensities rather than external ones.

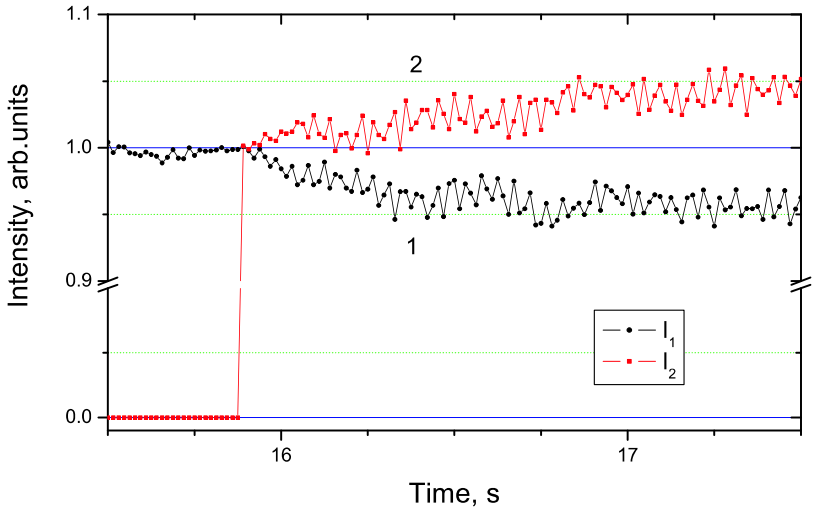

Figure 3.18: Typical data for the 2BC experiment. The electric field and the pump beam (beam 1) are initially on, and then at $t \sim 15.9\,s$ the signal beam (beam 2) is turned on, and intensities of both beams are recorded.

Thus, to calculate the corresponding external intensities, one should take into account the Fresnel factors that can be substantial due to the large incident angles used in this experiment. In Figure 3.18, both beams are normalized in such a way that their initial external intensities are equal to 1.

The data analysis for determining the gain coefficient from transients similar to those shown in Figure 3.18 is fairly simple. At the input (internal) beam ratio $\beta = 1$, the output intensities I_1 and I_2 are derived from Eqs. 2.23 to yield

$$I_1 = \frac{I_{10}}{1 + \exp\left(\tilde{\Gamma}\tilde{d}\right)} \qquad (3.15)$$
$$I_2 = \frac{I_{20}}{1 + \exp\left(-\tilde{\Gamma}\tilde{d}\right)}$$

where $\tilde{d}$ is the effective thickness of the sample which is connected to the sample thickness d by the relation $\tilde{d} = d/\cos[(\tilde{\theta_1} + \tilde{\theta_2})/2]$ where the angles are as defined in

Figure 2.3.

Then, the ratio of the output intensities I_1/I_2 is

$$\frac{I_1}{I_2} = \frac{I_{10}}{I_{20}} e^{-\tilde{\Gamma}\tilde{d}} = e^{-\tilde{\Gamma}\tilde{d}} \tag{3.16}$$

from which the gain coefficient is easily obtained:

$$\tilde{\Gamma} = -\frac{1}{\tilde{d}} \ln\left[\frac{I_1}{I_2}\right] \tag{3.17}$$

It should be noted that the output intensities $I_{1,2}$ in Eqs. 3.16, 3.17 are also internal intensities that have to be converted to external ones, which we actually measure. The simplest way to eliminate the Fresnel factors is the following. The external intensities $I^{ext}_{10,20}$ of the output beams in the absence of coupling (for example, when there is no electric field applied) are related to the internal intensities $I_{10,20}$ as follows:

$$I^{ext}_{10} = I_{10} f_1, I^{ext}_{20} = I_{20} f_2 \tag{3.18}$$

where f_1 and f_2 are transmission coefficients for s- and p-polarizations of the beams given by [32]

$$\begin{aligned} f^s_{1,2} &= \frac{n\cos\tilde{\theta}_{1,2}}{\cos\theta_{1,2}} \left(\frac{2\cos\theta_{1,2}}{\cos\theta_{1,2} + n\cos\tilde{\theta}_{1,2}}\right)^2 \\ f^p_{1,2} &= \frac{n\cos\tilde{\theta}_{1,2}}{\cos\theta_{1,2}} \left(\frac{2\cos\theta_{1,2}}{n\cos\theta_{1,2} + \cos\tilde{\theta}_{1,2}}\right)^2 \end{aligned} \tag{3.19}$$

In Eqs. 3.19, n is the refractive index of the film, and all the angles are the same as defined in Figure 2.3. Similar to Eqs. 3.18, the external intensities $I^{ext}_{1,2}$ in the presence

of beam coupling are represented as $I_{1,2}^{ext} = I_{1,2} f_{1,2}$ through the internal intensities $I_{1,2}$ and transmission factors. Then, at $\beta = I_{10}/I_{20} = 1$, the gain coefficient (Eq. 3.17) can be expressed in terms of the external intensities measured experimentally as

$$\tilde{\Gamma} = -\frac{1}{\tilde{d}} \ln \left[\frac{I_1}{I_2} \right] = -\frac{1}{\tilde{d}} \ln \left[\frac{I_1^{ext}}{I_2^{ext}} \frac{I_{20}^{ext}}{I_{10}^{ext}} \right] \tag{3.20}$$

The gain coefficient $\tilde{\Gamma}$ is electric field and beam polarization dependent. The range of applied electric fields for this measurement is $E_a \sim 30-150\, V/\mu m$ [30, 4]. The gain coefficient is larger for *p*-polarized writing beams than for *s*-polarized because of different coupling between the electro-optic tensor components and the beam optical field for these polarizations (refer to Section 2.4 for details).

Having measured the gain coefficient $\tilde{\Gamma}$ for *p*- and *s*-polarizations of the incident beams, we can learn about some of the microscopic features of the PR polymer composite. As an example, we consider the composite PVK(59 wt.%)/C_{60}(1 wt.%)/6CB(40 wt.%). In Section 2.4, we considered the mechanisms that lead to the refractive index modulation after the space charge field E_{sc} has been produced. We noted that for low T_g composites, the NLO chromophores can be oriented not only by the external electric field, but also by the space charge field E_{sc}, which leads to the orientational enhancement effect (Section 2.4). The glass transition temperature of this composite is $\sim 40^{\circ}C$ [4], so as we increase the temperature from room temperature to T_g, we expect the orientational enhancement effect to increase, since the chromophores become easier to orient at temperatures around T_g. The goal is

to explore experimentally which mechanism of the orientational enhancement effect, the electro-optic effect ($\Delta\chi^{(2)}$), or birefringence ($\Delta\chi^{(1)}$), dominates in this composite. For this we recall that at small angles between the incident beams, the ratio of gain coefficients for *p*- and *s*-polarizations has the simple relation, $\tilde{\Gamma}_p/\tilde{\Gamma}_s \approx C/A$ (Eq. 2.94), to the constants C and A of Eqs. 2.90 that provide a link to the microscopic properties of the material.

The gain coefficient calculated using Eq. 3.20 from the experimental data for composite PVK(58.2 wt.%)/C_{60}(0.2 wt. %)/6CB(40 wt.%) as a function of applied electric field for various temperatures and *p*- and *s*-polarizations of the incident beams is plotted in Figure 3.19. The first thing to notice in Figure 3.19 is that the gain coefficients for *p*- and *s*-polarized beams have opposite signs. This means that for *p*-polarized beams, the energy transfer is directed from beam 1 to beam 2, and for *s*-polarized beams, the energy transfer occurs from beam 2 to beam 1. If we calculate the ratio $\tilde{\Gamma}_p/\tilde{\Gamma}_s \approx C/A$ from the data shown in Figure 3.19, we find that this ratio is almost constant, and approximately equal to -2 for all the temperatures studied (Figure 3.20). From the definitions of the constants C and A (Eqs. 2.90), we can deduce that the case with $C/A = -2$ means that the birefringent mechanism in the orientational enhancement dominates the electro-optic one. Moreover, even at room temperature, which is $\sim 20^0\,C$ lower than the glass transition temperature T_g, the orientational effects are already as strong as near T_g.

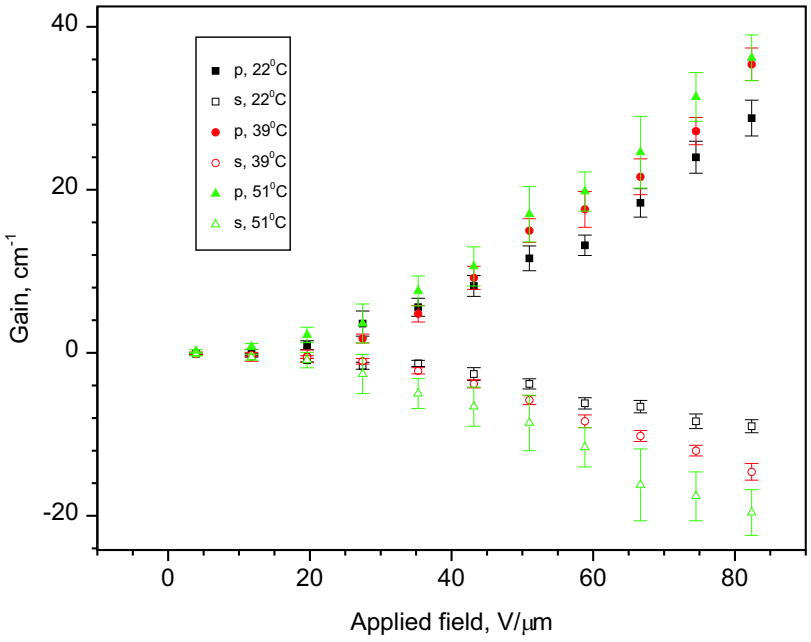

Figure 3.19: Electric field dependence of the gain coefficient for p- and s-polarized beams at various temperatures for composite PVK(58.2 wt.%)/C_{60}(0.2 wt.%)/6CB(40 wt.%).

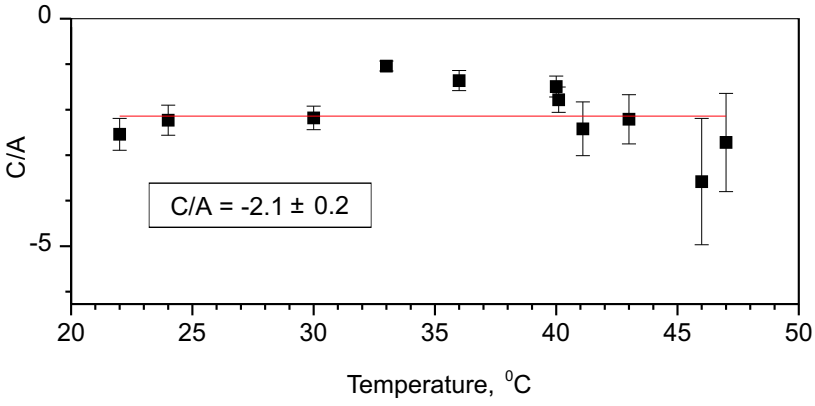

Figure 3.20: Ratio of the gain coefficients for p- and s-polarized incident beams as a function of temperature. The line corresponds to the fit with constant to the data points.

In most of the PR polymer composites, birefringence dominates the electro-optic contribution, which in practice means that the ratio C/A is negative. However, the value of C/A for composites with NLO chromophores stronger than cyanobiphenyls, such as the dyes PDCST and AODCST (Figure 3.1), departs from -2 which suggests that the electro-optic part also contributes to the effect. For example, the ratio C/A for the composite PVK(49.5 wt.%)/C_{60}(0.5 wt.%)/BBP(15 wt.%)/PDCST(35 wt.%) is -3.8 [30] at room temperature and may change as the temperature changes.

One also notices in Figure 3.19 that the gain coefficient increases as a function of temperature. This is expected, since at $T < T_g$ an increase in temperature leads to higher photogeneration efficiency (see Section 2.2.1), drift mobility (Section 2.2.2), and other rates that contribute to the space charge field E_{sc} formation, in addition to the enhancement of orientational effects. In the next section we will consider, among other things, how the temperature affects both steady-state diffraction efficiency and the PR grating dynamics.

3.4.2 Four-wave mixing

The four-wave mixing (FWM) experiment is a good choice for probing weak gratings (e.g. when operating at low electric fields) and studying the dynamics of the PR effect (refer to Section 2.1.3 for details).

The experimental set-up for the FWM (actually, DFWM, or degenerate FWM, since all the beams were of the same wavelength $\lambda = 632.8\,nm$) experiment which we

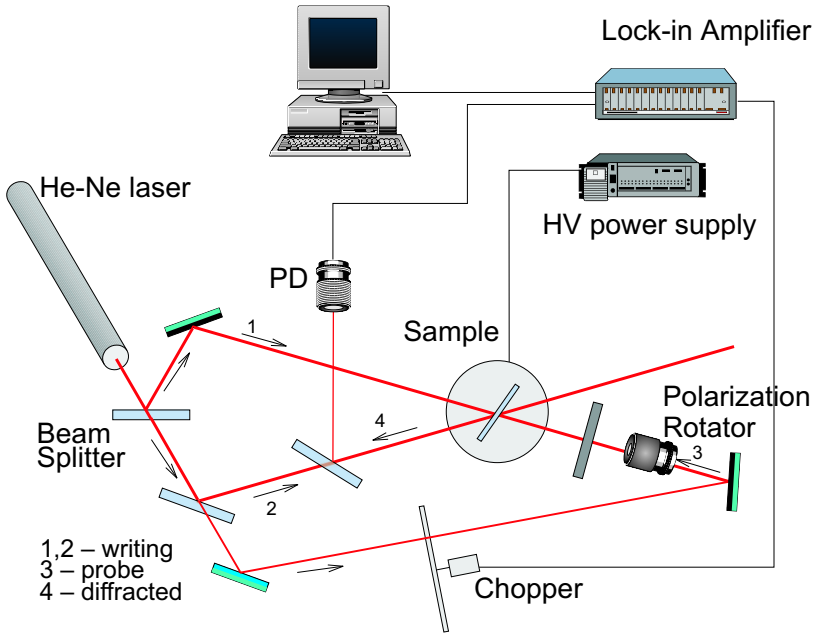

Figure 3.21: Experimental set-up used in the FWM experiment.

used for measurements is shown in Figure 3.21. The grating was written with two s-polarized HeNe 632.8 nm beams, usually of the same internal intensity. For the intensity dependence measurements, the total internal beam intensity varied from 25 to 400 mW/cm^2. The probe beam was usually p-polarized with intensity 5 mW/cm^2. The external angle between the crossing beams was 28^0, and the external angle between the sample normal and the bisector of two writing beams was 50^0. This experimental geometry along with the index of refraction $n = 1.63$ [30] yielded a diffraction grating of period $\Lambda \approx 1.8\,\mu m$.

A typical experiment included the following steps: first, we applied an electric field with one writing beam and the probe beam on, then when all the transients

disappeared, we opened the other writing beam with a shutter and recorded the diffracted signal with a photodetector, lock-in amplifier and computer. For PR grating formation studies, the light was blocked and the field was turned off after the diffracted signal reached the quasi-steady state. When studying the PR grating decay, either one or both beams were blocked, with the electric field kept on, and the PR decay was recorded. After each measurement, the electric field was turned off, and the samples were kept in the dark for $\sim 30\,\mathrm{min}$ before the next measurement to assure complete decay of the space charge field and the absence of ionized acceptors and filled traps.

For electric field dependence studies, the experiment was repeated in the range of electric fields from $10 - 80 V/\mu m$.

For polarization studies, the polarization of the probe beam was changed to s-polarization, and then the polarization anisotropy ratio η_p/η_s was calculated to check whether the orientational enhancement effect is present (see Section 2.4 for details).

Typical data observed in the FWM experiment is shown in Figure 3.22. Here the electric field and one of the writing beams are initially on, then the second writing beam is turned on at $t \approx 2s$, and the diffracted signal is monitored. At $t \approx 65s$, one of the writing beams is switched off, and the grating decay is observed.

The diffraction efficiency η is calculated from the incident intensity of the probe (reading) beam 3 and diffracted beam 4 as $\eta = I_4/I_3$. For the analysis of the diffraction efficiency, strictly speaking, the function of Eq. 2.59 ($\eta \sim \sin^2(CE_{sc})$) should be used

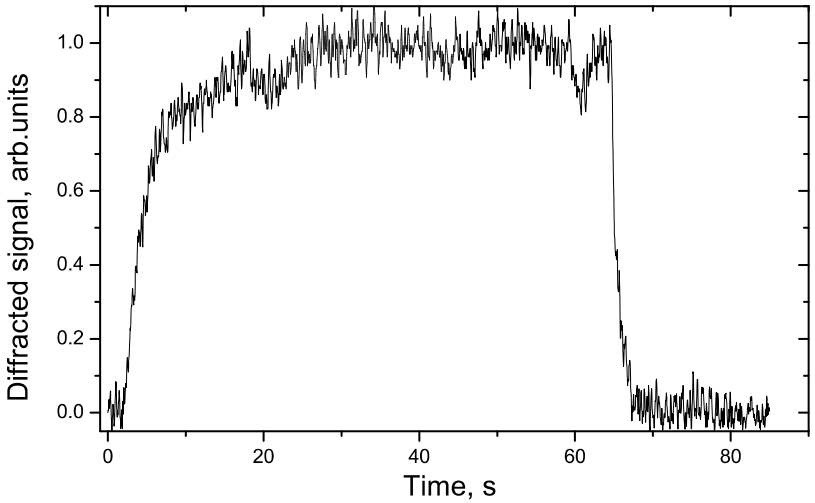

Figure 3.22: Typical transient of the diffracted signal (I_4) as observed in the FWM experiment.

as a fit function. However, we found that for the range of electric fields we used, the diffraction efficiency was small enough to be approximated by Eq. 2.60 ($\eta \sim (CE_{sc})^2$), and thus we fitted the PR grating formation dynamics with a bi-exponential

$$\eta = \eta_0 \left(1 - ae^{-\nu_1 t} - (1-a)e^{-\nu_2 t}\right)^2 \tag{3.21}$$

where η_0 is the amplitude (steady-state) value of the diffraction efficiency, $\nu_{1,2}$ are the faster and slower components of the PR speed, and a is the weight coefficient which shows which component dominates.

The PR grating decay is also fit with a bi-exponential

$$\eta = \eta_0 \left(be^{-\nu_1^{decay} t} + (1-b)e^{-\nu_2^{decay} t}\right)^2 \tag{3.22}$$

where $\nu_{1,2}^{decay}$ and b have meanings similar to those of $\nu_{1,2}$ and a of Eq. 3.21.

Now we describe the general trends of the diffraction efficiency amplitude (steady-state) and the components of the PR speed for both grating formation and decay processes.

Steady-state diffraction efficiency

Electric field dependence According to Eqs. 2.91, the steady-state diffraction efficiency in the presence of the orientational enhancement effect is determined by the applied electric field E_a, the space charge field amplitude E_{sc}^0 which is itself applied electric field-dependent, the orientational properties described by the coefficients C and A of Eq. 2.90 and the experimental geometry.

As an illustration of the applied electric field dependence of the diffraction efficiency, Figure 3.23 shows the diffracted signal transients for various electric fields for composite PVK(49.8 wt.%)/C_{60}(0.2 wt.%)/PDCST(35 wt.%)/BBP(15 wt.%).

Temperature dependence The dependencies of the diffraction efficiency other than on the electric field, e.g. temperature dependence, arise implicitly through E_{sc}^0, C and A.

If the theory of orientational enhancement is valid, then the diffraction efficiency should depend on the temperature T as $\eta \sim (E_{sc}^0(T)/T^2)^2$ (Eqs. 2.91, 2.89). However, this theory is based on the oriented gas model, which is applicable at temperatures around glass transition temperature T_g and higher. Below T_g, the diffraction effi-

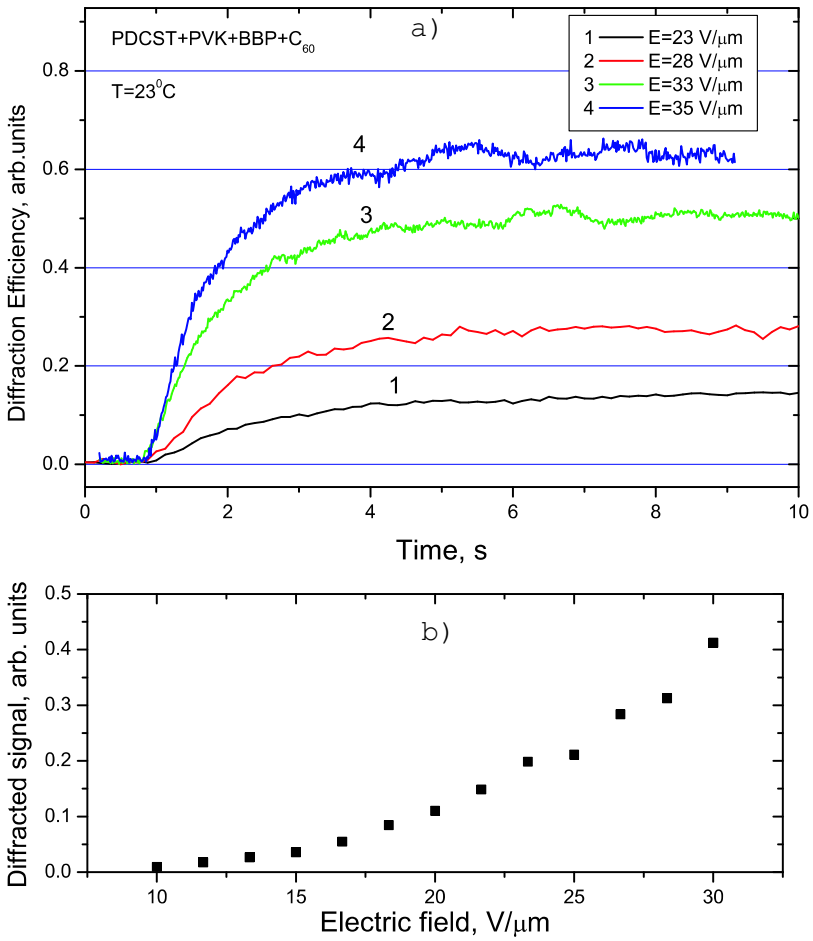

Figure 3.23: Electric field dependence of the diffraction efficiency: a) diffracted signal time evolution at various electric fields; b) electric field dependence of the steady-state diffraction efficiency.

ciency is an increasing function of the temperature. As an illustration, the diffracted signal time evolution at different temperatures for the composite PVK(58.2 wt.%)/ C_{60}(0.2 wt.%)/5CB(40 wt.%) is shown in Figure 3.24a. Figure 3.24b shows the dependence of the steady-state diffraction efficiency on the temperature for different composites. All these composites have their glass transition temperatures at around $40-50^{\circ}\,C$ and exhibit behavior similar to each other. As the temperature gets close to the glass transition temperature T_g, which around $40^{\circ}\,C$ for this composite, noise appears in the signal indicating the activation of processes due to thermal fluctuations (Figure 3.24a). If the temperature is increased well above the T_g, the diffraction efficiency rapidly decreases in accordance with the oriented gas model.

Intensity dependence The dependence of the diffraction efficiency on the intensity of the writing beams is due to the space charge field E_{sc}^0. The existing microscopic theory of the PR effect in polymers that is based on the small modulation approach (see Section 2.3) represents the amplitude of the space-charge field E_{sc}^0 as follows [3]

$$E_{sc}^0 = mE_q \frac{E_a}{\sqrt{(1+p\cos^2\theta_G)^2 E_q^2 + E_a^2}} \tag{3.23}$$

where m is the modulation as defined in Eq. 2.45 ($m = I_1/I_0$), E_a is applied electric field, p is the photogeneration efficiency electric field dependence parameter (Eq. 2.31) and θ_G is the angle defined in Figure 2.3. The field E_q is given $E_q = \frac{eM_1}{\varepsilon_0 \varepsilon K}$ where K is the grating vector and M_1 is the filled trap density ($M_1 = \sqrt{M_{11}^2 + M_{12}^2}$ where $M_{11,12}$

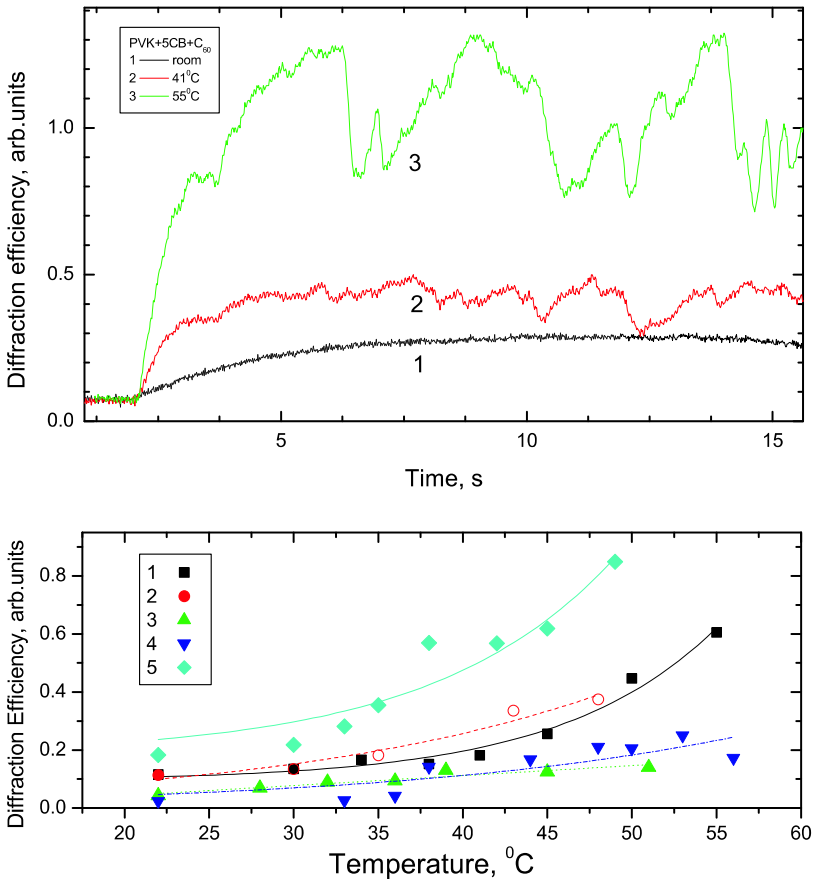

Figure 3.24: Temperature dependence of the diffracted signal: a) PR grating formation at various temperatures for composite PVK(59.8 wt.%)/C_{60}(0.2 wt.%)/5CB(40 wt.%); b) diffracted signal as a function of temperature for composites PVK(49.8 wt.%)/C_{60}(0.2 wt.%)/NLO(40 wt.%) where NLO is: 1 - 5CB, 2 - CB, branched, 3 - Tolane(10 wt.%)/CB, branched (30 wt.%), 4 - Tolane(10 wt.%)/BBP(30 wt.%), 5 - 6CB. Lines provide visual guidance.

are defined in Eqs. 2.58).

Eq. 3.23 suggests that the intensity dependence of E_{sc}^0 is determined by the modulation parameter m and the field E_q which can depend on intensity through the filled trap density M_1. However, since E_q appears in both numerator and denominator, the intensity dependence originating from E_q is not expected to be strong. Then, the diffraction efficiency would not depend on the total intensity of writing beams (I_0) itself, but rather on the modulation parameter $m = I_1/I_0$. In this case, the diffraction efficiency η should be quadratic in m ($\eta \sim (E_{sc}^0)^2$).

To check this property of the diffraction efficiency, we performed the following experiments for the composite PVK(49.5 wt.%)/C_{60}(0.5 wt.%)/BBP(15 wt.%)/ AODCST(35 wt.%):

(i) 1) The PR grating was written with writing beams that had the same internal total intensity (I_0), but different parameter m. For example, the gratings written with $4.35\,mW$ and $3\,mW$ as well as $5.4\,mW$ and $785\,\mu W$ beams satisfied this condition for the experimental geometry used.

2) The grating was written with beams of $9.5\,mW$ and $1.38\,mW$ that provided the same modulation m as in the case of the grating written with $5.4\,mW$ and $785\,\mu W$ beams, but with different total uniform intensity I_0.

For these three gratings, the diffraction efficiency was measured as a function of electric field. The results of the experiment are shown in Figure 3.25a. The steady-

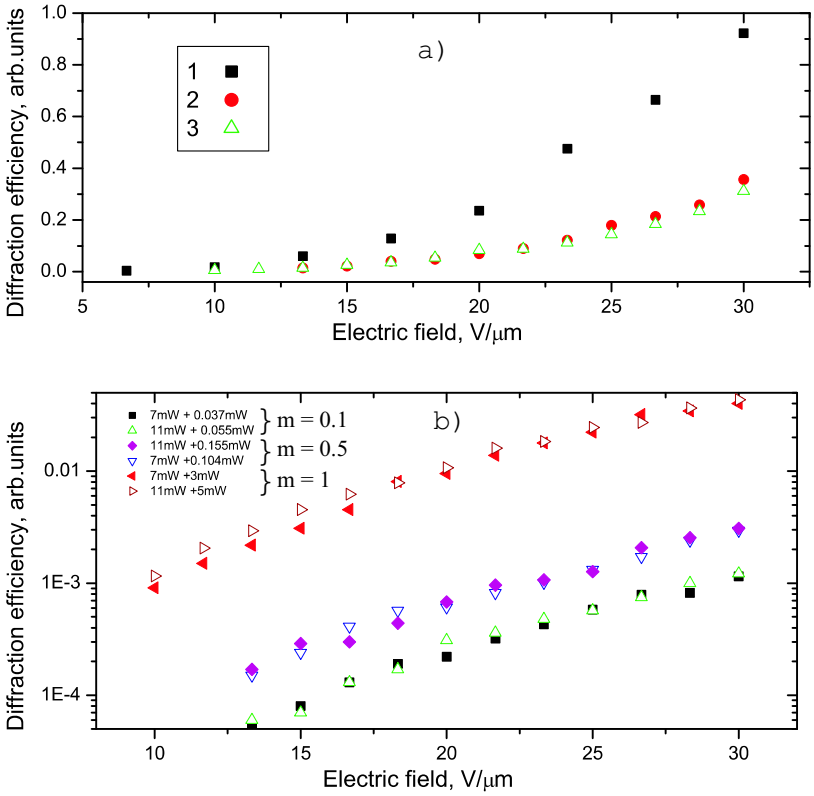

Figure 3.25: Dependence of the diffraction efficiency on the modulation parameter m: a) steady-state diffraction efficiency for the gratings written with: 1) $4.35\,mW$ and $3\,mW$; 2) $5.4\,mW$ and $785\mu W$; 3) $9.5\,mW$ and $1.38\,mW$. Cases 1 and 2 correspond to the same total writing beam intensity I_0, while cases 2 and 3 correspond to the same modulation parameter m; b) steady-state diffraction efficiency for the gratings written with beams of intensities that provide various parameters m: $m = 0.1$ – 1) $11\,mW$ and $55\,\mu W$, 2) $7\,mW$ and $37\,\mu W$; $m = 0.5$ – 1) $7\,mW$ and $104\,\mu W$, 2) $11\,mW$ and $155\,\mu W$; $m = 1$ – 1) $7\,mW$ and $3\,mW$, 2) $11\,mW$ and $5\,mW$.

state diffraction efficiency was the same for the gratings written with beams creating the interference pattern with same modulation parameter m. This shows that the space charge field indeed depends on m rather than on the total intensity I_0.

(ii) Two sets of incident intensities with the same parameter m for $m = 0.1$, 0.5 and 1 were used to produce the gratings. The diffraction efficiency was measured as a function of electric field. The results are shown in Figure 3.25b. As before, the steady-state diffraction efficiency proved to depend only on m rather than on the total intensity I_0 of the writing beams. However, it turned out that the m-dependence of the diffraction efficiency was not quadratic (Figure 3.25), and therefore the theory based on the small modulation approximation that was mentioned in Section 2.3 may not hold for the steady-state performance.

Photorefractive grating formation

Since a number of potential applications for PR materials require fast response times, it is important to understand what factors determine and limit the PR speed in the existing PR materials. We already devoted some attention to the theory of the PR rise in Section 2.3, and in the next section we will discuss how the content of the PR polymer composite influences the PR speed. In this section, we consider some general trends for the PR speed which are applicable to any PVK-based composite.

In the literature, the most widely used functions for fitting the diffracted signal rise are bi-exponentials (Eq. 3.21) [33] and stretched exponentials [5]. We used a

bi-exponential because in this case, it is easier to separate the processes that may be responsible for a faster and slower rise. As we discussed in Section 2.1.2, the main processes that lead to the photorefractive effect in polymers, are the photoconductivity and orientation of the NLO chromophores. The faster component of the PR speed (ν_1 of Eq. 3.21) is almost always determined by the photoconductive properties of the material, i.e. how fast a noticeable space charge field E_{sc} is formed. Then, depending on the material, the slower component ν_2 can be due either to photoconductivity (further development of E_{sc}) or to orientation which starts to contribute from the moment when a noticeable space charge field has been built. For example, for a material with no deep traps and high T_g, the slower speed ν_2 is likely to be due to the orientation. For the material with deep traps and low T_g, ν_2 is most certainly due to further development of E_{sc}. One can view this process as follows. As we discussed in Section 2.1.2, the space charge field forms when the traps get filled in the places of destructive interference, and thus the trapped charge and the ionized acceptors that stayed in the places of constructive interference create the field. Then, the initial space charge field formation that leads to the faster process described by ν_1 is due to shallow trap filling. If there are deep traps in the material (we consider the density of deep traps to be much smaller than that of shallow traps, because otherwise the grating could not be easily erased, and so such a material would not be suitable for dynamic applications), they are going to be filled slowly, and thus further increase the

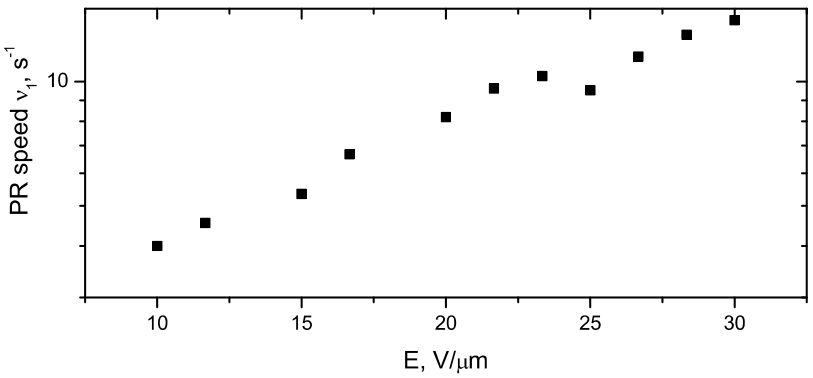

Figure 3.26: Dependence of the faster component of the PR speed ν_1 on the electric field, as observed for the composite PVK(49.5 wt.%)/C_{60}(0.5 wt.%)/BBP(15 wt.%)-/AODCST(35 wt.%).

space charge field. The nature of shallow and deep traps in the polymer composites will be discussed in the Section 3.5.

For dynamic applications such as optical switching, the ideal material would have been described by a single exponential, with ν_1 being the fast, and the only, speed. So, the faster speed is usually the point of interest, and now we will list its properties.

The PR speed increases as a function of applied electric field (Figure 3.26). As was shown by our numerical simulations, the PR speed depends on the photogeneration cross-section, mobility and other parameters (see Section 2.3). All of these parameters are electric field dependent which leads to the electric field dependence of the PR speed.

The PR speed increases as a function of temperature for $T < T_g$ (see, for example, the diffracted signal transient in Figure 3.24). As we already mentioned, the photo-generation efficiency and drift mobility, which are the main factors that determine

the PR speed, are increasing functions of temperature.

The PR speed increases as a function of the total intensity of the writing beams I_0. This is in contrast to the steady-state value of the diffraction efficiency which depends on the modulation m rather than the total intensity I_0. In Section 3.5, the experimental data illustrating the intensity dependence of the PR speed will be presented.

Photorefractive decay

Photorefractive grating decay characterization is of interest because of the potential application of PR materials for holographic data storage. Also, it can elucidate the microscopic properties of the PR material in which the PR grating is written.

There are several possible methods to study PR decay. One of them is to turn off the electric field and observe the grating decay. However, with modern materials with decay times on the order of $100\,ms$, it turns out that the time constant of the power supply for removing electric field is an order of magnitude higher ($\sim 1\,s$), and therefore removing the electric field is not efficient in PR decay studies.

The widely used methods for PR decay characterization are grating erasure under homogeneous illumination [34] and grating decay under no illumination [35], with the electric field on in both cases. Figure 3.27 shows the differences in processes during grating erasure with a uniform illumination and with no illumination.

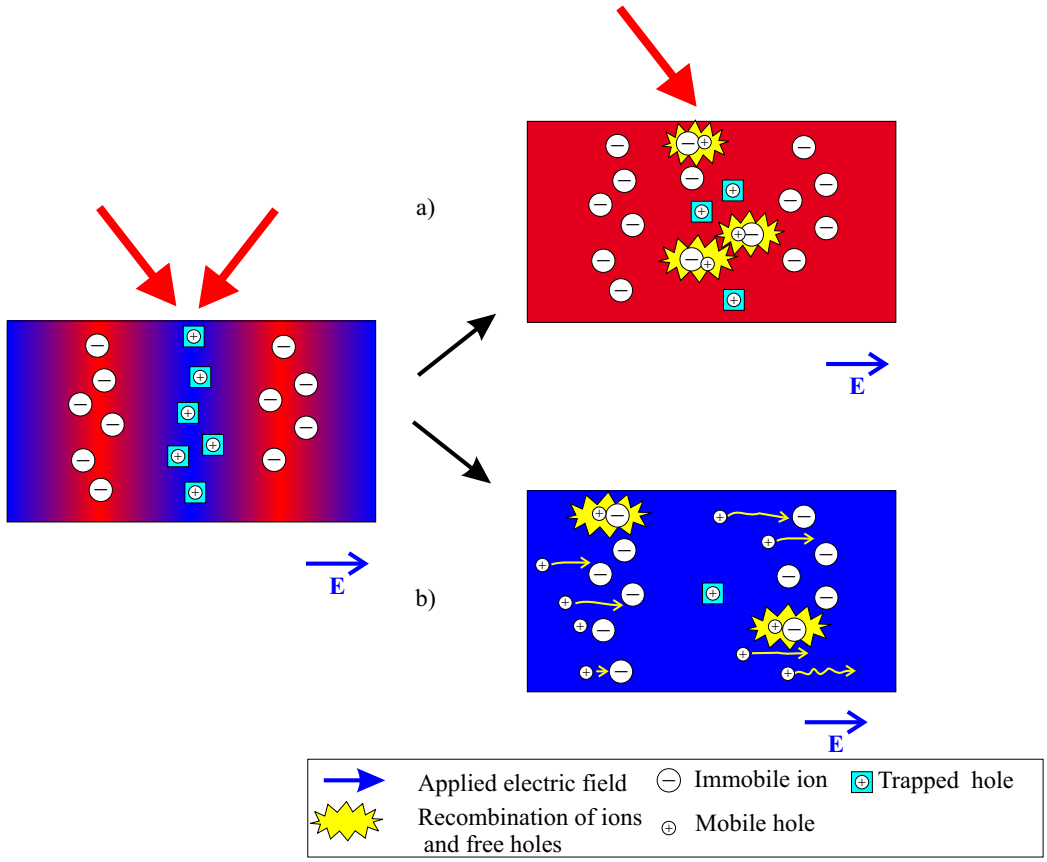

Figure 3.27: Schematic representation of the PR grating decay: a) in the presence of a uniform illumination; b) without any illumination.

Dark decay For grating decay without any illumination to occur, the filled traps ($M_{1,2}$) should get thermally emptied, then the carriers released from the traps, which became free and mobile, should move towards ionized acceptors (N_A^i) and recombine with them (Figure 3.27b). Thus, the constants $\nu_{1,2}^{decay}$ of Eq. 3.22 that characterize the dark grating decay should contain information about the detrapping rates, mobility and recombination. In Section 2.3.2, we showed that the faster component ν_1^{decay} of grating dark decay is indeed connected to the detrapping rate, while mobility and

recombination were obscured in the decay transient.

In PR polymer composites, not only the photoconductivity contribution described by Eqs. 2.29 of the PR effect is present, but also the orientation contribution. So, when the faster decay due to detrapping has occurred, and so some noticeable part of the space charge field has disappeared, the chromophores are no longer oriented by the space charge field and therefore start to rotate to align along the applied field. Therefore, the slower component of the decay ν_2^{decay} bears the information about both slower photoconductivity processes (such as deep trap detrapping) and orientation.

Decay under uniform illumination Grating decay under uniform illumination involves different processes than in case of dark decay. Rather than waiting for the filled traps to become empty as for the dark decay, here, as soon as the appropriate density of ionized acceptors (N_A^i, or C_{60}^- in my case) is created at former places of destructive interference, the space charge field vanishes. This process is sometimes confused in the literature with so called optical detrapping which would mean emptying the filled traps by optical excitation. Although such an effect exists in semiconductors [36], it does not appear to be relevant in polymer composites due to their components with specifically chosen absorption bands and ionization potentials (refer to Section 3.2). So, for grating decay under an erasing beam, the faster decay will be determined by the photogeneration efficiency, and thus will be strongly electric field and intensity-dependent which is illustrated in Figure 3.28 for

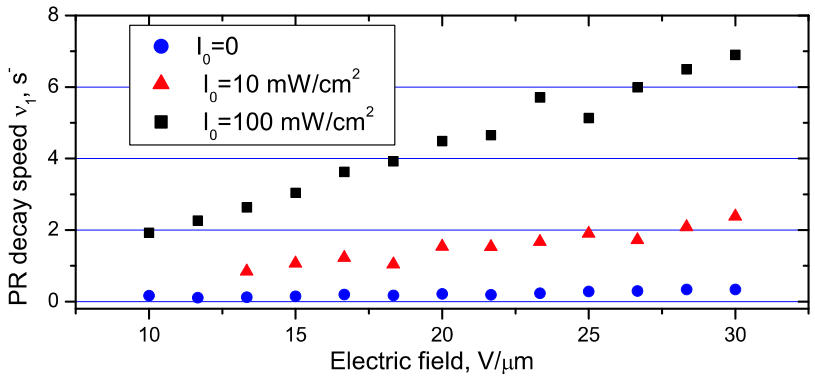

Figure 3.28: Dependence of the faster component of the PR decay on the electric field for various intensities of erasing beam.

the PVK(49.5 wt.%)/C_{60}(0.5 wt.%)/BBP(15 wt.%)/AODCST(35 wt.%) composite. Theoretical discussion of PR decay under the erasing beam involves solving Eqs. 2.58 without the interference term proportional to I_1. Otherwise, the same kind of analysis that we performed in Section 2.3 for both photocurrent rise and then the PR grating formation transients can be done for the speed of PR decay.

3.5 Photorefractive performance: in search of optimal polymer composite

So far, we have considered all kinds of theoretical models and experimental techniques used for photoconductivity and PR studies. However, it may seem that "the story" is lost behind the technical details described so verbosely. This section is designed to finally "tell the story". It is based on the experimental part of the dual paper [29] we recently wrote on PR in polymers. We will apply both the theoretical approach described in Chapter 2 and the experimental techniques described in this chapter so

far to materials research. In particular, we will study how the constituents of the polymer composite influence the dynamics of the PR grating formation.

So, in this section, we will present a complete study of various PR polymer composites. In particular, we will examine the contribution of chromophores and plasticizers to photoconductive and photorefractive performance of the PR polymers.

We use a modified Schildkraut and Buettner's [37, 29] photorefractive model (Section 2.2) and our procedure [29] developed in Section 2.3 to study the photoelectric and photorefractive properties of various PVK-based composites. One of the issues we address in this section is how the photoelectric properties such as mobility, charge generation efficiency, trapping, detrapping and recombination rates that appear to be relevant to photorefraction are influenced by characteristics of the composite such as degree of disorder, trap depths, ionization potentials of the constituents, presence of ionic impurities, etc. We analyze the photoconductive and photorefractive behavior of two classes of polymer composites. One class of polymer composites we studied consisted of the photoconductor poly(N-vinylcarbazole) (PVK), the sensitizer (C_{60}) and several chromophores ("unplasticized" composites). Another class of composites ("plasticized" composites) also includes a plasticizer that is added in many cases [5, 18, 38] to lower glass transition temperature. For composites of both classes, we determined the quantum efficiency, mobility, trapping, detrapping and recombination rates from photoelectric measurements. Then using these rates we

(i) calculate the PR speed as determined by four-wave mixing

(ii) compare corresponding rates for different chromophores and relate them to relevant ionization potentials

(iii) study the influence of plasticizer on photoconductivity and photorefractive performance of the composite and, finally

(iv) study the nature of shallow and deep traps in composites and investigate their influence on photoconductive and photorefractive properties of the materials.

3.5.1 Unplasticized composites

This class of composites under investigation included the following molar concentrations: PVK(99%)/C_{60}(1%) (composite 1) and PVK(89%)/C_{60}(1%)/NLO(10%) where NLO is a nonlinear chromophore which in our case was represented by AODCST (composite 2), PDCST (composite 3) or 5CB (composite 4) (see Figure 3.1).

Sample preparation for both photoconductive and photorefractive studies was conducted as described in Section 3.2.2.

Photoelectric properties

- The dielectric constant ε for each composite was determined using a capacitance bridge.

- The free carrier mobility μ was measured using the TOF technique described in Section 3.3.2. The parameter β_μ (Eqs. 2.31) was determined from the electric

field dependence of the mobility.

- The photogeneration cross-section s and its field dependence parameter p (Eqs. 2.31) were determined from the xerographic discharge experiment (Section 3.3.1).

- The product of trapping rate and density of available shallow traps $\gamma_T M_{T1}$, the recombination rate γ and the shallow trap detrapping rate β_1 were determined as functions of intensity and electric field from the short time scale DC photoconductivity experiment (Section 3.3.3) in accordance with the procedure described in Section 2.3. The parameter β_γ was determined from the electric field dependence of the trapping rate γ_T.

- The product of trapping rate and density of available deep traps $\gamma_T M_{T2}$ and the detrapping rate β_2 for deep traps were determined from the long time scale DC photoconductivity experiment (Section 3.3.3) as described in Section 2.3.

- The photoconductivity parameters and rates obtained at the electric field $E_0 = 40\,V/\mu m$ are summarized in Tables 3.1, 3.2. All the trends we describe in this section are applicable for composites 1-4 in the studied electric field range of $E \approx 20 - 80\,V/\mu m$.

Diagrams describing charge generation, transport and trapping for different composites are shown in Figure 3.29. Here we used the relative HOMO level energies for PVK

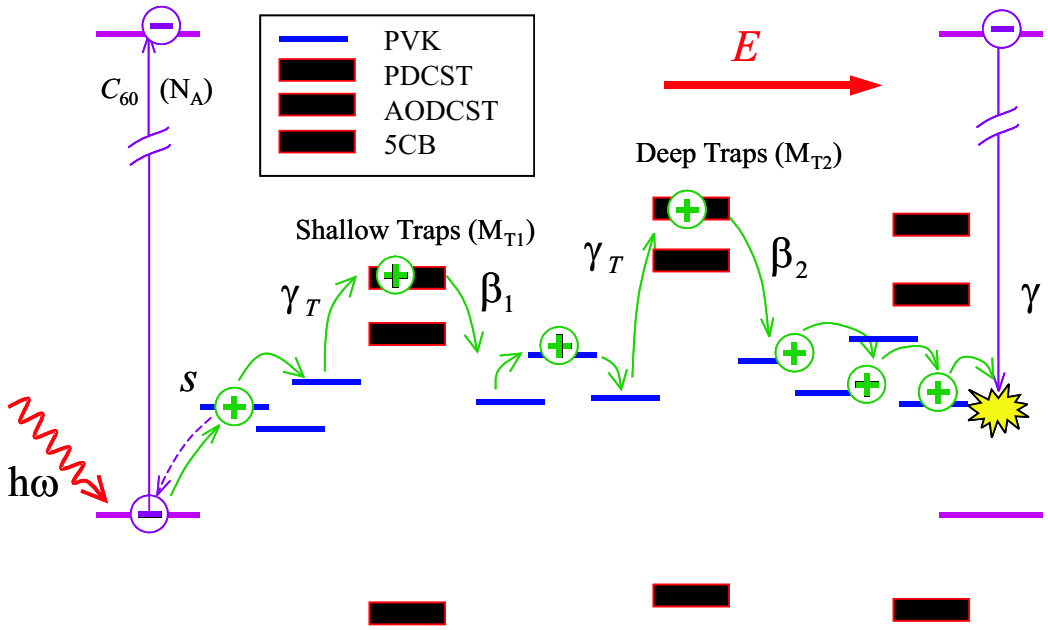

Figure 3.29: Schematic representation of the PR composite with different chromophores.

$(0eV)$, C_{60} $(-0.17\,eV)$, AODCST $(0.03\,eV)$, PDCST $(0.1\,eV)$ and 5CB $(< -0.4\,eV)$ provided in Ref. [39].

As all the photoconductivity parameters are measured and summarized (Tables 3.1, 3.2), we explore the contribution of the chromophores in differences in these parameters for composites 1-4.

Table 3.1: Photoelectric parameters relevant for photorefraction for composites 1-4. No plasticizers were added.

Composite	$s, 10^{-5}$ m^2/J	$\mu, 10^{-11}$ $m^2/(Vs)$	$\gamma_T M_{T1}$, s^{-1}	$\gamma_T M_{T2}$, s^{-1}	β_1, s^{-1}	β_2, $10^{-4}s^{-1}$	$\gamma, 10^{-19}$ m^3/s
1 Neat	1.7	5.3	850	–	2.7	–	2.5
2 AODCST	1.6	3.9	300	3	0.75	8.5	0.09
3 PDCST	0.84	2.5	770	23	0.3	1.5	0.08
4 5CB	0.83	1.7	550	–	1.5	–	0.09

Table 3.2: Photoelectric parameters relevant for photorefraction for composites 1-4 (ctd). No plasticizers were added.

Composite	$\beta_\mu, 10^{-4}$ $(m/V)^{1/2}$	$\beta_\gamma, 10^{-4}$ $(m/V)^{1/2}$	p	ε
1 Neat	4.9 ± 0.2	8.3 ± 0.5	2.04 ± 0.06	3.1
2 AODCST	5.8 ± 0.5	3.3 ± 0.4	2.04 ± 0.04	4.3
3 PDCST	4.9 ± 0.2	6.5 ± 0.3	2.04 ± 0.04	3.8
4 5CB	6.0 ± 0.3	4.6 ± 2.0	2.1 ± 0.2	4.5

- **Photogeneration cross-section (s)** As we discussed in Section 2.2.1, the photogeneration cross-section s is a measure of quantum efficiency and is given by Eq. 3.7. The photogeneration cross-section microscopically depends on the donor-acceptor charge transfer and electron-hole dissociation rates [40]. According to their HOMO levels, chromophores AODCST and PDCST as well as PVK are donors with respect to C_{60}, and thus could participate in photogeneration. If we take into account the dependence of the charge transfer rate k_{CT} on the energy difference $\Delta\mathcal{E}_{DA}$ between HOMO levels of donor and acceptor [41, 40] given by Eq. 2.34 ($k_{CT} \sim \exp[-(\Delta\mathcal{E}_{DA} - \lambda_0)^2/(4\lambda_0 k_B T)]$) then in the noninverted regime, the photogeneration efficiency would be highest for composite 3, followed by composites 2, 1 and 4. However, the donor-acceptor charge transfer is not the only factor that contributes to charge generation. The other factor is the electron-hole dissociation [40], which proceeds more strongly as the mobility increases. Based on our results for photogeneration cross-sections and mobilities for composites 1-4 (Table 3.1), we conclude that the mobility dif-

ferences that affect dissociation rather than the charge transfer rate k_{CT} could account for the differences in quantum efficiencies for the composites 1-4.

- **Mobility (μ)** The hole mobility of all of the composites 2-4 is smaller than that for the PVK/C_{60} (composite 1). This is expected when adding polar chromophores to the system due to the increase in energetic disorder [42, 43]. Based only on the dipole moment of the chromophore, composites 2 and 3 would be expected to yield similar mobilities due to almost equal dipole moments (6.9D for AODCST and 6.6D for PDCST), and composite 4 would yield the higher mobility than the composites 2 or 3 since the dipole moment of 5CB (4.1D) is lower than that of both AODCST and PDCST. Our results show that the composite 2 possesses the largest value for mobility out of three composites with chromophores (2-4). We attribute this to the fact that HOMO level of AODCST is situated inside the transport manifold of PVK, so that AODCST molecules participate in transport by increasing the density of transport states.

  All three chromophores influence the PVK/C_{60} system modifying the position and depth of shallow traps that are intrinsic to PVK [3]. Here we need to make a distinction between shallow traps whose release (detrapping) time is much smaller than the transit time, in other words shallow traps that broaden the tail of the current transients observed in our TOF experiment, and traps whose release time is much larger than the transit time relevant for photorefraction.

Current transients observed in TOF experiments showed dispersive behavior for all the composites 1-4, with a tail broadening parameter of Eq. 3.12 ($W = \frac{t_{1/2} - t_T}{t_{1/2}}$ where $t_{1/2}$ is the time required for the current to decrease to one half of its value at the transit time t_T) [44]. For composite 1 (no chromophore added) the parameter W was the lowest and yielded 0.44 at $40\,V/\mu m$. Composites 2-4 showed larger disorder ($W = 0.47$) similar for all chromophores. This is evidence that shallow traps relevant to the TOF experiment were modified by all three chromophores in a similar way. The picture is different for traps that are deeper than those contributing to the TOF tail broadening W. Further on we will consider only these "deeper" traps relevant to photorefraction – shallow traps with release time $\tau_1 = \frac{1}{\beta_1}$ and deep traps with release time $\tau_2 = \frac{1}{\beta_2}$ [29]. Of course, in a real system the traps are described by a continuous energy distribution function, but we confine our analysis to the case of well defined average trap depths whose release times τ_1 and τ_2 are at least an order of magnitude different.

- **Trapping and shallow detrapping rates (γ_T and β_1) and total shallow trap density (M_{T1})**

  The parameters describing shallow traps are the trapping rate γ_T, the total number density of available shallow traps M_{T1}, and the detrapping (releasing) rate β_1. Comparing detrapping rates β_1 for composites 1-4 (Table 3.1), we ob-

serve that the addition of all chromophores leads to a decrease in detrapping rate β_1 that may arise from a decrease in the overlap integral (intersite distance), an increase in the trap energy depth $\Delta\mathcal{E}_T$ (Figure 3.29) [44, 9] or both. Both AODCST and PDCST have a larger impact on β_1 than 5CB since they can provide sites that can serve as deeper traps. Since in our experiments we cannot measure the trapping rate γ_T and total trap density M_{T1}, but only the product $\gamma_T M_{T1}$, we can only speculate about possible contributions of each. The trapping rate γ_T at a given electric field is expected to depend on the free hole mobility and the neutral trap capture cross-section [9]. As we discussed in Section 2.2.3, we assume an activationless (Miller-Abrahams) trapping process (see Section 2.2.2 for details) for which the trapping rate (γ_T) does not depend on the trap depth ($\Delta\mathcal{E}_T$) [45]. In this case we should expect a smaller trapping rate γ_T value for the composites 2-4 in comparison to composite 1 due to decreased mobility. In composite 3 the product $\gamma_T M_{T1}$ is larger than that of composites 2 and 4 which could indicate that PDCST actually adds shallow traps to the system in addition to just changing the average depth of existing shallow traps in pure PVK. On the contrary, composite 2 has the smallest product $\gamma_T M_{T1}$ which could mean that AODCST reduces the relative density of relevant shallow traps intrinsic to PVK by providing extra transport sites.

- **Deep trap density (M_{T2}) and detrapping rate (β_2)**

Similar to shallow traps, we characterize deep traps by their number density M_{T2} and detrapping rate β_2. We could not detect deep traps in the PVK/C_{60} system and in composite 4 (with 5CB as chromophore) which means that the density of available deep traps (M_{T2}) in these composites is on the order of 1 % or less of the acceptor density N_A [29] (see Section 2.3). Both AODCST (composite 2) and PDCST (composite 3) create deep traps, with the trap depth larger for PDCST than for AODCST which is consistent with experimental studies performed with these chromophores in Ref. [39] and with our numerical simulations [29] described in Section 2.3. The deep trap number density M_{T2} is also expected to be smaller than the shallow trap number density M_{T1} since shallow traps in the system are due to both PVK and chromophore, and deep traps are due to the chromophore only. The product $\gamma_T M_{T2}$ is indeed much smaller than $\gamma_T M_{T1}$ (Table 3.1), and also from the comparison between $\gamma_T M_{T2}$ values for composites 2 and 3 we conclude that PDCST creates more deep traps than AODCST as would be expected by their HOMO levels. Here we need to mention that the approach we used above to analyze the dynamics of photoconductivity is valid for systems with available trap densities $M_{T1}, M_{T2} \gg N_A$ [29] (refer to Section 2.3.1), so that the amount of charge that can be possibly generated and trapped does not considerably affect the total number density of available traps. Then, $\gamma_T(M_{T1,2} - M_{1,2}) \approx \gamma_T M_{T1,2}$, and the analysis of photocurrent transients

is simplified. Knowing the available trap densities $M_{T1,2}$, one can check the validity of this approximation, although usually these quantities are not easily probed. The experiments that are performed to determine trap densities [30, 3] actually determine the average density of filled traps $M_{1,2}$ compensated by ionized acceptors N_A^i and determined by the balance of photogeneration, trapping, detrapping and recombination rates, but do not provide the information about relevant photorefraction trap densities ($M_{T1,2}$). We can crudely estimate the order of magnitude of trap densities based on the products $\gamma_T M_{T1}$, $\gamma_T M_{T2}$ and concentrations of carbazole units and chromophores. In the unplasticized composites 2-4, the concentration of carbazole units is $\sim 3.4 \cdot 10^{27}\, m^{-3}$ as estimated using the density $1.2 \cdot 10^6 g/m^3$ and molar weight $193\, g/mol$. The concentration of the chromophores is $\sim 4 \cdot 10^{26}\, m^{-3}$. For composite 3, where we do not expect a large contribution of the chromophore to transport but rather to trapping - both shallow and deep, we compare the product $\gamma_T M_{T1}$ for this composite with the one for pure PVK/C_{60} (composite 1). Assuming the rates γ_T scale as the mobilities (neglecting differences in overlap integral), we would expect the product $\gamma_T M_{T1}$ for composite 3 to be $\sim 400\, s^{-1}$. Since it is almost twice that number, we attribute this difference to the increase in shallow trap density M_{T1} due to PDCST. Then using the product $\gamma_T M_{T2}$ for composite 3 from Table 3.1, we obtain $M_{T1}/M_{T2} \sim 20$. Thus, we roughly obtain $3.8 \cdot 10^{26}\, m^{-3}$ shallow traps

and $2 \cdot 10^{25}\, m^{-3}$ deep traps due to PDCST in composite 3. Then, the other $\sim 400\, s^{-1}$ from the product $\gamma_T M_{T1}$ is due to carbazole units, and their contribution to the density of relevant shallow traps is $\sim 3.8 \cdot 10^{26}\, m^{-3}$, i.e. $\sim 10\,\%$ of all available carbazole sites. So, in composite 3 we estimated $\sim 7.6 \cdot 10^{26}\, m^{-3}$ shallow traps (M_{T1}) and $\sim 2 \cdot 10^{25}\, m^{-3}$ deep traps (M_{T2}). Comparing M_{T1}, M_{T2} with the total acceptor density $N_A \approx 3.8 \cdot 10^{24}\, m^{-3}$, we conclude that for composite 3 the condition $M_{T1}, M_{T2} \gg N_A$ is valid and therefore it is enough to know the products $\gamma_T M_{T1,2}$ to describe the photoconductive and photorefractive dynamics of the composite [29] (Section 2.3.1). In composite 2, however, the deep trap density is $\sim 4 \cdot 10^{24}\, m^{-3}$ as estimated from the ratio of mobilities and the products $\gamma_T M_{T2}$ for composites 2 and 3. So, for composite 2 the deep trap density M_{T2} is on the order of the acceptor density N_A. Our numerical simulations of photoconductivity dynamics with different ratios M_{T2}/N_A show that the $M_{T2}/N_A \sim 1$ case yields a $\sim 10\%$ error in determining M_{T2}/M_{T1} if the approximation $M_{T2}/N_A \gg 1$ is applied [29] (refer to Section 2.3). Thus, the approach we used is reasonable within $10\,\%$ error for the composite 2 as well. We can also estimate the trapping rate γ_T assuming the shallow trap density $M_{T1} \sim 10^{26}\, m^{-3}$. Then using the product $\gamma_T M_{T1} \sim 500\, s^{-1}$, we estimate the trapping rate $\gamma_T \sim 5 \cdot 10^{-24}\, m^3/s$.

- **Recombination rate (γ)** The recombination rate γ describes interaction of

the free hole with the ionized acceptor (C_{60}^{-}) and usually is treated as Langevin bimolecular recombination [9] given by Eq. 2.44. According to this relation, the ratio γ/μ depends only on dielectric constant ε of the material. In polymers, due to disorder, deviations from the Langevin form are observed [9]. Also, as discussed in Section 2.2.4, it is not clear whether the initial requirement for Langevin treatment that the mean free path of the carriers is less than the Coulomb radius of capture holds. Our measured recombination rate for PVK/C_{60} shows good agreement with the value obtained using Eq. 2.44. However, the measured values for composites 2-4 are considerably lower than the corresponding values calculated from Eq. 2.44.

Comparing the trapping rate γ_T estimated above and recombination rate γ, we observe that the recombination rate is several orders higher than the trapping rate. This is indeed physically reasonable and is due to the difference in free hole capture cross-sections in the case of neutral traps (M_{T1}) and charged recombination centers (N_A^i) [21], as we considered in Section 2.2.4.

Photorefractive properties

In this section we applied all the photoelectric parameters we determined above to the system of equations derived from Eqs. 2.29 for the first Fourier components (spatially variant) of space charge field and all appropriate number densities (Eqs. 2.58). When considering the space charge field formation, we used the values for mobility, trapping

and recombination rates calculated using the value of the projection of the electric field on grating vector while the photogeneration cross-section was calculated using the applied electric field. We solved these equations (Eqs. 2.58) to determine the dynamics of photorefractive grating formation ($E_1(t)$) for the composites 2-4. Then, we calculated the diffraction efficiency signal time evolution as it appears in the four wave mixing (FWM) experiment [6] $\eta \sim E_1(t)^2$ (Eq. 2.60) and fit with Eq. 2.62 to determine the PR speed ν.

On the time scale of our FWM experiment for unplasticized composites 2-4 ($\sim 20\,s$) the slow component of the photorefractive speed due to deep trap filling did not appear. Thus, we used the Eq. 2.60 to predict the photoconductive part of photorefractive speed ν due to shallow trap filling [29]. The calculated speed ν is to be compared with the measured ν_1 introduced in Section 3.4.2. The anticipated speed ν as a function of total internal intensity of two beams for the composites 1-4 is shown in Figure 3.30 (lines with symbols).

In the FWM experiment, diffracted signal transient that is typical for composites 2-4 is shown in Figure 3.31. Initially, the electric field and one of the writing beams are on. At time $\sim 1.7\,s$, the second writing beam is turned on, and the PR grating formation is recorded. We fit the PR grating formation dynamics with a bi-exponential function of Eq. 3.21 where the faster speed ν_1 was attributed to photoconductivity and dominated with weight $a \approx 0.8$. The slower speed ν_2 in the composites 2-4 is due

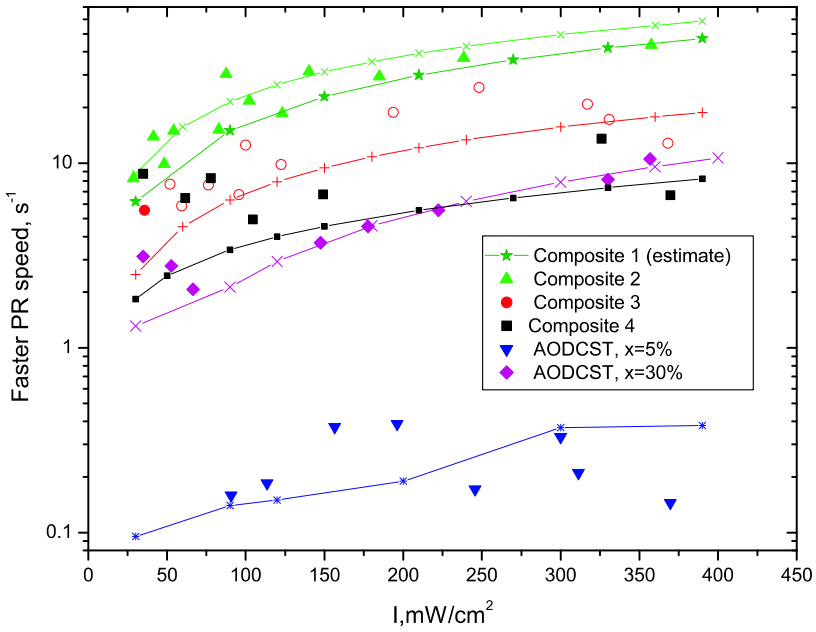

Figure 3.30: Intensity dependence of the faster PR speed for different composites: lines with symbols correspond to the calculated PR speed on the basis of photoelectric parameters; symbols are the FWM experimental data points.

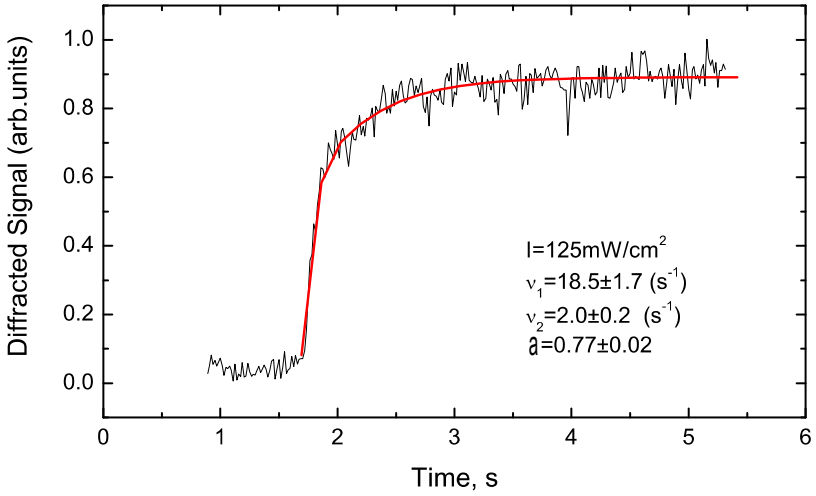

Figure 3.31: Time evolution of the diffracted signal as observed in the composite PVK(49%)/C_{60}(1%)/AODCST(10 %) at the applied electric field $E_a = 30\,V/\mu m$ at total writing beam intensity of $125\,mW/cm^2$. The smooth line corresponds to a bi-exponential fit to Eq. 3.21, with the parameters shown on the graph.

to orientational enhancement which was verified experimentally in a following way. First, we verified that the orientation mechanism is present by comparing of the ratio of p-polarized and s-polarized diffraction efficiencies η_p/η_s to this ratio calculated from geometry of the experiment and simple electro-optic effect [46] (see Section 2.4 for details). Then, we found that the slower speed was intensity independent and on the order of $1-2\,s^{-1}$, which is consistent with our electric field induced second harmonic generation (EFISHG) measurements of the dynamics of chromophore reorientation for these materials [47, 48] which will be considered in Chapter 4.

The data shown in Figure 3.31 is taken with composite 2 at total writing beam intensity $125\,mW/cm^2$ at applied electric field $E_a = 30\,V/\mu m$. The smooth line in Figure 3.31 corresponds to the bi-exponential fit with Eq. 3.21. At this intensity, the fit yields the faster speed $\nu_1 = 18.5 \pm 1.7\,s^{-1}$ dominating with the weight $a = 0.77 \pm 0.02$. This is attributed to shallow trap dynamics. The slower speed $\nu_2 = 2 \pm 0.2\,s^{-1}$ is due to chromophore reorientation. A similar experiment was repeated for different intensities of the writing beams.

The measured faster component of the photorefractive speed ν_1 for composites 2-4 is shown in Figure 3.30 (symbols) and is in a reasonable agreement with the speed ν predicted using experimentally determined photoelectric parameters for these composites.

3.5.2 Plasticized composites

This class of composites had the plasticizer at a loading complementary to the chromophore molar concentrations: PVK(49%)/C_{60}(1%)/BBP(50%-x%)/AODCST(x%) and PVK(49%)/C_{60}(1%)/BBP(50%-x%)/5CB(x%), where x was varied from 0% to 40%. Studying the chromophore concentration dependence of these composites where the chromophore is substituted with the plasticizer rather than just being added provides for consistent orientational effects since the glass transition temperature (T_g) was near room temperature for all the concentrations and thus, orientational effects are expected to be similar for all the composites. Also, the photoelectric properties of the materials connected to charge transport (mobility, trapping and recombination rates) change with temperature relative to T_g, $\Delta T = T_{exp} - T_g$ where T_{exp} is the temperature at which the experiment is conducted [49, 50, 20, 3]. We used purified materials and freshly made samples for all our experiments since we found that both chemical impurities and sample aging led to deep trap formation, which would confound the data.

In this section we consider the dependence of the PR properties of composites on the chromophore and plasticizer concentration. First, we consider how substitution of the chromophore molecule by the plasticizer (increase in parameter $x(\%)$) affects the photoelectric parameters such as mobility, photogeneration efficiency, recombination, trapping and detrapping rates. We studied this for two chromophores - 5CB and

AODCST to determine the influence of the chromophore ionization potential on these characteristics. Second, we used the parameters determined from photoconductivity to model the time evolution of a photorefractive grating (diffracted signal observed in FWM experiment) and compare it with experimental data for different concentrations. Finally, we discuss the dependence of the diffracted signal on the illumination history for different concentrations of AODCST and 5CB.

Photoelectric properties

- The dielectric constant ε for each concentration was determined using a capacitance bridge.

- The free carrier mobility μ was measured using TOF technique for high electric fields ($E_0 \gtrsim 40\,V/\mu m$) and estimated from DC photoconductivity experiment as described in Section 3.3.3 for low electric fields since at low fields, the TOF technique yielded too dispersive transients (Section 3.3.2). The parameter β_μ (Eqs. 2.31) was determined from the electric field dependence of the mobility.

- The photogeneration cross-section s and its field dependence parameter p (Eqs. 2.31) were estimated from DC photoconductivity experiment (Section 3.3.3) since the xerographic discharge experiment (Section 3.3.1) could not be performed due to high dark ionic current in these samples.

- The product of trapping rate and density of available shallow traps $\gamma_T M_{T1}$,

the recombination rate γ and the shallow trap detrapping rate β_1 were determined as functions of intensity and electric field from the short time scale DC photoconductivity experiment (Section 3.3.3) in accordance with the procedure described in Section 2.3. The parameter β_γ was determined from the electric field dependence of the trapping rate γ_T.

- The product of trapping rate and density of available deep traps $\gamma_T M_{T2}$ and the detrapping rate β_2 for deep traps were determined from the long time scale DC photoconductivity experiment (Section 3.3.3) as described in Section 2.3.

The most distinct feature of the plasticized composites in comparison to unplasticized ones is the presence of large dark current observed in "fresh" samples. Here "fresh" means that the sample was not exposed to either electric field or illumination. In this case the dark current is caused by both charge injection from the electrodes and ionic impurities that are always present in the polymeric systems [51] that become mobile under the electric field due to the conformational freedom of the polymer chains [9]. As the sample is kept under electric field, the mobile ions move towards the oppositely charged electrodes and either neutralize [15] or build up, reducing the electric field inside the polymeric film. Samples of all concentrations x for both 5CB and AODCST showed dark current behavior similar to that shown in Figure 3.15b. We performed all the measurements after the samples were electrically cleansed (see Section 3.3.3 for details) to avoid dynamic effects directly induced by moving impurity ions. Although

we tried to maintain exactly the same experimental conditions for the samples at all concentrations, our measurements of both photoconductivity and diffraction efficiency at different times after turning on the electric field without any prior illumination show that internal electric fields that are created by uncompensated traps filling with injected charge [28] vary for different samples. In addition, non-neutralized impurity ions differ for various concentrations of the chromophore. However, these effects were minor in comparison to the direct concentration effects that we investigated.

The energy diagram illustrating various composites studied is shown in Figure 3.32. Based on the ionization potentials of the plasticizer and chromophores, we expect that an increase in concentration of 5CB (relative to the concentration of plasticizer BBP) should not change the mobility, photogeneration efficiency, trapping and other photoelectric parameters for reasons other than increase in energetic disorder due to the difference in dipole moments of 5CB ($4.1D$) and BBP ($1.1D$). In case of AODCST, though, in addition to the change in energetic disorder, we also expect changes due to the contribution of AODCST sites in charge photogeneration and transport. Indeed, our results show that both mobility and photogeneration cross-section increase with concentration of AODCST and stay almost constant for all concentrations of 5CB. Although these trends were observed for the whole range of electric fields studied ($1-50\,V/\mu m$), the most pronounced concentration dependence was found at low electric fields ($< 15\,V/\mu m$). This could be due to the smaller influence of energetic

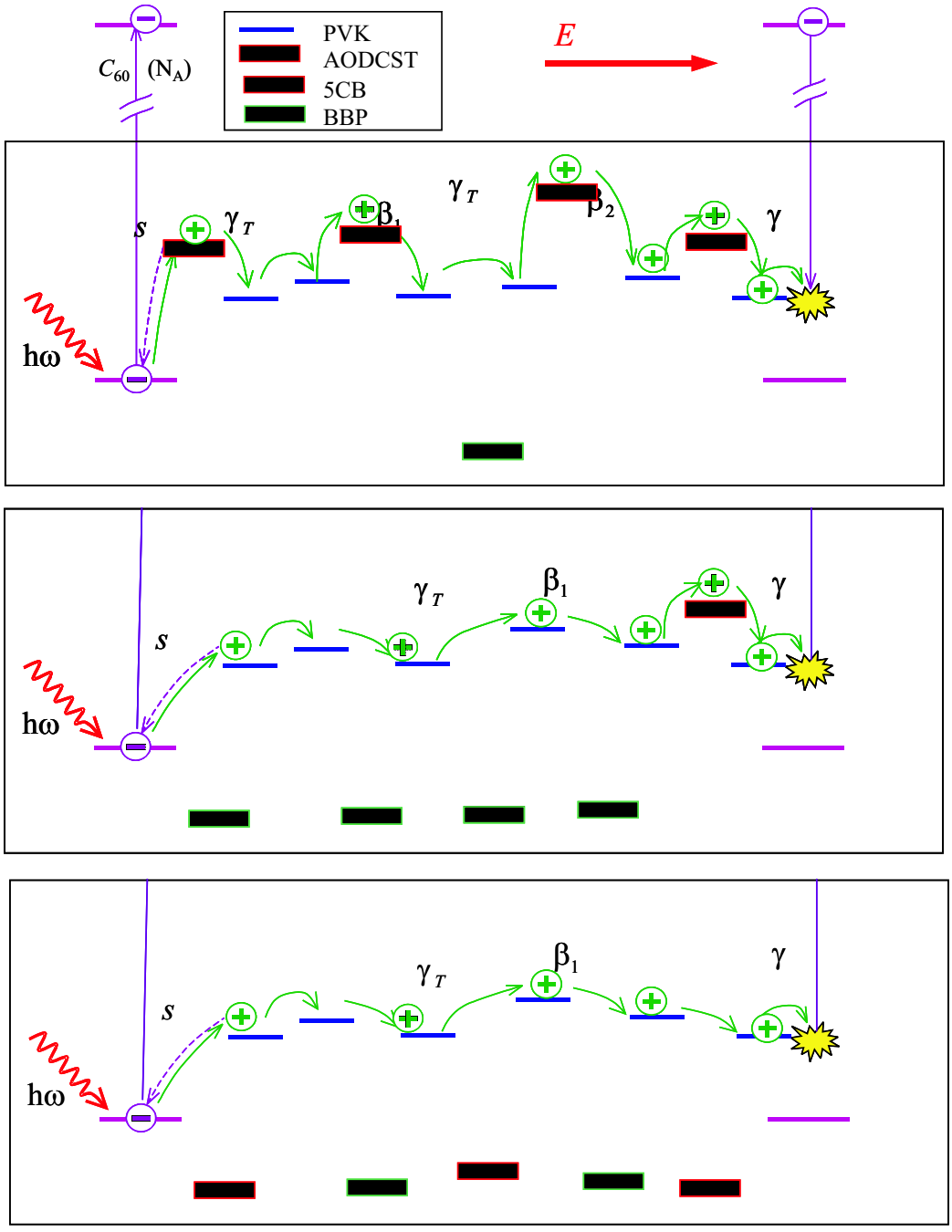

Figure 3.32: Illustration of chromophore and plasticizer roles in charge generation, transport and trapping.

disorder at low fields, so that the largest impact on concentration dependence is attributed to the effects only due to ionization potential of the chromophores relative to transport states. As a sign of the small influence of the energetic disorder at low fields, the following feature could be observed: at low fields, carrier mobilities turned out to be the decreasing functions of electric field for all composites. This can be attributed to the positional disorder prevailing over the energetic disorder (refer to Section 2.2.2).

The concentration dependence of mobility and photogeneration cross-section for 5CB and AODCST at electric field $E_0 = 10\,V/\mu m$ is shown in Figure 3.33a,b. As determined from DC photoconductivity at electric field $E_0 = 10\,V/\mu m$ and intensity $I_0 = 40\,mW/cm^2$, the product $\gamma_T M_{T1}$ increased in the case of AODCST and did not change in case of 5CB (Figure 3.33c). This change reflects increase in mobility and intersite distance that affect the trapping rate for AODCST and no changes in these for 5CB. The detrapping rate β_1 increased from $\sim 0.05\,s^{-1}$ to $\sim 0.1\,s^{-1}$ for AODCST, reflecting increase in the overlap integral (decrease in intersite distance). The recombination rate was $\sim 2 \cdot 10^{-21}\,m^3/s$ and did not change appreciably with concentration, probably because the increase in mobility in case of AODCST was partially compensated by an increase in dielectric constant which increased from 12 at $x = 5\,\%$ to 24 at $x = 40\,\%$.

The presence of deep traps in the composites was studied by monitoring DC pho-

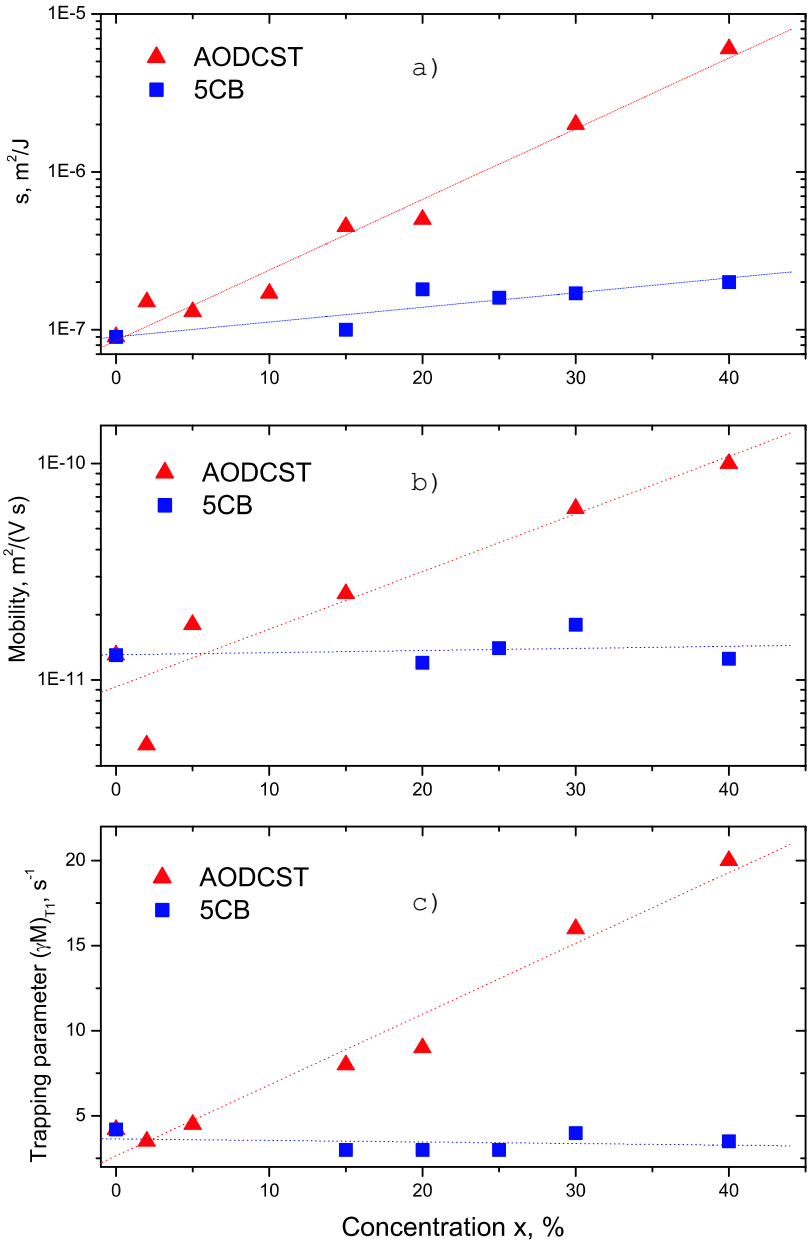

Figure 3.33: Concentration dependence of a)photogeneration cross-section; b)mobility; c)trapping parameter. The lines provide visual guidance.

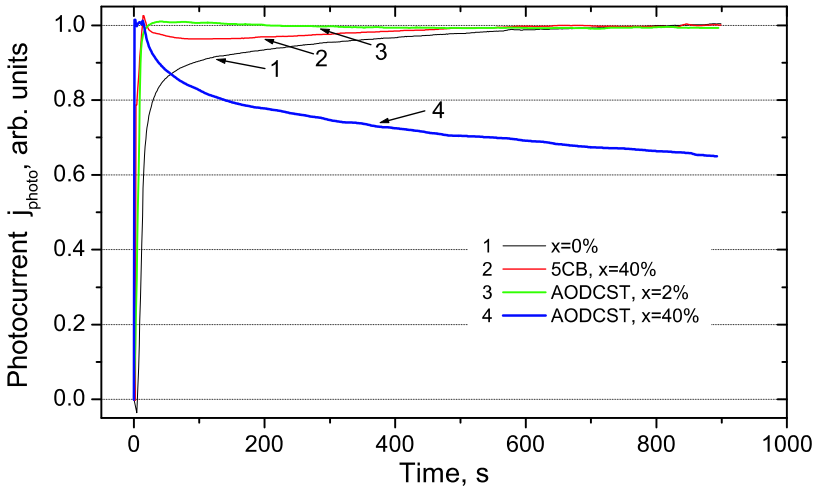

Figure 3.34: Long time scale photocurrent dynamics for different composites.

toconductivity on a long time scale (see Sections 2.3.1, 3.3.3). The transients for some of the studied composites are shown in Figure 3.34. The composites with $x=0$ (PVK/BBP/C_{60}) and with any concentration of 5CB showed no photodegradation (Figure 3.34) and thus the deep trap density in these composites was below our detection limit of $M_{T2} \leq 0.01 N_A$. Our numerical simulations of PR dynamics show that when the available density of deep traps is on the level $M_{T2} \sim N_A$ or less (provided shallow trap-unlimited regime $M_{T1} \gg N_A$), the PR grating time evolution is not influenced by deep traps. In the AODCST-containing composites, the degradation of the photocurrent increased as the concentration of AODCST increased, so that the product $\gamma_T M_{T2}$ describing deep trapping increased from $\sim 0.02\, s^{-1}$ for $x = 2\,\%$ to $\sim 1.6\, s^{-1}$ for $x = 40\,\%$, and the detrapping rate β_2 correspondingly changed from $1.1 \cdot 10^{-5}\, s^{-1}$ to $8.2 \cdot 10^{-4}\, s^{-1}$, although the values for low concentrations of the chro-

mophore may contain a large error due to the small concentration of deep traps M_{T2} in these composites.

Similar to the method described in Section 3.5.1, we substitute all the calculated values into the equations describing photorefractive grating formation (Eqs. 2.58) and model the PR performance of the composites. We fit the calculated diffraction efficiency $\eta(t)$ with a bi-exponential function (Eq. 3.21) since for these samples, both the slow and fast components of the photorefractive speed are due to photoconductivity. The calculated faster PR speed (ν_1) as a function of concentration of the chromophore with no adjustable parameters is presented in Figure 3.35 (line with symbols with symbols corresponding to concentrations for which we determined photoelectric parameters on whose basis the PR speed was calculated). The calculated speed ν_1 as a function of intensity for AODCST-containing composites with $x = 5\,\%$ and $x = 30\,\%$ is also shown in Figure 3.30 (line with symbols). The slower PR speed (ν_2) requires a more careful approach and will be discussed in the next section.

Photorefractive properties

In plasticized composites, both the faster (ν_1) and slower (ν_2) speeds of the bi-exponential fit given by Eq. 3.21 were determined by photoconductivity and varied from $0.1 - 20$ and from $0.01 - 1$ respectively depending on the chromophore concentration, applied electric field and incident light intensity. Thus, the chromophore reorientation time constant of about 40 ms (as determined by EFISHG - see Chapter

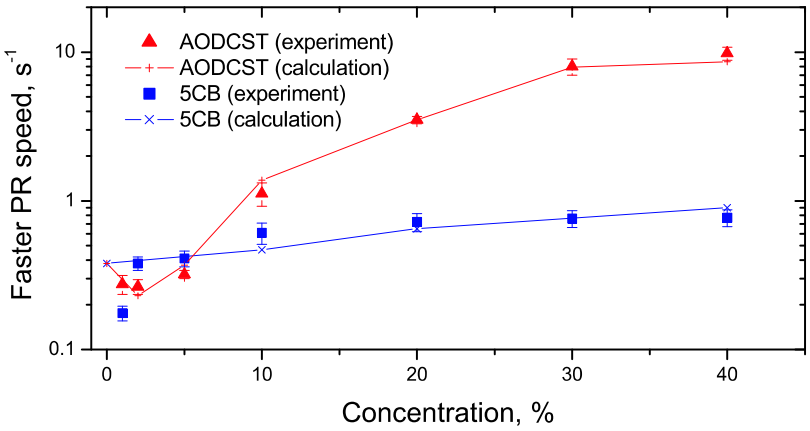

Figure 3.35: Concentration dependence of faster PR speed for 5CB and AODCST -containing composites. Lines with symbols correspond to calculated values for PR speed from the photoelectric rates with no adjustable parameters; symbols correspond to FWM experimental data at applied field $E_a = 10\, V/\mu m$ and total internal intensity $I = 300\, mW/cm^2$.

4), which is faster than both ν_1 and ν_2, does not contribute.

The faster PR speed ν_1 obtained from a bi-exponential fit of Eq. 3.21 to the experimentally measured diffraction efficiency for different concentrations is plotted in Figure 3.35 (symbols) and shows reasonable agreement with the values of ν_1 calculated from photoconductivity (line with symbols). For AODCST $x = 5\,\%$ and $x = 30\,\%$ the experimentally measured ν_1 as a function of the total internal intensity is shown in Figure 3.30 (symbols).

To model the long time scale behavior of PR signal described by slower speed ν_2 and to study the long term effects such as uniform illumination history dependence of the composites, it might be not enough to know just the trapping parameters - $\gamma_T M_{T1}$ and $\gamma_T M_{T2}$ that we are able to determine from the photoconductivity, but

rather requires knowing trapping rate γ_T and trap densities M_{T1}, M_{T2} separately. As mentioned above, the approach used to model the dynamics of photoconductivity and calculate the faster PR speed from the photoelectric parameters is valid for materials with available trap densities $M_{T1}, M_{T2} \gg N_A$ (Section 2.3.1). For our unplasticized composites described in Section 3.5.1 this condition appears to be valid for all the composites for shallow traps and for composites 2 and 3 for deep traps. In the case of plasticized composites, though, the total density of carbazole units is reduced (molar concentration is 50 %), so the density of shallow traps may also be reduced. However, since the room temperature measurements are close to the glass transition temperature for all our plasticized composites, this could be responsible for the increased energetic disorder in the system [20] and thus increase the relevant trap density due to broadening of the density of states. These processes are beyond the scope of our studies, and we will limit our estimate by assuming that the density of relevant shallow traps due to PVK in plasticized samples is $\sim 10\,\%$ of total density of carbazole units as calculated in Section 3.5.1 and as estimated to be $\sim 2 \cdot 10^{26}\, m^{-3}$. Thus, it seems that for all chromophore concentrations we studied, the condition for shallow traps $M_{T1} \gg N_A$ is valid. For deep traps, however, based on the values for product $\gamma_T M_{T2}$ we obtained for different concentrations of AODCST, it seems that for AODCST composites with $x \lesssim 10\,\%$ the deep trap density $M_{T2} \leq N_A$, and at approximately $x \sim 20\,\%$, we enter the deep trap-unlimited regime with $M_{T2} \gg N_A$. To check whether

our estimates of available deep trap densities are consistent with our FWM experimental data, we simulated the diffracted signal time evolution for three composites - 5CB with $x = 40\,\%$ ($M_{T1} \gg N_A, M_{T2} = 0.01 N_A$), AODCST with $x = 5\,\%$ ($M_{T1} \gg N_A$, $M_{T2} \sim N_A$) and AODCST with $x = 40\%$ ($M_{T1}, M_{T2} \gg N_A$). For this simulation we used the appropriate measured photoelectric parameters for these composites at an applied field $E_a = 10\, V/\mu m$ and total internal intensity $I = 300\, mW/cm^2$. Figure 3.36 shows the simulated diffraction efficiency signals for these composites superimposed with the corresponding FWM experimental data for these composites. Both simulated and experimentally obtained diffracted signals shown in Figure 3.36 are normalized to be unity at 100 s. The diffracted signal for 5CB-containing composites (as an example, the case $x = 40\,\%$ is shown in Figure 3.36) reflects space charge field formation due to shallow trap filling with the speed determined by the photoelectric rates intrinsic for these composites. For low concentration AODCST-containing composites, the diffracted signal reflects mostly shallow and some deep trap filling, and for high AODCST concentrations, the diffracted signal has a well-defined fast initial rise due to shallow trap filling and then slow rise due to deep trap filling.

One more issue we would like to address is the illumination history dependence of diffraction efficiency that is directly connected to the presence of deep traps in the system. Figure 3.37 illustrates the difference in history dependence for the same three composites (5CB, $x = 40\,\%$, AODCST, $x = 2\,\%$ and $x = 40\,\%$). The experimental run

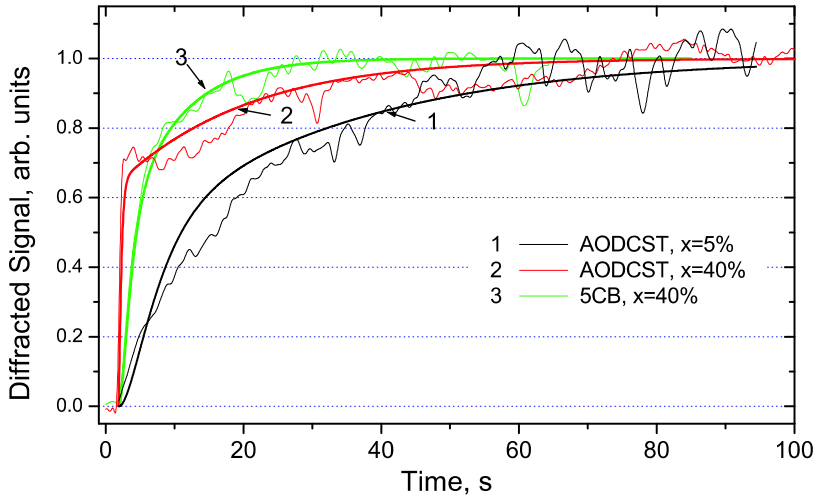

Figure 3.36: Time evolution of diffracted signal as observed in the FWM experiment: experimental data for three composites are superimposed with simulated with no adjustable parameters from Eqs. 2.58 with measured photoelectric parameters transients.

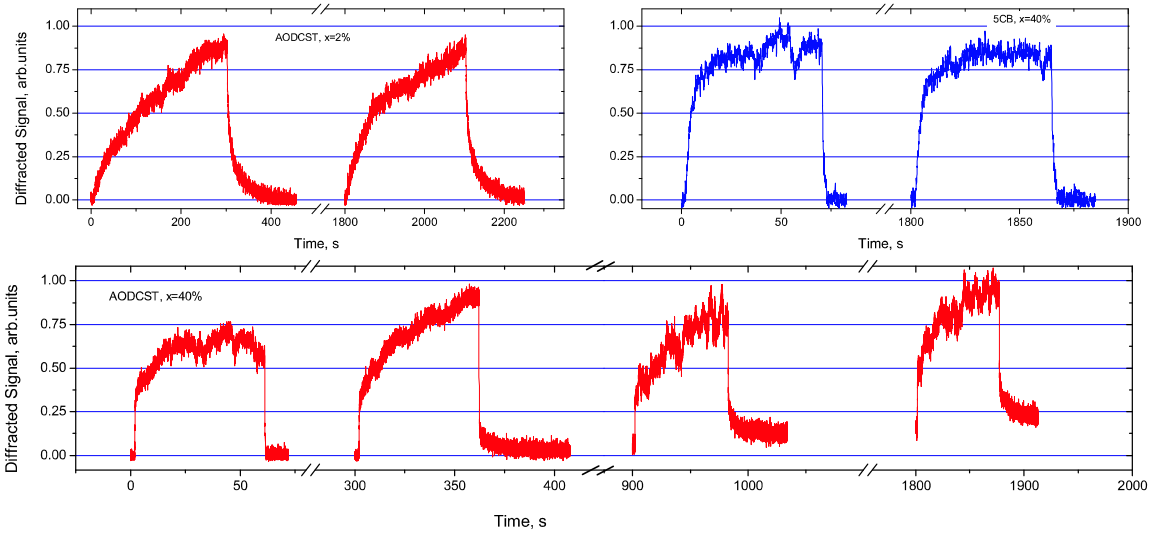

Figure 3.37: Influence of homogeneous illumination prior to FWM experiment on diffracted signals for different composites.

consisted of the following steps. First, the electric field was turned on and kept on for 60 min without any illumination. Then, one of the writing beams was turned on, and then after $\sim 20\,s$ the second writing beam was turned on, and the diffraction grating formation was monitored for $60-300\,s$ depending on the composite. Then, one writing beam was turned off, and the grating decay was monitored. The second writing beam (with the applied field on) illuminated the sample for $5-15\,\text{min}$, and then again the second beam was turned on and grating formation monitored. The cycle was repeated to up to 1 hour of homogeneous illumination. To ensure that the effects we observe in this experiment are due to illumination and not due to internal fields formed by uncompensated traps and impurity ions, we performed a similar experiment but without any illumination between the grating decay and formation measurements. Our results show that all the dependencies described here and shown at Figure 3.37 are due to illumination only. Figure 3.37 shows the transients without any prior illumination and after 30 min of illumination for 5CB, $x = 40\,\%$ and AODCST, $x = 2\,\%$ (the intermediate runs are skipped since they all show a similar behavior). The composites containing 5CB and low concentration of AODCST showed no substantial history dependence because the dynamics involves only shallow traps, and the equilibrium between photogeneration, trapping, detrapping and recombination processes in the system is reached within several seconds and then does not change over a long time scale. In such systems (as for 5CB-containing composites

and for low concentrations of AODCST) the long time scale illumination does not change the density of ionized acceptors and filled traps, and so the initial conditions for the onset of diffraction are the same at any time. Thus, there is no illumination history dependence (Figure 3.37). The behavior is different for the composites with high AODCST concentration. The "fresh" grating decays fast and down to the initial level (0) since the deep traps still do not play a major role at this time scale. As the sample is illuminated for 5 min, and then the grating formation and decay are monitored, the grating did not decay completely at the time scale we observed the signal. So, after 5 min more of homogeneous illumination, the diffracted signal starts to evolve from the level it decayed down to at previous run, and so on (Figure 3.37). This is because after long time illumination the initial conditions for the grating formation change dramatically due to deep trap filling and ionized acceptor growth, so that deep traps noticeably contribute to the grating formation, and thus the complete grating decay requires a much longer time. Due to the relatively slow dynamics of deep trapping and detrapping in comparison to shallow traps, the system does not reach an equilibrium for a long time that is determined by the ratio $\gamma_T M_{T2}/\beta_2$, and the photorefractive dynamics (both rise and decay) depends on the densities of traps and ionized acceptors when the PR experiment is performed. The illumination history dependence can be undesirable for applications requiring long time period grating formation/decay repetition in the presence of illumination and,

thus materials containing deep traps are not suitable for these applications.

3.5.3 Summary of results

Summarizing the results described in Section 3.5, we studied a set of unplasticized composites with 5CB, AODCST and PDCST as chromophores and chromophore concentration dependence of plasticized composites with 5CB and AODCST as chromophores. We applied the modified Schildkraut and Buettner's model [37, 29] introduced in Section 2.2 to compare both photoconductive and photorefractive properties of the composites under investigation. We found that the PR grating time evolution that is due to photoconductivity (space charge field formation) depends on trap densities and depths. There are shallow traps in all composites, intrinsic to PVK. The density of such traps was estimated to be on the order of $10^{26}\,m^{-3}$ which is two orders of magnitude larger than the acceptor density $N_A \sim 10^{24}\,m^{-3}$ and thus all our composites are not expected to show a shallow trap-limited behavior. However, depending on the ionization potential and concentration of the chromophore, the composite either shows or does not show a deep trap -limited behavior. We were able to successfully predict (with no adjustable parameters) the faster photorefractive speed for a variety of composites from the experimentally measured values of the relevant photoelectric rates. The slower PR dynamics was predicted with no adjustable parameters for composites with either no deep traps (composites with 5CB as a chromophore) or with the concentration of available deep traps $M_{T2} \gtrsim N_A$ that corresponds to the AODCST

concentration $x \gtrsim 10\,\%$. For the lower concentration of deep traps (AODCST concentration $x < 10\,\%$), we modelled the slower PR dynamics with an estimated value for the deep trap density and the calculated value of the product $\gamma_T M_{T2}$. For all the composites the slower PR grating formation showed reasonable agreement with experimental data. We studied experimentally and theoretically the influence of deep traps on the illumination history dependence of the photorefractive performance. The modified model seems to describe qualitatively the experimentally observed trends. Based on our study, we can suggest an optimal sensitizer-photoconductor-chromophore composite from the PR dynamical performance point of view. The photoconductor has to provide a high free carrier mobility and be a strong donor with respect to the sensitizer to maximize the photogeneration efficiency. The chromophore has to possess an ionization potential that is within the half width of the density of states of the photoconductor. In this case, if the molecular size of the chromophore is comparable with the size of the photoconductor functional group, so that the intersite distance does not change drastically when the chromophore is inserted into the photoconductor's matrix, the chromophore might participate in the charge generation and transport together with photoconductor. Also, the chromophore should possess a narrow density of states to avoid the formation of deep traps. A problem, however, might arise if we want to optimize both PR dynamic performance and the amplitude of the PR signal because the "ideal" material for dynamic performance may contain reduced

trap densities that will reduce the magnitude of the PR signal. Thus, as usual, in real systems, the composite design should be engineered to meet specific requirements.

Despite some successful predictions we were able to make using the modified model, there are issues to deal with. First of all, the composites with trap densities on the level of $M_T \sim 0.01-1 N_A$ cannot be treated the way elaborated for the case $M_{T1,2} \gg N_A$ in Section 2.3 and applied here. Second, the trapping, detrapping and recombination rates $(\gamma_T, \beta, \gamma)$ that are functions of electric field as accounted for in Eqs. 2.29 do not involve any dependence on the light intensity. Since we observed experimentally that these rates depend on the incident light intensity, it seems that some processes relevant for PR performance are not properly taken into account. Third, it might be helpful to include the effect of the formation of an internal electric field inside the sample due to the filling of uncompensated traps as well as non-neutralized impurity ions. Also, both photoconductivity and photorefractive signals are sensitive to the presence of deep traps in the composite, so that impurities that could serve as deep traps can obscure the performance of a purer system. A final remark is that the Eqs. 2.29 are written for an infinite bulk material and do not take into account the possible effects of electrodes. This requires further study.

3.6 Summary of Chapter 3

In Chapter 3, we considered several experimental techniques used for studies of the photoelectric and photorefractive properties of polymer composites.

For photoconductivity studies, such methods as xerographic discharge (Section 3.3.1), time-of-flight (Section 3.3.2) and DC photocurrent measurements (Section 3.3.3) were described.

For photorefractive studies, the two-beam coupling (Section 3.4.1) and four-wave mixing (Section 3.4.2) techniques were detailed.

We discussed the physical principles of each experimental method, listed all the technical details that can be useful in practise, illustrated the typical data observed in each of the experiments and showed the main points of the data analysis.

We used a number of PVK-based composites to demonstrate the typical behavior of such characteristics of the composite as photogeneration efficiency, mobility, trapping rate and other photoelectric parameters. In terms of the PR performance, the general trends such as temperature, electric field and intensity dependence of both steady-state and dynamic parameters describing the PR grating, were explored.

Finally, the connection between the theory (Chapter 2) and experiments (Chapter 3) was established as we predicted the PR dynamic performance on the basis of photoelectric rates and showed a reasonable agreement of the prediction with the PR experimental data.

Next Chapter is somewhat related to Chapter 3 and is devoted to the electric field induced second harmonic generation (EFISHG). From the first sight, the EFISHG does not have much to do with photorefraction. However, as we repetitively mentioned, the photorefractive effect in polymers includes two main mechanisms: photoconductivity and orientation of the NLO chromophores. The link between EFISHG and the PR effect is that the chromophore orientation can be studied using the EFISHG technique, and in the next Chapter we will consider how it can be done.

References

[1] W. E. Moerner and S. M. Silence. Polymeric photorefractive materials. *Chem. Rev.*, 94(1):127–155, 1994.

[2] S. Schloter, A. Schreiber, M. Grasruck, A. Leopold, M. Kol'chenko, J. Pan, C. Hohle, P. Strohriegl, S. J. Zilker, and D. Haarer. Holographic and photoelectric characterization of a novel photorefractive organic glass. *Appl. Phys. B*, 68(5):899–906, 1999.

[3] T. K. Daubler, R. Bittner, K. Meerholz, V. Cimrova, and D. Neher. Charge carrier photogeneration, trapping and space-charge field formation in pvk-based photorefractive materials. *Phys. Rev. B*, 61(20):13515–13527, 2000.

[4] J. Zhang and K. D. Singer. Homogeneous photorefractive polymer/nematogen composite. *Appl. Phys. Lett.*, 72:2948–2950, 1998.

[5] D. Wright, M. A. Diaz-Garcia, J. D. Casperson, M. DeClue, W. E. Moerner, and R. J. Twieg. High-speed photorefractive polymer composites. *Appl. Phys. Lett.*, 73(11):1490–1492, September 1998.

[6] W. E. Moerner, A. Grunnet-Jepsen, and C. Thompson. Photorefractive polymers. *Annu. Rev. Mater. Sci.*, 27:585–623, 1997.

[7] G. J. Kavarnos and N. J. Turro. Photosensitization by reversible electron-transfer - theories, experimental-evidence, and examples. *Chem. Rev.*, 86:401–449, 1986.

[8] J. Mort and D. Pai. *Photoconductivity and related phenomena*. Elsevier, 1976.

[9] M. Pope and C. Swenberg. *Electronic Processes in Organic Crystals and Polymers*. Oxford University Press, 1999.

[10] J. Mort, G. Pfister, and S. Grammatica. Charge transport and photogeneration in molecularly doped polymers. *Solid State Communications*, 18(6):693–696, 1976.

[11] J. Slowik and I. Chen. Effect of molecular rotation upon charge transport between disordered carbazole units. *J. Appl. Phys.*, 54(8):4467–4473, 1983.

[12] J. C. Scott, L. Th. Pautmeier, and W. E. Moerner. Photoconductivity studies of photorefractive polymers. *J. Opt. Soc. Am. B*, 9(11):2059–2064, 1992.

[13] P. M. Borsenberger and D. S. Weiss. *Organic photoreceptors for xerography*, volume 59 of *Optical engineering*. Marcell Dekker, Inc., New York, 1998.

[14] R. Wolfe, editor. *Applied Solid State Science*. Academic Press, New York, 1975.

[15] M. Pauley, H. Guan, and C. Wang. Poling dynamics and investigation into the behavior of trapped charge in poled polymer films for nonlinear optical applications. *J. Chem. Phys.*, 104:6834, 1996.

[16] J. Mort and G. Pfister. *Electronic properties of polymers*. Wiley, New York, 1982.

[17] S. J. Zilker, M. Grasruck, J. Wolff, S. Schloter, A. Leopold, M. A. Kol'chenko, U. Hoffmann, A. Schreiber, P. Strohriegl, C. Hohle, and D. Haarer. Characterization of charge generation and transport in a photorefractive organic glass: comparison between conventional and holographic time-of-flight experiments. *Chem. Phys. Lett.*, 306(5-6):285–290, 1999.

[18] E. Hendrickx, Y. Zhang, K. B. Ferrio, J. A. Herlocker, J. Anderson, N. R. Armstrong, E. A. Mash, A. Persoons, N. Peyghambarian, and B. Kippelen. Photoconductive properties of pvk-based photorefractive polymer composites doped with fluorinated styrene chromophores. *J. Mater. Chem.*, 9(9):2251–2258, September 1999.

[19] H. Scher and E. W. Montroll. Anomalous transit-time dispersion in amorphous solids. *Phys. Rev. B*, 12:2455–2477, 1975.

[20] L. Schein. Comparison of charge transport models in molecularly doped polymers. *Phil. Mag. B*, 65(4):795–810, 1992.

[21] R. Bube. *Photoconductivity of Solids*. Wiley, 1960.

[22] A. Patsis and D. Seanor, editors. *Photoconductivity in Polymers*. Technomic Publishing Co., Inc., Westport, Conn., 1976.

[23] R. Blum, M. Sprave, J. Sablotny, and M. Eich. High-electric-field poling of nonlinear optical polymers. *J. Opt. Soc. Am. B*, 15(1):318–328, 1998.

[24] P. Blom, M. de Jong, and M. van Munster. Electric-field and temperature dependence of the hole mobility in ppv. *Phys. Rev. B*, 55:R656, 1997.

[25] L. Bozano, S. Carter, J. Scott, G. Malliaras, and P. Brock. Temperature- and field-dependent electron and hole mobilities in polymer light emitting diodes. *Appl. Phys. Lett.*, 74(8):1132–1134, 1999.

[26] T. Daubler, D. Neher, H. Rost, and H. Horhold. Efficient bulk photogeneration of charge carriers and photoconductivity gain in arylamino-ppv polymer sandwich cells. *Phys. Rev. B*, 59:1964, 1999.

[27] J. Schildkraut and Y. Cui. Zero order and first order theory of the formation of space-charge gratings in photoconductive polymers. *J. Appl. Phys.*, 72(11):5055–5061, December 1992.

[28] L. Schein, A. Peled, and D. Glatz. The electric field dependence of the mobility in molecularly doped polymers. *J. Appl. Phys.*, 66(2):686–692, 1989.

[29] O. Ostroverkhova and K. D. Singer. Space-charge dynamics in photorefractive polymers I: Theoretical considerations. *Submitted to J. Appl. Phys.*, 2001.

[30] A. Grunnet-Jepsen, C. L. Thompson, and W. E. Moerner. Systematics of two-wave mixing in a photorefractive polymer. *J. Opt. Soc. Am. B*, 15(2):905–913, February 1998.

[31] C. Walsh and W. E. Moerner. 2-beam coupling measurements of grating phase in a photorefractive polymer. *J. Opt. Soc. Am. B*, 9(9):1642–1647, 1992.

[32] M. Born and E. Wolf. *Principles of optics : electromagnetic theory of propagation, interference and diffraction of light.* Pergamon Press, Oxford, New York, sixth edition, 1980.

[33] J. A. Herlocker, K. B. Ferrio, E. Hendrickx, B. D. Guenther, S. Mery, B. Kippelen, and N. Peyghambarian. Direct observation of orientation limit in a fast photorefractive polymer composite. *Appl. Phys. Lett.*, 74(16):2253–2255, April 1999.

[34] K. S. West, D. P. West, M. D. Rahn, J. D. Shakos, F. A. Wade, K. Khand, and T. A. King. Photorefractive polymer composite trapping properties and link with a chromophore structure. *J. Appl. Phys.*, 84(11):5893–5899, 1998.

[35] Y. Cui, B. Swedek, N. Cheng, J. Zieba, and P. N. Prasad. Dynamics of photorefractive grating erasure in polymeric composites. *J. Appl. Phys.*, 85:38–43, January 1999.

[36] P. Gunter and J.-P. Huignard, editors. *Photorefractive Materials and Their Applications I.* Springer-Verlag, Berlin, 1988.

[37] J. S. Schildkraut and A. V. Buettner. Theory and simulation of the formation and erasure of space-charge field gratings in photoconductive polymers. *J. Appl. Phys.*, 72(5):1888–1893, 1992.

[38] E. Mecher, C. Brauchle, H. H. Horhold, J. C. Hummelen, and K. Meerholz. Comparison of new photorefractive composites based on a poly(phenylene vinylene) derivative with traditional poly(n-vinylcarbazole) composites. *Phys. Chem. Chem. Phys.*, 1:1749, 1999.

[39] A. Grunnet-Jepsen, D. Wright, B. Smith, M. S. Bratcher, M. S. DeClue, J. S. Siegel, and W. E. Moerner. Spectroscopic determination of trap density in -sensitized photorefractive polymers. *Chem. Phys. Lett.*, 291(5-6):553–561, July 1998.

[40] E. Hendrickx, B. Kippelen, S. Thayumanavan, S. Marder, A. Persoons, and N. Peyghambarian. High photogeneration efficiency of charge-transfer complexes formed between low ionization potential arylamine and C_60. *J. Chem. Phys.*, 112(21):9557–9561, 2000.

[41] P. Marcus and P. Siders. Theory of highly exothermic electron transfer reactions. *J. Phys. Chem.*, 86:622, 1982.

[42] A. Goonesekera and S. Ducharme. Effect of dipolar molecules on carrier mobilities in photorefractive polymers. *J. Appl. Phys.*, 85(9):6506–6514, May 1999.

[43] R. Young. Effects of geometrical disorder on hole transport in molecularly doped polymers. *J. Chem. Phys.*, 103(15):6749–6767, 1995.

[44] P. Borsenberger and D. Weiss. *Organic Photoreceptors for Imaging systems.* Marcel Dekker, Inc., 1993.

[45] A. Miller and E. Abrahams. Impurity conditions at low concentrations. *Phys. Rev.*, 120(1):745–755, 1960.

[46] W. E. Moerner, S. M. Silence, F. Hache, and G. C. Bjorklund. Orientationally enhanced photorefractive effect in polymers. *J. Opt. Soc. Am. B*, 11(2):320–330, February 1994.

[47] G. T. Boyd, C. V. Francis, J. E. Trend, and D. A. Ender. Second-harmonic generation as a probe of rotational mobility in poled polymers. *J. Opt. Soc. Am. B*, 8(4):887–894, April 1991.

[48] J. C. Hooker, W. R. Burghardt, and J. M. Torkelson. Birefringence and second-order nonlinear optics as probes of polymer cooperative segmental mobility: Demonstration of debye-type relaxation. *J. Chem. Phys.*, 111(6):2779–2788, August 1999.

[49] M. Abkowitz, M. Stolka, and M. Morgan. Behavior of the drift mobility in the glass transition region of some hole-transporting amorphous organic films. *J. Appl. Phys.*, 52(5):3453–3457, 1981.

[50] M. Abkowitz, H. Bassler, and M. Stolka. Common features in the transport behavior of diverse glassy solids:exploring the role of disorder. *Phil. Mag. B*, 63(1):201–220, 1991.

[51] A. Blythe. *Electrical Properties of Polymers*. Cambridge University Press, 1979.

Chapter 4

Orientational processes in photorefractive polymer composites

4.1 Introduction

In this Chapter, I will describe our studies of the dynamics of nonlinear optical (NLO) chromophore orientation in photorefractive (PR) polymer composites.

For these experiments, we used the same composites as for the photorefractive studies described in Section 3.5. In terms of the orientational properties of the composites, the systems under study are essentially NLO chromophores (guests) introduced into a polymer matrix (host).

As mentioned in previous chapters, the orientation of the NLO chromophores in an electric field is an important part of the PR effect, and the goal of the experiments to be described in this Chapter is to study the chromophore orientational mobility and its influence on the PR performance of the composites.

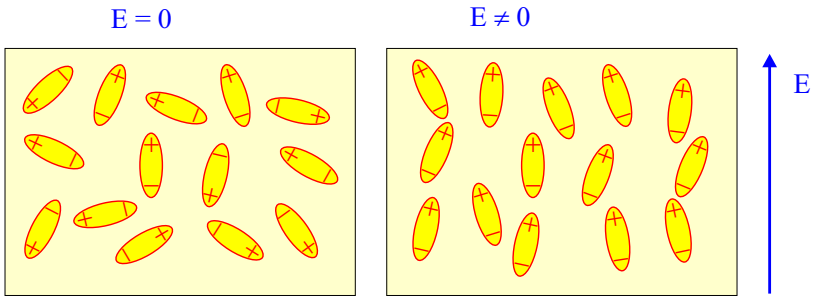

Figure 4.1: NLO chromophore orientation in the external electric field.

One of the requirements for a PR material (see Section 2.1.2) is that the material should be electro-optic. As we discussed in Chapter 1, the material has to be non-centrosymmetric to possess an electro-optic effect. Most PR polymer composites are isotropic unless some effort such as pre-poling is applied to break the inversion symmetry. Thus, for the electro-optic effect to exist, the centrosymmetry of the material needs to be broken. This can be achieved with an applied electric field.

In an external electric field, the NLO chromophores, which for these studies we treat as dipoles, align in the direction of the applied field (Figure 4.1). This alignment changes the symmetry of the composite to $C_{\infty v}$, which then lacks inversion symmetry and, therefore, admits the electro-optic effect.

Also, the orientational enhancement effect in low-T_g PR polymers [1] (refer to Section 2.4), which is *in situ* poling of the dipolar chromophores in the space charge field, is one of the main mechanisms participating in the PR effect.

As we discussed before, PR polymers are potentially useful for dynamic applications such as optical data processing, and that is why the factors limiting the PR

grating formation speed are extensively studied in the literature. In Section 2.1.2, we detailed the processes involved in the formation of the PR grating in PR polymers. In one sentence, the dynamics of the PR effect are determined by (i) how the fast spatially non-uniform space-charge field is generated and (ii) how fast the chromophores orient in this field. The photoconductivity mechanism (i) of space-charge field formation was considered in detail in Chapters 2 and 3. The speed of the chromophore orientation (ii), as mentioned above, is our concern in this Chapter.

4.2 Probes of the chromophore orientational dynamics

The most common experimental methods used for probing chromophore orientational mobility in poled polymers are NLO techniques [2, 3, 4] and ellipsometric techniques [5, 6]. Our goal is not only to measure the speed of chromophore orientation in an electric field, but also to relate the speed measured by either NLO methods or ellipsometry to the speed of PR grating formation.

Ellipsometric (ELP) technique involves a measurement of the changes of the bulk refractive index owing to the induced birefringence and the electro-optic effect. A $+45°$-polarized laser beam is incident at the internal angle $\tilde{\theta}$ upon the PR material, and the transmitted light is probed through a $-45°$ polarizer. A Soleil-Babinet compensator is located between the sample and the polarizer to compensate for the birefringence induced by the non-poled samples. Without an electric field applied, the

chromophores are randomly oriented in the bulk, and the polarization of the incident beam is not affected. Thus, the polarizer blocks all the transmitted light. With the electric field applied, the transmission T_{ELP} through the polarizer is given by [5]

$$T_{ELP} = \sin^2(C_{ELP}\Delta n') \tag{4.1}$$

where $\Delta n' = n_p - n_s$ is the difference between the bulk refractive indices for p- and s-polarization of the incident light, and $C_{ELP} = 2\pi d/\lambda \cos\tilde{\theta}$. Here, λ is the wavelength of incident light, and d is the sample thickness. The similarity of Eq. 4.1 to Eq. 2.59 for the diffraction efficiency $\eta \sim \sin^2(C\Delta n)$ shows that trends in η and T_{ELP} can be directly compared [5, 6]. We will consider the comparison in more detail in Section 4.3.

The drawback of the ELP technique is its low sensitivity compared to the NLO techniques, which limits its application.

Nonlinear optical techniques provide much better signal-to-noise ratios than ellipsometric techniques. This is why one of the NLO techniques, electric field induced second harmonic generation (EFISHG), was our choice for the molecular orientation studies. The next two sections are devoted to the theoretical and experimental aspects of EFISHG.

4.2.1 Electric field induced second harmonic generation: Theory

EFISHG is a well-established technique to determine the second order nonlinear optical response of molecules [7], although the third order nonlinearity contributes in

these circumstances as well.

Generally, EFISHG can be viewed as a third order process that can be described by the nonlinear polarization (see Chapter 1)

$$P_i^{2\omega} = \chi_{ijkl}^{(3)}(-2\omega;\omega,\omega,0)E_j^{\omega}E_k^{\omega}E_l^0 \tag{4.2}$$

where $E_{j,k}$ are the optical fields, and E_l^0 is the applied electric field.

When an electric field is applied to isotropic polymers doped with NLO chromophores, the dipole moments of the chromophores couple to the electric field causing a partial orientation of the dipolar molecules. This breaks the symmetry of the material allowing bulk coherent second harmonic generation. So, Eq. 4.2 can be rewritten in a form that resembles the second order nonlinear effect

$$P_i^{2\omega} = \chi_{ijk}^{(2)}(-2\omega;\omega,\omega)(E^0)E_j^{\omega}E_k^{\omega} \tag{4.3}$$

where the applied electric field dependent second order susceptibility

$$\chi_{ijk}^{(2)}(-2\omega;\omega,\omega)(E^0) = \chi_{ijkl}^{(3)}(-2\omega;\omega,\omega,0)E_l^0$$

has been introduced.

The microscopic (i.e. molecular) analog of Eq. 4.3 is the expression for the molecular dipole moment $p_i^{(2)}$ in terms of the hyperpolarizabilities β_{ijk} and γ_{ijkl} of Eq. 1.4 (refer to Chapter 1) as follows:

$$p_i^{(2)} = \beta_{ijk}f^2(\omega)f(2\omega)E_j^{\omega}E_k^{\omega} + \gamma_{ijkl}f^2(\omega)f(2\omega)f^0E_j^{\omega}E_k^{\omega}E_l^0 \tag{4.4}$$

where the local field factors are given by

$$f^0 = \frac{\varepsilon(n_\omega^2 + 2)}{2\varepsilon + n_\omega^2}, \quad f(\omega) = \frac{n_\omega^2 + 2}{3} \tag{4.5}$$

Here n_ω is the refractive index at light frequency ω, and ε is the static dielectric constant.

Next, we need to establish the connection between the field dependent $\chi^{(2)}_{ijk}(E^0)$ and the molecular susceptibilities β_{ijk} and γ_{ijkl}.

Within a volume V of material, the bulk polarization $\mathbf{P}$ is a sum over the induced dipole moments of the molecules within the volume [7]:

$$\mathbf{P} = \frac{1}{V}\sum_{n=1}^{M} \mathbf{p}_n$$

where M is the number of the NLO chromophores in the volume. Then, the i^{th} cartesian component of the bulk polarization can be expressed in terms of the chromophore dipole moments as

$$P_i = N\langle p^*_{i'}\rangle_i \tag{4.6}$$

where $N = M/V$ is the concentration of the chromophores, and the brackets denote an orientational average

$$\langle p^*_{i'}\rangle_i \equiv \frac{\int d\mathbf{\Omega} G(\mathbf{\Omega}) R_{ii'}(\mathbf{\Omega}) p^*_{i'}}{\int d\mathbf{\Omega} G(\mathbf{\Omega})} \tag{4.7}$$

where $\mathbf{\Omega}$ represents three Euler angles (Figure 4.2), $G(\mathbf{\Omega})$ is the orientational distribution function that describes the orientations of the chromophores, and $R_{ii'}$ is the

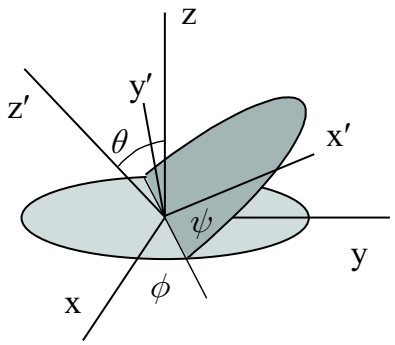

Figure 4.2: Euler angles relating the molecular to the laboratory reference frames.

rotation matrix that connects the dressed molecular frame to the laboratory frame given by

$$\overleftrightarrow{R}= \begin{pmatrix} \cos\phi\cos\psi - \cos\theta\sin\phi\sin\psi & -\cos\theta\cos\psi\sin\phi - \cos\phi\sin\psi & \sin\theta\sin\phi \\ \cos\psi\sin\phi + \cos\theta\cos\phi\sin\psi & \cos\theta\cos\phi\cos\psi - \sin\phi\sin\psi & -\cos\phi\sin\theta \\ \sin\theta\sin\psi & \cos\psi\sin\theta & \cos\theta \end{pmatrix}$$

Now we introduce a thermodynamic model of NLO chromophore-doped isotropic polymer that is poled with an electric field E_0 above the glass transition temperature T_g of the system. In the thermodynamic model, the chromophores are assumed to freely rotate in response to the applied electric field, so that the orientational distribution function of an ensemble of freely rotating dipoles is given by the Gibbs distribution [7]

$$G(\mathbf{\Omega}, E_0) = \frac{\exp[\frac{\mathbf{m}^*\cdot\mathbf{E_0}}{kT}]}{\int d\mathbf{\Omega}\exp[\frac{\mathbf{m}^*\cdot\mathbf{E_0}}{kT}]} \tag{4.8}$$

where $\mathbf{m}^*$ is the dressed dipole moment of a molecule in the ensemble, and includes local field corrections arising from the poling field E_0, T is the temperature of the

system, and k is Boltzmann's constant.

Then, in the limit of low electric fields

$$\exp[(\mathbf{m}^* \cdot \mathbf{E_0})/kT] \approx 1 + (\mathbf{m}^* \cdot \mathbf{E_0})/kT,$$

so, combining Eqs. 4.6, 4.7 and 4.8, we can rewrite the polarization P_i as follows

$$\begin{aligned} P_i &= \frac{N}{\int d\mathbf{\Omega}} \int d\mathbf{\Omega}\{1 + m^*_{l'} R_{l'l}(E_0)_l\}[\beta_{i'j'k'} R_{ii'} R_{jj'} R_{kk'} f^2(\omega) f(2\omega) E^\omega_j E^\omega_k \\ &\quad + \gamma_{i'j'k'l'} R_{ii'} R_{jj'} R_{kk'} R_{ll'} f^2(\omega) f(2\omega) f^0 E^\omega_j E^\omega_k E^0_l] \end{aligned} \tag{4.9}$$

For the simplest case of the optical fields parallel to the applied field ($\|$ z-axis in Figure 4.2), carrying out the integral of Eq. 4.9 yields the electric field dependent susceptibility $\chi^{(2)}_{zzz}(E_0)$ of Eq. 4.3 [7]:

$$\chi^{(2)}_{zzz}(E_0) = N f^0 f^2(\omega) f(2\omega) \left(\gamma + \frac{\beta m^*}{5kT}\right) E_0 \tag{4.10}$$

where

$$\gamma = \frac{1}{15} \sum_{u,v=x,y,z} (2\gamma_{uuvv} + \gamma_{uvvu})$$

and

$$\beta m^* = \frac{1}{3} \sum_{u,v=x,y,z} (2\beta_{uuv} m^*_v + \beta_{uvv} m^*_u).$$

In our experimental geometry which is to be described in the next section, it is not only $\chi^{(2)}_{zzz}(E_0)$ but rather a mixture of different components of the $\chi^{(2)}(E_0)$-tensor that contributes, and the measured quantity is the intensity of second harmonic light $I(2\omega) \sim P^2(2\omega) \sim (\chi^{(2)})^2$ that combines all the components. However, we are

interested in the transitional characteristics rather than the steady-state ones, and thus, the steady-state absolute values are not important for our studies.

The important point is that the component χ_{zzz} of Eq. 4.10, and, similarly, the other components of the χ-tensor, contains two separate contributions - from the second order polarizability β and the third order polarizability γ. The significance of this division for orientational dynamics studies is that the third order (γ) electronic contribution appears instantaneously when the electric field is applied, even in centrosymmetric materials, while the second order (β) contribution arises as the chromophores get aligned and is a feature of non-centrosymmetric materials.

We will not go into detail in considering the combinations of the $\chi^{(2)}$-tensor components that contribute to the second harmonic signal in our experimental geometry. Instead, we simplify our approach and assume that the second harmonic response of the material to the applied electric field, measured with EFISHG technique, is derived from Eq. 4.10

$$I(2\omega) \sim \left(\gamma + \frac{\beta m^*}{5kT}\right)^2 E_0^2 \tag{4.11}$$

As mentioned above, the time evolution of the second harmonic signal $I(2\omega)(t)$ can be considered as a two-step process: first, the instantaneous signal due to the γ-part appears; then the slow signal due to chromophore orientation (the β-part) which is of interest builds up. In practice, the γ-part of the signal is at least an order of magnitude smaller than the orientational part [7]. However, analyzing the experi-

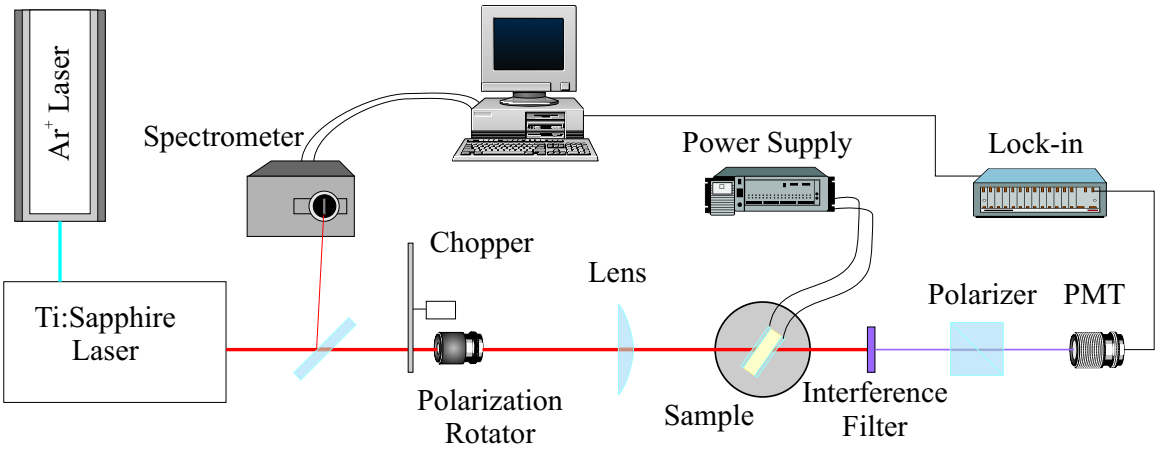

Figure 4.3: Experimental set-up for EFISHG measurements.

mental transients, one should keep in mind a possible contribution from the third order susceptibility γ.

4.2.2 Electric field induced second harmonic generation: Experiment

The experimental set-up used in our EFISHG studies is shown in Figure 4.3. We used a mode-locked Ti:Sapphire laser pumped with an Ar^+ laser. At the pump power of $6\,mW$, the average output power of the Ti:Sapphire laser was $\sim 0.5\,mW$. The pulse duration was $\sim 50\,fs$, and the wavelength range $\sim 760-800\,nm$. The Ti:Sapphire laser output is not monochromatic since the spectral bandwidth $\Delta\omega$ is inversely proportional to the pulse duration Δt which reflects the Heisenberg uncertainty principle ($\Delta\omega\Delta t \sim 1$).

The light of fundamental frequency ω was obliquely incident on the sample (refer to Chapter 5 for explanation), and the second harmonic (2ω) signal generated in the

sample upon application of the electric field was detected with a photomultiplier tube (PMT). To minimize low-frequency noise, we implemented lock-in detection using the fundamental light modulated with a chopper. For polarization measurements, a polarization rotator before the sample and a polarizer between the sample and the PMT were used. A filter that blocked the fundamental frequency ω and transmitted the second harmonic signal light of 2ω was placed after the sample.

For the EFISHG measurements, we used the same composites and essentially the same samples (polymer film between two ITO slides) as for the photorefractive studies. Sample preparation was described in Section 3.2.2.

The experimental run was as follows. First, with no applied electric field, the noise level was recorded. Then, the electric field was turned on, and the rise of the second harmonic signal was monitored. When the signal reached a steady-state, the electric field was switched off, and the second harmonic decay observed. The switching time of the power supply, a Keithley electrometer which we used as a voltage source, was below $5\,ms$. This is at least an order of magnitude faster than the orientation times obtained from the EFISHG transients in our composites. Thus, we ensured that our measurements are not the artifacts due to equipment, but are indeed related to the chromophore orientation. The experiment was performed at electric fields typically from $5-60\,V/\mu m$.

According to symmetry considerations, our system, which under applied electric

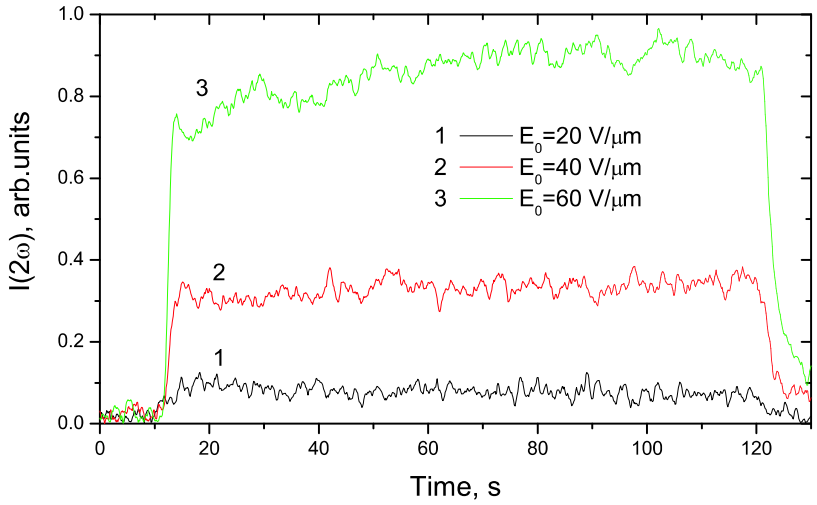

Figure 4.4: Typical data in the EFISHG experiment for the composite PVK(79%)-/C_{60}(1%)/5CB(20%) for various electric fields.

field is expected to possess the $C_{\infty v}$ symmetry, should exhibit only p-polarized second harmonic light (see Chapter 5 for details). In other words, from four possible combinations of the incident and second harmonic (SH) light linear polarizations (*p*-fundamental, *p*-SH; *p*-fundamental, *s*-SH; *s*-fundamental, *p*-SH, and *s*-fundamental, *s*-SH), only *pp* and *sp* configurations produce the SH signal in a material with $C_{\infty v}$ symmetry. Since in our polarization measurements, we observed only *pp* and *sp* signals, we confirmed that the symmetry of our poled polymer composite is indeed as expected.

Typical data taken in *pp*-configuration in the composite PVK(79%)/C_{60}(1%)-/5CB(20%) is shown in Figure 4.4 for various applied electric fields. As expected from Eq. 4.11, the amplitude of the second harmonic intensity is quadratic in electric field.

4.3 Relation of the orientational times measured in EFISHG to the ones observed in the photorefractive effect

As mentioned before, it is important to relate the orientational response as measured in the EFISHG experiment to the photorefractive grating dynamics due to orientational processes.

For this, we consider the chromophore orientation as the reorientation of a rigid dipolar molecule in an isotropic medium described by Debye rotational diffusion [8]. In this model, the dynamics of the orientational distribution function $f(\theta, t)$ is given by the classical rotational diffusion equation:

$$\frac{1}{D}\frac{\partial f(\theta,t)}{\partial t} = \frac{1}{\sin\theta}\frac{\partial}{\partial\theta}\left\{\sin\theta\left[\frac{\partial}{\partial\theta}f(\theta,t) + \frac{1}{kT}\frac{\partial U}{\partial\theta}f(\theta,t)\right]\right\} \tag{4.12}$$

where D is the rotational diffusion constant. U is the interaction energy between the electric field E_0 and the dipolar molecule given by $U = mE_0\cos\theta$, where m is the molecular dipole moment.

The orientational dynamics as measured by various techniques can be expressed through the n^{th} order moments $\langle\cos^n\theta(t)\rangle$ of the orientational autocorrelation functions (OACF) $\Phi_n(t)$ [8]. For example, in the low electric field limit ($mE_0 \ll kT$), the susceptibility $\chi^{(2)}(E_0)$ determined in the EFISHG experiment is proportional to the first moment:

$$\chi^{(2)}(E_0) \sim \Phi_1(t) \sim \langle\cos\theta(t)\rangle,$$

and the birefringence $\Delta n(t)$ is proportional to the second moment:

$$\Delta n(t) \sim \Phi_2(t) \sim \langle \cos^2 \theta(t) \rangle.$$

So, the time evolution of the EFISHG signal is determined by the dynamics of the first moment

$$I(2\omega)(t) \sim (\chi^{(2)}(E_0))^2 \sim \Phi_1^2(t).$$

The rise transient of the first moment is given by

$$\Phi_1(t) \sim (1 - \exp[-D_1 t]),$$

where $D_n = n(n+1)D$ and thus, $D_1 = 2D$. Therefore, the rise of $\sqrt{I(2\omega)(t)}$ is described by the speed $D_1 = 2D$.

In the ellipsometry measurements, the rise of the birefringence $\Delta n(t)$ is described in terms of the second moment as follows

$$\Delta n(t) \sim \Phi_2(t) \sim 1 - \frac{3P/Q}{2(P/Q+1)} \exp(-D_1 t) + \frac{P/Q-2}{2(P/Q+1)} \exp(-D_2 t)$$

where $P = m^2/(kT)^2$ and $Q = \Delta\alpha/(kT)$. Here, $\Delta\alpha = \alpha_{33} - \alpha_{11}$, where $\alpha_{11,33}$ are the molecular polarizabilities along the 1 and 3 axes of the molecule. So, the rise of the electric field induced birefringence is described by a bi-exponential with the inverse time constants given by $D_1 = 2D$ and $D_2 = 6D$.

The temporal development of the orientationally enhanced diffraction efficiency η as measured in the four-wave mixing (FWM) experiment discussed in the previous

chapters, can be also expressed in terms of the constants D_n [6]:

$$\eta \sim \{A_1[1-\exp(-D_1 t)] + A_2[1-\exp(-D_2 t)]\}^2$$

Then, the orientational dynamics of the $\sqrt{\eta}$ is also given by two inverse time constants - $D_1 = 2D$ and $D_2 = 6D$.

Summarizing the rotational diffusion approach, from the ellipsometry measurement (ELP) described in Section 4.2, both constants D_1 and D_2 can be determined from the birefringence rise and compared to the corresponding constants determined from the diffraction efficiency rise. From the EFISHG experiment, the constant D_1 can be determined and compared to the slower inverse time constant of the diffraction efficiency. The faster component D_2 can be calculated from the theory assuming that the relation $D_2 = 3D_1$ is valid.

The problem of the comparison described above is that the diffraction efficiency dynamics depends on both photoconductivity and orientational speed, and these two mechanisms are inseparable. So, in practice, the diffraction efficiency rise is fitted with a bi-exponential function (see Section 3.4), in which one component of the PR speed is determined by the photoconductivity, and another one by the orientation. Therefore, the two inverse time constants - D_1 and D_2 will be mixed into one in between D_1 and $D_2 = 3D_1$ due to orientation when the diffraction efficiency data is analyzed. Another problem is that the orientational speed as observed in both EFISHG and FWM, is electric field dependent. The only electric field in the EFISHG

experiment is the applied field. However, in the FWM experiment, the electric fields that matter for orientational purposes are both the projection of applied field on the grating vector and the space charge field. Therefore, the relatively easy theoretical comparison of the orientational dynamics observed with different techniques turns into a complicated task. Regardless of all the problems listed, an order of magnitude estimate of the orientational speed can be made quite accurately, as we demonstrate next.

As an example of relating the orientational dynamics observed in EFISHG and FWM experiments, we consider the example of the composites PVK(79%)/C_{60}(1%)-/5CB(20%) and PVK(49%)/C_{60}(1%)/BBP(45%)/AODCST(5%) (Figure 4.5a,b). The EFISHG measurements were performed at the electric field E_a equal to the projection of applied electric field on the grating vector $\tilde{E}_a$ in the FWM measurements. The composite PVK(79%)/C_{60}(1%)/5CB(20%) is a relatively high T_g composite ($T_g \sim 80^\circ C$), so that at room temperature the chromophore orientation is expected to be slower than for the composite PVK(49%)/C_{60}(1%)/BBP(45%)/AODCST(5%) which has $T_g \sim 20^\circ C$. This is supported by the experimental data: the single exponential fits of the $\sqrt{I(2\omega)(t)}$ shown in Figure 4.5 yield the coefficients $D_1 = 0.48 \pm 0.02\, s^{-1}$ and $D_1 = 19.6 \pm 2.6\, s^{-1}$ for these two composites respectively.

Let us now analyze the diffracted signal as measured in the FWM experiment. For both composites, we fit the transients $\sqrt{\eta(t)}$ with a bi-exponential function

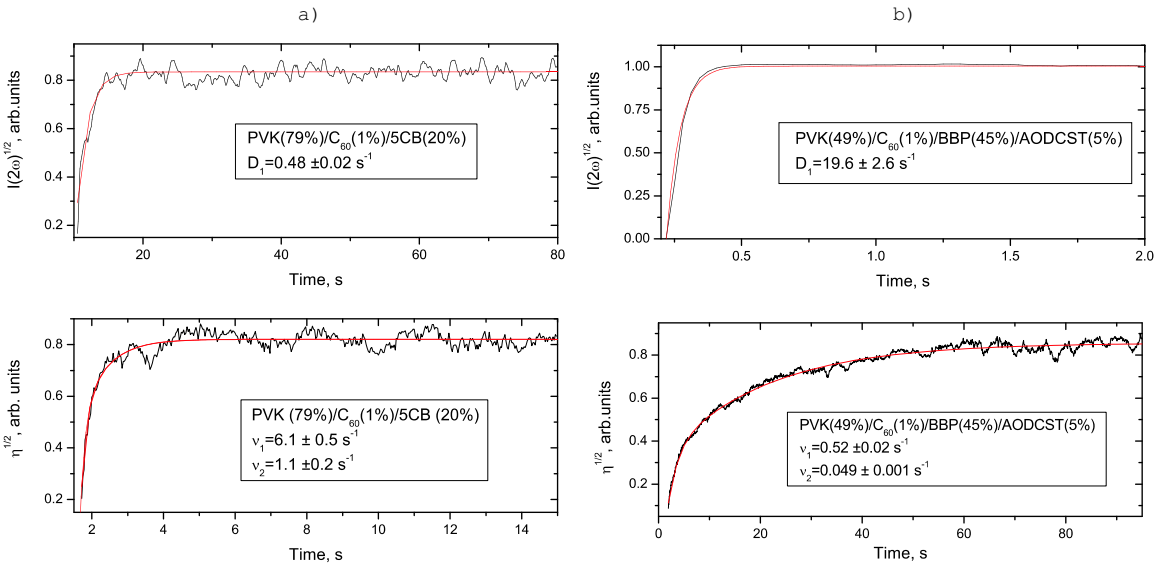

Figure 4.5: Example of data analysis for orientational dynamics studies: a) high-T_g composite PVK(79%)/C_{60}(1%)/5CB(20%) at $E_a = 30V/\mu m$; b) low-T_g composite PVK(49%)/C_{60}(1%)/BBP(45%)/AODCST(5%) at $E_a = 10V/\mu m$.

$\sqrt{\eta(t)} \sim (1 - a\exp[-\nu_1 t] - (1-a)\exp[-\nu_2 t])$. For the transient shown in Figure 4.5a (composite PVK(79%)/C_{60}(1%)/5CB(20%)), the fit yields $\nu_1 = 6.1 \pm 0.5\, s^{-1}$ and $\nu_2 = 1.1 \pm 0.2\, s^{-1}$. Comparing these constants to the orientational constant D_1 for this composite, we conclude that while the faster component ν_1 is much larger than the orientational speed $D_1 = 0.48\, s^{-1}$, the slower component ν_2 is rather close. Indeed, the faster component ν_1 is intensity dependent and is attributed to photoconductivity. The slower component ν_2 is intensity independent and could be attributed to the chromophore orientation. As we discussed above, the average orientational speed as measured in the FWM experiment can yield values ranging from D_1 to $D_2 = 3D_1$. The constant $\nu_2 = 1.1\, s^{-1}$ fits in the range of 0.48–1.44 s^{-1}, which confirms its orientational

nature.

For the transient shown in Figure 4.5b (composite PVK(49%)/C_{60}(1%)/ BBP(45%)/AODCST(5%)), the $\sqrt{\eta(t)}$ bi-exponential fit yields $\nu_1 = 0.52 \pm 0.02\, s^{-1}$ and $\nu_2 = 0.049 \pm 0.001$. If one compares these constants to the orientational speed D_1 determined from EFISHG, one concludes that since the orientational speed is much higher than both ν_1 and ν_2 photorefractive speed components, none of these is attributed to orientation. Indeed, as our FWM experiments showed, both ν_1 and ν_2 are intensity dependent and determined by the photoconductivity.

In PR polymer composites, the EFISHG technique can be used not only for the orientational dynamics studies, but also for elucidating the processes related to the internal fields forming in the material. In the next section, I will describe one such EFISHG experiment which we performed in PR polymers.

4.4 EFISHG study of internal electric fields

As considered in Section 4.2.1, the intensity of the second harmonic signal measured in EFISHG experiments is quadratic in electric field (Eq. 4.11). Therefore, this experiment is very sensitive to electric field changes. This property led to the idea of probing the space charge fields formed in the material by the EFISHG technique.

Kim *et al.* used second harmonic generation for a space-charge field measurement in the photorefractive (PR) crystal $LiNbO_3$ doped with MgO [9]. It appears that

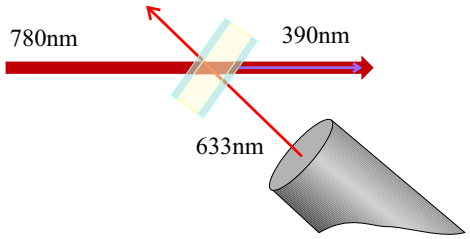

Figure 4.6: Modified EFISHG scheme for the space-charge field measurements.

similar studies in photorefractive polymers have not been reported in the literature. Our studies are currently in progress, and in this section I will present the work we have done so far on this topic.

As discussed in Chapters 2 and 3, photorefractive grating formation involves different processes that occur in the material under the interfering optical beams. Since originally we set up the EFISHG experiment to probe the chromophore reorientation in the PR polymer composites, it was reasonable to check whether the presence of light other than the Ti:Sapphire laser beam used for the EFISHG measurements (see Section 4.2.2) affects the orientational processes. In particular, we were interested in how the HeNe light of $\lambda = 633\,nm$ used for our PR measurements influences the chromophore orientational speed as measured by the EFISHG. Accordingly, we added the HeNe laser to the EFISHG set-up as shown in Figure 4.6. The measurement we performed included the following. First, with the HeNe light blocked, we applied an electric field and monitored the rise of the second harmonic (SH) signal due to the chromophores aligning in the electric field. Then, the electric field was turned off, and the SH signal decay was observed. Second, the HeNe light was allowed through,

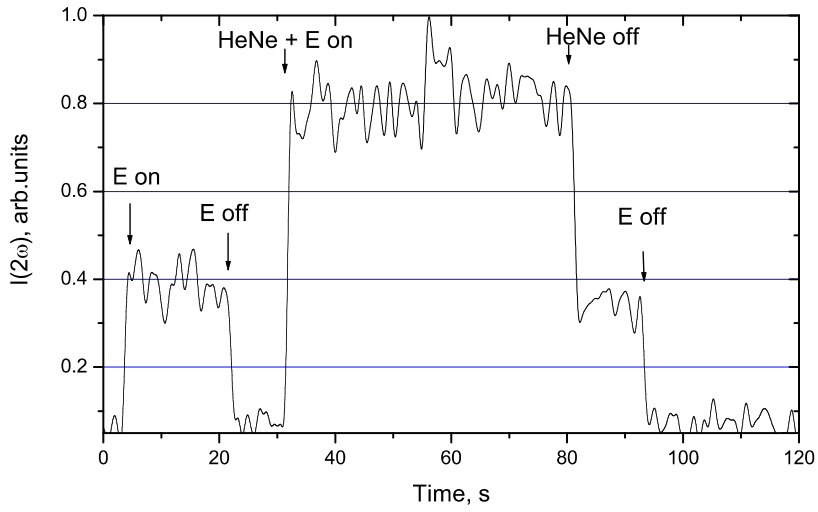

Figure 4.7: Illustration of the HeNe light influence on the second harmonic signal in the composite PVK(49%)/C_{60}(1%)/BBP(10%)/5CB(40%) at the external field $E_0 = 15\,V/\mu m$.

and the experiment was repeated in the presence of the HeNe light.

What we expected to see was the difference in the orientational speed with and without HeNe light. The reason for such an expectation was that since the PR composites are photoconductive, the charge generated with the HeNe light would change the environment (essentially, creating local electric fields) around the chromophores and, therefore, modify their orientational mobilities. In practice, we did not find a substantial difference in the orientational speed. However, we found that the second harmonic signal was enhanced in the presence of HeNe light as shown in Figure 4.7. The possibilities to explain this behavior included:

- The chromophore alignment improves.

  Since the intensity of the second harmonic is proportional to the square of the

first moment of the OACF (see the previous section) $I(2\omega) \sim (\langle \cos\theta \rangle)^2$, the more chromophores align along the direction of the applied field, the larger the intensity $I(2\omega)$. The alignment can be checked fairly easily by performing polarization measurements as will be detailed in Chapter 5. In one sentence, the average molecular tilt angle θ can be determined from the ratio of intensities measured in *sp*- and *pp*-polarization geometries. Our measurements showed that the chromophore alignment did not change in the presence of HeNe light.

- The effective hyperpolarizabilities β, γ changed due to the change in local field in the presence of HeNe light.

  In the previous section we established the connection between the intensity $I(2\omega)$ measured in EFISHG and the hyperpolarizabilities β and γ (Eq. 4.11). If the hyperpolarizabilities changed, we would be able to detect the changes in linear absorption in the presence of electric field. We did not see any changes in absorption which rules out this possibility.

- The electric field changes.

  So far, when we studied chromophore orientation by the EFISHG technique, we considered that the chromophores are aligned in the applied field E_0. However, as we mentioned before, the PR polymer composites are prone to a "parasite", as we called it in Chapter 3, space-charge field formation. This is essentially

the screening of the external electric field due to uncompensated trap filling with injected charge and non-neutralized ionic build-up at the electrodes [10]. When the HeNe light is incident, free holes are generated, they get transported to the electrode and partially recombine with the impurity ions that screen the electric field. Also, the C_{60}^{-} anions that are created (refer to Chapter 2) in the photogeneration process, partially compensate the trapped charge. So, the electric field partially loses its screening, and the intensity of the second harmonic ($I(2\omega) \sim E^2$) increases.

This possibility is the most plausible of all listed, and now we provide some evidence that supports this statement.

First of all, it is obvious that such an enhancement effect in the presence of HeNe light is a result of charge photogeneration and transport. This is based on the observation that the composites without a sensitizer (C_{60}) did not exhibit the enhancement. Also, the effect was not observed in the composites in which the photoconductor poly(N-vinyl-carbazole) (PVK) was replaced with a non-photoconductor poly(methyl-methacrylate) (PMMA). In addition, the enhancement increased as a function of HeNe light intensity, applied electric field and temperature, which corresponds to the trends observed in the photoconductivity.

Second, the largest enhancement was obtained in samples with high plasticizer or chromophore content. As we discussed in Section 3.5, upon application of the

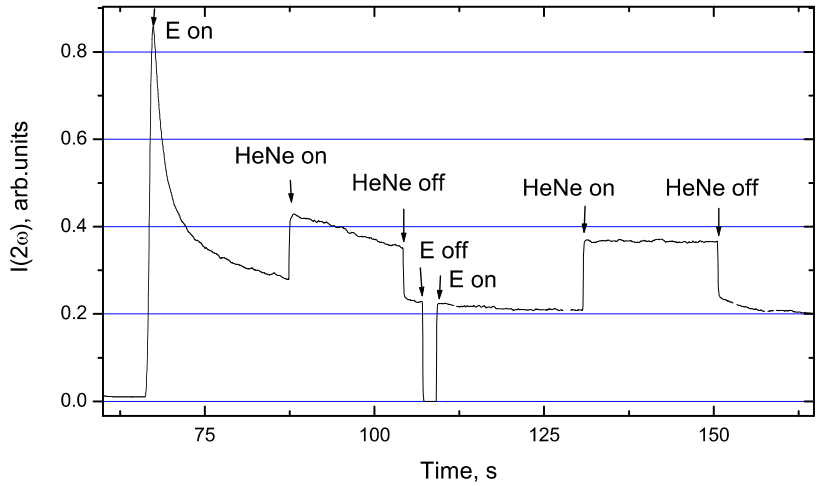

Figure 4.8: Enhancement effect in the presence of HeNe light as observed in the composite PVK(49%)/C_{60}(1%)/BBP(45%)/AODCST(5%) at applied electric field of $10\,V/\mu m$.

electric field, such composites exhibit high dark current (see Figure 3.15) due to ionic impurities moving towards the electrodes and uncompensated trap filling with injected charge. Therefore, in such composites, the screening of the applied field is larger than in "unplasticized" composites, and so that the effect due to HeNe light is observed more readily.

Third, let us analyze the following experimental run as illustrated for the highly plasticized composite PVK(49%)/C_{60}(1%)/BBP(45%)/AODCST(5%) (Figure 4.8). At time $t = 65\,s$, the electric field is applied, and the chromophores orient with the inverse time constant (orientational speed) $D_1 \sim 20\,s^{-1}$. In the meantime, the impurity ions start to move towards the opposite electrodes and build-up, creating the internal field that reduces the total electric field in the sample. This reduction

is accompanied by the reduction in the second harmonic signal observed (the peak in Figure 4.8). At $t = 90\,s$, the HeNe light is turned on, partially compensating the charge that screens the applied electric field, as we discussed above. The HeNe light is turned off at $t = 103\,s$, the screening again becomes uncompensated, and the second harmonic intensity reduces. The electric field is turned off ($t = 108\,s$) and then turned on again ($t = 110\,s$), and the peak that appeared in the beginning ($t = 65\,s$) does not appear which indicates that the internal electric field has reached equilibrium.

Work is currently in progress to quantify the observed effect.

4.5 Summary of Chapter 4

In this Chapter, we considered how chromophore orientation in polymer composites under applied electric field can be studied with EFISHG technique. We demonstrated that the chromophore reorientation in the low-T_g composites is faster than in the high-T_g composites as reflected in the second harmonic generation rise when the electric field is applied.

The relation between the orientational speed as measured in the FWM holographic experiment and EFISHG experiment was established. This is useful for the analysis of the chromophore orientational contribution to the PR dynamics.

A simple theoretical relationship between the orientational dynamics as observed in various experiments was established. However, in practice it is not an easy task

to establish this relationship due to many side effects not taken into account in the theoretical description. For example, the rotational diffusion theory is based on the orientation gas model which may not hold for the high-T_g composites when measured at room temperature. Also, the screening of the external electric field and the entanglement of the photoconductive and orientational processes in the PR polymer composites makes the studies more complex. Despite these difficulties, the orientational dynamics as studied by EFISHG, birefringence and PR experiments, can be directly compared.

Also, as we showed, the sensitivity of the EFISHG technique allows one to study various processes in the chromophore-doped polymers, such as internal electric field formation inside the material, and thus, can be used as an effective probe of material properties.

References

[1] W. E. Moerner, S. M. Silence, F. Hache, and G. C. Bjorklund. Orientationally enhanced photorefractive effect in polymers. *J. Opt. Soc. Am. B*, 11(2):320–330, February 1994.

[2] G. T. Boyd, C. V. Francis, J. E. Trend, and D. A. Ender. Second-harmonic generation as a probe of rotational mobility in poled polymers. *J. Opt. Soc. Am. B*, 8(4):887–894, April 1991.

[3] A. Dhinojwala, G. K. Wong, and J. M. Torkelson. Rotational reorientation dynamics of disperse red 1 in polysterene: α-relaxation dynamics probed by second harmonic generation and dielectric relaxation. *J. Chem. Phys.*, 100:6046–6054, 1994.

[4] C. H. Wang, S. H. Gu, and H. W. Guan. Polar order and relaxation of second order nonlinear optical susceptibility in an electric field polarized amorphous polymer. *J. Chem. Phys.*, 99:5597–5604, 1993.

[5] E. Mecher, C. Brauchle, H. H. Horhold, J. C. Hummelen, and K. Meerholz. Comparison of new photorefractive composites based on a poly(phenylene vinylene) derivative with traditional poly(n-vinylcarbazole) composites. *Phys. Chem. Chem. Phys.*, 1:1749, 1999.

[6] R. Bittner, C. Brauchle, and K. Meerholz. Influence of the glass transition temperature and the chromophore content on the grating buildup dynamics of poly(n-vinylcarbazole)-based photorefractive polymers. *Appl. Opt.*, 37:2843–2851, 1998.

[7] M. G. Kuzyk and C. W. Dirk, editors. *Characterization Techniques and Tabulations for Organic Nonlinear Optical Materials*, volume 60 of *Optical Engineering*. Marcel Dekker, New York, 1998.

[8] J. C. Hooker, W. R. Burghardt, and J. M. Torkelson. Birefringence and second-order nonlinear optics as probes of polymer cooperative segmental mobility: Demonstration of debye-type relaxation. *J. Chem. Phys.*, 111(6):2779–2788, August 1999.

[9] B. G. Kim, M. K. Rhee, and M. Cha. Simple measurement of space-charge field in a $LiNbO_3$ crystal doped with 0.65 mol. % MgO using second harmonic generation. *Opt. Comm.*, 173:377–380, 2000.

[10] M. Pauley, H. Guan, and C. Wang. Poling dynamics and investigation into the behavior of trapped charge in poled polymer films for nonlinear optical applications. *J. Chem. Phys.*, 104:6834, 1996.

Chapter 5

Second harmonic generation studies of polymers and liquid crystals

5.1 Introduction

In this Chapter I will describe several studies of properties of polymer films and liquid crystal (LC) monolayers using second harmonic generation (SHG) techniques.

SHG is a special case of the three-wave mixing process, in which a wave with frequency 2ω is created as result of the nonlinear optical interaction between two waves of frequency ω. Section 5.2 will be devoted to the theoretical background of SHG.

The most common use of SHG is frequency doubling of the output of a fixed-frequency laser, *i.e.* converting the laser output into a different spectral region. For example, inorganic frequency-doubling crystals, such as KDP, are routinely used to convert the $1.06\,\mu m$ output of the Nd:YAG laser to an output of $532\,nm$.

In addition, SHG has proved an efficient probe of the microscopic properties of the materials [1].

As mentioned in Chapter 1, SHG occurs only in non-centrosymmetric bulk materials or at surfaces or interfaces where the symmetry is necessarily broken [1]. In Section 5.3, I will discuss how materials that belong to different point symmetry groups can be studied by SHG. The characteristic SHG behavior for several symmetry groups that are of interest for organic optical materials will be considered.

In Sections 5.4.1 and 5.4.2, I will describe our SHG experimental studies of polymer Langmuir-Blodgett films and LC monolayers.

5.2 SHG: Theoretical background

In this section, I will introduce some theoretical background that is necessary to perform the SHG experiment and data analysis.

The theoretical treatment of SHG was introduced by Armstrong *et al.* [2] in 1962. Here I will present its main points.

An optical beam with electric field given by

$$E_1(z,t) = A_1(z)e^{[i(k_1 z - \omega_1 t)]} + c.c.$$

is incident upon a medium for which the second order nonlinear susceptibility $\chi^{(2)}$ is nonzero (Figure 5.1). Here $k_1 = n_\omega \omega/c$ is the wave vector, and $A_1(z)$ is the slowly varying amplitude of the wave. According to Eq. 1.1, the nonlinear polarization

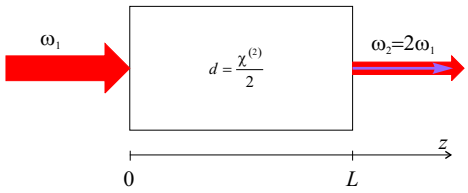

Figure 5.1: Schematic representation of second harmonic generation.

density created in such a medium is $P_2(z,t)=\chi^{(2)}E_1^2(z,t)$ which leads to the formation of a wave with frequency $\omega_2=2\omega_1$ described by the electric field

$$E_2(z,t) = A_2(z)e^{[i(k_2z-\omega_2t)]},$$

where $k_2=2n_{2\omega}\omega/c$.

The wave $E_2(z,t)$ starts to interact with the pump wave $E_1(z,t)$ creating the nonlinear polarization density $P_1(z,t)=2\chi^{(2)}E_1^*(z,t)E_2(z,t)$. Expressing the polarization density as $P_j(z,t)=P_j(z)\exp[-i\omega_j t)]+c.c.$, with $j=1,2$, we can rewrite the polarization densities $P_{1,2}(z,t)$ as [3]

$$P_1(z) = 4dA_2A_1^*e^{i(k_2-k_1)z} \tag{5.1}$$

$$P_2(z) = 2dA_1^2e^{2ik_1z}$$

where the notation $d=\chi^{(2)}/2$ was introduced.

Then, substituting Eqs. 5.1 into Maxwell's equations (Eq. 1.2), we obtain the coupled-amplitude equations for the two frequency components:

$$\frac{dA_1}{dz} = \frac{8\pi i\omega_1^2 d}{k_1c^2}A_2A_1^*e^{-i\Delta kz} \tag{5.2}$$

$$\frac{dA_2}{dz} = \frac{4\pi i\omega_2^2 d}{k_2c^2}A_1^2e^{i\Delta kz}$$

where $\Delta k = 2k_1 - k_2$.

In the undepleted-pump approximation ($A_1 = const$), the equation for A_2 can be integrated immediately to obtain an expression for the spatial dependence of the second harmonic field amplitude. Introducing the intensity of the waves as

$$I_{1,2} = \frac{n_{\omega_{1,2}} c}{2\pi} |A_{1,2}|^2,$$

we obtain the second harmonic intensity

$$I_2 = \kappa^2 I_1^2 L^2 \mathrm{sinc}^2(\Delta k L/2) \tag{5.3}$$

where $\kappa = \frac{4\pi i \omega_2^2 d}{k_2 c^2}$ is the coupling constant.

The expression Eq. 5.3 predicts a dramatic decrease in the second harmonic intensity when the condition of perfect phase matching, $\Delta k = 0$, is not satisfied. Such behavior was first observed experimentally by Maker *et al.* [4] in 1962. Their experiment involved focusing the output of a pulsed ruby laser onto a single crystal of quartz and measuring how the intensity of the SHG signal varied as the crystal was rotated, thus varying the effective path length L through the crystal.

Since 1970, the NLO coefficients d_{ijk} associated with SHG are measured almost exclusively by the Maker fringe technique as described in detail by Jerphagnon and Kurtz [5]. There are several modifications of this technique which go beyond the original assumptions and take into account birefringence, absorption and other properties of the materials [6]. We applied the Maker fringe technique for measurements

of the nonlinear susceptibilities in polymeric Langmuir-Blodgett films which will be described in Section 5.4.1.

5.3 SHG: Symmetry considerations

In this section, I will describe some of the symmetry properties of the second order nonlinear susceptibility $\chi^{(2)}$. Also, the simulated data for the azimuthal angular dependence of the second harmonic intensity as observed in SHG experiment, anticipated in the materials with various symmetries, will be presented.

As mentioned in Chapter 1, the nonlinear susceptibility $\chi^{(2)}_{jik}$ is a third rank tensor that, in the most general case, has 27 cartesian components. Fortunately, there are a number of restrictions resulting from symmetries that relate the various components of $\chi^{(2)}$, and hence far fewer than 27 numbers are usually needed to describe the nonlinear coupling. For second harmonic generation, the nonlinear polarization density can be written as follows:

$$P_i(2\omega) = \chi^{(2)}_{ijk} E_j(\omega) E_k(\omega) = \chi^{(2)}_{ikj} E_k(\omega) E_j(\omega)$$

which suggests that the nonlinear susceptibility $\chi^{(2)}_{ijk}$ is symmetric with respect to the two last indices. This reduces the number of independent tensor components to 18.

It is conventional to introduce the tensor $d_{ijk} = \frac{1}{2}\chi^{(2)}_{ijk}$, and then in case of symmetry with respect to the two last indices of $d^{(2)}_{ijk}$, to consider the contracted matrix d_{il} where the notation is as follows [3]:

jk:	11	22	33	23,32	31,13	12,21
l:	1	2	3	4	5	6

Then the nonlinear susceptibility tensor can be represented as the 3x6 matrix:

$$d_{il} = \begin{bmatrix} d_{11} & d_{12} & d_{13} & d_{14} & d_{15} & d_{16} \\ d_{21} & d_{22} & d_{23} & d_{24} & d_{25} & d_{26} \\ d_{31} & d_{32} & d_{33} & d_{34} & d_{35} & d_{36} \end{bmatrix}$$

When the nonlinear optical interactions involve optical waves whose frequencies are far from the resonance frequencies of the material, further simplifications can be made. In this case, the susceptibility $\chi^{(2)}$ does not depend on the frequencies, and therefore the indices can be permuted without permuting the frequencies, leading to the result

$$\chi^{(2)}_{ijk} = \chi^{(2)}_{jki} = \chi^{(2)}_{kij} = \chi^{(2)}_{ikj} = \chi^{(2)}_{jik} = \chi^{(2)}_{kji}.$$

This result is knows as the Kleinman symmetry condition. When this is valid, the number of independent components of $\chi^{(2)}$ is reduced to 10. Furthermore, any crystalline symmetries of the nonlinear material or the symmetry of molecular packing, which is the case in organic materials, can reduce this number still further. For example, for the crystal quartz which belongs to the point symmetry group 32, with valid Kleinman symmetry condition, the nonlinear susceptibility tensor is

$$d = \begin{bmatrix} d_{11} & -d_{11} & 0 & 0 & 0 & 0 \\ 0 & 0 & 0 & 0 & 0 & -d_{11} \\ 0 & 0 & 0 & 0 & 0 & 0 \end{bmatrix}$$

Thus, only one independent component d_{11} is present in quartz. This makes it a

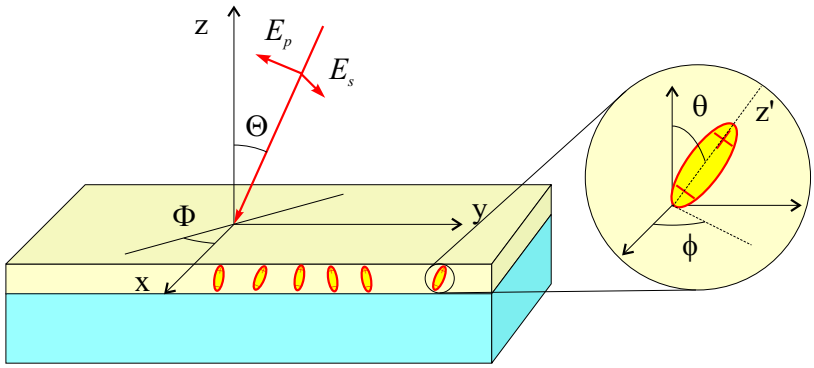

Figure 5.2: Schematic representation of the SHG angular dependence experiment.

convenient reference material in SHG studies, and we will use it in the LB film studies which will be described in Section 5.4.1.

Next we consider how the SHG technique can be applied in studies of molecular properties using the symmetry of the materials. In particular, we are interested in thin nonlinear optical polymeric and liquid crystalline films. We will demonstrate how the measurement of the azimuthal angular dependence of the SH intensity reflects the molecular arrangement in the bulk or on a surface.

The scheme of the experiment is the following. Light of frequency ω is incident on the film as shown in Figure 5.2. The coordinates are fixed to the sample, and the electric field of the *p*- and *s*-polarized light beams are given by

$$\mathbf{E_p} = \cos\Theta\cos\Phi, -\cos\Theta\sin\Phi, \sin\Theta \tag{5.4}$$

$$\mathbf{E_s} = \sin\Phi, \cos\Phi, 0 \tag{5.5}$$

where Θ and Φ are polar and azimuthal angles respectively.

In the experiment, the angular dependencies are measured while rotating the

sample as will be described in Section 5.4. However, for the theoretical treatment it is more convenient to fix the coordinates to the sample, and "rotate" the incident beam we introduced in Eqs. 5.4.

As discussed in Section 5.2, the incident wave creates a nonlinear polarization inside the material which results in the appearance of the second harmonic wave. In the case of a thin nonlinear optical film on an isotropic substrate (such as glass or fused silica), the nonlinear polarization is created only in the film, so that the centrosymmetric substrate does not contribute to the second harmonic signal. Therefore, the observed second harmonic intensity $I^{2\omega}$ provides information about the nonlinearity of the film. In particular, the angular dependencies of $I^{2\omega}$ in different polarizations of the incident and second harmonic light (*pp*,*sp*, *ps* and *ss*), reflect the symmetry of the system. This allows us to study properties such as molecular alignment on the surfaces, molecular packing in the bulk, etc.

In Appendix A, we describe the theoretical procedure used for calculating the azimuthal angular dependencies of $I^{2\omega}$. Here, we will just list the results for some symmetries which are of interest for nonlinear optical studies of organic materials.

5.3.1 $C_{\infty v}$ symmetry

This symmetry is characterized by an ∞ axis and a vertical mirror plane (Figure 5.3a) and describes systems such as poled polymers, isotropic Langmuir-Blodgett films, etc. The nonlinear susceptibility tensor for such systems contains only two independent

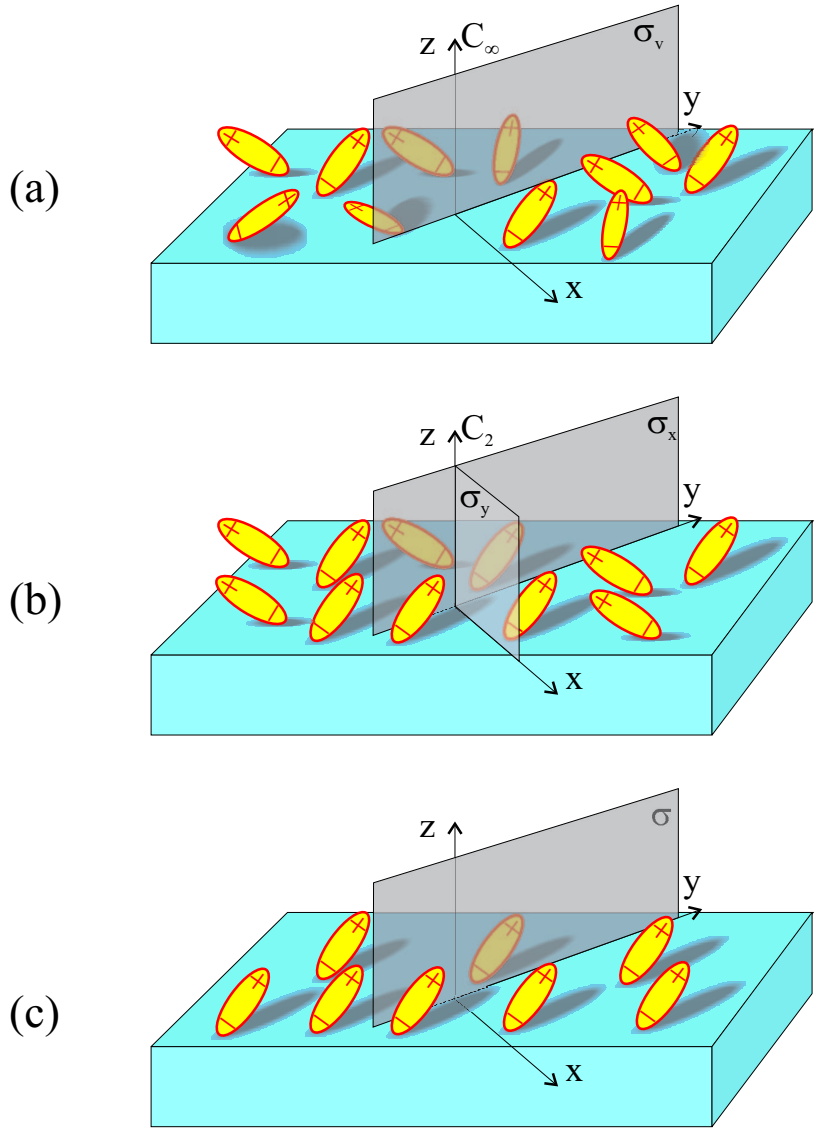

Figure 5.3: Symmetry groups common in NLO studies of organic optical materials: a) $C_{\infty v}$; b) C_{2v}; c) C_{1v}.

components d_{31} and d_{33}:

$$d = \begin{bmatrix} 0 & 0 & 0 & 0 & d_{31} & 0 \\ 0 & 0 & 0 & d_{31} & 0 & 0 \\ d_{31} & d_{31} & d_{33} & 0 & 0 & 0 \end{bmatrix}$$

The observed second harmonic intensities for the four polarization configurations (refer to Appendix A for details) are the following:

- *pp*-polarization. $I_{pp}^{2\omega} \sim (d_{33} \sin^2 \Theta - d_{31} \cos^2 \Theta)^2 \sin^2 \Theta$
- *sp*-polarization. $I_{sp}^{2\omega} \sim d_{31}^2 \sin^2 \Theta$
- *ps*-polarization. $I_{ps}^{2\omega} = 0$
- *ss*-polarization. $I_{ss}^{2\omega} = 0$

There are no *s*-polarized second harmonic waves, and there are azimuthally isotropic *p*-polarized second harmonic signals. Also, it can be seen why the oblique incidence is required for the SHG observation: at normal incidence $\Theta = 0$ and thus, there is no SHG signal in any polarization combination.

From the SHG measurements in the *sp*- and *pp*-polarization configurations, one can calculate the ratio d_{33}/d_{31} from which the average molecular tilt angle can be estimated. For this, we recall the connection between the bulk susceptibility χ_{ijk} (and therefore d_{ijk}) and molecular susceptibility $\beta_{i'j'k'}$ (refer to Section 4.2.1).

We consider the simplest case of rod-like molecules that have a dominant hyperpolarizability element $\beta_{z'z'z'}$ (Figure 5.2). Then, the *d*-tensor components are related

to $\beta_{z'z'z'}$ as follows [1]

$$d_{33} = \frac{N}{2}\langle\cos^3\theta\rangle\beta_{z'z'z'} \tag{5.6}$$
$$d_{31} = \frac{N}{4}\langle\sin^2\theta\cos\theta\rangle\beta_{z'z'z'}$$

where θ is the (polar) angle between z and z' (Figure 5.2), N is the molecular density and angular brackets denote the orientational averages.

If the polar distribution function is approximated with a δ-function around an angle θ_0, then the orientational averages are simplified to $\langle\cos^3\theta\rangle \approx \cos^3\theta_0$ and $\langle\sin^2\theta\cos\theta\rangle \approx \sin^2\theta_0\cos\theta_0$. Now the average molecular tilt can be determined from Eqs. 5.6:

$$\theta_0 = \arctan\sqrt{\frac{2d_{31}}{d_{33}}} \tag{5.7}$$

This approach to calculating the average molecular tilt angle is widely used in thin films. In Section 5.4.1, we will use it for Langmuir-Blodgett films.

5.3.2 C_{2v} symmetry

The next symmetry we consider is C_{2v} (Figure 5.3b).

This symmetry is characterized by a two-fold rotation axis and a vertical mirror plane (see Figure 5.3b). An example of a C_{2v} symmetry system is a LC monolayer photo-aligned with a linearly polarized light [7, 8, 9], which will be considered in Section 5.4.2.

The nonlinear susceptibility tensor for C_{2v} symmetry systems is similar to that of

the $C_{\infty v}$ but with one more independent component d_{32}:

$$d = \begin{bmatrix} 0 & 0 & 0 & 0 & d_{31} & 0 \\ 0 & 0 & 0 & d_{32} & 0 & 0 \\ d_{31} & d_{32} & d_{33} & 0 & 0 & 0 \end{bmatrix}$$

The second harmonic intensities for the four polarization configurations are the following:

- *pp*-polarization. $I_{pp}^{2\omega} \sim (d_{33}\sin^2\Theta - (d_{31}\cos^2\Phi + d_{32}\sin^2\Phi)\cos^2\Theta)^2\sin^2\Theta$
- *sp*-polarization. $I_{sp}^{2\omega} \sim (d_{31}\sin^2\Phi + d_{32}\cos^2\Phi)^2\sin^2\Theta$
- *ps*-polarization. $I_{ps}^{2\omega} \sim (d_{31} - d_{32})^2\sin^2 2\Theta\sin^2 2\Phi$
- *ss*-polarization. $I_{ss}^{2\omega} = 0$

In contrast to $C_{\infty v}$ symmetry, the second harmonic signals are azimuthally anisotropic. Also, a second harmonic signal is allowed in *ps*-polarization. In this polarization configuration, no second harmonic is observed in $C_{\infty v}$ symmetry systems.

At fixed polar angle Θ, the exact shape of the $I^{2\omega}$ azimuthal dependencies depends on the relative values of d_{31}, d_{32} and d_{33}. To understand which molecular arrangement corresponds to one or another set of ratios of the susceptibility tensor components, we relate these components to the molecular susceptibility $\beta_{z'z'z'}$ using the notation of Eqs. 5.6:

$$d_{33} = \frac{N}{2}\langle\cos^3\theta\rangle\beta_{z'z'z'} \tag{5.8}$$

$$d_{31} = \frac{N}{2}\langle \cos\theta \sin^2\theta \rangle \langle \cos^2\phi \rangle \beta_{z'z'z'}$$
$$d_{32} = \frac{N}{2}\langle \cos\theta \sin^2\theta \rangle \langle \sin^2\phi \rangle \beta_{z'z'z'}$$

where ϕ is the azimuthal angle defined in Figure 5.2.

If polar δ-function distribution around an angle θ_0 is assumed, then this angle θ_0 can be determined from Eqs. 5.8 as

$$\theta_0 = \arctan\sqrt{\frac{d_{31}+d_{32}}{d_{33}}} \tag{5.9}$$

As seen From Eqs. 5.8 and 5.9, the ratio $d_{33}/(d_{31}+d_{32})$ determines the polar alignment, while the ratio d_{31}/d_{32} determines the degree of azimuthal anisotropy.

We simulated the intensity of second harmonic observed in a SHG experiment when the sample is rotated around the z-axis, at fixed angle of incidence $\Theta = 45°$, for several cases:

- Nearly homeotropic alignment.

  In this case, the molecular tilt θ_0 is close to 0 which means that $d_{33} \gg d_{31}, d_{32}$.

  For the theoretical calculation of the azimuthal dependence, we chose $d_{31} = 1$, $d_{32} = 0.5$ and $d_{33} = 10$. The calculated second harmonic intensity as a function of the azimuthal angle Φ for *pp*, *sp* and *ps*-polarizations is shown in Figure 5.4.

- Nearly planar alignment.

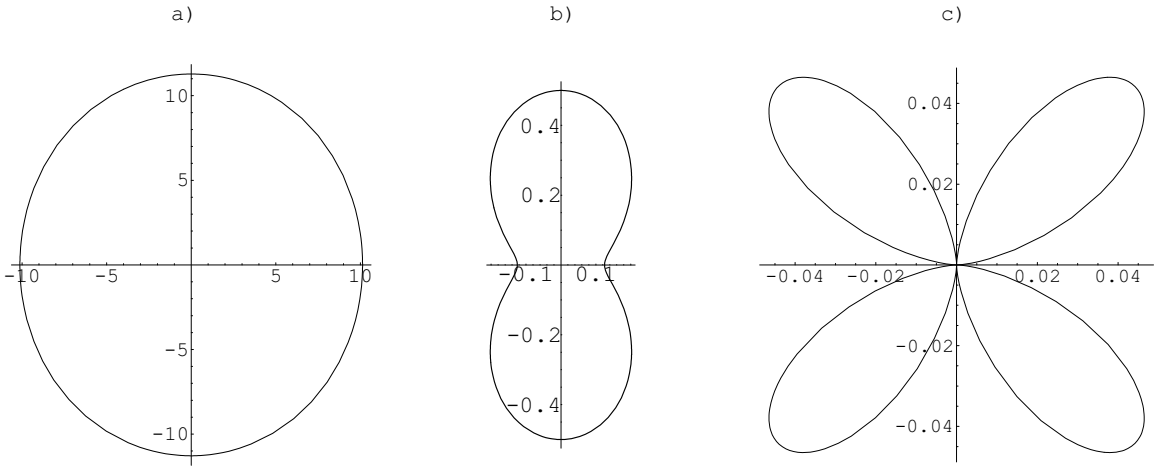

Figure 5.4: Azimuthal angle dependence of the second harmonic intensity calculated for the system with C_{2v} symmetry and homeotropic molecular alignment: a) *pp*; b) *sp*; c) *ps*.

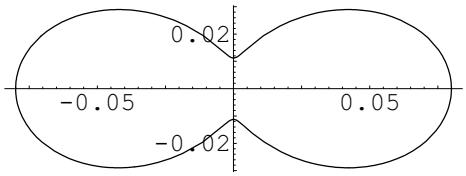

Figure 5.5: Azimuthal angle dependence of the second harmonic intensity for *pp*-polarization configuration, calculated for the system with C_{2v} symmetry and planar molecular alignment.

In this case, the molecular tilt θ_0 is close to 90°, and $d_{33} \lesssim d_{31}, d_{32}$.

For the calculation of the azimuthal dependence, we chose the same coefficients $d_{31} = 1$ and $d_{32} = 0.5$, but smaller $d_{33} = 0.2$. The *sp*- and *ps*-polarized signal shapes did not change since they do not contain d_{33}-dependence. The *pp*-polarized signal that changed is shown in Figure 5.5.

As one can see from Figures 5.4a and 5.5, the shapes of the angular dependence in the *pp* configuration for nearly homeotropic and planar alignment are quite different.

Thus, SHG measurements of the azimuthal angular dependence allow one to estimate the molecular tilt before performing any calculations.

5.3.3 C_{1v} symmetry

This is a low symmetry that has only one non-trivial symmetry element, a vertical mirror plane (see Figure 5.3c). An example of C_{1v} symmetry system is a LC monolayer on a rubbed surface [1].

The nonlinear susceptibility tensor for the C_{1v} symmetry has numerous non-vanishing components:

$$d = \begin{bmatrix} d_{11} & d_{12} & d_{13} & 0 & d_{31} & 0 \\ 0 & 0 & 0 & d_{32} & 0 & d_{12} \\ d_{31} & d_{32} & d_{33} & 0 & d_{13} & 0 \end{bmatrix}$$

As a result, the second harmonic intensities for the four polarization configurations have complicated angular dependencies:

- *pp*-polarization.

  $I_{pp}^{2\omega} \sim [\sin\Theta(d_{33}\sin^2\Theta + (d_{31}\cos^2\Phi + d_{32}\sin^2\Phi)\cos^2\Theta + d_{13}\cos\Phi\sin 2\Theta) - \frac{1}{2}\cos\Theta(\cos^2\Theta\cos\Phi(d_{11}+3d_{12}+(d_{11}-3d_{12})\cos 2\Phi)+\sin\Theta(2(d_{31}+d_{32})\cos\Theta + (d_{31}-d_{32})(\cos[\Theta-2\Phi]-\cos[\Theta+2\Phi])+d_{13}(\sin[\Theta-\Phi]+\sin[\Theta+\Phi])))]^2$

- *sp*-polarization.

  $I_{sp}^{2\omega} \sim [\cos\Theta\cos\Phi(d_{12}\cos^2\Phi+(d_{11}-2d_{12})\sin^2\Phi)-(d_{31}\sin^2\Phi+d_{32}\cos^2\Phi)\sin\Theta]^2$

- *ps*-polarization.

$$I_{ps}^{2\omega} \sim \sin^2\Phi[\tfrac{1}{2}(d_{11}-d_{12}+(d_{11}-3d_{12})\cos 2\Phi)\cos^2\Theta + d_{13}\sin^2\Theta + (d_{31}-d_{32})\cos\Phi\sin 2\Theta]^2$$

- *ss*-polarization.

$$I_{ss}^{2\omega} \sim \sin^2\Phi[3d_{12}\cos^2\Phi + d_{11}\sin^2\Phi]^2$$

The non-vanishing components of d for C_{1v} symmetry are related to the molecular susceptibility $\beta_{z'z'z'}$ as follows:

$$d_{33} = \frac{N}{2}\langle\cos^3\theta\rangle\beta_{z'z'z'} \tag{5.10}$$

$$\begin{aligned} d_{11} &= -\frac{N}{2}\langle\sin^3\theta\rangle\langle\cos^3\phi\rangle\beta_{z'z'z'} \\ d_{12} &= -\frac{N}{2}\langle\sin^3\theta\rangle\langle\cos\phi\sin^2\phi\rangle\beta_{z'z'z'} \\ d_{13} &= -\frac{N}{2}\langle\cos^2\theta\sin\theta\rangle\langle\cos\phi\rangle\beta_{z'z'z'} \\ d_{31} &= \frac{N}{2}\langle\cos\theta\sin^2\theta\rangle\langle\cos^2\phi\rangle\beta_{z'z'z'} \\ d_{32} &= \frac{N}{2}\langle\cos\theta\sin^2\theta\rangle\langle\sin^2\phi\rangle\beta_{z'z'z'} \end{aligned} \tag{5.11}$$

For this symmetry, the second harmonic intensity at $\Theta = 45^\circ$ assumes more complicated shapes as we show for nearly homeotropic and nearly planar alignment.

- Nearly homeotropic alignment.

  In C_{1v} symmetry, there are many non-vanishing components of the nonlinear susceptibility tensor. However, d_{33} being large in comparison to all other compo-

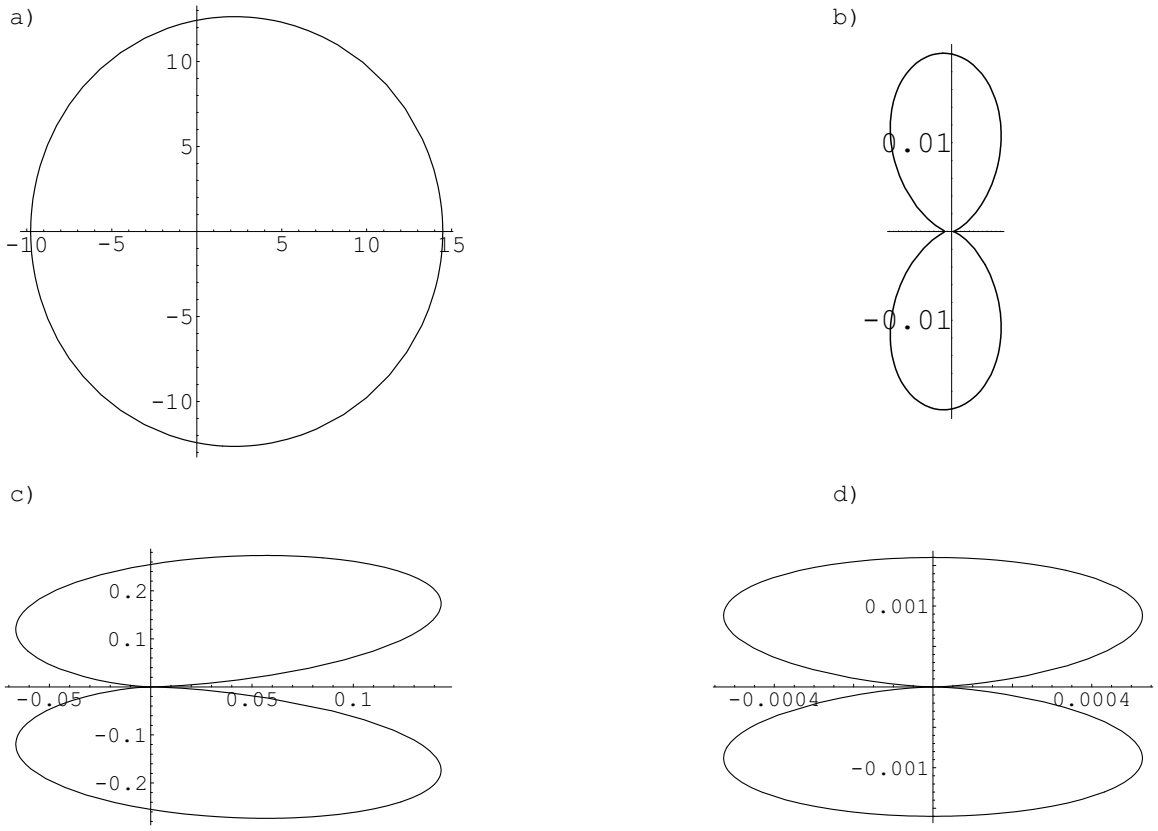

Figure 5.6: Second harmonic azimuthal angle dependence calculated for a system with C_{1v} symmetry and homeotropic molecular alignment: a) *pp*; b) *sp*; c) *ps*; d) *ss*

nents is still an indication of nearly homeotropic alignment. We chose $d_{11} = 0.04$, $d_{12} = 0.01$, $d_{13} = 1$, $d_{31} = 0.2$, $d_{32} = 0.03$ and $d_{33} = 10$. The calculated second harmonic intensity as a function of the azimuthal angle Φ for *pp*, *sp*, *ps* and *ss*-polarizations is shown in Figure 5.6.

- Nearly planar alignment.

  The indication of nearly planar alignment is a the large d_{11} component in comparison to d_{33}. So, we chose $d_{11} = 10$, $d_{12} = 0.2$, $d_{13} = 0.1$, $d_{31} = 1$, $d_{32} = 0.05$

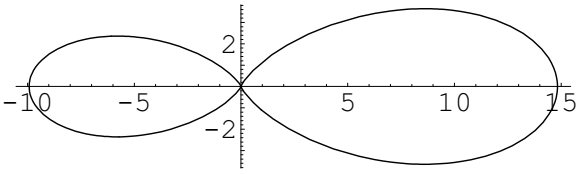

Figure 5.7: Azimuthal angle dependence of the *pp*-polarized second harmonic signal, calculated for the system with C_{1v} symmetry and planar molecular alignment.

and $d_{33} = 0.01$. The *pp*-polarized signal was the only signal that changed due to relative change of d_{11} and d_{33}. For nearly planar alignment, the *pp*-polarized second harmonic intensity is shown in Figure 5.7.

In summary of Section 5.3, we demonstrated the influence of the symmetry of the molecular arrangement on the second harmonic intensity angular dependence. In the next section, we will apply this property of SHG to real systems.

5.4 SHG: experiment

In this section we will consider the experimental technique used for the SHG measurement. Then, the study of the Langmuir-Blodgett polymeric films (Section 5.4.1) and LC monolayers (Section 5.4.2) will be presented.

The experimental set-up for the SHG measurements is shown in Figure 5.8. We used a Q-switched Nd:YAG laser with fundamental output wavelength $\lambda = 1.06\,\mu m$ or frequency doubled output of $532\,nm$. The incident laser beam was focused on the sample, and the second harmonic light was detected by a photomultiplier (PMT1) (signal channel). For polarization measurements, a polarization rotator was placed

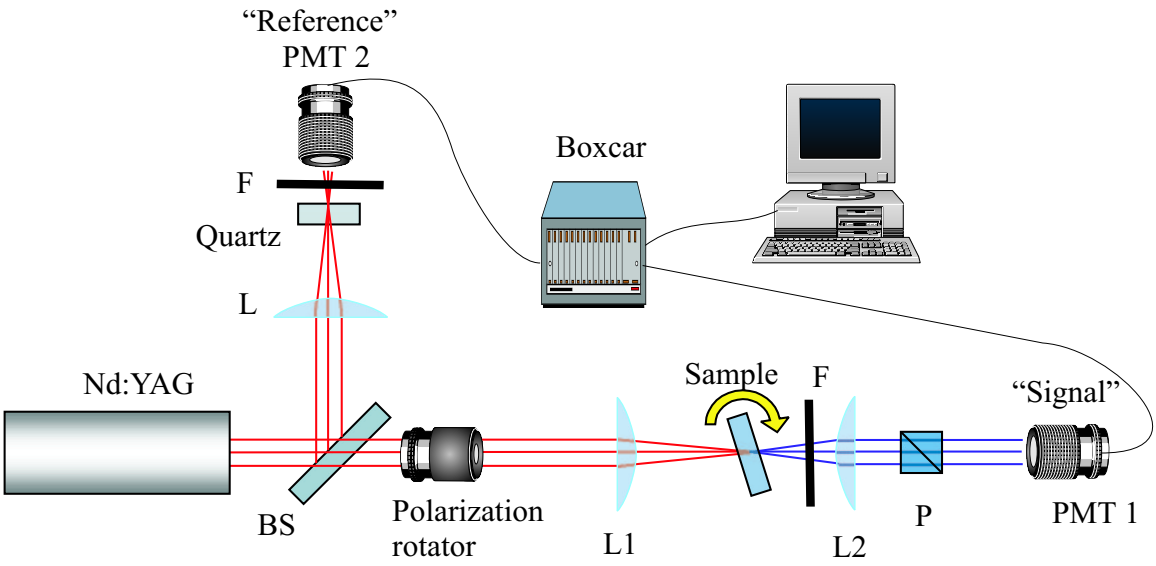

Figure 5.8: Experimental set-up for the SHG measurements.

before the sample to change the incident beam polarization, and a polarizer was placed between the sample and PMT1 to select the second harmonic signal of the specified polarization. Part of the fundamental light was directed to the reference channel and focused on a quartz crystal. The second harmonic signal generated in quartz was detected with PMT2. The quartz referencing was done to prevent the shot-to-shot instability of the laser from influencing the results. Both reference and signal channel data were averaged using a boxcar and recorded by a computer. Then, the signal channel data was divided by the reference channel data, thus eliminating possible fluctuations of the laser beam power.

The sample was mounted on a rotation stage. For the Maker fringe technique, the sample was rotated around the x-axis in the sample plane, and the second harmonic

intensity was recorded as a function of incident angle. For the surface symmetry studies, the sample was rotated around the axis perpendicular to the sample plane, and the second harmonic intensity was recorded as a function of azimuthal angle.

The polarization dependence of the SHG intensity allows one to calculate the relative d_{ijk}-tensor components but does not provide their absolute values. For the absolute measurements, the quartz crystal, whose only nonlinear susceptibility component d_{11} (see Section 5.2) is known from the literature, is placed in the sample channel, and the second harmonic intensity is recorded under the same conditions as for the materials under study. Then, the second harmonic intensity generated in quartz is compared to that of the material whose susceptibilities are being studied. From the ratios of intensities and known d_{11} of quartz, the susceptibility of the material is calculated. This procedure is detailed in Appendix B.

Next, I will describe two separate projects which illustrate the application of the SHG technique to materials research. In particular, we studied organic optical thin films.

5.4.1 SHG studies of Langmuir-Blodgett films

The goal of this study was to determine the NLO susceptibilities of two newly synthesized nonlinear optical polymers and investigate such properties as molecular alignment, dependence of the NLO susceptibility on the number of layers, temperature stability of the layers, etc.

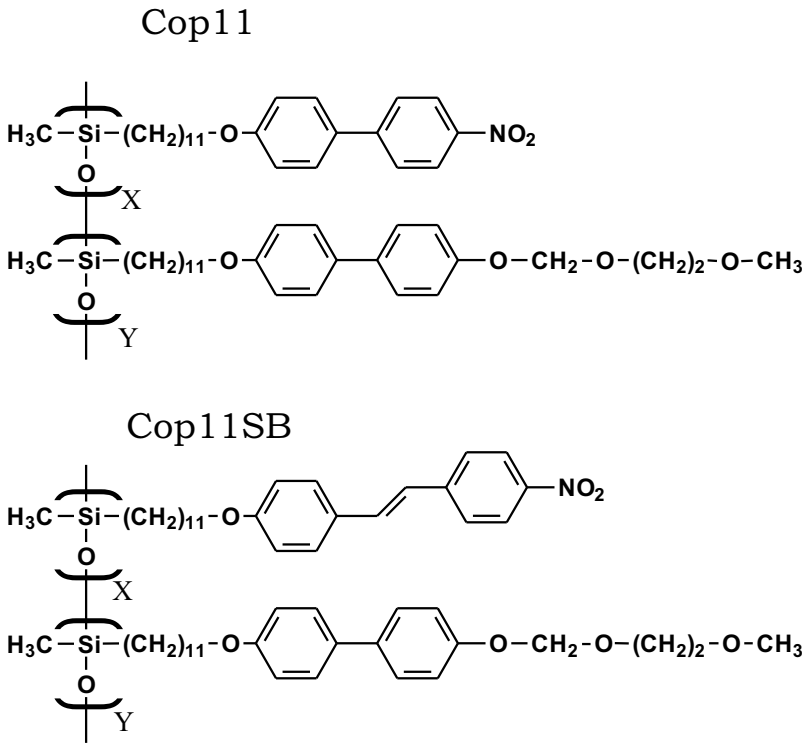

Figure 5.9: Copolymers used in our SHG studies.

The materials we studied are shown in Figure 5.9 [10, 11]. Generally, the Langmuir-Blodgett (LB) films are the assemblies of molecules with polar head groups and long aliphatic tails deposited onto a substrate from the surface of water [12]. A key feature of these films is that forces at the water surface and lateral surface pressure are used to condense a randomized set of such molecules from a gas-like phase to one that is highly organized and stabilized by van der Waals forces between molecules. These forces are sufficiently cohesive to allow the films to be transferred to a substrate as a coherent film. Depending on the preparation method, the film can be made either centrosymmetric or non-centrosymmetric.

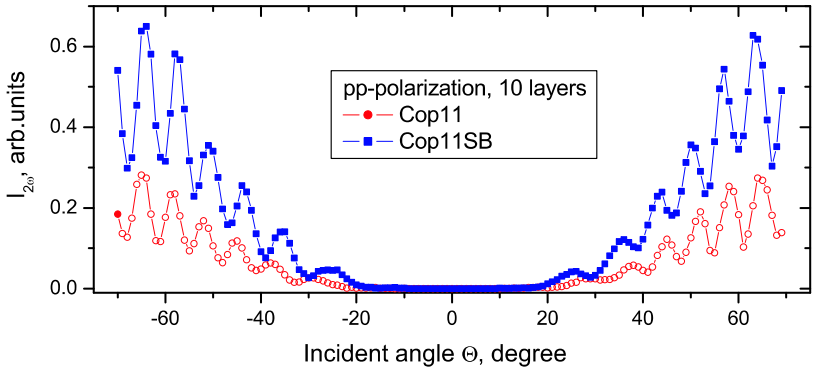

Figure 5.10: Typical data as observed in Maker fringe experiment for Cop11 and Cop11SB.

Our films were prepared by so called X-type horizontal deposition [12] that leads to non-centrosymmetric structure formation. The thickness of our monolayer was typically 35 Å. The LB films were deposited on glass substrates. The details of the sample preparation are presented in Ref. [10].

The rotational Maker fringe experiment [4] was performed in *pp* and *sp* configurations in the transmission geometry illustrated in Figure 5.2. We did not detect any *s*-polarized second harmonic signal as expected for this LB film since it belongs to the $C_{\infty v}$ point symmetry group. Typical SHG data from the rotational Maker fringe experiment is shown in Figure 5.10. The envelope of the fringes shown in Figure 5.10 reflects the phase-matching condition variation as given by Eq. 5.3 in Section 5.2. The fringes themselves are due to interference of the surface generated SHG at the glass-air and glass-film interfaces.

The second harmonic intensity $I^{2\omega}$ increased with the number of layers (Fig-

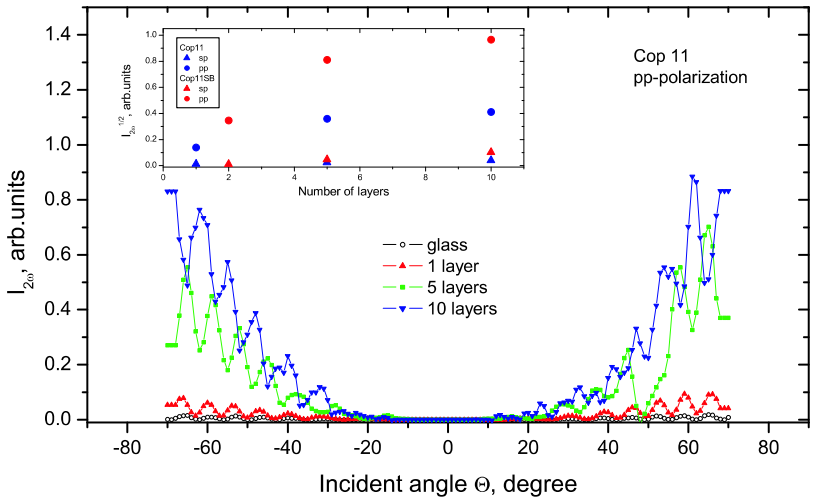

Figure 5.11: Maker fringes observed in Cop11 LB films with various number of layers. Inset shows the square root of the second harmonic intensity plotted as a function of the number of layers.

ure 5.11). The inset of Figure 5.11 shows the square root of $I^{2\omega}$ plotted versus the number of layers. From Eq. 5.3, a linear dependence $\sqrt{I^{2\omega}}(L)$ is expected. However, this is not the case for our system which indicates that the molecular alignment is disrupted as the number of layers increases, and this leads to reduced second harmonic generation. The ratio of d_{33}/d_{31} components of the susceptibility tensor was calculated from the intensities of the *pp* and *sp* configurations as detailed in Appendix B. For Cop11SB, d_{33}/d_{31} was determined to be equal to 67, from which the average molecular tilt was found in accordance with Eq. 5.7 to be $\sim 10°$.

The absolute values of d_{33} and d_{31} were obtained by referencing the second harmonic intensities obtained from the films to those of crystal quartz, and calculated using the quartz nonlinear coefficient $d_{11} = 0.85 \cdot 10^{-9}\, esu$. The components d_{33} and

Table 5.1: Nonlinear optical susceptibilities of the polymeric LB monolayers.

Polymer	d_{31}, esu	d_{33}, esu
Cop11	$5.4 \cdot 10^{-9}$	$2.9 \cdot 10^{-7}$
Cop11SB	$5.0 \cdot 10^{-9}$	$3.3 \cdot 10^{-7}$

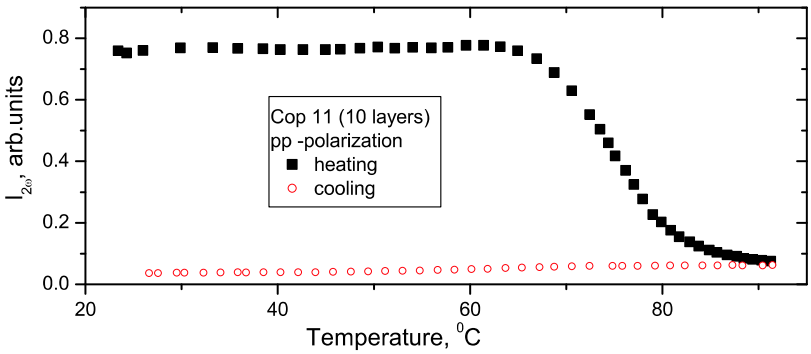

Figure 5.12: Temperature dependence of the second harmonic intensity for Cop11.

d_{31} for both Cop11 and Cop11SB are listed in Table 5.1.

The temperature stability of the LB films was studied by monitoring the temperature dependence of the SHG signal. We found that heating the sample irreversibly decreased the SHG intensity which indicates that the increased temperature destroyed the polar alignment (Figure 5.12).

In summary, we showed how SHG techniques can be applied to LB film characterization.

5.4.2 SHG studies of LC monolayers

This study was part of a project that investigated the properties of an adsorbed 4,4'-n-pentylcyanobiphenyl (5CB) (see Section 3.2) monolayer as an aligning layer for LC bulk [7].

We observed light-induced alignment of the nematic liquid crystal (5CB) on a fused quartz surface covered with a layer of adsorbed 5CB molecules. Irradiation of the adsorbed layer with polarized ultraviolet (UV) light produced homogeneous alignment in a 5CB-filled liquid crystal cell, with the axis of easy orientation perpendicular to the polarization direction. The SHG technique was used to probe the molecular alignment of the adsorbed layer before and after irradiation with UV light.

The sample preparation included the following. Fused quartz substrates were cleaned, and 5CB was adsorbed on the quartz surface by dipping in a dilute solution of 5CB in isopropyl alcohol (0.1% by weight) for 10-60 min. The substrates were then rinsed in pure isopropyl alcohol for 5-15 seconds to remove non-adsorbed molecules, and then gently dried. The presence of a LC layer on the substrate was monitored by the measuring the UV absorption of the 5CB layer using a Perkin-Elmer 19 spectrometer. The absorption saturated at times longer than 45 min. An adsorption time of 60 min was chosen to assure an equilibrium adsorption layer of 5CB on the substrate. We also found that the adsorbed layer was not stable with time, or at elevated temperatures. We observed a significant reduction in the absorption after maintaining the samples at room temperature for 6-8 h or upon heating to $90^{\circ}C$ for 5 min perhaps due to evaporation.

As mentioned before, SHG was used to probe the structure of the adsorbed aligning layer [1]. By measuring the intensity of the second harmonic (SH) for different

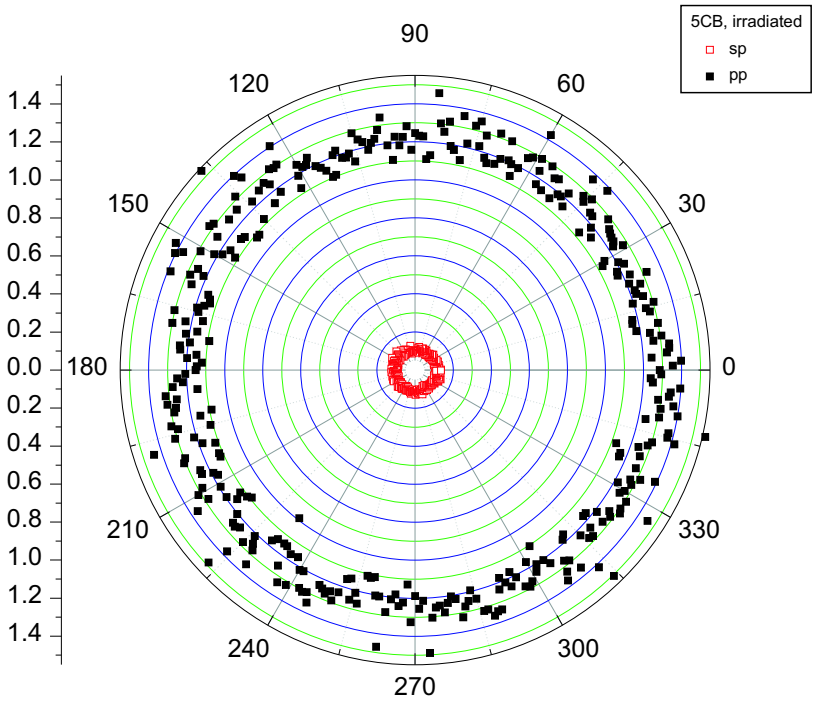

Figure 5.13: Second harmonic intensity as a function of azimuthal angle.

polarizations of the incident and SH beams, we investigated the orientation of the LC molecules on the surface.

The SHG experiments were carried out with a $532\,nm$ wavelength to obtain the near-resonant enhancement of the SH signal due to proximity of the absorption band of 5CB ($\sim 280\,nm$) to the SH wavelength of $266\,nm$. The sample was set at an incident angle of about 35° with the azimuth angle as the dependent variable. The SHG experiment was performed for four combinations of polarization directions of polarizer and analyzer - pp, sp, ps, and ss. The pp- and sp-signals from the 5CB monolayer on the fused quartz substrate were the only ones larger than that of the substrate, with data shown in Figure 5.13. All signals were unchanged upon irradiation with

polarized UV light. The intensity of the *pp*-signal from the 5CB+substrate system was 16 times larger than that of the substrate, and the *sp*-signal 2.25 times larger. Thus, the contribution of the substrate to the total signal is not negligible and should be taken into account when deducing the components of the susceptibility tensor of the 5CB monolayer. This can be done by considering the surface nonlinear susceptibility [13]

$$d_{total} = d_{sub} + d_{5CB} \tag{5.12}$$

where d_{sub} is the contribution of the bare substrate and d_{5CB} is the contribution of the monolayer. Any contribution to the susceptibility arising from a symmetry altering interaction between the surface and the monolayer is neglected. Using this formalism, we determined the ratio of out-of-plane and in-plane components of the susceptibility tensor to be $\frac{2d_{33}}{d_{31}+d_{32}} \approx 46$, which, assuming a delta-function polar distribution of the molecules, yields a molecular tilt angle from the substrate normal of $\theta_0 \approx 12^{\circ}$ (Eq. 5.9). Thus, the adsorbed layer is slightly tilted from normal.

To study the in-plane anisotropy induced by polarized UV light,we express the molecular distribution function in the form

$$f(\phi) = \frac{1}{2\pi}(1 + a_2 \cos 2\phi) \tag{5.13}$$

where a_2 determines the degree of anisotropy in the system. The surface possesses C_{2v} symmetry as confirmed by the pretilt measurements. Thus, $f(\phi)$ reflects this symmetry.

For a system described by C_{2v} symmetry, anisotropic angular dependencies of the SH intensity similar to those shown in Figures 5.4 and 5.5 are expected. However, we observed the isotropic dependencies shown in Figure 5.13. We attribute this to a large isotropic signal from the fused quartz substrate which obscured the anisotropy in both the *pp*- and *sp*-signal.

Next, we will calculate an upper limit to a_2 that is consistent with our experimental data. For simplicity, we assume that the substrate has only d_{31}^{sub} and d_{33}^{sub} nonlinear susceptibility components. Then, using the same formalism as in case of thin films (see Appendix B), the ratio $d_{33}^{sub}/d_{31}^{sub}$ can be determined from the ratio of the SH intensities for *pp*- and *sp* configurations. From our data, we determined this ratio to be 9.

According to Eq. 5.12, and taking into account Eqs. 5.8, we write the total susceptibility of the substrate-5CB system as follows

$$d_{33} = d_{33}^{sub} + \frac{N}{2}\langle\cos^3\theta\rangle\beta_{z'z'z'} \tag{5.14}$$
$$d_{31} = d_{31}^{sub} + \frac{N}{2}\langle\cos\theta\sin^2\theta\rangle\langle\cos^2\phi\rangle\beta_{z'z'z'}$$
$$d_{32} = d_{31}^{sub} + \frac{N}{2}\langle\cos\theta\sin^2\theta\rangle\langle\sin^2\phi\rangle\beta_{z'z'z'}$$

Assuming a δ-function polar distribution and performing the azimuthal averages using the distribution function of Eq. 5.13, we obtain

$$\langle\cos^2\phi\rangle = \frac{1}{2}\left(1+\frac{a_2}{2}\right), \langle\sin^2\phi\rangle = \frac{1}{2}\left(1-\frac{a_2}{2}\right)$$

and then

$$d_{33} = d_{33}^{sub} + \frac{N}{2}\cos^3\theta_0\beta_{z'z'z'} \tag{5.15}$$

$$d_{31} = d_{31}^{sub} + \frac{N}{4}\cos\theta_0\sin^2\theta_0\left(1+\frac{a_2}{2}\right)\beta_{z'z'z'}$$

$$d_{32} = d_{31}^{sub} + \frac{N}{4}\cos\theta_0\sin^2\theta_0\left(1-\frac{a_2}{2}\right)\beta_{z'z'z'}$$

Since we do not need the absolute values of the d_{ij}-components for analyzing the shapes of the angular dependencies, we will operate with relative values. We set $d_{31}^{sub} = 1$. Then, as mentioned above, $d_{33}^{sub} = 9$. Comparing the *pp* and *sp* signals for bare substrate and the substrate+5CB system, we determine the values of 5CB susceptibilities relative to d_{31}^{sub} be $d_{31}^{5CB} = 0.6$ and $d_{33}^{5CB} = 27$.

Then, using the average tilt angle θ_0 of 12° calculated above, we obtain the relative value of $N\beta_{z'z'z'}/2 \approx 27$ from the first equation in Eqs. 5.15. Next, we use this value together with d_{31}^{sub}, d_{33}^{sub} and θ_0 to simulate the shape of the angular dependencies of the SH intensity. Varying the anisotropy parameter a_2, we find its largest value at which the SHG angular dependence of the substrate+5CB is still isotropic within 10% error as observed experimentally (Figure 5.13).

The upper limit of a_2 was determined to be ~ 0.11. Using this value, we calculated an upper limit to the in-plane order parameter $Q = \langle\cos 2\phi\rangle$ which describes a degree of in-plane ordering intermediate between isotropic ($Q = 0$) and completely ordered ($Q = 1$). For our system $Q \approx 0.06$, which is twice as large as the reported value for the LC monolayer on a UV-treated polyimide (PI), but half as large as for a LC

monolayer on a rubbed PI [14].

In addition to the polarization and angle dependence of the SHG,we also measured the magnitude of the nonlinear optical susceptibility by referencing the second harmonic signal from our sample to both the quartz reference crystal ($d_{11} = 0.85 \cdot 10^{-9}\, esu$) and the Langmuir-Blodgett film described in Section 5.4.1 ($d_{33} \approx 1.5 \cdot 10^{-14}\, esu/cm^2$). These measurements yielded a value of $d_{33} \approx 7.5 \cdot 10^{-15}\, esu/cm^2$. Given a surface density of $N \approx 5 \cdot 10^{14}\, cm^{-2}$ calculated from the approximate packing of the molecules on the surface and an order parameter $\langle \cos^3 \theta_0 \rangle \sim 1$, the molecular hyperpolarizability $\beta_{z'z'z'}$ is estimated from Eqs. 5.8 to be $\beta_{z'z'z'} \approx 8 \cdot 10^{-29}\, esu$ which is consistent with the literature [15] ($\beta_{z'z'z'} \approx 1.5 \cdot 10^{-29}\, esu$ at $\lambda = 1.06\, \mu m$) when the dispersion factors are taken into account.

In summary, we investigated the structure of an alignment layer that is an adsorbed 5CB monolayer. The alignment layer can be viewed as being composed of the 5CB amphiphile with the polar CN group anchored to the polar quartz surface with its dipole axis oriented with a 12° tilt from normal along the easy axis. The in-plane orientation is described by a distribution with order parameter $Q \approx 0.06$.

5.5 Summary of Chapter 5

In Chapter 5, we considered several applications of the second harmonic generation technique to studies of the molecular properties of organic thin films.

The angular dependence of the second harmonic intensity was simulated for several point symmetry groups which are of interest to polymeric systems.

Two experimental examples, a Langmuir-Blodgett film and an adsorbed 5CB monolayer, were considered, and it was demonstrated how a variety of molecular properties can be probed with the SHG technique.

Appendix A

Azimuthal rotation of sample around z with an angle of incidence Θ

The azimuthal rotation of the beam around z-axis is described by the rotation matrix:

$$\overleftrightarrow{R}\,[0,\Phi,0] = \begin{pmatrix} \cos\Phi & \sin\Phi & 0 \\ -\sin\Phi & \cos\Phi & 0 \\ 0 & 0 & 1 \end{pmatrix}$$

Consider two cases of incident polarization being in the plane of incidence (p) and perpendicular to it (s). Due to the sample rotation, the components of the electric field vector $\mathbf{E}$ in the coordinate system fixed on the sample are functions of the rotation angle Φ. In case of the most general second harmonic tensor d, both s and p-polarized incident waves will induce the nonlinear polarization of the medium that has both s and p contributions. These polarizations contribute differently into the second harmonic signal and can be treated separately. Experimentally, these contributions are separated by selective detection of the s- and p-polarized light.

P-input polarization

The components of a p-polarized optical field are given by the following expression:

$$\mathbf{E}_p = \begin{pmatrix} E_x \\ E_y \\ E_z \end{pmatrix} = \overleftrightarrow{R}\,[0,\Phi,0]\cdot\begin{pmatrix} \cos\Theta \\ 0 \\ \sin\Theta \end{pmatrix} = \begin{pmatrix} \cos\Theta\cos\Phi \\ \cos\Theta\sin\Phi \\ \sin\Theta \end{pmatrix}$$

The nonlinear polarization vector depends on the angles as follows:

$$\mathbf{P}^{NL} = d\otimes\mathbf{E}_p\mathbf{E}_p = \begin{pmatrix} d_{11}\cos^2\Theta\cos^2\Phi + 2d_{15}\cos\Theta\cos\Phi\sin\Theta \\ +d_{13}\sin^2\Theta - 2d_{16}\cos^2\Theta\cos\Phi\sin\Phi \\ -2d_{14}\cos\Theta\sin\Theta\sin\Phi + d_{12}\cos^2\Theta\sin^2\Phi \\ \\ d_{21}\cos^2\Theta\cos^2\Phi + 2d_{25}\cos\Theta\cos\Phi\sin\Theta + d_{23}\sin^2\Theta \\ -2d_{26}\cos^2\Theta\cos\Phi\sin\Phi - 2d_{24}\cos\Theta\sin\Theta\sin\Phi \\ +d_{22}\cos^2\Theta\sin^2\Phi \\ \\ d_{31}\cos^2\Theta\cos^2\Phi + 2d_{35}\cos\Theta\cos\Phi\sin\Theta \\ +d_{33}\sin^2\Theta - 2d_{36}\cos^2\Theta\cos\Phi\sin\Phi \\ -2d_{34}\cos\Theta\sin\Theta\sin\Phi + d_{32}\cos^2\Theta\sin^2\Phi \end{pmatrix}$$

It is quite straightforward to project it onto the s-direction by finding a dot product of $\mathbf{P}^{NL}$ with the unit vector $\hat{y}$ rotated by the same azimuthal angle:

$$\begin{aligned} P_s &= \mathbf{P}^{NL}\cdot\hat{e}_s = \mathbf{P}^{NL}\cdot\overleftrightarrow{R}\,[0,\Phi,0]\cdot\begin{pmatrix} 0 \\ 1 \\ 0 \end{pmatrix} \\ &= d_{25}\cos^2\Phi\sin 2\Theta + \sin\Theta\sin\Phi(d_{13}\sin\Theta - 2d_{14}\cos\Theta\sin\Phi) \\ &\quad + \cos\Phi\left[d_{23}\sin^2\Theta + (d_{15}-d_{24})\sin 2\Theta\sin\Phi\right] \\ &\quad + \cos^2\Theta\left[d_{21}\cos^3\Phi + (d_{11}-2d_{26})\cos^2\Phi\sin\Phi\right. \\ &\quad \left. -(2d_{16}-d_{22})\cos\Phi\sin^2\Phi + d_{12}\sin^3\Phi\right] \end{aligned}$$

The polarization vector that produces s-polarized SHG output is

$$\mathbf{P}_s^{NL} = P_s\hat{e}_s$$

$$= \begin{pmatrix} \sin\Phi\left\{d_{25}\cos^2\Phi\sin 2\Theta + \sin\Theta\sin\Phi(d_{13}\sin\Theta - 2d_{14}\cos\Theta\sin\Phi)\right. \\ +\cos\Phi\left[d_{23}\sin^2\Theta + (d_{15}-d_{24})\sin 2\Theta\sin\Phi\right] \\ +\cos^2\Theta\left[d_{21}\cos^3\Phi + (d_{11}-2d_{26})\cos^2\Phi\sin\Phi\right. \\ \left.\left.-(2d_{16}-d_{22})\cos\Phi\sin^2\Phi + d_{12}\sin^3\Phi\right]\right\} \\ \\ \cos\Phi\left\{d_{25}\cos^2\Phi\sin 2\Theta + \sin\Theta\sin\Phi(d_{13}\sin\Theta - 2d_{14}\cos\Theta\sin\Phi)\right. \\ +\cos\Phi\left[d_{23}\sin^2\Theta + (d_{15}-d_{24})\sin 2\Theta\sin\Phi\right] \\ +\cos^2\Theta\left[d_{21}\cos^3\Phi + (d_{11}-2d_{26})\cos^2\Phi\sin\Phi\right. \\ \left.\left.-(2d_{16}-d_{22})\cos\Phi\sin^2\Phi + d_{12}\sin^3\Phi\right]\right\} \\ \\ 0 \end{pmatrix}$$

Projection of $\mathbf{P}^{NL}$ on the plane of incidence is usually not collinear with the electric vector of the incident field and hence cannot be determined by a simple multiplication by the unit vector as it is not known *a priori*. However, using the orthogonality of s and p- projections, one finds

$$\begin{aligned} \mathbf{P}_p^{NL} &= (\mathbf{P}^{NL} - \mathbf{P}_s^{NL}) \\ &= \begin{pmatrix} -d_{14}\cos^2\Phi\sin 2\Theta\sin\Phi + \cos\Phi\left\{\sin^2\Theta(d_{13}\cos\Phi - d_{23}\sin\Phi)\right. \\ +\sin 2\Theta\left[d_{15} - d_{25}\cos\Phi\sin\Phi + (-d_{15}+d_{24})\sin^2\Phi\right]\ \} \\ -\cos^2\Theta\left\{d_{21}\cos^3\Phi\sin\Phi - (2d_{16}-d_{22})\cos\Phi\sin^3\Phi\right. \\ \left.+\cos^2\Phi\left[-d_{11} + (d_{11}-d_{12}-2d_{26})\sin^2\Phi\right] + d_{16}\sin 2\Phi\right\} \\ \\ \frac{1}{4}\sin\Phi\left\{\cos^2\Theta\left[-(3d_{11}+d_{12}+2d_{26})\cos\Phi + (-d_{11}+d_{12}+2d_{26})\cos 3\Phi\right.\right. \\ +2\left[2d_{16}+d_{21}+d_{22} + (2d_{16}+d_{21}-d_{22})\cos 2\Phi\right]\sin\Phi\Big] \\ +4\left[\sin^2\Theta(-d_{13}\cos\Phi + d_{23}\sin\Phi)\right. \\ +\cos\Phi\sin 2\Theta\left[(-d_{15}+d_{24})\cos\Phi + d_{25}\sin\Phi\right]\Big] \\ \left.+4\cos\Theta\sin\Theta(-2d_{24} + d_{14}\sin 2\Phi)\right\} \\ \\ d_{33}\sin^2\Theta + d_{35}\cos\Phi\sin 2\Theta - 2d_{34}\cos\Theta\sin\Theta\sin\Phi \\ +\cos^2\Theta(d_{31}\cos^2\Phi - 2d_{36}\cos\Phi\sin\Phi + d_{32}\sin^2\Phi) \end{pmatrix} \end{aligned}$$

Out of entire $\mathbf{P}_p^{NL}$ vector, only its projection perpendicular to the light propagation direction will result in second harmonic. The intensity of the p-polarized second

harmonic will be defined as

$$I_{pp}^{2\omega} \sim (P_{p,\perp} \cos\Theta - P_{p,z} \sin\Theta)^2 \tag{5.16}$$

Projection of the $\mathbf{P}_p$ on the xy plane (perpendicular to rotation axis z) can be found as

$$\begin{aligned}
P_{p,\perp} &= \mathbf{P}_p^{NL} \cdot \overleftrightarrow{R}\,[0,\Phi,0] \cdot \begin{pmatrix} 1 \\ 0 \\ 0 \end{pmatrix} \\
&= -d_{23}\sin^2\Theta\sin^3\Phi \\
&\quad +\frac{1}{4}\cos^2\Theta\left\{(3d_{11}+d_{12}+2d_{26})\cos\Phi + (d_{11}-d_{12}-2d_{26})\cos 3\Phi\right. \\
&\quad \left. -2\left[2d_{16}+d_{21}+d_{22}+(2d_{16}+d_{21}-d_{22})\cos 2\Phi\right]\sin\Phi\right\} \\
&\quad +\cos^2\Phi(d_{15}\sin 2\Theta - d_{23}\sin^2\Theta\sin\Phi) \\
&\quad +\cos\Phi\sin^2\Phi(d_{13}\sin^2\Theta - d_{25}\sin 2\Theta\sin\Phi) \\
&\quad +\cos^3\Phi\left[d_{13}\sin^2\Theta - (d_{14}+d_{25})\sin 2\Theta\sin\Phi\right] \\
&\quad +\cos\Theta\sin\Theta\sin^2\Phi(2d_{24} - d_{14}\sin 2\Phi)
\end{aligned} \tag{5.17}$$

Combining Eqs. 5.16 and 5.17 result in the azimuthal dependencies quoted in Section 5.4.2.

S-polarized output is defined by the s-component:

$$I_{ps}^{2\omega} \sim (P_s)^2$$

S-input polarization

The case of s-polarized input is treated similarly. The incident field vector is defined by

$$\mathbf{E}_s = \begin{pmatrix} E_x \\ E_y \\ E_z \end{pmatrix} = \overleftrightarrow{R}\,[0,\Phi,0] \cdot \begin{pmatrix} 0 \\ 1 \\ 0 \end{pmatrix} = \begin{pmatrix} \sin\Phi \\ \cos\Phi \\ 0 \end{pmatrix}$$

resulting in the NLO polarization density being

$$\mathbf{P}^{NL} = d \cdot \mathbf{EE} = \begin{pmatrix} d_{12}\cos^2\Phi + 2d_{16}\cos\Phi\sin\Phi + d_{11}\sin^2\Phi \\ d_{22}\cos^2\Phi + 2d_{26}\cos\Phi\sin\Phi + d_{21}\sin^2\Phi \\ d_{32}\cos^2\Phi + 2d_{36}\cos\Phi\sin\Phi + d_{31}\sin^2\Phi \end{pmatrix}$$

$$\begin{aligned} P_s &= \mathbf{P}^{NL} \cdot \overleftrightarrow{R}\,[0,\Phi,0] \cdot \begin{pmatrix} 0 \\ 1 \\ 0 \end{pmatrix} \\ &= d_{22}\cos^3\Phi + (d_{12}+2d_{26})\cos^2\Phi\sin\Phi + \\ &\quad (2d_{16}+d_{21})\cos\Phi\sin^2\Phi + d_{11}\sin^3\Phi \end{aligned}$$

$$\mathbf{P}_s^{NL} = \overleftrightarrow{R}\,[0,\Phi,0] \cdot \begin{pmatrix} 0 \\ 1 \\ 0 \end{pmatrix} = \begin{pmatrix} \sin\Phi\left[d_{22}\cos^3\Phi + (d_{12}+2d_{26})\cos^2\Phi\sin\Phi \right. \\ \left. (2d_{16}+d_{21})\cos\Phi\sin^2\Phi + d_{11}\sin^3\Phi\right] \\ \\ \cos\Phi\left[d_{22}\cos^3\Phi + (d_{12}+2d_{26})\cos^2\Phi\sin\Phi \right. \\ \left. (2d_{16}+d_{21})\cos\Phi\sin^2\Phi + d_{11}\sin^3\Phi\right] \\ \\ 0 \end{pmatrix}$$

$$\mathbf{P}_p^{NL} = (\mathbf{P}^{NL} - \mathbf{P}_s^{NL})$$

$$= \begin{pmatrix} d_{12}\cos^2\Phi + d_{11}\sin^2\Phi \\ -\sin\Phi\left[d_{22}\cos^3\Phi + (d_{12}+2d_{26})\cos^2\Phi\sin\Phi \right. \\ \left. +(2d_{16}+d_{21})\cos\Phi\sin^2\Phi + d_{11}\sin^3\Phi\right] + d_{16}\sin 2\Phi \\ \\ d_{22}\cos^2\Phi + d_{21}\sin^2\Phi \\ -\cos\Phi\left[d_{22}\cos^3\Phi + (d_{12}+2d_{26})\cos^2\Phi\sin\Phi \right. \\ \left. +(2d_{16}+d_{21})\cos\Phi\sin^2\Phi + d_{11}\sin^3\Phi\right] \\ +d_{26}\sin 2\Phi \\ \\ d_{32}\cos^2\Phi + d_{31}\sin^2\Phi + d_{36}\sin 2\Phi \end{pmatrix}$$

$$\begin{aligned} P_{p,\perp} &= \mathbf{P}_p^{NL} \cdot \overleftrightarrow{R}\,[0,\Phi,0] \cdot \begin{pmatrix} 1 \\ 0 \\ 0 \end{pmatrix} \\ &= d_{12}\cos^3\Phi + (2d_{16}-d_{22})\cos^2\Phi\sin\Phi \\ &\quad +(d_{11}-2d_{26})\cos\Phi\sin^2\Phi - d_{21}\sin^3\Phi \end{aligned}$$

Appendix B

The phase mismatch factor that results in second harmonic intensity oscillations known as Maker fringes is given by

$$\psi = \frac{2\pi}{\lambda}\left[n_\omega \cos\theta'_\omega - n_{2\omega}\cos\theta'_{2\omega}\right]$$

where θ' is the internal polar angle.

The only output polarization possible for both quartz and a polar film ($C_{\infty v}$) is p-polarization. Projection factors for p-polarized output second harmonic intensity for the measured film (f) and reference quartz plate (q) are:

$$p_{f,x} = 0$$

$$
\begin{aligned}
p_{f,y} &= 0 \\
p_{f,x} &= 1 \\
b_{f,x} &= p_{f,x} - \left(\frac{n_f^\omega}{n_f^{2\omega}}\right)^2 \sin\theta_f^\omega \left(\sin\theta_f^\omega p_{f,x} + \cos\theta_f^\omega p_{f,z}\right) \\
&= -\left(\frac{n_f^\omega}{n_f^{2\omega}}\right)^2 \sin\theta_f^\omega \cos\theta_f^\omega \\
p_{q,x} &= \cos 2\theta_q^\omega \\
p_{q,z} &= 2\cos\theta_q^\omega \sin\theta_q^\omega \\
b_{q,x} &= p_{q,x} - \left(\frac{n_q^\omega}{n_q^{2\omega}}\right)^2 \sin\theta_q^\omega \left(\sin\theta_q^\omega p_{q,x} + \cos\theta_q^\omega p_{q,z}\right) \\
&= \cos 2\theta_q^\omega - \left(\frac{n_q^\omega}{n_q^{2\omega}}\right)^2 \sin\theta_q^\omega \sin 3\theta_q^\omega
\end{aligned}
$$

Using these expressions, one can get the expression for p-polarized output second harmonic intensity as a function of propagation direction for a thin film:

$$
\begin{aligned}
I_{f,p}^{2\omega} \sim \Omega_f = & \left[\frac{2n_g^{2\omega}\cos\theta_g^{2\omega}}{\left(\cos\theta_g^{2\omega} + n_g^{2\omega}\cos\theta\right)\left(n_g^{2\omega}\cos\theta_f^{2\omega} + n_f^{2\omega}\cos\theta_g^{2\omega}\right)}\right]^2 \\
& \times \left\{ 4(n_f^{2\omega})^2 \cos^2\theta_f^{2\omega} \left[\frac{b_{f,x} + n_f^\omega \cos\theta_f \left(\cos\theta_f^\omega p_{f,x} - \sin\theta_f^\omega p_{f,z}\right)}{n_f^{2\omega}\cos\theta_f + \cos\theta_f^{2\omega}}\right]^2 \right. \\
& + \left[n_f^{2\omega} b_{f,x} + n_f^\omega \cos\theta_f^{2\omega}\left(p_{f,x}\cos\theta_f^\omega - p_{f,z}\sin\theta_f^\omega\right)\right]^2 \\
& -4n_f^{2\omega}\cos 2\psi_f \cos\theta_f^{2\omega}\left[n_f^{2\omega} b_{f,x} + n_f^\omega \cos\theta_f^{2\omega}\left(p_{f,x}\cos\theta_f^\omega - p_{f,z}\sin\theta_f^\omega\right)\right] \\
& \left. \times \frac{b_{f,x} + n_f^\omega \cos\theta_f \left(p_{f,x}\cos\theta_f^\omega - p_{f,z}\sin\theta_f^\omega\right)}{n_f^{2\omega}\cos\theta_f + \cos\theta_f^{2\omega}} \right\}
\end{aligned}
$$

Subscripts g and f refer to the constants and parameters for the glass substrate and

the film. Similar relation can be written for a crystalline quartz plate:

$$
\begin{aligned}
I^{2\omega}_{q,p} \;\sim\; \Omega_q = & \left[\frac{1}{n_g^{2\omega}\cos\theta_f^{2\omega} + n_f^{2\omega}\cos\theta_g^{2\omega}}\right]^2 \\
& \times \left\{ 4(n_q^{2\omega})^2 \cos^2\theta_q^{2\omega} \left[\frac{b_{q,x} + n_q^{\omega}\cos\theta_q\left(\cos\theta_q^{\omega} p_{q,x} - \sin\theta_q^{\omega} p_{q,z}\right)}{n_q^{2\omega}\cos\theta_q + \cos\theta_q^{2\omega}}\right]^2 \right. \\
& + \left[n_q^{2\omega} b_{q,x} + n_q^{\omega}\cos\theta_q^{2\omega}\left(p_{q,x}\cos\theta_q^{\omega} - p_{q,z}\sin\theta_q^{\omega}\right)\right]^2 \\
& -4n_q^{2\omega}\cos 2\psi_q \cos\theta_q^{2\omega}\left[n_q^{2\omega} b_{q,x} + n_q^{\omega}\cos\theta_q^{2\omega}\left(p_{q,x}\cos\theta_q^{\omega} - p_{q,z}\sin\theta_q^{\omega}\right)\right] \\
& \left. \times \frac{b_{q,x} + n_q^{\omega}\cos\theta_q\left(p_{q,x}\cos\theta_q^{\omega} - p_{q,z}\sin\theta_q^{\omega}\right)}{n_q^{2\omega}\cos\theta_q + \cos\theta_q^{2\omega}} \right\}
\end{aligned}
$$

The intensities of the SHG signal from the film and quartz slab can are generally detected at different incident angles θ_f and θ_q. Taking into account the appropriate Fresnel transmission factors t_s and t_p (see Eq. 3.19) for the fundamental frequency in both materials and using the experimentally determined ratio of the intensities, one can express the SHG tensor coefficients for the film in terms of known d_q for quartz:

$$
\begin{aligned}
d_{33} &= d_q \sqrt{\frac{I^f_{pp}}{I^q_{pp}} \frac{(n_f^{2\omega})^2 - (n_f^{\omega})^2}{(n_q^{2\omega})^2 - (n_q^{\omega})^2}} \left(\frac{t^{\omega}_{q,p}(\theta_q)}{t^{\omega}_{f,p}(\theta_f)}\right)^2 \sqrt{\frac{\Omega_q(\theta_q)}{\Omega_f(\theta_f)}} \frac{1}{\sin^2\theta_f^{\omega}} \\
d_{31} &= d_q \sqrt{\frac{I^f_{sp}}{I^q_{pp}} \frac{(n_f^{2\omega})^2 - (n_f^{\omega})^2}{(n_q^{2\omega})^2 - (n_q^{\omega})^2}} \left(\frac{t^{\omega}_{q,p}(\theta_q)}{t^{\omega}_{f,s}(\theta_f)}\right)^2 \sqrt{\frac{\Omega_q(\theta_q)}{\Omega_f(\theta_f)}}
\end{aligned}
$$

Practically, it is more reliable to use the "envelope" profile of the fringes as the phase of the oscillations is very sensitive to the thickness of the film and of the quartz slab, so that the entire fringe pattern can be shifted and result in large variations of the intensity. The envelope, however, does not change so rapidly, which provides a more reliable measurement.

References

[1] M. B. Feller, W. Chen, and Y. R. Shen. Investigation of surface-induced alignment of liquid-crystal molecules by optical second-harmonic generation. *Phys. Rev. A*, 43:6778–6792, 1991.

[2] J. A. Armstrong, N. Bloembergen, J. Ducuing, and P. S. Pershan. Interaction between light waves in a nonlinear dielectric. *Phys. Rev.*, 127(6):1918–1939, 1962.

[3] R. Boyd. *Nonlinear optics*. Academic press, San Diego, 1992.

[4] P. D. Maker, R. W. Terhune, M. Nisenoff, and C. M. Savage. Effect of dispersion and focusing on the production of optical harmonics. *Phys. Rev. Lett.*, 8(1):21–22, 1962.

[5] J. Jerphagnon and S. K. Kurtz. Maker fringes: A detailed comparison of theory and experiment for isotropic and uniaxial crystals. *J. Appl. Phys.*, 41(4):1667–1681, 1970.

[6] M. G. Kuzyk and C. W. Dirk, editors. *Characterization Techniques and Tabulations for Organic Nonlinear Optical Materials*, volume 60 of *Optical Engineering*. Marcel Dekker, New York, 1998.

[7] Y. Reznikov, O. Ostroverkhova, K.D. Singer, J.-H. Kim, S. Kumar, O. Lavrentovich, B. Wang, and J.L. West. Photoalignment of liquid crystals by liquid crystals. *Phys. Rev. Lett.*, 84:1930, 2000.

[8] M. Schadt, K. Schmitt, V. Kozinkov, and V. Chigrinov. Surface-induced parallel alignment of liquid crystals by linearly polymerized photopolymers. *Jpn. J. Appl. Phys.*, 31:2155–2164, 1992.

[9] T. Marusii and Yu. Reznikov. *Mol. Mater.*, 3:1614, 1993.

[10] D. Nguyen, T. Mayer, S. Hubbard, K. Singer, J. Mann, and J. Lando. Polar polymeric Langmuir-Blodgett films for optical applications. *Macromolecules*, 30:6150–6157, 1997.

[11] J. Lando, T. Srikhirin, D. Schuele, O. Ostroverkhova, K. Singer, P. Taylor, and J. A. Mann. Electronic and optical properties of polysiloxanes with polar sidechains. *Bull. Am. Phys. Soc.*, 44:1737, 1999.

[12] P. N. Prasad and D. J. Williams. *Introduction to Nonlinear Optical Effects in Molecules and Polymers*. John Wiley and Sons, New York, 1991.

[13] Y. R. Shen. Optical 2nd harmonic-generation at interfaces. *Annu. Rev. Phys. Chem.*, 40:327–350, 1989.

[14] B. Park, H. Choi, H. Kim, H. Hwang, J. Lee, Y. Kim, and H. Woo. Anisotropic orientational distributions of liquid crystal monolayers on photo-isomerisable alignment polymer films. *J. Kor.Phys. Soc.*, 30:202–208, 1997.

[15] M. I. Barnik, L. M. Blinov, A. M. Dorozhkin, and N. M. Shtykov. Polar polymeric Langmuir-Blodgett films for optical applications. *Mol. Cryst. Liq. Cryst.*, 98(1-4):1–12, 1983.

Chapter 6

Summary

In this, final, Chapter of my thesis I will summarize all the work described in the previous chapters.

In this thesis, I presented both theoretical and experimental descriptions of several nonlinear optical (NLO) effects.

The photorefractive (PR) effect, which has a lot of applications, both educational and technological, is one of the most fascinating and complicated NLO effects. It is excellent for educational purposes, as I observed while working with undergraduate students, because the variety of processes that contribute to the PR effect broadens one's views, requiring thinking in a number of directions. It is useful for industrial applications such as optical switching, image processing, associative memories, etc.

The PR effect involves various photoconductivity processes such as charge photogeneration, transport, trapping, etc., and NLO processes such as the linear electro-optic effect and chromophore reorientation in an electric field. In my thesis, I de-

scribed the main points necessary for providing a sensible phenomenological description of each process and maintaining the correct experimental conditions. Chapters 2 and 3 were devoted to space charge field formation which reflects the photoconductivity mechanism of the PR effect. Chapter 4 presented our studies of chromophore reorientation.

In Chapter 2, a PR model that takes into account all the photoconductivity processes was introduced, and the contribution of each process to the PR properties was studied.

First, numerical simulations were performed. We investigated what information could be obtained from the experiment and what conditions were required for this. The outcome of the numerical simulations was the following:

- developed a procedure for determining trapping, detrapping and recombination rates from the experimentally measured photocurrent transients
- predicted the PR speed on the basis of the photoconductivity
- predicted the homogeneous illumination history dependence of the PR dynamics
- studied the processes that influence the PR speed in polymers

Second, the data obtained from the photoconductivity experiments were used to predict the PR speed according to the procedure described in Chapter 2. The predicted values were compared with experimental data (Chapter 3). The behavior

anticipated from the theoretical model was experimentally supported, which showed the validity of the PR model used.

Then, a detailed study of photoconductivity and PR properties of various PVK/C_{60}-based polymer composites was presented in Chapter 3. In particular, the influence of the plasticizer, chromophore content and ionization potential on the photoconductivity and PR dynamics was investigated.

Chapter 4 described our studies of the molecular orientational properties by means of electric field induced second harmonic generation (EFISHG). We showed that the dynamics of the second harmonic generation-rise as the electric field was applied reflected the NLO chromophore reorientational speed. Then, the rotational diffusion model was used to relate the orientational speed measured in the EFISHG experiment to that observed in the holographic measurements of the diffraction efficiency dynamics. Also, we demonstrated how the EFISHG technique can be used as a probe of the internal electric fields in the PR polymer composites.

Chapter 5 illustrated the applications of the second harmonic generation (SHG) experiment to studies of monolayers.

First, we considered Langmuir-Blodgett polymer films. The average molecular tilt angle from the substrate normal for a monolayer and multi-layer films was determined from the polarization dependence of the SHG intensity. The absolute values of the nonlinear susceptibility tensor components of the films were calculated by referencing

the SHG signal from the films to that of quartz and using the known value of quartz nonlinearity. The temperature stability of the films was studied by monitoring the temperature dependence of the SHG signal.

Second, the properties of the 5CB adsorbed and UV-illuminated layer on the fused silica substrate were investigated. The average molecular tilt angle was determined to be 12° from the substrate normal. The azimuthal molecular distribution was numerically simulated for several symmetry groups and compared to the experimentally measured SHG signal under sample rotation around its normal. The UV-illuminated adsorbed 5CB monolayer was shown to possess the C_{2v} symmetry, and the upper limit on the in-plane order parameter $\langle \cos 2\phi \rangle$ yielded 0.06.

In one sentence, the summary of my thesis is that nonlinear optical effects provide an exciting field for applications, can be used as sensitive probes for material properties and constitute a great educational experience.

Bibliography

Abkowitz, M., Bassler, H., and Stolka, M. "Common features in the transport behavior of diverse glassy solids:exploring the role of disorder." *Phil. Mag. B* **63** [**1**] (1991), 201–220.

Abkowitz, M., Stolka, M., and Morgan, M. "Behavior of the drift mobility in the glass transition region of some hole-transporting amorphous organic films." *J. Appl. Phys.* **52** [**5**] (1981), 3453–3457.

Armstrong, J. A., Bloembergen, N., Ducuing, J., and Pershan, P. S. "Interaction between light waves in a nonlinear dielectric." *Phys. Rev.* **127** [**6**] (1962), 1918–1939.

Ashkin, A., Boyd, G. M., Dziedzic, J. M., Smith, R. G., Ballman, A. A., Levinstein, J. J., and Nassau, K. "Optically-induced refractive index change inhomogeneities in $LiNbO_3$ and $LiTaO_3$." *Appl. Phys. Lett.* **9** [**1**] (1966), 72–74.

Barnik, M. I., Blinov, L. M., Dorozhkin, A. M., and Shtykov, N. M. "Polar polymeric Langmuir-Blodgett films for optical applications." *Mol. Cryst. Liq. Cryst.* **98** [**1-4**] (1983), 1–12.

Bassler, H. "Charge transport in disordered organic photoconductors - a monte-carlo simulation study." *Phys. Status Solidi (b)* **175** [**1**] (Jan. 1993), 15–56.

Bittner, R., Brauchle, C., and Meerholz, K. "Influence of the glass transition temperature and the chromophore content on the grating buildup dynamics of poly(n-vinylcarbazole)-based photorefractive polymers." *Appl. Opt.* **37** (1998), 2843–2851.

Blom, P., de Jong, M., and van Munster, M. "Electric-field and temperature dependence of the hole mobility in ppv." *Phys. Rev. B* **55** (1997), R656.

Blum, R., Sprave, M., Sablotny, J., and Eich, M. "High-electric-field poling of nonlinear optical polymers." *J. Opt. Soc. Am. B* **15** [**1**] (1998), 318–328.

Blythe, A. *Electrical Properties of Polymers* Cambridge University Press, 1979.

Born, M., and Wolf, E. *Principles of optics : electromagnetic theory of propagation, interference and diffraction of light*, sixth ed. Pergamon Press, Oxford, New York, 1980.

Borsenberger, P., and Weiss, D. *Organic Photoreceptors for Imaging systems* Marcel Dekker, Inc., 1993.

Borsenberger, P. M., and Weiss, D. S. *Organic photoreceptors for xerography*, vol. 59 of *Optical engineering* Marcell Dekker, Inc., New York, 1998.

Boyd, G. T., Francis, C. V., Trend, J. E., and Ender, D. A. "Second-harmonic generation as a probe of rotational mobility in poled polymers." *J. Opt. Soc. Am. B* **8** [**4**] (Apr. 1991), 887–894.

Boyd, R. *Nonlinear optics* Academic press, San Diego, 1992.

Bozano, L., Carter, S., Scott, J., Malliaras, G., and Brock, P. "Temperature- and field-dependent electron and hole mobilities in polymer light emitting diodes." *Appl. Phys. Lett.* **74** [**8**] (1999), 1132–1134.

Braun, C. L. "Electric-field assisted dissociation of charge-transfer states as a mechanism of photocarrier production." *J. Chem. Phys.* **80** [**9**] (1984), 4157–4161.

Bube, R. *Photoconductivity of Solids* Wiley, 1960.

Chemla, D. S., and Zyss, J., Eds. *Nonlinear optical properties of organic molecules and crystals*, vol. 1,2 Academic, Orlando, 1987.

Chen, F. S. "A laser-induced inhomogeneity of refractive indices in KTN." *J. Appl. Phys.* **38** [**8**] (1967), 3418–3420.

Chen, F. S., LaMacchia, J. T., and Fraser, D. B. "Holographic storage in lithium niobate." *Appl. Phys. Lett.* **13** [**7**] (1968), 223–225.

Cui, Y., Swedek, B., Cheng, N., Zieba, J., and Prasad, P. N. "Dynamics of photorefractive grating erasure in polymeric composites." *J. Appl. Phys.* **85** (Jan. 1999), 38–43.

Daubler, T., Neher, D., Rost, H., and Horhold, H. "Efficient bulk photogeneration of charge carriers and photoconductivity gain in arylamino-ppv polymer sandwich cells." *Phys. Rev. B* **59** (1999), 1964.

Daubler, T. K., Bittner, R., Meerholz, K., Cimrova, V., and Neher, D. "Charge carrier photogeneration, trapping and space-charge field formation in pvk-based photorefractive materials." *Phys. Rev. B* **61** [**20**] (2000), 13515–13527.

Dhinojwala, A., Wong, G. K., and Torkelson, J. M. "Rotational reorientation dynamics of disperse red 1 in polysterene: α-relaxation dynamics probed by second harmonic generation and dielectric relaxation." *J. Chem. Phys.* **100** (1994), 6046–6054.

Ducharme, S., Scott, J. C., Twieg, R. J., and Moerner, W. E. "Observation of the photorefractive effect in a polymer." *Phys. Rev. Lett.* **66** [**14**] (1991), 1846–1849.

Eiermann, R., Parkinson, G. M., Bassler, H., and Thomas, J. M. "Structural investigations of amorphous tetracene and pentacene by low-temperature electron-diffraction." *J. Phys. Chem.* **87** [**4**] (1983), 544–551.

Feller, M. B., Chen, W., and Shen, Y. R. "Investigation of surface-induced alignment of liquid-crystal molecules by optical second-harmonic generation." *Phys. Rev. A* **43** (1991), 6778–6792.

Goonesekera, A., and Ducharme, S. "Effect of dipolar molecules on carrier mobilities in photorefractive polymers." *J. Appl. Phys.* **85** [**9**] (May 1999), 6506–6514.

Goonesekera, A., Ducharme, S., Takacs, J. M., and Zhang, L. "Low-field hole mobility in a photorefractive polymer." *J. Chem. Phys.* **107** [**20**] (Nov. 1997), 8709–8712.

Grunnet-Jepsen, A., Thompson, C. L., and Moerner, W. E. "Systematics of two-wave mixing in a photorefractive polymer." *J. Opt. Soc. Am. B* **15** [**2**] (Feb. 1998), 905–913.

Grunnet-Jepsen, A., Wright, D., Smith, B., Bratcher, M. S., DeClue, M. S., Siegel, J. S., and Moerner, W. E. "Spectroscopic determination of trap density in -sensitized photorefractive polymers." *Chem. Phys. Lett.* **291** [**5-6**] (July 1998), 553–561.

Gunter, P., and Huignard, J.-P., Eds. *Photorefractive Materials and Their Applications I* Springer-Verlag, Berlin, 1988.

Hendrickx, E., Kippelen, B., Thayumanavan, S., Marder, S., Persoons, A., and Peyghambarian, N. "High photogeneration efficiency of charge-transfer

complexes formed between low ionization potential arylamine and C_60." *J. Chem. Phys.* **112** [**21**] (2000), 9557–9561.

Hendrickx, E., Zhang, Y., Ferrio, K. B., Herlocker, J. A., Anderson, J., Armstrong, N. R., Mash, E. A., Persoons, A., Peyghambarian, N., and Kippelen, B. "Photoconductive properties of pvk-based photorefractive polymer composites doped with fluorinated styrene chromophores." *J. Mater. Chem.* **9** [**9**] (Sept. 1999), 2251–2258.

Herlocker, J. A., Ferrio, K. B., Hendrickx, E., Guenther, B. D., Mery, S., Kippelen, B., and Peyghambarian, N. "Direct observation of orientation limit in a fast photorefractive polymer composite." *Appl. Phys. Lett.* **74** [**16**] (Apr. 1999), 2253–2255.

Herlocker, J. A., Fuentes-Hernandez, C., Ferrio, K. B., Hendrickx, E., Blanche, P.-A., Peyghambarian, N., and Kippelen, B. "Stabilization of the response time in photorefractive polymers." *Appl. Phys. Lett.* **77** [**15**] (Oct. 2000), 2292–2294.

Hooker, J. C., Burghardt, W. R., and Torkelson, J. M. "Birefringence and second-order nonlinear optics as probes of polymer cooperative segmental mobility: Demonstration of debye-type relaxation." *J. Chem. Phys.* **111** [**6**] (Aug. 1999), 2779–2788.

Jerphagnon, J., and Kurtz, S. K. "Maker fringes: A detailed comparison of theory and experiment for isotropic and uniaxial crystals." *J. Appl. Phys.* **41** [**4**] (1970), 1667–1681.

Kavarnos, G. J., and Turro, N. J. "Photosensitization by reversible electron-transfer - theories, experimental-evidence, and examples." *Chem. Rev.* **86** (1986), 401–449.

Kim, B. G., Rhee, M. K., and Cha, M. "Simple measurement of space-charge field in a $LiNbO_3$ crystal doped with 0.65 mol. % MgO using second harmonic generation." *Opt. Comm.* **173** (2000), 377–380.

Kogelnik, H. "Coupled wave theory for thick hologram gratings." *The Bell system technical journal* **48** [**9**] (1969), 2909–2947.

Kukhtarev, N. V., Markov, V. B., Soskin, M., and Vinetskii, V. L. "Holographic storage in electro-optic crystals." *Ferroelectrics* **22** (1979), 961.

Kuzyk, M. G., and Dirk, C. W., Eds. *Characterization Techniques and Tabulations for Organic Nonlinear Optical Materials*, vol. 60 of *Optical Engineering* Marcel Dekker, New York, 1998.

Lando, J., Srikhirin, T., Schuele, D., Ostroverkhova, O., Singer, K., Taylor, P., and Mann, J. A. "Electronic and optical properties of polysiloxanes with polar side-chains." *Bull. Am. Phys. Soc.* **44** (1999), 1737.

Maker, P. D., Terhune, R. W., Nisenoff, M., and Savage, C. M. "Effect of dispersion and focusing on the production of optical harmonics." *Phys. Rev. Lett.* **8** [**1**] (1962), 21–22.

Marcus, P., and Siders, P. "Theory of highly exothermic electron transfer reactions." *J. Phys. Chem.* **86** (1982), 622.

Marusii, T., and Reznikov, Y. *Mol. Mater.* **3** (1993), 1614.

Mecher, E., Brauchle, C., Horhold, H. H., Hummelen, J. C., and Meerholz, K. "Comparison of new photorefractive composites based on a poly(phenylene vinylene) derivative with traditional poly(n-vinylcarbazole) composites." *Phys. Chem. Chem. Phys.* **1** (1999), 1749.

Meerholz, K., Mecher, E., Bittner, R., and Nardin, Y. "Competing photorefractive gratings in organic thin-film devices." *J. Opt. Soc. Am. B* **15** (1998), 2114.

Miller, A., and Abrahams, E. "Impurity conditions at low concentrations." *Phys. Rev.* **120** [**1**] (1960), 745–755.

Moerner, W. E., Grunnet-Jepsen, A., and Thompson, C. "Photorefractive polymers." *Annu. Rev. Mater. Sci.* **27** (1997), 585–623.

Moerner, W. E., and Silence, S. M. "Polymeric photorefractive materials." *Chem. Rev.* **94** [**1**] (1994), 127–155.

Moerner, W. E., Silence, S. M., Hache, F., and Bjorklund, G. C. "Orientationally enhanced photorefractive effect in polymers." *J. Opt. Soc. Am. B* **11** [**2**] (Feb. 1994), 320–330.

Mort, J., and Pai, D. *Photoconductivity and related phenomena* Elsevier, 1976.

Mort, J., and Pfister, G. *Electronic properties of polymers* Wiley, New York, 1982.

Mort, J., Pfister, G., and Grammatica, S. "Charge transport and photogeneration in molecularly doped polymers." *Solid State Communications* **18** [**6**] (1976), 693–696.

Mott, N. F., and Davis, E. A. *Electronic processes in non-crystalline materials* Clarendon press, Oxford, 1971.

Movaghar, B. "Transport in polymers." *Phil. Mag. B* **65** [**4**] (1992), 811–816.

Mozumder, A. "Effects of an external electric field on the yield of free ions. II The initial distribution of ion pairs in liquid hydrocarbons." *J. Chem. Phys.* **60** [**11**] (1974), 4305–4310.

Nguyen, D., Mayer, T., Hubbard, S., Singer, K., Mann, J., and Lando, J. "Polar polymeric Langmuir-Blodgett films for optical applications." *Macromolecules* **30** (1997), 6150–6157.

Novikov, S. V., and Vannikov, A. V. "Field-dependence of charge mobility in polymer matrices." *Chem. Phys. Lett.* **182** [**6**] (Aug. 1991), 598–602.

Onsager, L. "Initial recombination of ions." *Phys. Rev.* **54** (1938), 554–557.

Ostroverkhova, O., and Singer, K. D. "Space-charge dynamics in photorefractive polymers I: Theoretical considerations." *Submitted to J. Appl. Phys.* (2001).

Ostroverkhova, O., and Singer, K. D. "Space-charge dynamics in photorefractive polymers II: Material considerations." *submitted to J. Appl. Phys.* (2001).

Park, B., Choi, H., Kim, H., Hwang, H., Lee, J., Kim, Y., and Woo, H. "Anisotropic orientational distributions of liquid crystal monolayers on photoisomerisable alignment polymer films." *J. Kor.Phys. Soc.* **30** (1997), 202–208.

Patsis, A., and Seanor, D., Eds. *Photoconductivity in Polymers* Technomic Publishing Co., Inc., Westport, Conn., 1976.

Pauley, M., Guan, H., and Wang, C. "Poling dynamics and investigation into the behavior of trapped charge in poled polymer films for nonlinear optical applications." *J. Chem. Phys.* **104** (1996), 6834.

Pope, M., and Swenberg, C. *Electronic Processes in Organic Crystals and Polymers* Oxford University Press, 1999.

Prasad, P. N., and Williams, D. J. *Introduction to Nonlinear Optical Effects in Molecules and Polymers* John Wiley and Sons, New York, 1991.

Reznikov, Y., Ostroverkhova, O., Singer, K., Kim, J.-H., Kumar, S., Lavrentovich, O., Wang, B., and West, J. "Photoalignment of liquid crystals by liquid crystals." *Phys. Rev. Lett.* **84** (2000), 1930.

Rudenko, A. I. *Non-Cryst. Solids* **22** (1976), 215.

Schadt, M., Schmitt, K., Kozinkov, V., and Chigrinov, V. "Surface-induced parallel alignment of liquid crystals by linearly polymerized photopolymers." *Jpn. J. Appl. Phys.* **31** (1992), 2155–2164.

Schein, L. "Comparison of charge transport models in molecularly doped polymers." *Phil. Mag. B* **65** [**4**] (1992), 795–810.

Schein, L., Peled, A., and Glatz, D. "The electric field dependence of the mobility in molecularly doped polymers." *J. Appl. Phys.* **66** [**2**] (1989), 686–692.

Scher, H., and Montroll, E. W. "Anomalous transit-time dispersion in amorphous solids." *Phys. Rev. B* **12** (1975), 2455–2477.

Schildkraut, J., and Cui, Y. "Zero order and first order theory of the formation of space-charge gratings in photoconductive polymers." *J. Appl. Phys.* **72** [**11**] (Dec. 1992), 5055–5061.

Schildkraut, J. S., and Buettner, A. V. "Theory and simulation of the formation and erasure of space-charge field gratings in photoconductive polymers." *J. Appl. Phys.* **72** [**5**] (1992), 1888–1893.

Schloter, S., Schreiber, A., Grasruck, M., Leopold, A., Kol'chenko, M., Pan, J., Hohle, C., Strohriegl, P., Zilker, S. J., and Haarer, D. "Holographic and photoelectric characterization of a novel photorefractive organic glass." *Appl. Phys. B* **68** [**5**] (1999), 899–906.

Scott, J. C., Pautmeier, L. T., and Moerner, W. E. "Photoconductivity studies of photorefractive polymers." *J. Opt. Soc. Am. B* **9** [**11**] (1992), 2059–2064.

Shen, Y. R. "Optical 2nd harmonic-generation at interfaces." *Annu. Rev. Phys. Chem.* **40** (1989), 327–350.

Silence, S. M., Bjorklund, G. C., and Moerner, W. E. "Optical trap activation in a photorefractive polymer." *Opt. Lett.* **19** [**22**] (Nov. 1994), 1822–1824.

Silver, M., Risko, K., and Bassler, H. "A percolation approach to exciton diffusion and carrier drift in disordered media." *Philos. Mag. B* **40** [**3**] (1979), 247–252.

Singer, K. D., Kuzyk, M. G., and Sohn, J. E. "2nd-order nonlinear-optical processes in orientationally ordered materials - relationship between molecular and macroscopic properties." *J. Opt. Soc. Am. B* **4** (1987), 968–976.

Slowik, J., and Chen, I. "Effect of molecular rotation upon charge transport between disordered carbazole units." *J. Appl. Phys.* **54** [**8**] (1983), 4467–4473.

Solymar, L., Webb, D. J., and Grunnet-Jepsen, A. *The physics and applications of photorefractive materials*, vol. 11 of *Oxford series in optical and imaging sciences* Clarendon press, Oxford, 1996.

Sutter, K., and Gunter, P. "Photorefractive gratings in the organic-crystal 2-cyclooctylamino-5-nitropyridine doped with 7,7,8,8-tetracyanoquinodimethane." *J. Opt. Soc. Am. B* **7** (1990), 2274–2278.

Walsh, C., and Moerner, W. E. "2-beam coupling measurements of grating phase in a photorefractive polymer." *J. Opt. Soc. Am. B* **9** [**9**] (1992), 1642–1647.

Wang, C. H., Gu, S. H., and Guan, H. W. "Polar order and relaxation of second order nonlinear optical susceptibility in an electric field polarized amorphous polymer." *J. Chem. Phys.* **99** (1993), 5597–5604.

West, K. S., West, D. P., Rahn, M. D., Shakos, J. D., Wade, F. A., Khand, K., and King, T. A. "Photorefractive polymer composite trapping properties and link with a chromophore structure." *J. Appl. Phys.* **84** [**11**] (1998), 5893–5899.

Wolfe, R., Ed. *Applied Solid State Science* Academic Press, New York, 1975.

Wright, D., Diaz-Garcia, M. A., Casperson, J. D., DeClue, M., Moerner, W. E., and Twieg, R. J. "High-speed photorefractive polymer composites." *Appl. Phys. Lett.* **73** [**11**] (Sept. 1998), 1490–1492.

Yeh, P. *Introduction to photorefractive nonlinear optics* Wiley series in pure and applied optics. Wiley, New York, 1993.

Young, R. "Effects of geometrical disorder on hole transport in molecularly doped polymers." *J. Chem. Phys.* **103** [**15**] (1995), 6749–6767.

Zhang, J., and Singer, K. D. "Homogeneous photorefractive polymer/nematogen composite." *Appl. Phys. Lett.* **72** (1998), 2948–2950.

Zilker, S. J., Grasruck, M., Wolff, J., Schloter, S., Leopold, A., Kol'chenko, M. A., Hoffmann, U., Schreiber, A., Strohriegl, P., Hohle, C., and Haarer, D. "Characterization of charge generation and transport in a photorefractive organic glass: comparison between conventional and holographic time-of-flight experiments." *Chem. Phys. Lett.* **306** [**5-6**] (1999), 285–290.